

Characterization and Development of Fired Passivating Contacts for Silicon Solar Cells

Présentée le 16 mars 2022

Faculté des sciences et techniques de l'ingénieur
Laboratoire de photovoltaïque et couches minces électroniques
Programme doctoral en physique

pour l'obtention du grade de Docteur ès Sciences

par

Mario Joe LEHMANN

Acceptée sur proposition du jury

Prof. F. Mila, président du jury
Dr F.-J. Haug, Prof. C. Ballif, directeurs de thèse
Prof. S. Glunz, rapporteur
Dr S. Dubois, rapporteur
Prof. P. Mural, rapporteur

Many small people,
in small places,
doing small things
can change the world.
— Eduardo Galeano

To my family, friends and colleagues. You all contributed directly or indirectly to this work. It is a privilege to be part of such a wonderful network of friendships. I hope that this thesis will also be part of something much bigger than itself, that it will provide some support to other researchers and be a humble contribution to a renewable tomorrow.

Abstract

One of the key elements to improve mainstream crystalline silicon (c-Si) solar cell performance is surface passivation, which is at the center of the ongoing transition from cells with direct silicon-metal contacts to full area passivating contacts. In theory, these contacts combine an optimal passivation and current extraction. Among those, the fired passivating contact (FPC) studied in this thesis is a promising candidate. Based on a 1.3 nm thin tunneling oxide capped with a doped SiC_x layer, it is compatible with the high temperature firing process typically used in industry for metallization. Moreover, its fabrication does not require a long annealing step, reducing its thermal budget.

In this thesis, effective minority carrier lifetime measurements were combined with advanced characterization techniques, such as Secondary Ion Mass Spectrometry (SIMS), to investigate the surface passivation mechanism. Chemical passivation was found to be predominant, achieved through hydrogen diffusion from a $\text{SiN}_x\text{:H}$ reservoir layer to the c-Si/ SiO_x interface where it accumulates. The composition of the interfacial oxide was found to influence the surface passivation quality too, reaching implied open circuit voltage (iV_{oc}) values around 710, 720 and 740 mV with chemical, UV- O_3 and thick thermal oxides, respectively. After firing, the boron-doped $\text{SiC}_x(p)$ layer was observed to consist of 5–10 nm large c-Si grains embedded in a carbon rich amorphous matrix.

Surprisingly, it was found that the firing step can induce shallow bulk defects within the used Float-Zone (FZ) wafers, which can be passivated by hydrogen. Kinetics experiments indicate a rapid passivation of the c-Si/ SiO_x interface, happening in less than 1 min, followed by a slower passivation of the bulk. The kinetics of the hydrogenation process seem to be limited by the available hydrogen supply, rather than by its diffusivity within the bulk. In addition, the possibility to hydrogenate both surfaces with a $\text{SiN}_x\text{:H}$ layer deposited on only one side of the wafer was demonstrated, providing further flexibility to the fabrication process of FPC based solar cells.

Pursuing the same goal, diffusion of fluorine from $\text{SiC}_x(p)\text{:F}$ layers upon firing was tested. The results indicate that this approach can also passivate the c-Si/ SiO_x interface even though the iV_{oc} after firing seems to be limited by the creation of shallow bulk defects. Nevertheless, values over 730 mV could be reached with UV- O_3 SiO_x layers upon subsequent hydrogenation. Regarding the stability of this passivation, no degradation was observed for FPCs upon 80 days

of light soaking at 80 °C. Moreover, it remained stable upon thermal treatments of 30 min up to 170 °C.

Finally, metallization of these FPCs was studied. A layer stack with a total thickness of ~90 nm was developed to be contacted by a screen printed Al paste fired through the SiN_x:H layer. Unfortunately, so far good contact resistivities could only be achieved at the expense of passivation. Closer microstructural investigations revealed diffusion of Al from the metallic paste into the SiN_x:H layer, forming an Al-N compound, and in some cases accumulating in the SiO_x layer. Nevertheless, using a low temperature metallization approach, solar cells featuring co-fired SiC_x(*n*) and SiC_x(*p*) FPCs at the front and rear were processed, reaching up to 20.5% in efficiency. This corroborates the potential of FPCs for high efficiency solar cells with a simple and low-cost fabrication process.

Key words: crystalline silicon solar cells, passivating contacts, hydrogenation, firing, metallization, stability, float-zone, SIMS, PECVD, fluorine.

Zusammenfassung

Eines der Schlüsselemente zur Verbesserung der Leistung von Solarzellen aus kristallinem Silizium (c-Si) ist die Oberflächenpassivierung, die im Mittelpunkt des derzeitigen Übergangs von Zellen mit direkten Kontakt zwischen Silizium und Metall zu vollflächigen passivierenden Kontakten steht. Theoretisch kombinieren diese Kontakte eine optimale Passivierung und Stromabnahme. Der in dieser Arbeit untersuchte gefeuerte passivierende Kontakt (FPC) ist in dieser Hinsicht ein vielversprechender Kandidat. Er basiert auf einem 1.3 nm dünnen Tunneloxid, das mit einer dotierten SiC_x -Schicht überzogen ist, und ist mit dem Hochtemperatur-Feuerverfahren kompatibel, welches in der Industrie üblicherweise für die Metallisierung verwendet wird. Darüber hinaus ist bei der Herstellung kein langer Temperprozess erforderlich, was das thermische Budget reduziert.

In dieser Arbeit wurden Messungen der effektiven Lebensdauer von Minoritäts-Ladungsträgern mit fortgeschrittenen Charakterisierungstechniken wie der Sekundärionen-Massenspektrometrie (SIMS) kombiniert, um den Mechanismus der Oberflächenpassivierung zu untersuchen. Es wurde festgestellt, dass die chemische Passivierung vorherrscht, welche erreicht werden kann, indem Wasserstoff aus einer $\text{SiN}_x\text{:H}$ -Reservoir-Schicht ausdiffundiert und sich an der c-Si/ SiO_x -Grenzfläche anreichert. Des Weiteren wurde festgestellt, dass auch die Zusammensetzung des Grenzflächenoxids die Qualität der Oberflächenpassivierung beeinflusst, und es wurden implizite Leerlaufspannungen (iV_{oc}) von respektive 710, 720 bzw. 740 mV mit chemischen, UV- O_3 bzw. dicken thermischen Oxiden erreicht. Ausserdem zeigte sich, dass die mit Bor dotierte $\text{SiC}_x(p)$ -Schicht nach dem Feuern aus 5–10 nm grossen c-Si-Körnern besteht, die in eine kohlenstoffreiche amorphe Matrix eingebettet sind.

Überraschenderweise wurde beobachtet, dass der Feuer-Schritt in den verwendeten Float-Zone (FZ) Wafern Volumendefekte nahe einer der Bandkanten induzieren kann, die durch Wasserstoff passiviert werden können. Kinetik-Experimente deuten auf eine schnelle Passivierung der c-Si/ SiO_x -Grenzfläche innerhalb von weniger als 1 min hin, gefolgt von einer langsameren Passivierung der Volumendefekte. Die Kinetik des Wasserstoff-Passivierungs-Prozesses scheint durch die verfügbare Menge von Wasserstoff begrenzt zu sein und nicht durch seine Diffusionsgeschwindigkeit im Volumen. Dies liess sich nutzen, um beide Oberflächen mit Wasserstoff-Diffusion aus einer einzigen $\text{SiN}_x\text{:H}$ -Schicht auf einer Seite des Wafers zu passivieren, was dem Herstellungsprozess von Solarzellen auf FPC-Basis weitere Flexibilität verleiht.

Mit dem gleichen Ziel wurde die Diffusion von Fluor aus $\text{SiC}_x(p):F$ -Schichten während dem Feuern getestet. Die Ergebnisse deuten darauf hin, dass auch mit diesem Ansatz die $c\text{-Si/SiO}_x$ -Grenzfläche passiviert werden kann. Leider schienen auch in diesem Experiment die iV_{oc} -Werte durch die Bildung von Volumendefekten während des Feueerschrittes begrenzt zu sein. Dennoch konnten mit UV- O_3 SiO_x -Schichten und anschliessender Wasserstoff-Passivierung Werte über 730 mV erreicht werden.

Was die Stabilität dieser Passivierung anbelangt, so wurde bei den FPCs nach 80 Tagen Lichtbehandlung bei 80 °C keine Degradation beobachtet. Darüber hinaus blieb die Passivierung bei thermischen Behandlungen von 30 min bis zu 170 °C stabil.

Schliesslich wurde die Metallisierung der FPCs untersucht. Es wurde ein Schichtstapel mit einer Gesamtdicke von ~90 nm entwickelt, mit dem Ziel jenen mit einer siebgedruckten Al-Paste zu kontaktieren, die durch die $\text{SiN}_x\text{:H}$ -Schicht gefeuert wird. Leider konnten bisher gute Kontakt-Widerstände nur auf Kosten der Passivierung erreicht werden. Genauere mikrostrukturelle Untersuchungen ergaben, dass Al aus der Metallpaste in die $\text{SiN}_x\text{:H}$ -Schicht diffundiert, wo es eine Al-N-Verbindung bildet, und sich in einigen Fällen auch in der SiO_x -Schicht anreichert. Mit einer Niedertemperatur-Metallisierung liessen sich dennoch Solarzellen mit Wirkungsgraden bis zu 20.5% herstellen. Die thermische Behandlung der $\text{SiC}_x(n)$ - und $\text{SiC}_x(p)$ -FPCs auf der Vorder- und Rückseite dieser Zellen erfolgte im gleichen Feuerschritt und unterstreicht dadurch noch einmal das Potenzial von FPCs für hocheffiziente Solarzellen mit einem einfachen und kostengünstigen Herstellungsprozess.

Stichwörter: kristalline Silizium-Solarzellen, passivierende Kontakte, Wasserstoff-Passivierung, Feuern, Metallisierung, Stabilität, Float-Zone, SIMS, PECVD, Fluor.

Résumé

L'un des éléments clés pour améliorer les performances de cellules solaires en silicium cristallin (c-Si) est la passivation des surfaces, qui est au centre de la transition actuelle de cellules avec des contacts directs entre métal et le substrat en c-Si, vers des contacts passivants sur toute la surface. En théorie, ces contacts combinent une passivation et une extraction de courant optimales. Parmi ceux-ci, le contact passivant avec recuit rapide (FPC) étudié dans cette thèse est un candidat prometteur. Basé sur un oxyde tunnel de 1.3 nm d'épaisseur recouvert d'une couche de SiC_x dopée, il est compatible avec le procédé de recuit rapide à haute température généralement utilisé dans l'industrie pour la métallisation. De plus, sa fabrication ne nécessite pas d'étape de recuit lent, réduisant ainsi son budget thermique.

Dans cette thèse, des mesures de durée de vie effectives des porteurs de charge minoritaires ont été combinées avec des techniques de caractérisation avancées, telles que la spectrométrie de masse des ions secondaires (SIMS), pour étudier le mécanisme de passivation des surfaces. La passivation chimique s'est avérée être prédominante, réalisée par la diffusion d'hydrogène d'une couche réservoir $\text{SiN}_x\text{:H}$ vers l'interface c-Si/ SiO_x où il s'accumule. La composition de l'oxyde interfacial s'est également avérée influencer la qualité de la passivation des surfaces, atteignant des tensions implicites de circuit ouvert (iV_{oc}) d'environ 710, 720 et 740 mV avec des oxydes chimiques, UV- O_3 et thermiques épais, respectivement. Après le recuit rapide, la couche de $\text{SiC}_x(p)$ dopée au bore a été observée être constituée de grains de c-Si d'une taille de 5–10 nm, incorporés dans une matrice amorphe riche en carbone.

Il a été constaté avec surprise que l'étape de recuit rapide peut induire des défauts peu profonds dans le volume des substrats à zone flottante (FZ) utilisés, qui peuvent être passivés à l'aide d'hydrogène. Des expériences de cinétique indiquent une passivation rapide de l'interface c-Si/ SiO_x , achevée en moins d'une minute, suivie d'une passivation plus lente du volume. La cinétique du processus d'hydrogénation semble être limitée par l'approvisionnement en hydrogène, plutôt que par sa diffusivité dans le volume des substrats. En outre, la possibilité d'hydrogéner les deux surfaces avec une couche réservoir $\text{SiN}_x\text{:H}$ déposée sur un seul côté du substrat a été démontrée, ce qui apporte davantage de flexibilité au processus de fabrication des cellules solaires intégrant des FPCs.

Dans le même but, la diffusion de fluor à partir de couches de $\text{SiC}_x(p)\text{:F}$ lors du recuit rapide a été testée. Les résultats indiquent que cette approche peut également passiver l'interface c-Si/ SiO_x , même si l' iV_{oc} après recuit rapide semble limitée par la création de défauts peu

profonds dans le volume. Néanmoins, des valeurs supérieures à 730 mV ont pu être atteintes après hydrogénation avec des couches UV-O₃ SiO_x.

En ce qui concerne la stabilité de cette passivation, aucune dégradation n'a été observée pour les FPCs après 80 jours d'illumination à 80 °C. De plus, elle est restée stable lors de traitements thermiques de 30 min jusqu'à 170 °C.

Enfin, la métallisation de ces FPCs a été étudiée. Un empilement de couches d'une épaisseur totale de ~90 nm a été développé pour être contacté par une pâte d'Al sérigraphiée brûlée à travers la couche de SiN_x:H. Malheureusement, jusqu'à présent, de bonnes résistivités de contact n'ont pu être obtenues qu'au détriment de la passivation. Des études microstructurales ont révélé la diffusion d'Al de la pâte métallique dans la couche de SiN_x:H, formant un composé Al-N, et dans certains cas, s'accumulant dans la couche de SiO_x. Néanmoins, à l'aide d'une approche de métallisation à basse température, des cellules solaires comportant des FPCs SiC_x(*n*) et SiC_x(*p*) à l'avant et à l'arrière, recuits en parallèle, ont été fabriquées, atteignant des efficacités jusqu'à 20.5%. Cela corrobore le potentiel des FPC à permettre la réalisation de cellules solaires à haut rendement avec un processus de fabrication simple et peu coûteux.

Mots clefs : cellules solaires en silicium cristallin, contacts passivants, hydrogénation, recuit rapide, métallisation, stabilité, zone flottante, SIMS, PECVD, fluor.

Contents

Abstract (English/Français/Deutsch)	i
List of figures	xi
List of tables	xiii
List of abbreviations and symbols	xv
1 Introduction	1
1.1 Solar energy and climate change	1
1.2 Theoretical background	2
1.2.1 Working principles of solar cells	2
1.2.2 Characterization of solar cells	4
1.2.3 Recombination and passivation	7
1.3 Photovoltaic technologies	13
1.4 High Temperature stable Passivating Contacts (HTPC)	15
1.4.1 History and state of the art	15
1.4.2 Fired Passivating Contacts (FPC)	16
1.4.3 Surface passivation	18
1.4.4 Firing	21
1.4.5 Metallization	21
1.5 Objectives and structure of this thesis	22
1.6 Contribution to the field	23
2 Experimental details	25
2.1 Sample preparation and systems	25
2.1.1 Wafer preparation	26
2.1.2 Oxide growth	27
2.1.3 Deposition of doped layers	28
2.1.4 Rapid Thermal Processing (RTP)	28
2.1.5 Hydrogenation	28
2.1.6 Metallization	29
2.1.7 Wet-chemical layer removal	31
2.2 Characterization techniques	31

2.2.1	Quasi-Steady State Photoconductance	31
2.2.2	Photoluminescence imaging	33
2.2.3	Modulated Photoluminescence	33
2.2.4	Secondary Ion Mass Spectrometry	34
2.2.5	Atom Probe Tomography	35
2.2.6	Ion Beam Analysis	36
2.2.7	Spectroscopic Ellipsometry	36
2.2.8	Fourier-Transform Infrared spectroscopy	37
2.2.9	Raman Spectroscopy	38
2.2.10	Scanning Electron Microscopy	39
2.2.11	Transmission Electron Microscopy	39
2.2.12	Transfer Length Method	40
2.2.13	Current-voltage cell characterization	40
3	Hydrogenation of the interface	43
3.1	Introduction	43
3.2	Experimental details	46
3.3	Hydrogen distribution and migration as a function of the processing step . . .	48
3.4	Hydrogen distribution and migration for different thicknesses of the interfacial oxide	50
3.5	Effect of the interfacial oxide's nature on the passivation quality	53
3.6	Nature of the passivation	54
3.7	Conclusions	56
4	Bulk defects and kinetics	59
4.1	Introduction	59
4.2	Experimental details	60
4.3	Shallow bulk defects created upon firing	61
4.4	Hydrogenation kinetics	65
4.5	In situ lifetime measurements in real time	68
4.6	Single sided hydrogen source	70
4.7	Conclusions	76
5	Stability of the passivation	79
5.1	Introduction	79
5.2	Experimental details	80
5.3	Long-term evolution of the passivation upon light soaking	81
5.4	Hydrogen outdiffusion	83
5.5	Passivation changes upon storage	84
5.6	Conclusions	85

Contents

6 Metallization of Fired Passivating Contacts	87
6.1 Introduction	88
6.2 Experimental details	89
6.3 Thick firing stable layers	92
6.4 Firing through	96
6.5 Aluminium evaporation	101
6.6 Co-fired solar cells	102
6.7 Conclusions	105
7 Summary and perspectives	109
7.1 Summary	109
7.2 Perspectives	110
A Analysis of SiC_x layers	113
B Quantification of H and D in SiN_x:H/D layers	117
C Chemical passivation using fluorine	121
Bibliography	125
List of publications	151
Curriculum Vitae	153
Acknowledgements	155

List of Figures

1.1	IPCC: Change in global temperature	2
1.2	Picture of a modern commercial solar cell	3
1.3	J-V curve and two-diode model	5
1.4	Recombination processes in a semiconductor	7
1.5	Surface recombination process in a semiconductor	11
1.6	Effect of recombination on lifetime curve	12
1.7	Surface passivation in FPCs	14
1.8	Al-BSF and PERC solar cells	15
1.9	TOPCon and POLO solar cells	17
1.10	Ideal cell fabrication process featuring FPCs	18
2.1	Fabrication process of FPC test structures	26
2.2	AFM image of a SE wafer surface	27
2.3	Various designs of metallized samples	30
2.4	Picture of the WCT-120TS setup	32
2.5	Schematic of the MPL setup	34
2.6	Raman spectra of a-Si:H and μ c-Si:H	39
2.7	Schematic explanation of the TLM measurement	41
3.1	Process flow of surface hydrogenation experiment	46
3.2	Lifetime and deuterium distribution as a function of the processing step	49
3.3	Hydrogen distribution as a function of the processing step	50
3.4	Deuterium distribution for several oxide types	51
3.5	APT profile through $\text{SiC}_x(p)$	52
3.6	Lifetime curves for several oxide types	54
3.7	Passivation in function of SiC_x layer type	56
4.1	PL images of bulk passivation during processing	62
4.2	Linearized lifetime curves, DPSS and residuals	63
4.3	PL images of samples after bulk curing tests	65
4.4	PLI evolution	66
4.5	Passivation in function of hotplate temperature	66
4.6	Lifetime evolution of symmetrical samples	67
4.7	Evolution of lifetimes over n/p of symmetrical samples	68

4.8	MPL measurements	70
4.9	H-diffusion from single-side $\text{SiN}_x\text{:H/D}$ layer	71
4.10	PL images of samples without $\text{SiN}_x\text{:H}$ during processing	74
4.11	Lifetime evolution of samples with $\text{SiN}_x\text{:H/D}$ on front side only	75
4.12	Compilation of kinetic fits	76
4.13	Linearized lifetime curves of samples with $\text{SiN}_x\text{:H/D}$ on front side only	77
5.1	LID in FZ silicon	80
5.2	Light spectrum of light soaker	81
5.3	Long-term lifetime evolution upon light soaking	82
5.4	Lifetime evolution during post-hydrogenation hotplate treatment	83
5.5	Lifetime changes upon storage	84
5.6	Changes in J_0 and τ_{bulk} upon storage	86
6.1	Firing-through test sample fabrication process	90
6.2	Cell fabrication process featuring FPCs	91
6.3	PL images of metallized test samples	92
6.4	Optical microscope images of blistering	93
6.5	SIMS measurements on blistered layers	94
6.6	STEM image of a $\text{SiO}_x/\text{SiC}_x(p)/\text{a-Si:H}(p)/\text{SiN}_x\text{:H}$ stack	95
6.7	FTIR and RS measurements of $\text{SiC}_x(p)/\text{a-Si:H}(p)$ stacks	96
6.8	STEM-EDX images of a metallized $\text{SiO}_x/\text{SiC}_x(p)/\text{a-Si:H}(p)/\text{SiN}_x\text{:H}$ stack	97
6.9	STEM-EDX images of a metallized $\text{SiO}_x/\text{SiC}_x(p)/\text{a-Si:H}(p)/\text{SiN}_x\text{:H}$ stack 2	98
6.10	SEM image of fired-through finger	99
6.11	SEM-EDX images of metallized regions after removing fingers	100
6.12	SEM images comparing finger and TLM pad regions	100
6.13	STEM-EDX images of fired-through evaporated Al	101
6.14	PL images of evaporated Al TLM pads	102
6.15	Cell parameters measured by J-V	104
6.16	J-V curves of co-fired cells	105
6.17	Efficiency evolution upon sintering	106
6.18	V_{oc} loss upon metallization	107
A.1	APT analysis of SiC_x layers	114
A.2	STEM, STEM-EDX and EELS images of SiC_x layers	115
A.3	Raman spectroscopy of SiC_x layers	115
A.4	SIMS analysis of hydrogenated SiC_x sample	116
B.1	FTIR measurements of $\text{SiN}_x\text{:H/D}$ layers with varying D content	117
B.2	RBS and ERDA measurements of $\text{SiN}_x\text{:H/D}$ layers with varying D content	118
C.1	Schematic illustration of fluorine passivation	122
C.2	HR-TEM and STEM-HAADF of a fluorinated FPC	123
C.3	PL images of fluorinated FPCs	124

List of Tables

4.1	S_{back} values for various samples	74
6.1	Passivation and contact resistivity of $\text{SiC}_x(p)/\text{a-Si:H}(p)$ stacks metallized by firing-through.	97
B.1	H and D content of $\text{SiN}_x\text{:H/D}$ from FTIR and ERDA	119
C.1	Best iV_{oc} values obtained with fluorinated FPCs	124

List of abbreviations and symbols

Basics

PV	Photovoltaic
ARC	Anti-Reflective Coating
n	refractive index
BSF	Back Surface Field
MCD	Minority Carrier Density
SRH	Shockley-Read-Hall
DPSS	Defect Parameter Solution Surface
E_g	Bandgap energy
E_F	Fermi level
τ_{eff}	Effective minority carrier lifetime
$\tau_{\text{eff}@10^{15}\text{cm}^{-3}}$	τ_{eff} at MCD of $1 \cdot 10^{15} \text{cm}^{-3}$
S_{eff}	Effective surface recombination velocity
$S_{\text{eff}@10^{15}\text{cm}^{-3}}$	S_{eff} at MCD of $1 \cdot 10^{15} \text{cm}^{-3}$
J_0	Dark saturation current density
D_{it}	Interfacial defect density
iV_{oc}	Implied open circuit voltage
V_{oc}	Open circuit voltage
J_{sc}	Short circuit current
FF	Fill factor
η	Energy conversion efficiency
ρ_c	Specific contact resistivity
LID	Light-Induced Degradation
LeTID	Light- and elevated Temperature-Induced Degradation

Materials

Si	Silicon
c-Si	Crystalline silicon
FZ	Float-Zone

Cz	Czochralski
SE	Shiny-Etched
DSP	Double Side Polished
SiO _x	Silicon oxide (sub-stoichiometric)
SiO ₂	Silicon dioxide (stoichiometric)
Chem SiO _x	Chemically grown SiO _x (HNO ₃)
UV-O ₃ SiO _x	SiO _x grown by exposition to ultraviolet/ozone
Therm SiO ₂	Thermally grown SiO ₂
a-Si:H	Hydrogenated amorphous silicon
a-Si:H(<i>i</i>)	Intrinsic hydrogenated amorphous silicon
a-Si:H(<i>n</i>)	<i>n</i> -type hydrogenated amorphous silicon
a-Si:H(<i>p</i>)	<i>p</i> -type hydrogenated amorphous silicon
μc-Si:H	Hydrogenated microcrystalline silicon
μc-Si:H(<i>p</i>)	<i>p</i> -type hydrogenated microcrystalline silicon
poly-Si	Polycrystalline silicon
SiC _x	Silicon carbide
SiC _x (<i>p</i>)	<i>p</i> -type silicon carbide
SiC _x (<i>n</i>)	<i>n</i> -type silicon carbide
SiC _x (<i>i</i>)	Intrinsic silicon carbide
a-SiC _x	Amorphous silicon carbide
nc-SiC _x	Nanocrystalline silicon carbide
SiN _x	Silicon nitride
SiN _x :H	Hydrogenated silicon nitride
SiN _x :D	deuterated silicon nitride
AlO _x /Al ₂ O ₃	Aluminum oxide
ARC	Anti-Reflective Coating
TCO	Transparent Conductive Oxide
ITO	Indium-Tin-Oxide
AZO	Aluminum-doped Zinc Oxide
Ag	Silver
Al	Aluminum

Fabrication Processes

PECVD	Plasma Enhanced Chemical Vapor Deposition
LPCVD	Low Pressure Chemical Vapor Deposition
PVD	Physical Vapor Deposition
ALD	Atomic Layer Deposition
RTP	Rapid Thermal Processing
HP	Hotplate
FGA	Forming Gas Annealing
RPHP	Remote Plasma Hydrogen Passivation

List of abbreviations and symbols

HF	Hydrofluoric acid
HNO ₃	Nitric acid
KOH	Potassium hydroxide
H ₃ PO ₄	Phosphoric acid
CP4	Chemical Polish (to etch c-Si)
SiH ₄	Silane
H ₂	Hydrogen
D ₂	Deuterium
CH ₄	Methane
B(CH ₃) ₃	Trimethylborane (2% in H ₂)
PH ₃	Phosphine (2% in H ₂)
NH ₃	Ammonia
BF ₃	Boron trifluoride
SiF ₄	Silicon tetrafluoride

Characterization Techniques

QSSPC	Quasi-Steady-State Photoconductance
PL	Photoluminescence
MPL	Modulated Photoluminescence
SIMS	Secondary Ion Mass Spectrometry
RBS	Rutherford Backscattering Spectrometry
ERDA	Elastic Recoil Detection Analysis
APT	Atom Probe Tomography
RS	Raman Spectroscopy
FTIR	Fourier-Transform Infrared spectroscopy
FIB	Focused Ion Beam
SEM	Scanning Electron Microscopy
TEM	Transmission Electron Microscopy
HR-TEM	High Resolution Transmission Electron Microscopy
STEM	Scanning Transmission Electron Microscopy
HAADF	High-Angle Annular Dark Field
AFM	Atomic Force Microscopy
EELS	Electron Energy Loss Spectroscopy
EDX	Energy-Dispersive X-ray spectroscopy
TLM	Transfer Length Method
J-V	Current-voltage cell characterization

Solar Cell Technologies

HTPC	High Temperature stable Passivating Contacts
------	--

List of abbreviations and symbols

FPC	Fired Passivating Contact
SHJ	Silicon Heterojunction
PERC	Passivated Emitter and Rear Cell
Al-BSF	Aluminum Back Surface Field
SIPOS	Semi-Insulating POLycrystalline Silicon
TOPCon	Tunnel Oxide Passivating Contact
POLO	POLycrystalline silicon on Oxide
IBC	Interdigitated Back-Contact

1 Introduction

This chapter is meant to provide the general context and motivation for the the work presented in this thesis. It describes the role of photovoltaics (PV) in the transition to renewable energies, provides some theoretical background on the working principles of solar cells and describes several existing PV technologies. In this context, the advantages of high temperature stable passivating contacts (HTPC), and especially fired passivating contacts (FPC), are given, along with a short overview of the state of the art and remaining challenges. Finally, the objectives and structure of this thesis are explained, and its contribution to the field highlighted.

1.1 Solar energy and climate change

At the time of writing of this thesis, the 26th Conference of Parties (COP 26), also called the United Nations climate summit, was held in Glasgow, negotiating once more the actions to be taken by the signing nations to meet the goals of the Paris Agreement (reached at COP21 in 2015), which aims at keeping the rise in mean global temperature below 2 °C above pre-industrial levels. Indeed, as shown in Fig. 1.1, a dramatic increase of temperature occurred during the last century, caused by human greenhouse gas emissions, and rapid actions are needed to limit the negative consequences of climate change [IPCC et al., 2021], [IRENA, 2021b]. The main source of these emissions is the burning of fossil fuels, accounting for more than 80% of the world total energy supply in 2019 [IEA, 2021]. Hence, decarbonizing the energy sector is one of the major challenges of our time, and PV is forecasted to play a key role in this transition to renewable energies [IRENA, 2021b]. Indeed, the potential for PV is huge. On the one hand, the energy reaching earth's surface in form of solar irradiation in a single hour is almost equivalent to the world total energy consumption in a full year. On the other hand, crystalline silicon (c-Si) based PV has grown to a mature technology over the past decades, reaching efficiencies up to 26.7% in laboratories [NREL, 2021], exceeding 25% in industrial R&D [Smith et al., 2016], [Meyer Burger, 2020], [LONGi Solar, 2021], [JinkoSolar, 2021], and prices per kWh competing with fossil fuels [IRENA, 2021a]. Increasing the conversion efficiency of solar cells is one of the main levers to reduce the cost of PV generated electricity. At the

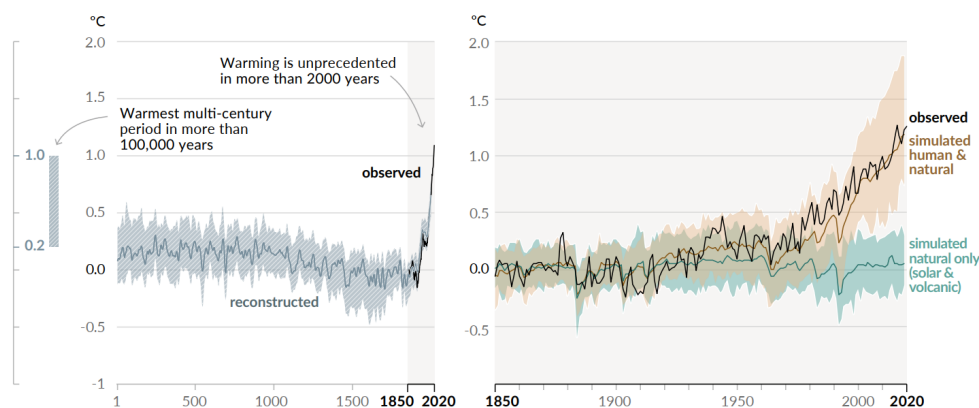


Figure 1.1 – (a) Change in global surface temperature (decadal average) as reconstructed (in blue, 1–2000) and observed (in black, 1850–2020). (b) Change in global surface temperature (annual average) as observed (in black) and simulated using human & natural (in orange) and only natural (in green) factors (both 1850–2020). Reproduced without modifications from [IPCC et al., 2021] licensed under a (CC BY) license (<https://creativecommons.org/licenses/by/4.0/>). Copyright ©2021, Intergovernmental Panel on Climate Change.

same time, it reduces their material consumption and embodied greenhouse gas emissions per kWh, making them an even more sustainable product. Thanks to ongoing research and development, these figures will continue to improve, facilitating the desperately needed energy transition. Moreover, providing access to clean, affordable and locally produced energy, is a key element for sustainable human development, reducing poverty and inequalities, without compromising the goal of carbon neutrality [UNDP, 2020].

1.2 Theoretical background

1.2.1 Working principles of solar cells

Fundamentally, a solar cell consists of an absorber region and selective contacts. The absorber consists of a semiconductor material (such as c-Si) in which photogeneration takes place: incoming photons transfer their energy to an electron, exciting it from the valence band to the conduction band and thus creating an electron-hole pair. The selective contacts consist generally of doped regions, featuring much higher conductivity for one of the two carrier types (holes or electrons), and hence extracting this carrier type while blocking the other [U. Würfel et al., 2015]. A picture of a modern commercial solar cell is shown in Fig. 1.2. The visible features are mainly the metallic lines printed on top of the selective contacts for current collection (needed since the conductivity of c-Si is too low for long range current transport). This is a so-called bifacial cell, allowing to absorb light on both sides, as can be deduced from the presence of metallic fingers and busbars also on the rear (instead of an opaque full area metallic contact). Its blue color is due to the presence of an antireflective coating (ARC), enhancing the absorption of light. Further details regarding solar cell designs and schematic

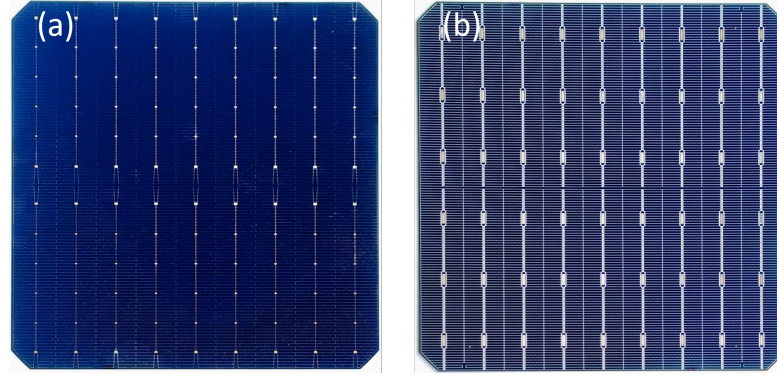


Figure 1.2 – Picture of a modern commercial bifacial solar cell, featuring metallic busbars and fingers on both the front (a) and rear (b) side.

representations of various architectures are provided in sections 1.3 and 1.4.

In order to generate an electron-hole pair, an incoming photon must have an energy $E_{ph} = hc/\lambda$ larger than E_g , the bandgap of the semiconductor material. For c-Si, $E_g = 1.12$ eV at room temperature. Therefore, c-Si effectively absorbs photons with wavelengths $\lambda < 1100$ nm. As c-Si is an indirect bandgap semiconductor, sub-bandgap absorption occurs too, but with a sharp drop in the absorption coefficient's value for wavelengths $\lambda > 1100$ nm [Green, 2008]. Note that the excess energy $E_{ph} - E_g$ is lost by the charge carriers in the form of heat transmitted to the crystalline lattice (thermalization process), and can not be extracted as electrical power. The electron-hole pair generation $G(x, \lambda)$ as function of the depth into the absorbing semiconductor for a single wavelength λ can be approximated by:

$$G(x, \lambda) = \alpha(\lambda)\Phi(\lambda)e^{-\alpha(\lambda)x} \quad (1.1)$$

where $\alpha(\lambda)$ is the absorption coefficient of the material, $\Phi(\lambda)$ the photon flux at the surface and x the depth into the material. The above formula holds for a semi-infinite semiconductor. Taking into account the reflections at the front and rear surfaces of a semiconductor with finite thickness d , the generation becomes:

$$G(x, \lambda) = \Phi(\lambda)(1 - R_f) \frac{\alpha(\lambda)e^{-\alpha(\lambda)x} + \alpha(\lambda)R_r e^{-\alpha(\lambda)(2d-x)}}{1 - R_f R_r e^{-2\alpha(\lambda)d}} \quad (1.2)$$

where R_f and R_r are the reflectivities at the front and rear surfaces, respectively.

At temperatures above 0 K, thermal generation of carriers (electron and holes) occurs. Without carrier extraction, the generated electron-hole pairs eventually recombine. The semiconductor therefore reaches a thermal equilibrium state, in which the thermal generation G_{th} and the recombination rate R_{th} cancel each other out. The temperature dependent intrinsic carrier

density n_i (without illumination) of a semiconductor is given by:

$$n_i^2 = n_0 p_0 = N_C e^{-\frac{E_C - E_F}{k_B T}} N_V e^{-\frac{E_F - E_V}{k_B T}} = N_C N_V e^{-\frac{E_C - E_V}{k_B T}} \quad (1.3)$$

where n_0 and p_0 are the electron and hole densities, respectively, N_C and N_V the densities of states in the conduction band and valence band, respectively, E_C and E_V the energy levels of the conduction band and valence band, respectively, E_F the Fermi energy, k_B the Boltzmann constant and T the temperature.

Under illumination, the injected excess carrier densities $\Delta n = \Delta p$ coming from photogeneration are added to n_0 and p_0 , leading to:

$$n = n_0 + \Delta n = N_C e^{-\frac{E_C - E_{Fn}}{k_B T}} \quad \text{and} \quad p = p_0 + \Delta p = N_V e^{-\frac{E_{Fp} - E_V}{k_B T}} \quad (1.4)$$

$$np = n_i^2 e^{\frac{E_{Fn} - E_{Fp}}{k_B T}} \quad (1.5)$$

where E_{Fn} and E_{Fp} are the so-called quasi Fermi levels, representing the electrochemical potential of the electrons and holes, respectively. Hence, they define the maximum voltage than can be delivered by the solar cell, the so-called implied voltage iV :

$$iV = \frac{E_{Fn} - E_{Fp}}{q_e} = \frac{k_B T}{q_e} \ln \left(\frac{(n_0 + \Delta n)(p_0 + \Delta p)}{n_i^2} \right) \quad (1.6)$$

where q_e is the elementary charge.

1.2.2 Characterization of solar cells

The ideal current-voltage (J-V) characteristic of a solar cell under illumination is given by the superposition of a photogenerated current density J_L and a recombination current density, described by the following diode-like equation [P. Würfel and Würfel, 2016]:

$$J(V) = J_L - J_{0,tot} \left(e^{\frac{q_e V}{k_B T}} - 1 \right) \quad (1.7)$$

where $J_{0,tot}$ is called the reverse saturation current density and represents the total recombination current. A more detailed presentation of various recombination mechanisms will be given in the following subsection.

A typical J-V curve is shown in Fig. 1.3a. Such measurements are usually performed under standard test conditions, *i.e.* a cell temperature of 25 °C, an illumination intensity of 1 sun (1000 W/m²) and a light spectrum corresponding to AM1.5G (solar spectrum on earth when

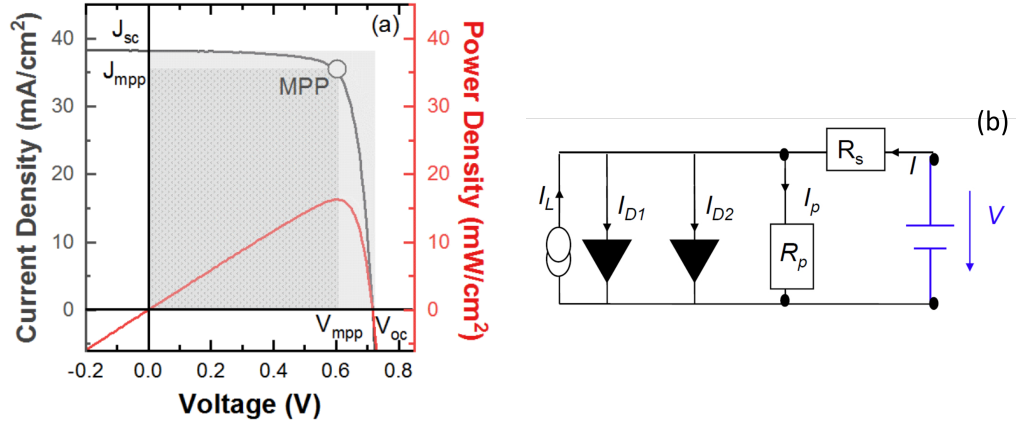


Figure 1.3 – (a): In grey: typical J-V curve measured under standard test conditions. In red: corresponding power density curve. Reproduced with the author's permission and without modifications from [Nogay, 2018]. Copyright ©2018, G. Nogay. (b) Equivalent circuit for the two-diode model of a solar cell. Reproduced with the author's permission from [Haug et al., 2021a]. Copyright ©2021, F-J. Haug.

light has travelled a distance through air corresponding to 1.5 times the atmosphere's thickness).

The two-diode model, shown in Fig. 1.3b, is a more realistic representation of a solar cell, taking into account two different recombination mechanisms (J_{01} and J_{02}), a shunt resistance R_p and series resistance R_s , respectively in parallel and in series with the diodes, as well as ideality factors n_1 and n_2 , accounting for non-ideal behaviors of the diodes:

$$J(V) = J_L - J_{01} \left(e^{\frac{q_e V - J(V) R_s}{n_1 k_B T}} - 1 \right) - J_{02} \left(e^{\frac{q_e V - J(V) R_s}{n_2 k_B T}} - 1 \right) - \frac{V - J(V) R_s}{R_p} \quad (1.8)$$

The resulting J-V curve still typically looks like the one shown in Fig. 1.3a, allowing the extraction of several parameters defining the performance of a solar cell:

- **Short-circuit current density:** J_{sc} is the maximum current density that the solar cell can deliver, corresponding to the scenario where the cell is in short-circuit, *i.e.* $V = 0$. In the ideal case of $R_s = 0$ and $R_p = \infty$, $J_{sc} = J_L$. It depends on the number of electron-hole pairs generated and collected, and therefore mainly on the number of photons reaching the absorber. As the intensity and spectrum of the incident light are fixed under standard test conditions, J_{sc} can be increased by reducing reflection losses, shadowing and parasitic absorption. This is achieved by using anti-reflective coatings (ARC), texturing the surface [Campbell and Green, 1987], optimizing the metallization pattern and using transparent layers at the front. The J_{sc} of the optimum c-Si solar cell was determined to be 43.4 mA/cm² [Niewelt et al., 2022].

- **Open-circuit voltage:** V_{oc} is the maximum voltage that the solar cell can reach, corresponding to the scenario where the cell is in open-circuit, *i.e.* $J = 0$. In the case of the one-diode model (equation 1.7):

$$V_{oc} = \frac{k_B T}{q_e} \ln \left(\frac{J_{sc}}{J_{0,tot}} + 1 \right) \quad (1.9)$$

As can be seen, the V_{oc} depends strongly on the recombination current J_0 . Hence, reducing the recombination losses increases V_{oc} . The V_{oc} of the optimum c-Si solar cell was determined to be 757 mV [Niewelt et al., 2022].

- **Maximum power density:** P_{max} is the maximum power density delivered by the solar cell. As shown in Fig. 1.3a, $P = J \cdot V$ is equal to zero both in short-circuit and open-circuit condition, and passes through a maximum in between. The current density and voltages associated with this maximum power point (MPP) are J_{mpp} and V_{mpp} .
- **Fill factor:** FF is a measure of the "squareness" of the J-V curve, given by:

$$FF = \frac{J_{mpp} V_{mpp}}{V_{oc} J_{sc}} = \frac{P_{max}}{V_{oc} J_{sc}} \quad (1.10)$$

Assuming negligible shunt and series resistances, FF can be approximated by:

$$FF_0 = \frac{v_{oc} - \ln(v_{oc} + 0.72)}{v_{oc} + 1} \quad (1.11)$$

where $v_{oc} = \frac{V_{oc} q_e}{n k_B T} > 10$, with n being the ideality factor [Green, 1982]. As one can observe, a lower n results in higher FF_0 . As we will see later, the value of n varies depending on which recombination mechanism is dominant. Lifting the assumption of negligible resistances, FF becomes dependent on the so-called open-circuit resistance R_{OC} and the short-circuit resistance R_{SC} , defined as:

$$R_{OC} = \left. \frac{dV}{dJ} \right|_{V=V_{oc}} \approx R_s \quad \text{and} \quad R_{SC} = \left. \frac{dV}{dJ} \right|_{V=0} \approx R_p \quad (1.12)$$

where R_s and R_p are the series and shunt resistances described in the two-diode model (Fig. 1.3). Therefore, maximizing R_p and minimizing R_s leads to high FF values. The FF of the optimum c-Si solar cell was determined to be 89.5% [Niewelt et al., 2022].

- **Energy conversion efficiency:** η is the ratio between P_{max} and P_{in} , the power density reaching the cell in form of illumination, calibrated to 1000 W/m² under standard test conditions:

$$\eta = \frac{P_{out}}{P_{in}} = \frac{V_{OC} J_{SC} FF}{P_{in}} \quad (1.13)$$

The maximum theoretical η that can be reached by a c-Si solar cell was determined to be 29.4% [Niewelt et al., 2022].

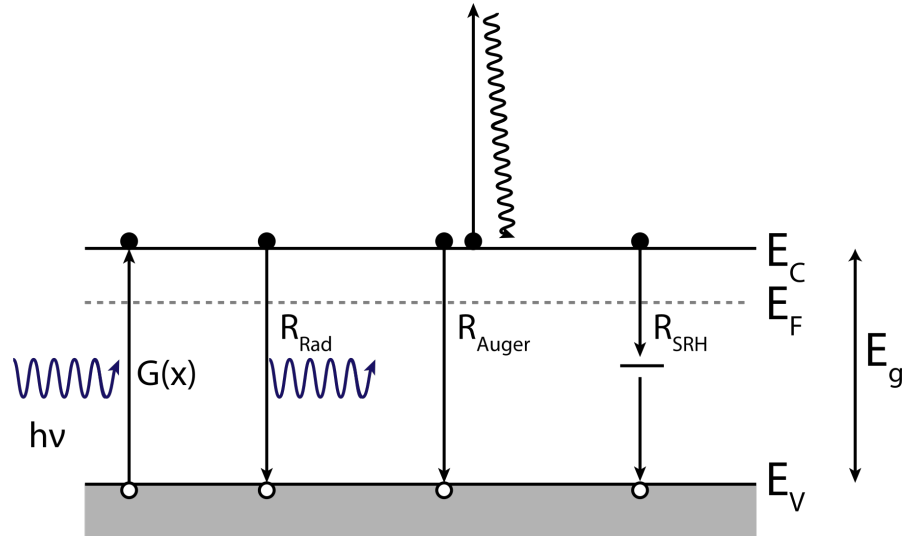


Figure 1.4 – Schematic representation of the generation of electron-hole pairs in a semiconductor and the various possible bulk recombination mechanisms. Adapted from [Stuckelberger, 2018].

1.2.3 Recombination and passivation

As mentioned earlier, an electron excited to the conduction band can fall back to the valence band, recombining with a hole and hence annihilating the previously generated electron-hole pair. The time interval between generation and recombination is characterized by the minority carrier lifetime:

$$\tau = \frac{\Delta n}{U} \quad (1.14)$$

where U is the net recombination rate. There are various possible recombination mechanisms in semiconductors, described in more details below. One distinguishes between surface and bulk recombination, and in the latter case between radiative, Auger and Shockley-Read-Hall (SRH) recombination, schematically represented in Fig. 1.4. All of them occur in parallel. The resulting effective lifetime is therefore given by:

$$\frac{1}{\tau_{eff}} = \frac{1}{\tau_{bulk}} + \frac{1}{\tau_{surf}} \quad (1.15)$$

where

$$\frac{1}{\tau_{bulk}} = \frac{1}{\tau_{rad}} + \frac{1}{\tau_{Auger}} + \frac{1}{\tau_{SRH}} \quad (1.16)$$

Radiative recombination

In radiative recombination an excited electron makes a direct band-to-band transition and recombines with a hole. The excess energy is released by emission of a photon. The net recombination rate is proportional to the hole and electron concentration:

$$U_{rad} = r_{rad}(np - n_i^2) \quad (1.17)$$

where r_{rad} is the radiative recombination coefficient. Therefore:

$$\tau_{rad} = \frac{\Delta n}{r_{rad}(np - n_i^2)} = \frac{1}{r_{rad}(n_0 + p_0) + r_{rad}\Delta n} \quad (1.18)$$

For low injection ($\Delta n \ll n_0 + p_0$) τ_{rad} depends on $(n_0 + p_0)$, which is approximately equal to the dopant concentration in the case of a doped material. On the other hand, for high injection ($\Delta n \gg n_0 + p_0$), τ_{rad} is inversely proportional to Δn .

Radiative recombination is an intrinsic process, that cannot be avoided, since it is inherent to the semiconductor material. However, c-Si being an indirect semiconductor, the radiative recombination rate is low (reflected in a small value of $r_{rad} = 4.73 \cdot 10^{-15} \text{ cm}^3/\text{s}$ at 300 K [Trupke et al., 2003]) and can usually be neglected compared to Auger and SRH recombination. The ideality factor (see equation 1.8) associated with this type of recombination is equal to 1.

Auger recombination

In Auger recombination, the energy set free by the band-to-band recombination process is transferred to a free electron or hole as kinetic energy, and subsequently to the lattice by thermalization of this excited carrier, as depicted in Fig. 1.4. This process hence involves three carriers, and for high doping concentration its recombination rate is given by:

$$U_{Auger} = C_n(n^2p - n_0^2p_0) + C_p(np^2 - n_0p_0^2) \quad (1.19)$$

where C_n and C_p are the Auger coefficients. For a doped semiconductor at low or high injection, the following approximations can be made:

$$\tau_{Auger,low} = \frac{1}{C_n/p N_{dop}^2} \quad \text{and} \quad \tau_{Auger,high} = \frac{1}{(C_n + C_p)\Delta n^2} \quad (1.20)$$

where N_{dop} is the dopant concentration. At low injection, τ_{Auger} is constant at a value depending on the dopant concentration, similar to the case of radiative recombination. However, at high injection, τ_{Auger} is inversely proportional to the square of the excess carrier density. Therefore, Auger recombination is predominant in highly doped materials and at high injection levels. It is also an intrinsic process that cannot be fully avoided, since high levels of excess carriers are required to reach high voltages (see equation 1.6). The ideality factor (see equation 1.8) associated with this type of recombination is equal to 2/3.

Note that in the equations above, the carriers involved in the Auger process are assumed to be noninteracting quasifree particles. This model delivers results that are in good agreement with lifetime measurements for highly doped materials ($N_{dop} > 5 \cdot 10^{18} \text{ cm}^{-3}$). However, for lower dopant concentrations, Coulomb interactions of charged carriers increase the Auger recombination probability [Hangleiter and Häcker, 1990]. A parametrisation including this Coulomb enhancement, was proposed by Richter *et al.* [Richter et al., 2012].

Shockley-Read-Hall (SRH) recombination

In Shockley-Read-Hall recombination, the excited electron recombines via a state within the bandgap, as shown in Fig. 1.4. Such states within the bandgap are introduced by dopants, impurities (for example Fe or Cu) or lattice defects, such as vacancies or dislocations. It was first described, independently, in two publications, after who's authors the process is named [Shockley and Read, 1952], [Hall, 1952].

Depending on their position E_t within the bandgap, such states are classified in three categories: dopant states, if they are closer than 0.1 eV from the valence or conduction band; trap states, if they are 0.1–0.2 eV away from the band edges; and recombination centers, if they are close to midgap. A free carrier captured by a trap state is likely to be released again to the its band by thermal excitation. Therefore, trap state impact the carrier mobility, but have only little effect on recombination. On the other hand, when captured by a recombination center, an additional capture of a free carrier of the other type is more likely than thermal excitation back to the band, leading to recombination. The recombination rate of this process is given by:

$$U_{SRH} = \frac{v_{th} N_t (np - n_i^2)}{\frac{1}{\sigma_p} (n + n_1) + \frac{1}{\sigma_n} (p + p_1)} \quad (1.21)$$

where v_{th} is the thermal velocity of the minority carriers, N_t the density of recombination centers, σ_p and σ_n the capture cross sections of holes and electrons, respectively, characterizing the probability of a hole or electron being capture by the defect, and n_1 and p_1 defined by:

$$n_1 = n_i e^{\frac{E_t - E_F^i}{k_B T}} \quad \text{and} \quad p_1 = n_i e^{\frac{E_F^i - E_t}{k_B T}} \quad (1.22)$$

where E_F^i is the intrinsic Fermi energy level. Hence:

$$\tau_{SRH} = \frac{\frac{1}{\sigma_p} (n_0 + n_1 + \Delta n) + \frac{1}{\sigma_n} (p_0 + p_1 + \Delta p)}{v_{th} N_t (n_0 + p_0 + \Delta n)} \quad (1.23)$$

At high injection ($\Delta n = \Delta p \gg n_0, p_0, n_1, p_1$), the SRH lifetime becomes:

$$\tau_{SRH, high} = \frac{1}{\sigma_n v_{th} N_t} + \frac{1}{\sigma_p v_{th} N_t} = \tau_{n0} + \tau_{p0} \quad (1.24)$$

As one can observe, the minority carrier lifetime at high injection does not depend on E_t nor on the doping concentration. In contrast, at low injection ($\Delta n = \Delta p \ll n_0, p_0, n_1, p_1$), the following approximation holds for a n -type semiconductor ($n_0 \approx N_{dop}$, $p_0 \ll p_1$):

$$\tau_{SRH,low} = \frac{1}{\sigma_n v_{th} N_t} \left(\frac{p_1}{N_{dop}} \right) + \frac{1}{\sigma_p v_{th} N_t} \left(1 + \frac{n_1}{N_{dop}} \right) \quad (1.25)$$

Assuming $\sigma_n = \sigma_p$, one obtains:

$$\tau_{SRH,low} = \frac{1}{\sigma_n v_{th} N_t} \left(1 + \frac{2n_i}{N_{dop}} \cosh \left(\frac{E_t - E_F^i}{k_B T} \right) \right) \quad (1.26)$$

This relation shows that $\tau_{SRH,low}$ becomes lower the closer E_t comes to the midgap position E_F^i , making midgap states the most recombination active.

In a semiconductor containing impurities or defects, SRH recombination can quickly become the dominant process limiting the minority carrier lifetime. Luckily, such recombination centers are not inherent and can be avoided by working with highly purified single-crystal material. At high injection, the ideality factor (see equation 1.8) associated with this type of recombination is equal to 2, while at low injection it is equal to 1, and takes values in between in the transition between these two regimes.

Surface recombination

At the surface of c-Si, or more generally at its interfaces with layers deposited on top, the abrupt ending of the crystal lattice leads to the presence of unsaturated bonds (also called dangling bonds), which create localized electronic states within the bandgap, acting as recombination centers. This recombination process can therefore be described similarly to SRH recombination, with the difference that the states are continuously distributed across the bandgap, as depicted in Fig. 1.5. Note that other models have been proposed, such as the description of dangling bonds at the surface as amphoteric defects, which assume different energy levels within the bandgap depending on their charge state [Olibet et al., 2007].

In contrast to bulk recombination processes, the net surface recombination rate U_{surf} has units of $[\text{cm}^{-2}\text{s}^{-1}]$ (instead of $[\text{cm}^{-3}\text{s}^{-1}]$). In analogy with the minority carrier lifetime, one can define a surface recombination velocity:

$$S = \frac{\Delta n_{surf}}{U_{surf}} \quad (1.27)$$

where Δn_{surf} is the excess carrier density at the surface. Assuming surface recombination to be a process similar to SRH, the surface recombination rate is given by:

$$U_{surf} = \frac{v_{th} D_{it} (n_{surf} p_{surf} - n_i^2)}{\frac{1}{\sigma_p} (n_{surf} + n_1) + \frac{1}{\sigma_n} (p_{surf} + p_1)} \quad (1.28)$$

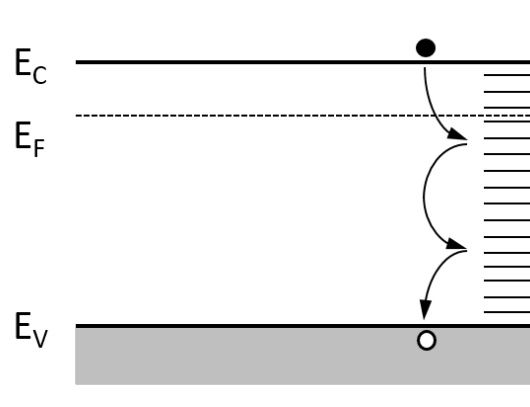


Figure 1.5 – Schematic representation of the surface recombination process in a semiconductor, occurring via surface states continuously distributed across the bandgap. Adapted from [P. Wurfel and Wurfel, 2016].

where D_{it} is the density of surface defects and n_{surf} and p_{surf} the carrier densities near the surface. Note that n_1 and p_1 are not defined by a single value of E_t , but by defect states continuously distributed across the bandgap. Moreover, D_{it} , σ_p and σ_n usually vary with the energy. Hence:

$$U_{surf} = v_{th}(n_{surf}p_{surf} - n_i^2) \int_{E_V}^{E_C} \frac{D_{it}(E)}{\frac{1}{\sigma_p(E)}(n_{surf} + n_1(E)) + \frac{1}{\sigma_n(E)}(p_{surf} + p_1(E))} dE \quad (1.29)$$

In the presence of band bending, one type of charge carriers accumulates at the surface, while the other one is repelled, hence $\Delta n_{surf} \neq \Delta p_{surf}$, complicating the computations even further. In this case, one generally computes the effective surface recombination velocity S_{eff} defined at a distance $x = d$ from the surface where the bands are still flat and the assumption $\Delta n(x = d) = \Delta p(x = d)$ holds:

$$S_{eff} = \frac{\Delta n(x = d)}{U_{surf}(x = d)} \quad (1.30)$$

The values for S_{eff} range from 10^7 cm/s in the case of direct contact between metal and c-Si, down to < 10 cm/s for passivated surfaces.

In the case of well passivated surfaces, the minority carrier lifetime associated to the surface recombination mechanism is given by:

$$\frac{1}{\tau_{surf}} = \frac{S_{front} + S_{rear}}{W} \quad (1.31)$$

where W is the wafer thickness. Further ways to compute the effective surface recombination velocities are presented in subsection 2.2.1.

The surface recombination can also be characterized by the dark saturation current density

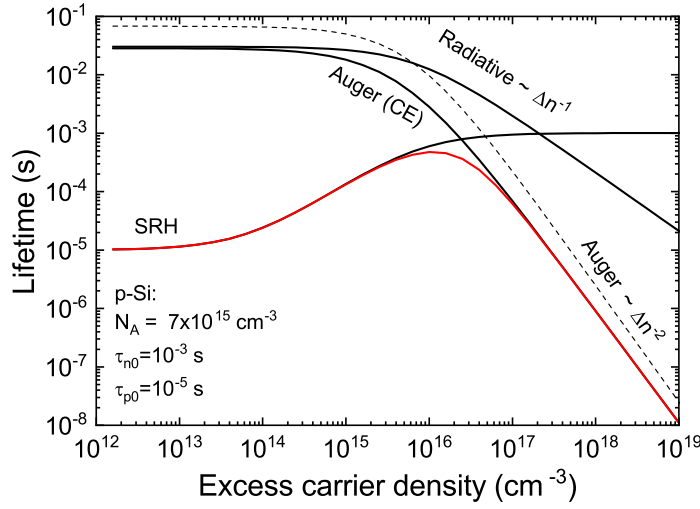


Figure 1.6 – Numerical computation of the radiative, Auger and SRH lifetimes as function of excess carrier density (black solid lines), using typical parameter values for c-Si(*p*). The red line is the resulting τ_{eff} . The dotted line is the Auger lifetime without taking into account Coulomb enhancement. Courtesy of Dr. Franz-Josef Haug.

J_0 associated to it. A method to obtain this J_0 value from the measurement of $\tau_{\text{eff}}(\Delta n)$ was introduced by Kane and Swanson [Kane and Swanson, 1985]. In 2015, Kimmerle *et al.* revisited it and published an improved method, implemented in a spreadsheet calculator [Kimmerle et al., 2015]. This characterization is more general, since the saturation current includes not only the recombination at interfacial defects, but also a potential contribution from a minority carriers flowing into adjacent highly doped regions where they recombine [Kane and Swanson, 1985], [Haug et al., 2021b].

Injection dependent τ_{eff}

As described in the previous sections, the lifetimes associated to the various recombination mechanisms vary with Δn and feature characteristic dependencies at low and high injection. Hence, plotting τ_{eff} as function of Δn provides information about the recombination mechanisms at work [Cuevas and Macdonald, 2004], [Leilaouioun and Holman, 2016], as shown in Fig. 1.6.

Since surface recombination and bulk SRH display similar behaviour, deconvoluting the contribution of bulk and surface is often complicated. Doing so can be tried numerically by studying τ_{eff} at high Δn [Kane and Swanson, 1985], [Kimmerle et al., 2015], [Haug et al., 2021b]. However, often additional experimental results are required for a reliable discrimination between τ_{bulk} and τ_{surf} , such as lifetime measurements on wafers of varying thickness featuring identical surface layers [Morisset, 2019], [Grant et al., 2017], or direct measurement of τ_{bulk} using methods allowing close to perfect surface passivation [Grant and Murphy, 2017].

Passivation

In order to minimize recombination losses and hence maximize V_{oc} , electronic states within the bandgap need to be avoided within the bulk and at the surfaces/interfaces. Hence, working in clean conditions is crucial, especially making sure to keep the samples away from metallic contaminants.

In this thesis, bulk SRH recombination was minimized by working with high quality Float-Zone (FZ) c-Si wafers. For cells fabricated on Czochralski (Cz) wafers, containing more impurities, processes like gettering [Seibt et al., 2006], [J. S. Kang and Schroder, 1989], tabula rasa [LaSalvia et al., 2018], [Falster et al., 1997] or illumination at elevated temperature [Walter et al., 2017] are used to reduce the contaminant concentration or to annihilate defects.

Since it is possible to achieve high τ_{bulk} values using appropriate silicon ingot growth techniques, a lot of research and development was performed in the past decades to passivate the surfaces/interfaces [A. G. Aberle, 2000], [Bonilla et al., 2017]. Surface passivation can be achieved in two ways:

- **Chemical passivation:** Defect states at the surface/interface are passivated by saturating the dangling bonds, reducing D_{it} . This can be achieved by hydrogenation [Johnson et al., 1981], growing of an interfacial oxide [Kerr and Cuevas, 2002] or deposition of amorphous silicon layers [Pankove and Tarnag, 1979].
- **Reduction of the minority carrier density:** In this process, the recombination rate is reduced by reducing n_{surf} or p_{surf} . This is achieved by inducing band bending close to the interface (see Fig. 1.7), repelling one of the charge carrier types. Such band bending occurs in the presence of fixed charges in dielectric layers or by adding highly doped regions [Cuevas et al., 2015], [Ingenito et al., 2018].

A schematic representation of these passivation mechanisms is shown in Fig. 1.7, using the FPC investigated in this thesis as example.

1.3 Photovoltaic technologies

As mentioned, surface passivation has been a major topic of research and development in the past decades. Indeed, the main upgrades in solar cell architectures in industry were aiming at improving the passivation of the rear side. While Aluminium-Back Surface Field (Al-BSF) cells made up more than 70% of the market share in 2017 [ITRPV, 2018], the industry nowadays produces mainly Passivated Emitter and Rear Cells (PERC) [ITRPV, 2021]. These two cell architectures are schematically depicted in Fig. 1.8. As one can observe, the front side features a heavily n -doped emitter, creating a selective contact and repelling holes. For Al-BSF cells, the rear side is directly contacted with aluminium. During a rapid thermal processing at the end of the manufacturing process, the Al melts and forms an eutectic liquid at the rear of the wafer.

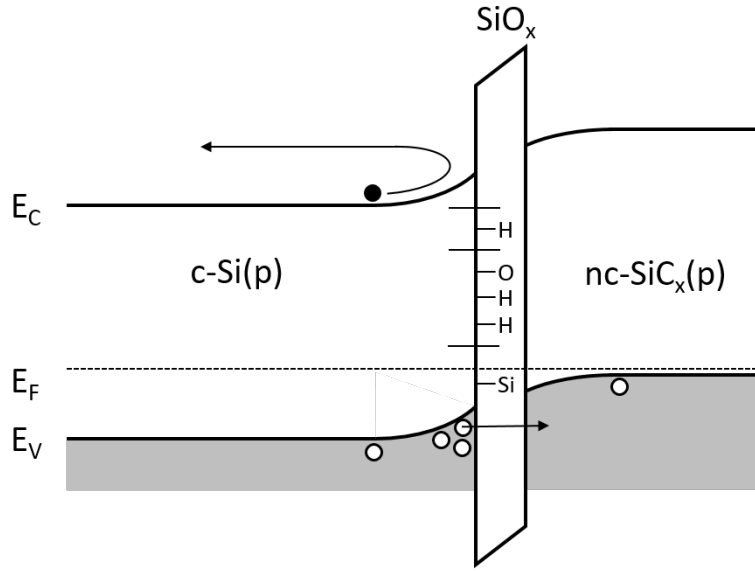


Figure 1.7 – Schematic representation of the surface passivation mechanisms at work in the FPC samples investigated in this thesis.

Upon cooling, the liquid solidifies into silicon heavily doped with Al, creating the so-called back surface field that gives this cell architecture its name. The success of this cell design was mainly driven by the simplicity and the availability of the production technology [Glunz et al., 2012]. However, the direct contact between Al and c-Si at the rear remains a major source of recombination, yielding saturation current densities J_0 of 100–1000 fA/cm² [Cuevas, 2013].

The PERC architecture addresses this issue by introducing a stack of passivating layers between the c-Si and the Al [Blakers and Green, 1986]. Since these layers are insulating, they are locally opened to allow carrier extraction. Therefore, the area with direct contact between Al and c-Si is minimized, lowering the recombination losses (J_0 of ~35 fA/cm² [Ye et al., 2016]). However, the lower the contact area, the higher the resistance for current extraction, requiring to settle with a trade-off [Swanson, 2005].

To overcome this limitation, full area passivating contacts were introduced. Among these, two main approaches exist. The first one are the Silicon HeteroJunction (SHJ) solar cells. In this architecture, both sides are typically passivated with a few nanometers thin intrinsic amorphous silicon (a-Si:H(*i*)) layer, capped with doped amorphous silicon layers (a-Si:H(*p*) or a-Si:H(*n*)) for carrier selectivity [DeWolf et al., 2012]. The metallization is made via sputtering of a Transparent Conductive Oxide (TCO) on both sides, contacted with silver (sputtered or screen printed). SHJ solar cells feature excellent passivation and hold the world record for conversion efficiency of silicon solar cells (26.7% [K. Yamamoto et al., 2017]). However, since relying on amorphous layers, these cells are not compatible with firing, a high temperature process typically used in industry for metallization. The fabrication of SHJ cells therefore requires a low temperature metallization approach [Louwen et al., 2016], such as the SmartWire

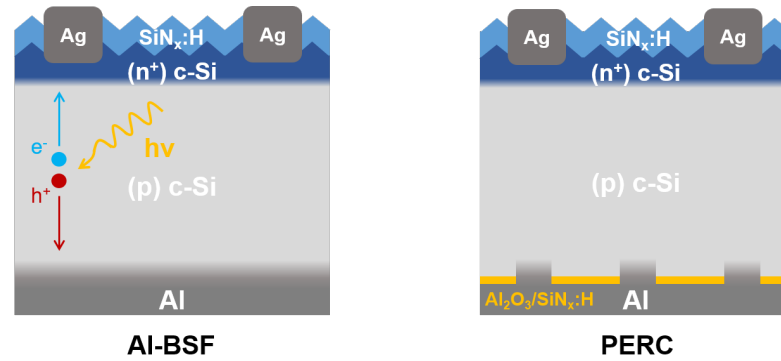


Figure 1.8 – Schematic representation of Al-BSF and PERC solar cells. Adapted from [Morisset, 2019].

Contacting Technology [Faes et al., 2014], and overall major changes in the production lines compared to current industrial mainstream c-Si PV technology, hindering their widespread transfer to industry [Allen et al., 2019]. Nevertheless, several new production lines for SHJ cells are starting, including in Europe [Meyer Burger, 2021], and their market share is predicted to continue to grow [ITRPV, 2021].

In contrast, HTPC provide full area surface passivation too, while being compatible with the industrial high temperature processes. Implementing them on the rear side of solar cells represents an upgrade of the PERC architecture requiring only few changes in the production lines, making them a promising candidate for the next generation of mainstream high efficiency solar cells [Yan et al., 2021], with first production lines being ramped up [Y. Chen et al., 2019], [Wu et al., 2019], [Bao et al., 2020].

1.4 High Temperature stable Passivating Contacts (HTPC)

1.4.1 History and state of the art

Typically, HTPCs are made of a thin (1.2 – 3.6 nm) SiO_x layer capped with a doped polycrystalline silicon (poly-Si) layer. The concept of poly-Si based contacts goes back to the 1980s and was inspired by the use of these materials in transistor applications. Applied to solar cells, these so-called semi-insulating polycrystalline silicon (SIPOS) structures featured J_0 values $< 10 \text{ fA/cm}^2$, corresponding to 720 mV iV_{oc} [Yablonovitch et al., 1985], [Kwark et al., 1984], [Tarr, 1985]. However, the high oxygen content of these SIPOS layer lead to high contact resistances, limiting the performances of the fabricated solar cells.

Although not disclosed, it is assumed that SunPower's Generation 3 cells featured poly-Si based passivating contacts [Cousins et al., 2010]. In 2013, this approach was rediscovered by the PV community when Feldmann *et al.* from the Fraunhofer-ISE published a solar cell with a conversion efficiency of 23.0% based on a so-called Tunnel Oxide Passivating Contact (TOP-

Con), schematically depicted in Fig. 1.9a [Feldmann et al., 2014a]. In this approach, an ultra thin (1.4 nm) oxide is grown on the rear surface, allowing current transport through tunneling [Feldmann et al., 2018]. A ~20 nm thick phosphorus-doped poly-Si layer is deposited on top for carrier selectivity [Brendel and Peibst, 2016] and subsequently annealed at temperatures around 800 °C [Richter et al., 2017] to promote the activation of dopants in the layer. Remote Plasma Hydrogen Passivation (RPHP) is then applied, providing chemical passivation to the interface. Finally, the TOPCon is metallized by evaporation of Ag [Feldmann et al., 2017a]. These contacts feature $J_0 < 10 \text{ fA/cm}^2$ and contact resistivities $\rho_c < 10 \text{ m}\Omega\text{cm}^2$ [Glunz et al., 2015], [Gao et al., 2019]. Recently, a record efficiency of 26.0% was achieved with a double-side contacted solar cell featuring a TOPCon on the rear surface. Moving to *p*-type wafers, and hence a back junction architecture, revealed to be key in this case [Richter et al., 2021].

Poly-Si on SiO_x based HTPC rapidly became a "hot" research topic, with many groups publishing results on various layer stacks and architectures, such as the monoPoly™ from SERIS [Duttagupta et al., 2018], the High Temperature Silicon Heterojunction from CEA [Desrues et al., 2021], or the mixed-phase nanocrystalline silicon oxide from EPFL [Stuckelberger et al., 2016b], [Wyss et al., 2020b], with single-side application of HTPCs as in Fig. 1.9a, full area HTPCs on both sides [Nogay et al., 2018], [Peibst et al., 2018], [Feldmann et al., 2017b], [Nicolai et al., 2018], [Ingenito et al., 2019], [Stuckelberger et al., 2018] or localized HTPCs on the front to reduce parasitic absorptions [K. Chen et al., 2021], [Young et al., 2019], [Stuckelberger et al., 2019], [Meyer et al., 2022].

A further design is ISFH's Interdigitated Back-Contact (IBC) POLycrystalline silicon on Oxide (POLO) cell, schematically depicted in Fig. 1.9b. In this architecture, both contacts are implemented on the rear side, reducing shadowing losses at the front at the expense of a more complicated fabrication process. Applying this approach, a record efficiency for *p*-type solar cells of 26.1% was published by Haase *et al.* in 2018 [Haase et al., 2018]. In contrast with most other HTPCs, POLO contacts feature a 2.2 nm thick thermally grown interfacial oxide, making current flow through pinholes or spots with locally reduced SiO_x thickness the main charge carrier transport mechanism through the oxide (rather than tunneling) [Peibst et al., 2016], [Campa et al., 2019], [Folchert et al., 2018].

1.4.2 Fired Passivating Contacts (FPC)

As mentioned, the formation of HTPC includes an annealing step, crystallizing the deposited layer into poly-Si. This has been reported to be beneficial for transparency and contact resistivity as it yields a higher density of active dopants [Haug et al., 2019], [Seif et al., 2016]. Moreover, it densifies the SiO_x [Polzin et al., 2020], and, in the case of POLO contacts, creates the pinholes required for current extraction [Kale et al., 2018]. This annealing is usually performed in a tube furnace at temperatures $> 800 \text{ °C}$ and with heating ramps of $1\text{--}10 \text{ °C/min}$, leading to the formation of a shallow doped region below the poly-Si/ SiO_x stack by in-diffusion of dopants into the silicon wafer [Nogay et al., 2017]. This shallow doped region induces band

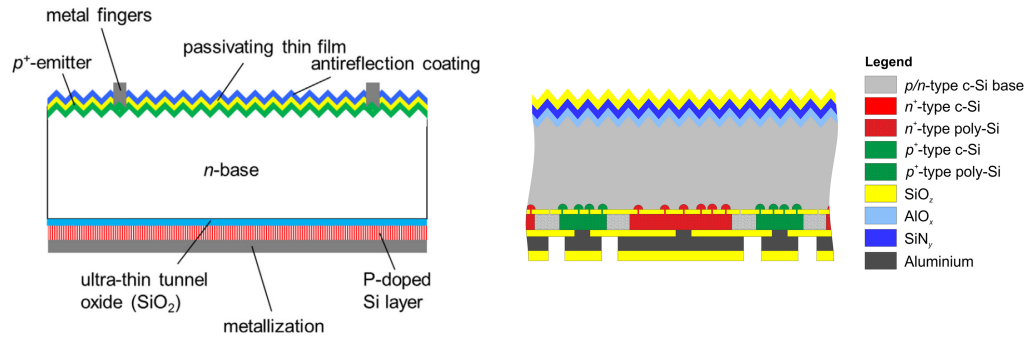


Figure 1.9 – (a) Schematic representation of a solar cell featuring a TOPCon at the rear side. Reprinted from [Feldmann et al., 2014a] with permission from Elsevier. Copyright ©2013, Elsevier. (b) Schematic representation of a IBC-POLO solar cell. Reprinted from [Hollemann et al., 2019] with permission from Wiley. Copyright ©2019, John Wiley & Sons.

bending, thus promoting the carrier selectivity of the contact [Brendel and Peibst, 2016] and reducing surface recombination [A. G. Aberle, 2000].

In contrast, FPCs are fabricated in a Rapid Thermal Processing (RTP) step, also called firing [Ingenito et al., 2018], [Merkle et al., 2018], [Desthieux et al., 2020a], [Winter et al., 2020], [Ingenito et al., 2021]. This process requires a much lower thermal budget than tube furnace annealings, since temperatures $> 750^\circ\text{C}$ are reached with ramps of $\sim 50^\circ\text{C/s}$ and maintained for a few seconds only. In industry, such firings are used to metallize the solar cells [Ye et al., 2016], [Duttagupta et al., 2018]. These fast temperature ramps lead to rapid effusion of hydrogen, incorporated into the deposited layers during Plasma Enhanced Chemical Vapor Deposition (PECVD), which can lead to blistering. Avoiding such layer delamination is thus a major challenge for the FPCs (and HTPCs in general). It can for example be overcome by reducing layer thickness, increasing the deposition temperature or a stronger dilution of SiH_4 in H_2 , leading to the deposition of microcrystalline layers containing less hydrogen [Morisset et al., 2019], [Desthieux et al., 2020a]. In the case of the FPCs used in this thesis, blister-free layers were achieved by the addition of carbon into the Si-network [Ingenito et al., 2018]. However, an increased carbon content reduces the crystallisation of the layer and the activation of dopants, thus increasing the contact resistivity. Therefore, the C content was tuned such as to be just high enough to avert blistering. The integration of the FPC as rear hole selective contact, co-fired with a screen printed Ag grid contacting a POCl_3 diffused front emitter, resulted in a conversion efficiency of 22.5% [Ingenito et al., 2021]. These cells featured J_0 values of $\sim 7 \text{ fA/cm}^2$ and $\rho_c < 80 \text{ m}\Omega\text{cm}^2$ which are not FF limiting for full area contacts [Schmidt et al., 2018]. Despite excellent rear side passivation, the fabricated cells achieved only V_{oc} values around 680 mV. The limitation comes from the front side, featuring direct contact between Ag and c-Si, leading to major recombination losses.

Therefore, the ideal FPC based solar cell would feature co-fired passivating contacts at the front and the rear side. A imagined ideal process flow is depicted in Fig. 1.10. Such an approach

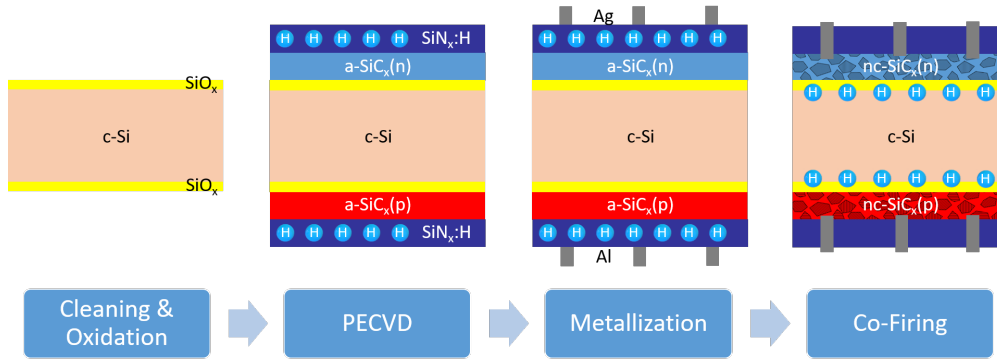


Figure 1.10 – Imagined lean fabrication process for a low thermal budget solar cell, featuring FPCs on both front and rear side. A single firing step would at the same crystallize the SiC_x layers, diffuse the hydrogen from the $\text{SiN}_x\text{:H}$ reservoir layers and metallize the cell by firing-through of screen printed contacts.

would enable high V_{oc} values while keeping the fabrication process simple and with a low thermal budget, since a single firing step would crystallize the deposited layers, hydrogenate the interfaces and metallize the contacts. More details regarding hydrogenation, firing and metallization are provided below.

To reach this goal, further research is necessary, as so far cells with a FPC at the back display either a SHJ front or a diffused front emitter [Ingenito et al., 2018], [Merkle et al., 2018], [Ingenito et al., 2021], and cells with passivating contacts on both sides rely on long high temperature annealings for contact formation [Ingenito et al., 2017], [Feldmann et al., 2017b], [Nogay et al., 2018], [Peibst et al., 2018], [Wang et al., 2019], [Stuckelberger et al., 2019], [Ingenito et al., 2019], [Lozac'h et al., 2020], [Hermle et al., 2020], [Meyer et al., 2021]. As reported in chapter 6, an electron-selective FPC was developed and implemented on the front side of a co-fired solar cell. Remaining challenges are the metallization of such layers by firing-through and minimizing optical losses. Indeed, > 100 nm thick poly-Si layers are usually needed for firing-through in order to stop the metallic paste from reaching the SiO_x layer [Padhamnath et al., 2020]. However, thick layers are more prone to blistering. Moreover, when implemented at the front side, layers should be as thin as possible to avoid parasitic light absorption. A possible approach would be to localize the front FPC, depositing thick layers under the fingers only. Such approaches (implementing annealed HTPCs) have been reported, but did not yet manage to outperform direct metallic contacts on locally higher doped regions [Ingenito et al., 2017], [K. Chen et al., 2021], [Young et al., 2019], [Stuckelberger et al., 2019], [Meyer et al., 2022].

1.4.3 Surface passivation

The thermal budget of the firing process is too low to enable dopant diffusion from the doped poly-Si layer into the c-Si. Hence, no shallow doped region is formed. As reported in [Ingenito

et al., 2018] and [Haug et al., 2019], the high doping of the $\text{SiC}_x(p)$ layer nevertheless induces some band-bending. However, it is by itself not sufficient to suppress recombination at the interface. FPCs therefore strongly rely on chemical passivation of said interface to achieve high minority carrier lifetimes. This is achieved by introducing thin tunneling SiO_x between the c-Si wafer and the poly-Si layer deposited on top, followed by a hydrogenation process. A schematic representation of the band diagram of FPCs and passivated electronic surface states is shown in Fig. 1.7.

Interfacial oxide

The introduction of a thin SiO_x layer between the c-Si wafer and the doped layers deposited on top is the key difference between HTPCs and SHJ solar cells, enabling high temperature treatments. Indeed, the interfacial SiO_x prevents epitaxial regrowth of the deposited layers, which was reported to be detrimental for solar cell performance [Fujiwara and Kondo, 2007]. Compared to other dielectric layers, SiO_2 features a low density of fixed charges and therefore relies on chemical passivation of the interface [Glunz and Feldmann, 2018], [Cuevas et al., 2015]. Usually, the as-deposited tunneling oxides provide only poor surface passivation, requiring a subsequent hydrogenation step to reach their full potential [Grant and McIntosh, 2009].

Various methods have been reported to grow such interfacial oxides, as for example by a wet-chemical treatment [Kobayashi et al., 2003], exposure to O_3 created by UV radiation in ambient air [Fukano and Oyanagi, 2003], or thermal oxidation [Fossum and Burgess, 1978]. The resulting oxide layers differ in composition and passivation performance. Thermally grown SiO_2 (Therm SiO_2) layers feature the composition closest to the stoichiometric ratio and provide the best passivation [Stegemann et al., 2017]. However, growing them thin enough for efficient current extraction is a challenge, often requiring to lower the oxidation temperature, reducing the oxide quality [Lee et al., 2012]. Similarly, UV- O_3 SiO_x layers feature a composition closer to the stoichiometric ratio and provide better passivation than wet-chemically grown oxide layers (Chem SiO_x) [Moldovan et al., 2015], [Stegemann et al., 2017]. The reason for this trend is believed to be lower interfacial defect density for SiO_x compositions closer to the stoichiometric ratio, as well as decreased diffusion of boron into such layers [Melskens et al., 2017], [Polzin et al., 2020]; a process that was reported to degrade the oxide quality and its passivation [Liu et al., 2019], [T. Yamamoto et al., 1999], [Snel, 1981]. In addition, the temperature stability of the passivation of interfacial SiO_x layers was reported to be enhanced for SiO_x compositions closer to stoichiometric SiO_2 [Moldovan et al., 2015].

Hydrogenation

Hydrogenation is an essential processing step for HTPC in general, during which dangling bonds at the c-Si/ SiO_x interface are saturated by hydrogen, hence reducing the density of interfacial defects, allowing to reach high V_{oc} values [Stesmans, 2000], [Hezel et al., 1983],

[A. Aberle et al., 1991], [Deal et al., 1969], [Johnson et al., 1981]. In the case of FPCs, this process is even more important for surface passivation, since no shallow doped region is formed upon firing [Ingenito et al., 2018]. Even though structural rearrangements of the SiO_x layer were reported to contribute to surface passivation improvement [Liu et al., 2019], [Polzin et al., 2020], hydrogenation remains a key step for low recombination values of most proposed architectures [Tao et al., 2016], [Römer et al., 2014], [Feldmann et al., 2014a], [Nogay et al., 2018], [Stuckelberger et al., 2016b]. In addition, hydrogen diffusion was also reported to improve the bulk quality [A. G. Aberle, 2000], [B. Hallam et al., 2017], [Rougieux et al., 2015], passivate defects within poly-Si layers [Truong et al., 2019b], and to induce positive fixed charges at the c-Si/ SiO_x interface [Lozac'h et al., 2019].

Surprisingly, Kang *et al.* reported an optimal hydrogen density near the c-Si/ SiO_x interface, with excess hydrogen actually increasing the recombination again [D. Kang et al., 2021a]. Hollemann *et al.* also reported degradation of surface passivation in the presence of excess hydrogen [Hollemann et al., 2021a], which they speculated to be related to the formation of platelets [Johnson et al., 1987]. Moreover, creation of defects within the bulk was reported, by the formation of carbon-oxygen-hydrogen complexes in Cz material [Vaqueiro-Contreras et al., 2017], or by excess hydrogen itself [Ciesla et al., 2018], for example. In addition, it is assumed that hydrogen also plays a role in some forms of long-term degradation mechanisms [Bredemeier et al., 2019], [Jensen et al., 2018], [D. Chen et al., 2020]. Therefore, an optimization of the hydrogenation process is required, aiming at saturating dangling bonds, without introducing excess hydrogen.

The passivation level achieved after hydrogenation depends on various parameters. One of them being, whether hydrogen is diffused in atomic form or as H_2 molecule, the former leading to better results [Dekkers et al., 2006], [Sopori et al., 1996]. In the case of $\text{SiN}_x\text{:H}$ layers, the fraction of hydrogen released in atomic form depends on the composition of the layer [Dekkers et al., 2006], [Weeber et al., 2005], [Lelièvre et al., 2009]. Hydrogen can be provided by different sources, such as a remote hydrogen plasma [Feldmann et al., 2017a] or an Al_2O_3 or $\text{SiN}_x\text{:H}$ layer [van de Loo et al., 2020], [Truong et al., 2019a]. Moreover, these layers can be optimized for hydrogen release upon firing or hotplate treatment [Lelièvre et al., 2009], [Steinhauser et al., 2020], [Ingenito et al., 2021], [Haug et al., 2021c], [Nogay et al., 2017].

Regarding the kinetics of the hydrogenation process, the diffusivity of hydrogen within c-Si material or poly-Si layers is influenced by their crystallinity and doping [B. Hallam et al., 2020], [D. Kang et al., 2022]. Carlson and Magee reported slower diffusion of hydrogen in a-Si:H than in c-Si [Carlson and Magee, 1978]. While hydrogen diffuses fastest in its neutral form [Hamer et al., 2018], [B. Hallam et al., 2020], [Beyer and Zastrow, 2000], the passivation kinetics depend on the charge states of both hydrogen and the defects [Rougieux et al., 2018]. These charge states are influenced by the position of the Fermi level, and hence by the doping of the material [Herring et al., 2001], [Ciesla et al., 2018]. Hence, optimization of the hydrogenation process by, for example, illumination have been proposed [Hamer et al., 2014], [B. J. Hallam et al., 2015], [Yang et al., 2018].

1.4.4 Firing

As stated previously, a firing is part of the mainstream industrial metallization approach, and compatibility with this process essential for straightforward technology transfer from laboratories to industry [Allen et al., 2019]. FPCs rely on this firing step to crystallizing the deposited layers, decreasing contact resistivity [Haug et al., 2019], [Seif et al., 2016]. In addition, structural rearrangements occur during the firing, leading to SiO_x layer compositions closer to stoichiometric SiO_2 [Ingenito et al., 2018], which was reported to be beneficial [Polzin et al., 2020].

On the other hand, despite the low thermal budget, it was speculated that carbon and boron diffuse from the $\text{SiC}_x(p)$ layer into the SiO_x upon firing [Ingenito et al., 2021], which creates additional interfacial defects [Liu et al., 2019], [T. Yamamoto et al., 1999], [Snel, 1981]. In addition, strain resulting from mismatch in thermal expansion coefficients between poly-Si and SiO_x facilitates defect formation, increasing the interfacial defect density [Hu, 1991], [Hollemann et al., 2020], [Hollemann et al., 2021a], [Hollemann et al., 2021b], [D. Kang et al., 2021b]. Excess hydrogen might accumulate at such strained defects, leading to the formation and growth of platelets, further degrading the surface passivation and increasing the risk of blistering of the layer [Hollemann et al., 2021a], [Johnson et al., 1987]. Next to damages to the surface passivation, rapid thermal annealings at temperatures around 550 °C have also been reported to severely reduce bulk lifetime in FZ silicon material [De Guzman et al., 2021].

Increased firing stability was reported when capping the SiO_x /poly-Si stack with AlO_x or SiN_x [Hollemann et al., 2020], [Bruhat et al., 2020], [Hollemann et al., 2021b]. In their publication, Hollemann *et al.* speculate that Si-O bonds broken due to thermal strain get directly repassivated to Si-H by hydrogen diffusing from the AlO_x layer. However, this might lead to long-term stability issues [Hollemann et al., 2020]. In a recent publication, Stöhr *et al.* demonstrated that excellent surface passivation ($J_0 = 1.5 \text{ fA/cm}^2$) can be maintained upon firing when using PECVD deposited SiO_xN_y /poly-Si(*n*) stacks instead of SiO_x /poly-Si(*n*) stacks featuring thermally grown oxides [Stöhr et al., 2021]. This was speculated to be linked to the thermal expansion coefficient of SiO_xN_y being much closer to that of (poly-)Si than the one of thermally grown SiO_2 [Hollemann et al., 2021b].

1.4.5 Metallization

The ideal process flow suggested in Fig. 1.10 combines hydrogenation and metallization by firing-through in a single firing step. As mentioned previously, this approach often results in passivation damages due to metal spiking through the SiO_x layer, hence requiring thick poly-Si layers [Stodolny et al., 2016], [Çiftçinar et al., 2017], [Bivour et al., 2017], [Mack et al., 2017], [Duttagupta et al., 2018], [Lanterne et al., 2020], [Wyss et al., 2020a], [Ingenito et al., 2021]. Implementing such a fabrication process, Feldmann *et al.* reached conversion efficiencies of almost 23% on industrial TOPCon solar cells [Feldmann et al., 2020]. However, such thick layers lead to parasitic light absorption, hindering their implementation on the front side, as

well as on the rear in the case of bifacial architectures. Localized passivating contacts are one approach to overcome this limitation as described earlier.

Another approach is to use thin poly-Si layers, capped with a TCO. The latter is transparent and provides good lateral conductivity, enabling an efficient charge carrier extraction despite thin doped layers. Bruhat *et al.* reported $J_0 < 100 \text{ m}\Omega\text{cm}^2$ and $iV_{oc} > 715 \text{ mV}$ for $\text{SiN}_x\text{:H}/\text{AlO}_x/\text{AZO}/\text{poly-Si}(n)$ stacks fired up to 900°C [Bruhat et al., 2020]. A further interesting approach was presented by Tutsch *et al.*, implementing hydrogen-rich TCOs, which act as hydrogen source upon a subsequent annealing at $\sim 400^\circ\text{C}$ [Tutsch et al., 2020]. Compatibility with firing was not reported, but it simplifies the fabrication process by avoiding a dedicated hydrogenation step. Using a simple process featuring TCO layers too, CEA reported 22.7% of conversion efficiency for a solar cell featuring 15 nm thick poly-Si on tunneling SiO_x , capped with Indium-Tin-Oxide (ITO) or ITO:H on both sides [Oliveau et al., 2020], [Desrues et al., 2021]. The metallization was done by screen printing of a low temperature metallic paste, followed by a sintering at 350°C .

Such low temperature metallization approaches yield the advantage of reduced mechanical and thermal impact on the wafer compared to firing-through [Balaji et al., 2019], as well as the ability to contact thin poly-Si layers without damaging the passivation (no metal spiking). Next to screen printing of low temperature pastes, common approaches are sputtering [Hayes et al., 2019], evaporation [Stuckelberger et al., 2016b] or electroplating [Grübel et al., 2019]. For example, HTPC cell designs involving Ni/Cu/Ag plating demonstrated conversion efficiencies up to 23.4% [Steinhauser et al., 2018]. A further interesting result was recently reported by Qiu *et al.*: They evaporated Ag on a $\text{SiO}_x/\text{poly-Si}(n)/\text{SiC}_x(p)\text{:H}$ stack [Qiu et al., 2020]. In this design, the $\text{SiC}_x(p)\text{:H}$ acts as a conductive hydrogen reservoir, avoiding again the need for a dedicated hydrogenation step via a sacrificial $\text{SiN}_x\text{:H}$ layer, as used in [Ingenito et al., 2018], for example.

1.5 Objectives and structure of this thesis

The main objective of this thesis was a thorough investigation of the hydrogenation process of FPCs, using advanced characterization techniques such as Secondary Ion Mass Spectrometry (SIMS), Atom Probe Tomography (APT), Transmission Electron Microscopy (TEM), Rutherford Backscattering Spectrometry (RBS), Elastic Recoil Detection Analysis (ERDA) and Modulated Photoluminescence (MPL). Such measurements were done in collaboration with various institutions. Further, the microstructure of the used SiC_x layers was analyzed, as well as the impact of various processing steps, such as the firing, on the passivation of the sample. Moreover, several metallization approaches were tested, aiming to develop a simple process flow for FPC based solar cells.

After this introduction, providing a brief overview on the theory and state of the art of solar cells in general, and HTPCs in particular, the individual chapters of this thesis are structured as follows:

- **Chapter 2:** Description of the experimental details, *i.e.* of the fabrication process of FPC test structures and solar cells, as well as of the characterization techniques used in this thesis.
- **Chapter 3:** Detailed analysis of the hydrogenation process of FPCs. The impact of the various processing steps on minority carrier lifetime was studied, as well as the distribution of hydrogen within the deposited layers throughout the fabrication. Various types of oxides and SiC_x layers were used to elucidate the passivation mechanism.
- **Chapter 4:** Investigation of the kinetics of the hydrogenation process. Using experimental and numerical approaches, the bulk and surface lifetimes were discriminated, and their evolution throughout the fabrication process studied. In addition, hydrogenation with a SiN_x:H reservoir layer on one side of the wafer only was tested, which would provide more flexibility to the cell fabrication process.
- **Chapter 5:** Testing of the stability of the passivation provided by hydrogenated FPCs. Long-term experiments under illumination were performed, as well as exposing the samples to elevated temperatures.
- **Chapter 6:** Development of thick firing stable layers and investigation of firing-through metallization. Moreover, low temperature metallization via aluminium evaporation or ITO and silver sputtering was tested. Finally, solar cells featuring co-fired FPCs on both sides were fabricated.
- **Chapter 7:** Summary of the presented results and outlook on future investigation and development possibilities.
- **Appendices:** Further results regarding the microstructure of SiC_x layers, the quantification of hydrogen and deuterium content in SiN_x:H/D layers, and the use of fluorine instead of hydrogen to passivate dangling bonds.

1.6 Contribution to the field

This work contributed to a better understanding of FPCs, a novel contact type introduced in 2018 [Ingenito et al., 2018], and provided further insight on various mechanisms valid for HTPCs in general. In particular, it was shown that the surface passivation of FPCs relies on the accumulation of hydrogen at the c-Si/SiO_x interface, where it passivates interfacial defect states (dangling bonds). The key role of chemical passivation was corroborated by the finding that the doping of the SiC_x layer does not influence the passivation quality, and that this layer can even be removed with only minor loss in iV_{oc} . Further, the influence of the type of oxide layer on the achieved passivation was highlighted, achieving up to 737 mV of iV_{oc} with thick thermal oxides. The advanced characterization techniques applied to the SiO_x/SiC_x stacks provided new insight on their microstructure, revealing that carbon and boron form clusters upon firing. The current interpretation being, that the nc-SiC_x layer is made of 5–10 nm small

c-Si grains within an a-SiC_x matrix. These results explain some of the mechanisms at work in FPCs and corroborate similar findings of other groups on different contact types.

A surprising finding was that despite using high quality FZ wafers, the effective minority carrier lifetime before hydrogenation was not only limited by the surface, but also by shallow bulk defects created upon firing. In fact, the kinetics of the hydrogenation process is mainly determined by the passivation of these bulk defects. This highlights the importance of deconvoluting the impact of the bulk and the surface on the effective lifetime and to consider potential bulk defects no matter the quality of the wafers used. It is also an encouraging results, as it indicated that the surface passivation is achieved much faster than previously assumed. First tests indicate the potential for surface passivation by fluorine diffusing from a SiC_x:F layer upon firing, or from a SiN_x:H reservoir layer deposited on one side only of the wafer, which would provide some more flexibility to the fabrication process of solar cells based on FPCs.

Regarding the stability of the passivation provided by FPCs, it was shown to be maintained over 80 days of exposure to 1 sun of illumination at 80 °C. Moreover, the measured lifetime remained stable upon thermal treatments of 30 min at temperatures up to 170 °C. These are the first reports on long-term stability of FPCs and corroborate the viability of this technology.

The last part of this thesis contributed towards the metallization of HTPCs, one of the main remaining challenges for their large scale and double-sided implementation in industry. Unfortunately, good contact upon firing-through of screen printed contacts could not be achieved without losses in passivation. Nevertheless, a thermal pre-treatment allowing for thicker firing-stable layers was developed. Finally, using low temperature metallization via sputtering of ITO and silver, first proof-of-concept solar cells featuring co-fired FPCs at the front and rear were fabricated. They reached up to 20.5% of conversion efficiency, demonstrating the potential of such an architecture.

Moreover, thanks to several collaborations, the work presented in this thesis also directly contributed to the research of other groups, for example by applying our hydrogenation process to their contact structures, in order to compare the passivation results achieved with their baseline. Note that most of the work presented in this thesis was part of a collaboration with the Luxembourg Institute of Science and Technology (LIST). In addition to performing SIMS measurements on our FPC structures, they used dedicated samples fabricated by our laboratory to push further their characterization capabilities.

A list of publications resulting from this work and the mentioned collaborations is given at the end of this document. Overall, the feedback received on these results throughout the journey of this thesis, especially during conferences, indicates their relevance to the PV community, endorsing the value of the performed work.

2 Experimental details

This chapter gives an overview of the tools and processes used in this thesis. A first part describes the sample preparation, while a second one focuses on the characterization techniques. The fabrication process consists of many steps, several of which were performed in close collaboration by colleagues at the Swiss Center for Electronics and Microtechnology (CSEM). Regarding sample characterization, many advanced techniques such as SIMS, TEM or APT were applied, requiring expertise for data acquisition and analysis. These measurements were therefore performed in collaboration with several institutions, such as the Luxembourg Institute of Science and Technology (LIST). External contributions to sample fabrication and characterization are acknowledged in the respective sections of this chapter.

2.1 Sample preparation and systems

Several type of samples were fabricated for the various experiments performed for this thesis, ranging from simple test structures to complete cells. This section hence gives a general overview of the various processing steps, while the details are given in the experimental parts of the specific experiments.

The most frequently processed sample type was a symmetrical FPC test structure, featuring a ~25 nm thick *p*-type nc-SiC_x layer on top of a tunneling SiO_x on both sides of a FZ c-Si wafer. These samples allow assessing the performance of the FPC in terms of surface passivation. Their fabrication process is represented in Fig. 2.1. It starts with a chemical cleaning of the wafer, followed by the growth of an oxide layer at its surface. Doped a-SiC_x layers are subsequently grown on top of it by PECVD on both sides of the wafer. A rapid thermal treatment (typically 3 s at 800 °C), called firing, is then performed, crystallizing the layers and activating the dopants. As stated in the previous chapter, FPCs rely strongly on chemical passivation of the interface, achieved thanks to a hydrogenation step. To do so, a SiN_x:H layer, acting as hydrogen reservoir, is deposited by PECVD on both sides of the wafer, followed by a 30 min long hotplate treatment at 450 °C, during which the hydrogen diffuses towards the c-Si/SiO_x interface and attaches to dangling bonds. Finally, the SiN_x:H reservoir layers are

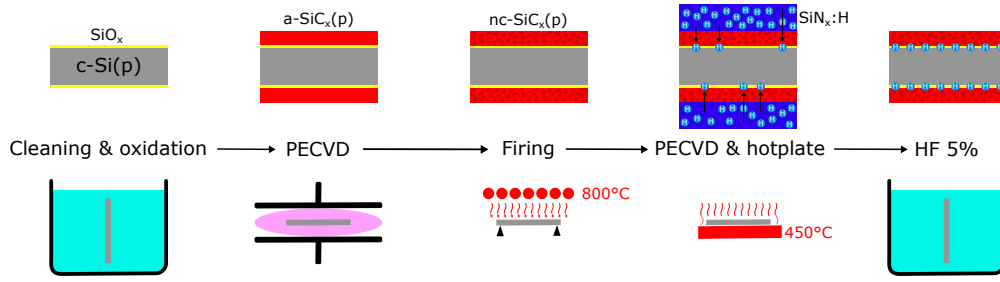


Figure 2.1 – Schematic representation of the fabrication process of symmetrical FPC test structures.

removed during a 12 min long etch in a 5% HF solution.

More details and possible variations of these processing steps are given in the following subsections. Note that a subsequent metallization, not present in the fabrication process explained above, is required to assess the electrical performance of the passivating contact.

2.1.1 Wafer preparation

Since high temperature processes are involved, it is crucial to work with very clean wafers, to avoid diffusion of contaminants. Therefore, the fabrication process starts with a so called "RCA Standard Clean" of the wafers [Kern, 1990], consisting mainly of two cleaning sequences, SC-1 and SC-2. Both remove impurities by simultaneously oxidizing the wafer surface and etching this oxide. The SC-1 solution consists of water (H_2O), hydrogen peroxide (H_2O_2) and ammonium hydroxide (NH_4OH), and removes organic contaminants, while in the SC-2 the ammonium hydroxide is replaced by hydrochloric acid (HCl) such as to remove metallic contaminants.

Most samples were prepared on p -type FZ (100) wafers, with either a Shiny-Etched (SE) or Double Side Polished (DSP) surface finish. DSP wafers feature an atomically flat surface and were used for samples to be analyzed by SIMS, TEM, APT, RBS and ERDA. They were purchased from Topsil GlobalWafers A/S, had a thickness of $280\mu\text{m}$ and a resistivity of $3\Omega\text{cm}$. On the other hand, SE wafers were purchased from Siltronic AG, had a thickness of $200\mu\text{m}$ and a resistivity of $2\Omega\text{cm}$. While still considered flat, SE wafers display some surface roughness [Breitenstein et al., 2011]. An image of a SE wafer surface, taken by atomic force microscopy (AFM), is shown in Fig. 2.2. Note that for some experiments, wafers with higher resistivities or n -type doping were used. Moreover, solar cells were processed on wafers with a textured front surface, featuring micron-scale random pyramids enhancing light trapping [Campbell and Green, 1987].

Chemical wafer cleanings were performed by Xavier Niquille, as well as Fabien Debrot and Patrick Wyss. Their contribution is gratefully acknowledged.

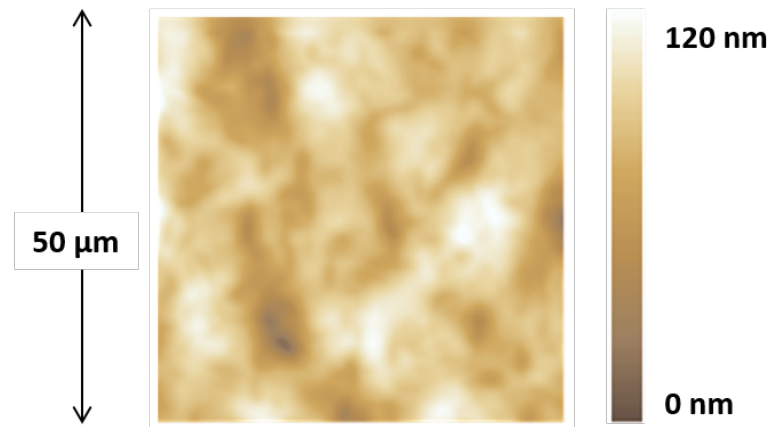


Figure 2.2 – AFM image of a SE wafer surface. The color map represents the topography of the sample. Courtesy of Dr. Franz-Josef Haug.

2.1.2 Oxide growth

Following the RCA wafer clean, an oxide layer was grown on both sides of the wafer. To do so, the wafers were first dipped for 1 min in a 5% HF solution to remove any native surface oxide already present. Then, a controlled oxidation was performed, either by wet chemistry, UV-Ozone exposure or a thermal treatment.

Chemical oxides are grown by submerging the wafers for 10 min in a hot HNO_3 solution (69 %, 80 °C), resulting in a ~ 1.3 nm thick SiO_x layer [Kobayashi et al., 2003], [Grant and McIntosh, 2009]. As for UV-Ozone (UV- O_3) oxides, they are grown by exposing the wafer to UV radiation in ambient air for 2–3 min on each side, resulting in a ~ 1.3 nm thick SiO_x layer too [Moldovan et al., 2015], [Fukano and Oyanagi, 2003], [Moldovan et al., 2014]. Both of the above processes are self-limiting, resulting in homogeneous oxides layers thin enough to enable current transport through tunneling [Ingenito et al., 2021]. In contrast, thermal oxides can be grown much thicker. In this thesis, ~ 25 nm thick SiO_2 layers were grown in a tube furnace by exposing the wafer to an oxygen ambient at 900 °C for 90 min [Fossum and Burgess, 1978], [Blakers and Green, 1985], [Snel, 1981], [Yablonovitch et al., 1985]. An N_2 ambient was applied while ramping the temperature up and down. The resulting oxide layers feature a composition closer to stoichiometric SiO_2 than their chemical and UV- O_3 counterparts [Stegemann et al., 2017]. However, growing them thin enough for current transport by tunneling is very challenging. The ~ 25 nm thick thermal SiO_2 layers used in this thesis were obviously insulating and used for specific investigations only.

Chemical and UV- O_3 SiO_x layers were grown by Xavier Niquille, thermal SiO_2 layers by Jörg Horzel, as well as Christophe Allebé, Andrea Ingenito and Stéphane Ischer. Their contribution is gratefully acknowledged.

2.1.3 Deposition of doped layers

Thin silicon-based layers (mainly a-SiC_x(*p*)) were deposited on top of the SiO_x layer by PECVD. Two different reactors were used for these processes: An Octopus-I from INDEOtec and a KAI-M from Unaxis (which became part of Oerlikon Solar and now TEL Solar). The Octopus consists of four chambers in a cluster configuration, dedicated to different processes. The wafers are processed one by one. The Kai-M on the other hand has a larger reactor area, allowing deposition on up to 12 wafers simultaneously. It consists of two chambers, dedicated to the deposition of intrinsic and doped layers, respectively. Both reactors feature two parallel electrodes. One of them holds the samples, while the other one contains a shower head injecting the precursor gases. Applying an alternating electric field between the electrodes dissociates the molecules of the precursor gases, creating a plasma of free radicals and ions that deposit on the sample (and the reactor walls), growing a layer. PECVD is a highly versatile technique, allowing control of layer doping, crystallinity, chemical composition, growth rate and thickness by adjusting the plasma parameters (gas flows of precursor gases, temperature, pressure, deposition time, excitation power and frequency). All layers presented within this thesis were deposited at 200 °C using mainly SiH₄, H₂, D₂, CH₄ and B(CH₃)₃ as precursor gases. Doped layers were deposited using an excitation frequency of 40.68 MHz, whereas 13.56 MHz were applied for intrinsic ones. Further details are provided in the experimental parts of the specific experiments.

2.1.4 Rapid Thermal Processing (RTP)

As mentioned earlier, a key feature of FPCs is that they are formed with a low thermal budget, applying a rapid thermal annealing called "firing". This processing step was performed in a Jetfirst 200 lamp furnace from Jipelec. The applied temperature profile, mimicking those of industrial firing-through processes, consisted of a rather slow (5 °C/s) heating phase up to 400 °C, followed by a rapid (50 °C/s) heating up to a peak temperature of typically 800 °C, kept for typically 3 s and followed by a rapid cooling. During this step, the initially amorphous film (a-SiC_x(*p*):H) crystallizes into nanocrystalline nc-SiC_x(*p*), dopants are activated and hydrogen effuses from the layers. The carrier density after firing at 800 °C was reported to be around $5 \cdot 10^{19} \text{ cm}^{-3}$ [Haug et al., 2019]. Based on APT and TEM observations, we assume the nc-SiC_x(*p*) layer to be formed of nc-Si grains embedded in an a-SiC_x matrix. More details are given in appendix A.

2.1.5 Hydrogenation

The main hydrogenation route applied in this thesis was hydrogen diffusion from a SiN_x:H reservoir layer. To do so, a ~70 nm thick layer of SiN_x:H was deposited in an in-house built PECVD tool called "XL". It is a parallel plate reactor, operating with an excitation frequency of 81.36 MHz and a plate size for up to 8 wafers. The deposition was performed at 250 °C, with an excitation power of 130 W. The butterfly valve controlling the chamber pressure during

deposition was kept open, resulting in pressures around 0.025 mbar, depending on the gas flows. The latter were 5.5 sccm of SiH_4 , 10.4 sccm of NH_3 , with a deposition time of 7 min. This recipe was optimized for release of hydrogen during a subsequent 30 min hotplate (HP) treatment at 450 °C [Nogay et al., 2017]. In some cases, 25 sccm of D_2 were added to the precursor gases, in order to incorporate deuterium alongside hydrogen into the $\text{SiN}_x\text{:H/D}$ layer. This was mainly done for samples to be analyzed by SIMS, since in contrast to hydrogen, the measured deuterium signal is not affected by residual gas present in the chamber or humidity adsorbed on the sample surface. The refractive index of these layers, measured by spectroscopic ellipsometry, was found to be 2.0 at a wavelength of 632 nm, and their composition, measured by RBS, close to Si_3N_4 , with a total hydrogen and deuterium content of ~19%. More details are given in appendix B.

Even though there is no apparent difference in SiN_x layer properties upon addition of a D_2 flow, it was kept or replaced by an H_2 flow for most experiments, in order to keep the experimental conditions as similar as possible. Due to its higher mass, deuterium has a lower diffusivity than hydrogen [Carlson and Magee, 1978]. The impact of this difference on the kinetics of the hydrogenation process is investigated in chapter 4. However, the passivation mechanism should be identical, as the nature of both isotope's bond with Si is the same. Note that the term hydrogenation is used indifferently whether deuterium is diffused alongside hydrogen for passivation or not.

In a few cases, hydrogenation was performed either via Forming Gas Annealing (FGA) for comparison with the hydrogen diffusion from a $\text{SiN}_x\text{:H}$ reservoir layer. FGA consists of a 30 min long annealing at 500 °C in forming gas (4% H_2 in N_2), performed in the Jetfirst 200 lamp furnace. Here too, the H_2 gas flow was replaced by D_2 for some samples.

For some experiments, the $\text{SiN}_x\text{:H}$ reservoir layers were deposited in a MAiA PECVD tool from Meyer Burger Technology AG, according to a recipe developed by colleagues at CSEM and Meyer Burger, optimized for hydrogen release during a subsequent firing, instead of a hotplate treatment at 450 °C. The hydrogen diffusion was then performed in a Meyer Burger Camini ceramic roller furnace with a peak temperature set to 830 °C.

The deposition of these firable $\text{SiN}_x\text{:H}$ layers and the subsequent Camini furnace firing was performed by Christophe Allebé, Andrea Ingenito and Juan Diaz Leon. Their contribution is gratefully acknowledged.

2.1.6 Metallization

Several approaches were tested to metallize the FPCs. A first one consisted of sputtering ITO on top of the nc- SiC_x layer, and contacting this ITO either with sputtered Ag or a screen-printed Ag paste. After screen-printing, the paste was dried by sintering the samples for 30 min at 130 °C. Another approach was to evaporate aluminium directly on the nc- $\text{SiC}_x(p)$ layer. Both methods are performed at low temperatures and require removal of the SiN_x layer before

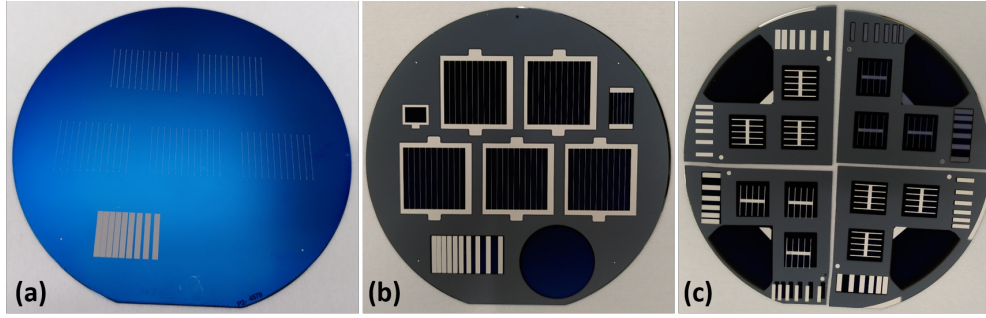


Figure 2.3 – Pictures of various samples after metallization. (a) Sample featuring a TLM pad and fingers screen printed on $\text{SiN}_x\text{:H}$ for firing-through experiments. (b) Solar cells with screen-printed Ag on ITO. (c) Solar cells with sputtered Ag on ITO.

metallization. A third approach consisted in screen printing aluminium pastes on the firable $\text{SiN}_x\text{:H}$ layer, followed by a firing during which the paste burns through the $\text{SiN}_x\text{:H}$ layer and contacts the doped silicon-based layer below.

For Physical Vapor Deposition (PVD) of ITO and Ag, a MRC Sputtering System P603 from NIHON MRC Co., LTD was used. Aluminium evaporation was performed by e-beam in a Leybold-Heraeus L560 system, with a deposition rate of $\sim 8 \text{ \AA/s}$. The screen printing was done with commercial Ag or Al pastes, using a XH STS screen-printer from EKRA. As for the firing-through, it was performed in a Meyer Burger Camini ceramic roller furnace with a peak temperature set to 830°C .

For PVD and screen printing, various masks were used, depending on the experiment. The different designs are shown in Fig. 2.3. For firing-through experiments, the mask design features five $15 \times 21 \text{ mm}^2$ areas of $\sim 70 \pm 15 \text{ }\mu\text{m}$ wide fingers, alongside a Transfer Length Method (TLM) pattern (Fig. 2.3a). The exact finger width depends on the paste, the properties of the $\text{SiN}_x\text{:H}$ layer and the firing conditions, and may change slightly from run to run. As for the TLM pattern, it consists of 12.5 mm wide and 1.45 mm long pads, separated by 0.27 , 0.41 , 0.61 , 0.81 and 1.01 mm . Note that actually the pattern is made of 9 pads, but due to inhomogeneity in the print the first three pads are most often in contact with each other. Fig. 2.3b shows the design of $2 \times 2 \text{ cm}^2$ solar cells, with screen printed fingers and bus bars outside the active cell area. This design features $30 \text{ }\mu\text{m}$ wide fingers with a 1.85 mm finger pitch, resulting in $\sim 3\%$ shading losses, $\sim 2 \text{ }\Omega/\text{cm}$ finger line resistance, and ρ_c between ITO and Ag $\leq 1 \text{ m}\Omega\text{cm}^2$. The design shown in Fig. 2.3c features $1 \times 1 \text{ cm}^2$ cells with fingers and busbars sputtered through a hard mask. This design results in 18–25% shading losses. An additional design of hard masks (not shown here), used for aluminium evaporation, featured 6 TLM patterns with 10 pads each, being 6 mm wide and 1.6 mm long, and separated by 0.25 , 0.5 , 1.0 , 1.5 , 2.0 , 2.5 , 3.0 , 4.0 and 5.0 mm .

Screen printings were performed by Patrick Wyss, Ludovic Lauber, Nicolas Badel and Juan Diaz Leon; Camini furnace firings by Christophe Allebé, Andrea Ingenito and Juan Diaz Leon;

aluminium evaporation by Sofia Libraro and Sylvain Dunand. Their contribution is gratefully acknowledged.

2.1.7 Wet-chemical layer removal

In many of the experiments, the $\text{SiN}_x\text{:H}$ reservoir layer was removed after hydrogenation. Most of the time, this was done by a 12 min long etching in a 5% HF solution at room temperature. In some cases, where the $\text{SiN}_x\text{:H}$ layer was deposited directly on top of a thick thermal SiO_2 layer, H_3PO_4 (85%, 170 °C) was used, as HF would also etch the SiO_2 layer below. Finally, in cases where the $\text{SiN}_x\text{:H}$ layer was to be removed on one side of the wafer only, it was etched by vapor HF by placing it on top of a beaker filled with a 50% HF solution at room temperature.

To remove the SiC_x layers, the samples were etched in a 20% KOH solution at 60 °C. KOH also attacks SiO_2 only slowly, allowing a selective etch of the SiC_x layer on top of 25 nm thick thermal SiO_2 . SiC_x layers deposited in the Octopus could be removed within 20 min (faster etching for $\text{SiC}_x(n)$ than $\text{SiC}_x(p)$). However, the etching took several hours for $\text{SiC}_x(p)$ layers deposited in the Kai-M, and was inhomogeneous, resulting in locally removed SiO_2 . The reason behind this huge difference in etch rate between layers deposited in one or the other reactor is unknown so far. For experiments where the removal of all layers was wanted (including the SiO_x and the first few microns of the c-Si wafer), the samples were submerged for 2 min in a CP4 solution at room temperature. The latter consists of a mixture of HF (50%), HNO_3 (69%) and Acetic acid (99.9%), in volume ratios of 10%, 73% and 17%, respectively.

2.2 Characterization techniques

2.2.1 Quasi-Steady State Photoconductance

The passivation quality of the samples was assessed by measuring their photoconductance using a Sinton WCT-120TS instrument (see Fig. 2.4). This technique is non-destructive, contactless and fast [Kane and Swanson, 1985], [R. Sinton and Cuevas, 1996]. The samples are placed on top of a coil that inductively measures their conductance. Excess charge carriers are generated by a flash, increasing the conductance of the sample. A reference cell measures the intensity of the flash. Recording these values allows the extraction of the injection dependent effective minority carrier lifetime (τ_{eff}) via the following formula [Nagel et al., 1999]:

$$\tau_{\text{eff}}(\Delta n) = \frac{\Delta n(t)}{G(t) - \frac{\partial \Delta n(t)}{\partial t}} \quad (2.1)$$

where $G(t)$ is the photogeneration rate, and Δn the excess charge carrier density. $G(t)$ and Δn are determined thanks to the recorded flash intensity and sample conductance, respectively. Several measurement modes exist: For samples featuring low carrier lifetime values, quasi-steady state photoconductance (QSSPC) [R. Sinton et al., 1996] is measured, while



Figure 2.4 – Pictures of the WCT-120TS setup used for QSSPC measurements. Image reproduced with permission from [Sinton Instruments, n.d.]. Copyright ©2021, Sinton Instruments.

photoconductance decay is measured, in transient [Kane and Swanson, 1985] or generalized [Nagel et al., 1999] mode, for samples featuring higher lifetime values. All these measurements can be performed using a Sinton WCT-120TS instrument, varying only the duration of the flash and the simplifications made to formula 2.1 for lifetime computations. Therefore, to keep the terminology simple, the term "QSSPC" is used in this manuscript for all lifetime measurements, independently of the measurement mode actually used.

Plotting τ_{eff} as function of Δn provides information about the recombination mechanisms at work, as shown in Fig. 1.6. In this thesis, $\tau_{\text{eff}@10^{15}\text{cm}^{-3}}$, the value of τ_{eff} at $\Delta n = 1 \cdot 10^{15} \text{ cm}^{-3}$, is used to compare the passivation of various samples among each other. Using equation 1.6, the implied open circuit voltage (iV_{oc}) at 1 sun can be computed, providing another way to compare the passivation of various samples [Kane and Swanson, 1985], [R. Sinton et al., 1996], [Cuevas and Sinton, 1997]. The software provided with the instrument automatically calculates iV_{oc} . Note that the Sinton WCT-120TS features a temperature stage, allowing for measurements at sample temperatures up to 200 °C.

To quantify the surface passivation quality, the dark saturation current density (J_0) was extracted from the data measured by QSSPC according to the method published by Kimmerle *et al.* [Kimmerle et al., 2015]. The J_0 values are given per wafer side throughout this thesis. Note that Kimmerle *et al.* recommend to fit around Δn values 10 times higher than the wafer doping. The QSSPC measurements providing values up to $\Delta n = 3 \cdot 10^{16} \text{ cm}^{-3}$, this implies to work with wafers (*p*-type) featuring a resistivity higher than 5 Ωcm . Since most of our samples

were processed on 2–3 Ωcm wafers, the J_0 values obtained in this thesis have to be considered with some caution.

Knowing τ_{eff} and τ_{bulk} , hence also τ_{surf} (see equation 1.15), another way to assess the surface passivation, is to compute the effective surface recombination velocity (S_{eff}). This was done using the method described by Sproul [Sproul, 1994]. In the case of symmetrical samples, for which one can assume $S_{\text{front}} = S_{\text{rear}} = S_{\text{eff}}$, the following approximation holds:

$$\tau_{\text{surf}} = \frac{W}{2S_{\text{eff}}} + \frac{1}{D} \left(\frac{W}{\pi} \right)^2 \quad (2.2)$$

where W is the wafer thickness and D the diffusivity of minority carriers. For asymmetrical samples, the solution was obtained graphically, using Fig. 1 of Sproul's publication [Sproul, 1994]. The value of the diffusivity needed for these computations was determined from the wafer resistivity with the help of PV Lighthouse's mobility calculator [McIntosh et al., 2011].

2.2.2 Photoluminescence imaging

Photoluminescence (PL) imaging is a further tool to assess passivation. It does so by illuminating the sample with a laser, generating excess carriers, and detecting light emission from band-to-band recombination using a CCD camera. Sample regions with defects and impurities are strongly dominated by non-radiative recombination and appear dark on the acquired PL image, whereas regions with high signal indicate good passivation, making radiative recombination more prevalent. Like QSSPC, this technique is fast, contactless and non-destructive. More details can be found in [Trupke et al., 2006], for example. Within this thesis, the signal was not calibrated (*i.e.* the signal intensity not correlated with $\tau_{\text{eff}@10^{15}\text{cm}^{-3}}$). PL imaging was therefore mainly used to assess the homogeneity of the passivation.

For these measurements, an in-house built setup was used. The samples are excited using an Ostech laser with a wavelength of 808 nm, providing a generation rate equivalent to 1.2 Suns, and the images are recorded with a silicon-based camera (PIXIS. Princeton Instruments).

2.2.3 Modulated Photoluminescence

Modulated Photoluminescence (MPL) assesses the minority carrier lifetime of a sample by measuring the phase shift between a modulated laser illumination and the photoluminescence signal of the sample. The link between these quantities is described by the following formula [Brüggemann and Reynolds, 2006]:

$$\tan(\Phi) = -\omega\tau_m \quad (2.3)$$

where Φ is the measured phase shift, ω the modulation frequency, and τ_m the so-called differential lifetime. The effective minority carrier lifetime τ_{eff} is then given by [Giesecke et al.,

2013]:

$$\tau_{eff}(G) = \tau_m(G) \left(1 - G \frac{d\tau}{d\Delta n} \Big|_{\Delta n} \right) \quad (2.4)$$

where G is the photogeneration rate, and Δn the excess charge carrier density. Repeating the measurement at various laser intensities and modulation frequencies enables to compute $\tau_{eff@10^{15}\text{cm}^{-3}}$. Further details can be found in [Sreng, 2019], [Desthieux et al., 2020b] and [Desthieux, 2021].

An in-house built setup at the Institut Photovoltaïque d'Ile de France, shown in Fig. 2.5, enables in situ MPL measurements of a sample within a PECVD reactor [Sreng, 2019]. Treating fired $\text{SiO}_x/\text{SiC}_x$ stacks capped with $\text{SiN}_x\text{:H/D}$ layers for 30 min at 450 °C within this setup, $\tau_{eff@10^{15}\text{cm}^{-3}}(t)$ could be measured in real time during the hydrogenation process.

The MPL measurements presented in this thesis were performed at the Institut Photovoltaïque d'Ile de France by Anatole Desthieux. His contribution, as well for data acquisition as for its treatment and interpretation, is gratefully acknowledged.

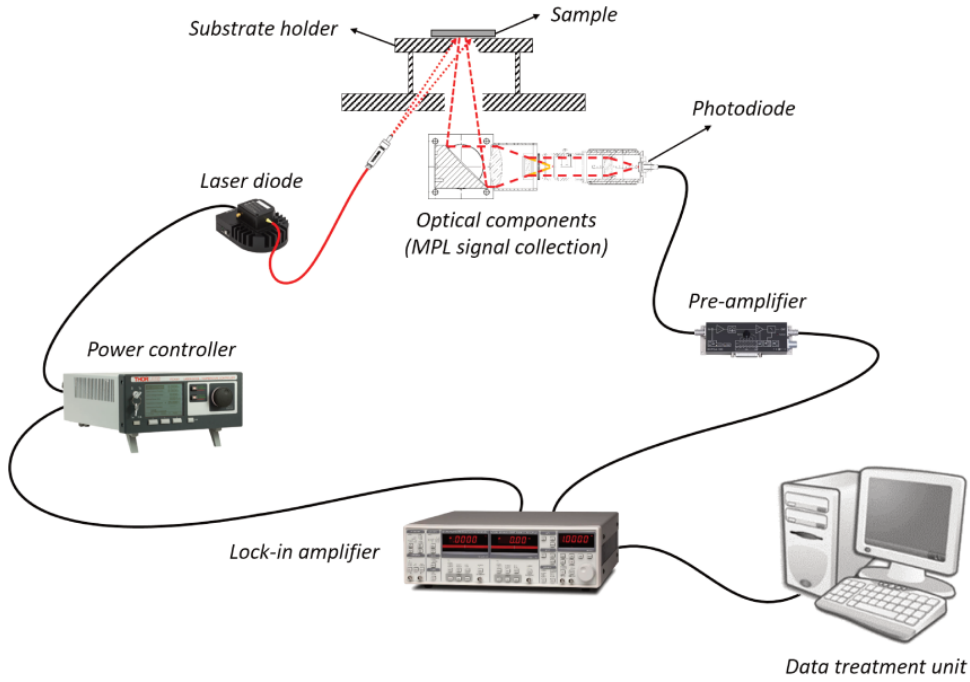


Figure 2.5 – Schematic of the setup used for MPL measurements. Reproduced with the author's permission and without modifications from [Sreng, 2019]. Copyright ©2019, M. Sreng.

2.2.4 Secondary Ion Mass Spectrometry

Secondary Ion Mass Spectrometry (SIMS) was used to analyze the chemical composition of the deposited layers. In this technique, a focused primary ion beam is used to sputter the sample

surface. The ejected secondary ions are collected and analyzed using a mass spectrometer. Advantages of SIMS are its high chemical sensitivity, detecting concentrations down to parts per billion, and its high mass resolution, enabling to distinguish ions with similar masses, such as D^+ and H_2^+ . A detailed description of SIMS can be found in [McPhail and Dowsett, 2009], for example.

The interpretation of SIMS measurements is not as straightforward as it might seem. Indeed, the secondary ion yield depends on the species, as well as its chemical surrounding. A change in signal can therefore occur when moving from one layer to another, even if the concentration of the analyzed species did not change. This limitation can be overcome by measuring in MCs_2^+ mode, which is much less sensitive to this so called "matrix effect". In this mode, the species "M" is detected attached to Cs^+ from the primary ion beam, instead of being detected directly as M^+ or M^- . As said, the secondary ion yield depends also on the species. As a consequence, the M^- mode is most sensitive when measuring deuterium or hydrogen, whereas M^+ (using O_2^+ as primary ions) is most sensitive for boron detection.

Due to these effects, calibrating the SIMS with known reference samples is necessary to acquire quantitative data. Since measurements were performed on various layers within this thesis, which would require to fabricate dedicated reference samples for each of them, the calibration was omitted. The obtained results are therefore qualitative.

Another possible measurement artefact is the sputtering rate varying from one layer to another, influencing the signal intensity. In MCs_2^+ mode, the validity of the observed trends can be verified by taking the ratio of the intensity measured for each element with the one measured for silicon.

For this thesis, SIMS measurements were performed using a CAMECA SC-Ultra instrument with a 1 keV Cs^+ primary ions bombardment. Elements were analyzed as M^- and MCs_2^+ . Ions were collected from an area of $60\mu m$ in diameter, with a depth resolution of ~ 4 nm (not element dependent) [Chanbasha and Wee, 2008].

SIMS measurements were performed at the Luxembourg Institute of Science and Technology, by Nathalie Valle and Brahime El Adib. Their contribution, as well for data acquisition as for its treatment and interpretation, is gratefully acknowledged.

2.2.5 Atom Probe Tomography

Atom Probe Tomography (APT) is a destructive material analysis technique, basically combining a field ion microscope with time of flight mass spectrometry, allowing 3-dimensional imaging and chemical mapping of the measured sample at atomic scale. To do so, very sharp tips are prepared by Focused Ion Beam (FIB) from the sample to be analyzed. High voltage is then applied to the cooled tip, such as to bring its surface just below the point of atom evaporation. A pulsed laser is then used to evaporate a few ionized atoms of the surface of the tip. The electric field accelerates them towards a detector, where their time and position

of impact are recorded. From these information, the original position of the atom, as well as its mass, can be computed. The chemical sensitivity is not as high as the one of SIMS, but it features exceptional spatial resolution (0.1–0.3 nm in depth, 0.3–0.5 nm laterally).

The measurements presented in this thesis were taken with a LEAP 3000X HR atom probe from CAMECA. Datasets were reconstructed and analyzed by the commercial CAMECA Integrated Visualization and Analysis Software (IVAS 3.6.8) package. More details can be found in [Pal et al., 2021].

APT measurements and data processing were performed by Jenifer Barrirero, Universität des Saarlandes, Germany, and Soupitak Pal, Luxembourg Institute of Science and Technology, Luxembourg. Their contribution is gratefully acknowledged.

2.2.6 Ion Beam Analysis

For quantitative information on chemical composition of the samples, Rutherford Backscattering Spectrometry (RBS) and Elastic Recoil Detection Analysis (ERDA) were performed.

For both techniques, a high energy He^{2+} ion beam (2 MeV in the experiments presented in this thesis) is focused on the sample. Upon elastic interaction with nuclei heavier than themselves within the sample (Si and N in these experiments), some of the incident He ions are scattered back (with respect to the direction of the incident ion beam). The kinetic energy of the backscattered ions depends, among other factors, on the mass of the nuclei it interacted with, enabling chemical analysis. This phenomenon is exploited in RBS. In the case of ERDA, lighter atoms (H and D in this work) knocked out by the incident beam are analyzed. More details can be found in [Nastasi et al., 2015].

For this thesis, RBS and ERDA measurements were performed at the ETH Laboratory of Ion Beam Physics. RBS was measured using a silicon PIN diode detector under 168° . The collected data was analyzed by the RUMP code [Doolittle, 1986]. ERDA was measured under 30° , using the absorber foil technique [Nastasi et al., 2015]. Hydrogen content was normalized using a mica standard containing 9.5 at.% of H. Note that the depth resolution of H in Si of this measurement technique is about 50 nm [Nastasi et al., 2015].

Ion beam analysis measurements were performed by Max Döbeli. His contribution, as well for data acquisition as for its treatment and interpretation, is gratefully acknowledged.

2.2.7 Spectroscopic Ellipsometry

Spectroscopic ellipsometry is a contactless and non-destructive measurement technique, used to assess the thickness and optical properties of layers on a flat substrate. To do so, a collimated beam of linearly polarized light of a given wavelength is shone on the sample surface. Upon reflection, the polarization state of the beam changes, depending on the layer

thicknesses and material properties. A detector measures the complex ratio $\frac{r_p}{r_s}$ after reflection, where r_p and r_s are the amplitudes of the polarization components oscillating parallel and perpendicular to the plane of incidence, respectively, normalized to their initial value (before reflection). From this data, the more intuitive amplitude ratio (Ψ) and the phase difference (Δ) between p- and s-polarizations can be extracted ($\frac{r_p}{r_s} = \tan(\Psi)e^{i\Delta}$). The measurement is repeated for various wavelengths and incidence angles. The acquired data are then fitted with a spectroscopic model that contains the thicknesses and the permittivities of the constituent layers. Hence, spectroscopic ellipsometry is an indirect characterization technique.

The instrument used within this thesis is a UVISSEL™ ellipsometer from HORIBA Jobin Yvon S.A.S., giving access to Ψ and Δ from 0.6 to 6.0 eV. Typically, measurements were taken at three angles of incidence, usually 50, 60 and 70°. Modelling was performed using the software DeltaPsi2, also from HORIBA Jobin Yvon S.A.S. The main parameters of interest for this work were layer thicknesses and refractive indexes, fitted using Tauc-Lorentz models for the deposited layers.

2.2.8 Fourier-Transform Infrared spectroscopy

Fourier-Transform Infrared spectroscopy (FTIR) is a contactless and non-destructive technique, giving access to the absorption of a sample. In FTIR, data is usually given as a function of the wavenumber ω . To do so, a beam of infrared light is focused on the sample and the transmitted (or reflected) intensity is measured. The energy of IR radiation is in the same energy range as atomic or molecular vibrations. Hence, the absorption at given frequencies is characteristic of the chemical bonds present in the material. The absorption spectrum as function of the wavenumber is obtained using a Michelson interferometer and applying a Fourier transformation to the measured interferogram. More details can be found in [Dutta, 2017], for example.

For the FTIR measurements presented in this thesis, a Nicolet 8700 spectrometer from Thermo Fisher Scientific was used. It features a beamsplitter made of KBr and a deuterated triglycine sulfate detector. Typical measurements were averaged over 32 scans. The setup is purged with N₂, reducing artefacts from H₂O and CO₂ due to air present in the beam path. Samples were loaded on a wheel holder, enabling to purge the setup for several hours (typically overnight) and subsequently measure up to 14 samples without opening the setup.

In the case of a layer deposited on a c-Si wafer, the transmitted intensity I_t is approximately (neglecting interferences) given by:

$$I_t(\omega) = I_0(\omega) \cdot e^{-\alpha_{Si}(\omega)d_{Si}} \cdot e^{-\alpha_l(\omega)d_l} \quad (2.5)$$

where I_0 is the intensity of the incident beam, α_{Si} and α_l the absorption coefficients of the wafer and the deposited layer, respectively, and d_{Si} and d_l the wafer and layer thicknesses. Therefore, the absorption spectrum of the deposited layers can be extracted by measuring the

transmitted intensity of a bare c-Si wafer (I_{ref}) alongside those of processed samples (I_{sample}). Since $I_{ref}(\omega) = I_0(\omega) \cdot e^{-\alpha_{Si}(\omega)d_{Si}}$, the absorption spectrum of the deposited layers is obtained by plotting:

$$-\ln\left(\frac{I_{sample}(\omega)}{I_{ref}(\omega)}\right) = \alpha_l(\omega) \cdot d_l \quad (2.6)$$

Note that in figures featuring several FTIR spectra, these have been manually shifted along the y-axis for better readability. A method to estimate the hydrogen and deuterium content of SiN_x:H/D layers from their FTIR spectra is presented in appendix B.

2.2.9 Raman Spectroscopy

Raman spectroscopy (RS) is another contactless and non-destructive technique, used in this thesis for assessing the crystallinity of the layers. A laser beam is focused on the sample, and the energy of the scattered photons is measured. The energy (and hence the frequency) of these photons can change upon inelastic interactions with vibration modes in the sample. The loss (or gain) in energy, and thus the frequency shift, is characteristic of the chemical bonds present in the material. Typical spectra for c-Si, a-Si:H and μ c-Si:H are shown in Fig. 2.6. Raman spectra are plotted over wavenumbers, taking the energy of the incident laser as reference. Scattered light with less energy (Stokes/Raman shift) is generally plotted over positive ω . Monocrystalline c-Si gives rise to a sharp peak at a wavenumber of 520 cm⁻¹, representing the energy required for the excitation of a transverse optical vibrational mode of Si-Si bonds in the crystal. The other modes are usually too weak to be detected. On the other hand, the disordered structure of a-Si:H yields broad peaks at 150 cm⁻¹ (transverse acoustic vibrational mode), 310 cm⁻¹ (longitudinal acoustic), 380 cm⁻¹ (longitudinal optical) and 480 cm⁻¹ (transverse optical) [Bermejo and Cardona, 1979].

According to Smit *et al.*, one can extract the crystallinity fraction by fitting the measured spectra with a series of Gaussian peaks and taking the ratio of the transverse optical peak areas of the crystalline and amorphous parts, centered around 520 cm⁻¹ and 480 cm⁻¹, respectively [Smit et al., 2003]. A MATLAB[®] script developed in-house by Luca Antognini was used to do so.

The measurements presented in this thesis were performed on a MonoVista CRS+ instrument from Spectroscopy & Imaging GmbH, using a laser in the UV (325 nm) or blue (442 nm) spectral range. The penetration depth of the laser into the sample depends on its wavelength [Carpenter et al., 2017]. The UV laser probes only the first 15–20 nm below the surface, hence characterizing only the deposited layers (usually featuring thicknesses ≥ 25 nm), whereas the blue laser penetrates deeper, resulting in a c-Si peak from the wafer appearing in the measured spectra.

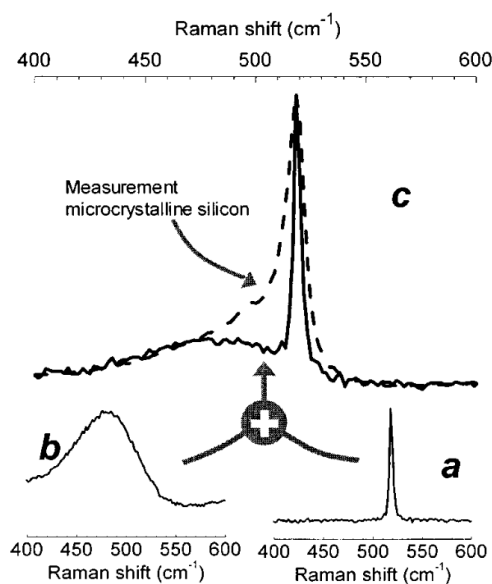


Figure 2.6 – (a) Raman spectrum of monocrystalline silicon (c-Si). (b) Raman spectrum of a-Si:H. (c) Summation of (a) and (b) (solid line), scaled before summation so that the peak and the "bump" in (c) fit the peak and the "tail" of the Raman spectrum of μc -Si:H (dashed line). Reprinted from [Smit et al., 2003], with the permission of AIP Publishing. Copyright ©2003 American Institute of Physics.

2.2.10 Scanning Electron Microscopy

Scanning Electron Microscopy (SEM) images were mainly taken on a Zeiss Gemini 2 microscope, equipped with an Energy-Dispersive X-ray (EDX) detector, typically operated with a 5 keV incident e-beam. In some cases, a FIB/SEM Zeiss NVision 40 was used. To image their surface in top view, the samples were glued horizontally on a holder using conductive tape. Others were cleaved and mounted vertically on dedicated holders to analyze the deposited stacks in cross-section. However, this resulted in an aluminium background signal in EDX coming from the holder. To avoid this, some cleaved samples were embedded in resin and subsequently polished.

SEM images were taken by Quentin Jeangros and Sofia Libraro. Their contribution is gratefully acknowledged.

2.2.11 Transmission Electron Microscopy

Transmission Electron Microscopy (TEM) images presented in this thesis were taken at EPFL's Centre Interdisciplinaire de Microscopie Electronique (CIME), on two different microscopes.

For the results presented in chapter 6, a Tecnai Osiris microscope from Thermo Fisher Scientific was used, operated at 200 kV in scanning TEM (STEM) mode. EDX chemical maps were obtained using a super-X system featuring 4 silicon-drift detectors. As for the results

in appendix A, an aberration corrected Thermo Fisher Scientific Titan Themis microscope was used, which was operated in STEM mode at 200 kV with a beam current of 400 pA at a convergence semi-angle of 29 mrad and with a collection semi-angle of 35 mrad. A Gatan GIF Quantum ERS high energy resolution spectrometer and energy filter was used to collect electron energy-loss spectroscopy (EELS) data, while 4 silicon drift-detectors were used to collect EDX spectra, both in STEM mode. Low-loss EELS data was analyzed using the methodology detailed in [Duchamp et al., 2013] to extract the plasmon peak energy and its full width at half maximum. EDX data was analyzed using the Thermo Fisher Scientific Velox software.

Regarding sample preparation, cross-sections were extracted using the conventional FIB lift-out method, which was performed in a Zeiss NVision 40 FIB/SEM using a final Ga⁺ voltage of 2 kV.

TEM imaging was performed by Quentin Jeangros. His contribution is gratefully acknowledged.

2.2.12 Transfer Length Method

The Transfer Length Method (TLM) is a measurement technique used to determine the contact resistivity ρ_c of the metallized FPCs. To do so, TLM pads were screen-printed, sputtered or evaporated on top of the FPC, as shown in Fig. 2.3. The electrical resistance between each pair of pads is measured with a set of 4-point probes and plotted as a function of the distance separating them. A linear fit of the measured data points provides the values of the sheet resistance R_S , the contact resistance R_C and the transfer length L_T , as explained in Fig. 2.7. The transfer length being the average distance travelled by an electron (or hole) beneath the contact before flowing up into it. A rough and intuitive estimation of the contact resistivity ρ_c is then given by:

$$\rho_c = R_C W L_T \quad (2.7)$$

where W is the width of the TLM pads. More details can be found in [Berger, 1972] and [Reeves and Harrison, 1982].

The setup and software used for TLM measurements was built in-house. For a more exact determination of ρ_c , a MATLAB[®] script developed in-house by Frank Meyer was used, implementing the 2-D analytical theory proposed by Eidelloth and Brendel [Eidelloth and Brendel, 2014].

2.2.13 Current-voltage cell characterization

The performance of solar cells were determined by measuring their current-voltage (J-V) characteristic. A typical J-V curve is shown in Fig. 1.3a, and the relevant parameters V_{oc} , J_{sc} , FF and η , as well as R_{OC} and R_{SC} explained in chapter 1.

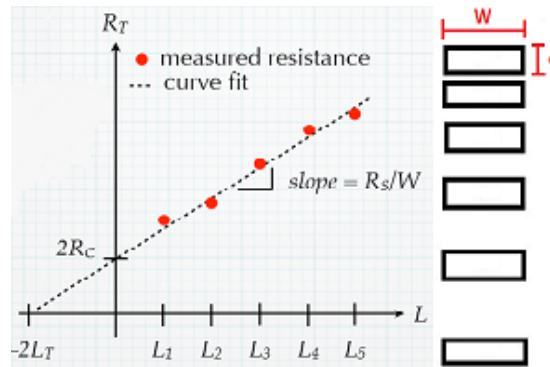


Figure 2.7 – Schematic explanation of the TLM measurement. The squares on the right represent the contact pads increasingly spaced. The graph on the left explains how to extract the contact resistance R_C , the sheet resistance R_s and the transfer length L_T using a linear fit of the data points. R_T is the total resistance measured between two pads with an increasing distance L_1, L_2, L_3, L_4 or L_5 between them. Figure copied from the in-house developed software used for the TLM measurements, inspired from [Reeves and Harrison, 1982].

Measurements were performed under standard test conditions, *i.e.* a cell temperature of 25 °C, an illumination intensity of 1 sun (1000 W/m²) and a light spectrum corresponding to AM1.5G (solar spectrum on earth when light has travelled a distance through air corresponding to 1.5 times the atmosphere's thickness). A WXS-90S-L2,AM1.5G class AAA solar simulator from Wacom Electric Co., Ltd. (Japan) was used as illumination source. A Keithley-2601A sourcemeter was used to sweep the voltage and record simultaneously the electrical current generated by the solar cell. The latter is placed on a chuck, maintained at 25 °C by Peltier elements cooled by a water chiller. The rear side of the cell is contacted by the chuck, while 4-point probes contact the busbars at the front. A shadow mask with an opening corresponding to the cell dimensions (typically 2x2 cm²) was used to restrict the illuminated region, avoiding carrier generation outside of the cell area.

3 Hydrogenation of the interface

Summary

This chapter presents the findings on the hydrogenation mechanism of fired passivating contacts based on c-Si/SiO_x/nc-SiC_x(*p*) stacks. More specifically, the correlation between passivation and local re-distribution of hydrogen resulting from the application of different types of interfacial oxides and hydrogenation processes was analyzed. To do so, the applied processing sequence was interrupted at different stages in order to characterize the samples. To assess the hydrogen content, deuterium was introduced (alongside/instead of hydrogen) and SIMS was used for depth profiling. Combining these results with lifetime measurements, the key role played by hydrogen in the passivation of defects at the c-Si/SiO_x interface is discussed. The SIMS profiles show that hydrogen almost completely effuses out of the SiC_x(*p*) during firing, but can be re-introduced by hydrogenation via FGA or by release from a hydrogen reservoir layer such as SiN_x:H. A pile-up of H at the c-Si/SiO_x interface was observed and identified as a key element in the FPC's passivation mechanism. Moreover, the samples hydrogenated with SiN_x:H exhibited higher H content compared to those treated by FGA, resulting in higher iV_{oc} values. Further investigations revealed that the doping of the SiC_x layer does not affect the amount of interfacial defects passivated by the hydrogenation process presented in this work. Eventually, an effect of the oxide's nature on passivation quality is evidenced. Thus, iV_{oc} values of up to 706 mV and 720 mV were reached with FPC test structures using chemical and UV-O₃ tunneling oxides, respectively, and up to 739 mV using a reference passivation sample featuring a ~25 nm thick thermal oxide.

This chapter is partially based on a paper published in *Solar Energy Materials and Solar Cells* and is reproduced with permission from [Lehmann et al., 2019]. Copyright ©2019, Elsevier.

3.1 Introduction

In the past years, solar cells based on full area passivating contacts resisting high temperatures attracted a lot of attention thanks to conversion efficiencies $\geq 26\%$ being published [Haase

et al., 2018], [Richter et al., 2021] and their compatibility with the high temperature ($> 800^\circ\text{C}$) processes typically used in industry for emitter diffusion and metallization. This combination makes them a promising successor for PERC cells in the mainstream c-Si PV industry [Allen et al., 2019] and first production lines are being ramped up [Y. Chen et al., 2019], [Wu et al., 2019], [Bao et al., 2020].

Most of these passivating contacts are made of a thin (1.2 – 3.6 nm) SiO_x layer capped with a doped poly-Si layer. The stack is then annealed at high temperature and subsequently hydrogenated to provide chemical passivation [Tao et al., 2016], [Römer et al., 2014], [Feldmann et al., 2014a], [Nogay et al., 2018], [Stuckelberger et al., 2016a], [Stuckelberger et al., 2016b]. This annealing is usually performed in a tube furnace at temperatures $> 800^\circ\text{C}$ and with heating ramps of $1\text{--}10^\circ\text{C}/\text{min}$, leading to a crystallization of the deposited silicon layers and the formation of a shallow doped region below the poly-Si/ SiO_x stack by in-diffusion of dopants into the silicon wafer [Nogay et al., 2017]. This shallow doped region induces band bending, thus promoting the carrier selectivity [Brendel and Peibst, 2016] of the contact and reducing surface recombination [A. G. Aberle, 2000]. As for the layer crystallization, it has been reported to be beneficial for transparency and contact resistivity as it yields a higher density of active dopants [Haug et al., 2019], [Seif et al., 2016].

To date, the highest reported efficiency for such a HTPC cell is 26.1 % [Haase et al., 2018], which at the same time is a world record for p-type solar cells. This cell features an IBC architecture with a rear side POLO contact that consists of a 2.2 nm thick thermal oxide capped with a 225 nm thick Low Pressure Chemical Vapor Deposition (LPCVD) a-Si:H(i) layer. The later is subsequently doped by boron and phosphorus implantation, annealed for more than 60 min at temperatures $> 900^\circ\text{C}$ and hydrogenated via a sacrificial $\text{SiN}_x\text{:H}$ layer. The fingers of the IBC structure are laser patterned and contacted by evaporated aluminum. The front side is textured and passivated with a 20 nm thick AlO_x layer grown by Atomic Layer Deposition (ALD) and capped with a PECVD $\text{SiN}_x/\text{SiO}_x$ layer stack. Regarding both-sides-contacted HTPC cells, the records are 26.0 % (back junction) [Richter et al., 2021] and 25.8 % (front junction) [Richter et al., 2017], [Richter et al., 2019]. These cells feature a TOPCon contact on the rear side that consists of a 1.4 nm thick wet-chemical tunneling SiO_x covered with a 15 nm thick poly-Si(n) layer deposited by PECVD. The stack is then annealed in a tube furnace at 900°C and metalized by thermal evaporation of Ag. For front junction cells, n -type wafers are used. The textured front side features a boron-doped emitter, with locally higher doping under the fingers, formed by BBr_3 tube furnace diffusion at 870°C followed by a drive-in. The surface is then passivated with a 10 nm thick Al_2O_3 layer, capped with a $\text{SiN}_x/\text{MgF}_2$ double layer ARC. The rear side is hydrogenated via RPHP. For back junction cells, p -type wafers are used. The key difference to front junction cells, is that the holes to be extracted on the front side are majority carriers, which can flow through the wafer. This allows the removal of the boron-diffused region (except below the fingers), reducing Auger recombination. Hydrogenation of the rear side was performed via a 10 nm thick sacrificial Al_2O_3 layer, annealed in forming gas (H_2/N_2) for 25 min at 425°C . Cell architectures with passivating contacts on both the front and the rear side have been investigated too, in order to fully avoid c-Si-metal contact [Nogay et al.,

2018], [Peibst et al., 2018], [Feldmann et al., 2017b], [Nicolai et al., 2018], [Ingenito et al., 2019], [Stuckelberger et al., 2018]. Full area deposited passivating contacts allow for a simpler process flow, but their use at the front yields parasitic absorption losses, while architectures with passivating contacts located under the fingers have not yet managed to outperform direct metallic contacts on locally higher doped regions [K. Chen et al., 2021], [Young et al., 2019], [Stuckelberger et al., 2019], [Meyer et al., 2022].

All the above approaches include a long high temperature annealing in their fabrication process. In contrast, the recently published FPC is fabricated in a short RTP step, also called firing [Ingenito et al., 2018], [Merkle et al., 2018], [Desthieux et al., 2020a], [Ingenito et al., 2021]. This step is used to metallize industrial solar cells [Ye et al., 2016], [Duttagupta et al., 2018]. Such a process typically requires temperatures $> 750^\circ\text{C}$, which are reached with ramps of $\sim 50^\circ\text{C/s}$ and maintained for a few seconds only. The fabrication of an FPC thus requires a much lower thermal budget than HTPCs based on long annealings. As firing is too short to promote dopant in-diffusion, field effect passivation is less pronounced, and therefore excellent interface passivation is needed to avoid recombination losses and to achieve high open circuit voltages (V_{oc}). Further, the fast temperature ramps lead to rapid hydrogen effusion, which can lead to blistering. Avoiding such layer delamination is thus a challenge for the FPCs but could be overcome by the addition of carbon into the Si-network [Ingenito et al., 2018]. However, an increased carbon content reduces the crystallisation of the layer and the activation of dopants, thus increasing the contact resistivity. Therefore, the C content was tuned such as to be just high enough to avert blistering. The integration of the FPC as rear hole selective contact, co-fired with a screen printed Ag grid contacting a POCl_3 diffused front emitter, resulted in a conversion efficiency of 22.5 % [Ingenito et al., 2021].

Since no shallow doped region is formed upon firing, the FPC relies strongly on the hydrogenation process for surface passivation. Moreover, hydrogenation is an essential processing step for HTPC in general, during which interfacial defects are passivated, allowing to reach high V_{oc} values. It also plays a key role in surface passivation of many other types of solar cell architectures, and even in bulk quality improvement [A. G. Aberle, 2000], [B. Hallam et al., 2017]. Here, we present our findings on the distribution and migration of hydrogen in FPCs, analyzed by means of SIMS. The impact of hydrogen re-distribution on surface passivation was studied. A special focus was set on the effect of the various processing steps as well as the influence of the oxide nature on passivation and hydrogen distribution. The study was performed with fired $\text{SiC}_x(p)$ layers on p-type wafers, in order to investigate an alternative rear contact to the mainstream technologies. Deuterium was incorporated in the samples analyzed by SIMS. The advantage of this being that, in contrast to hydrogen, the deuterium signal is not affected by residual gas present in the chamber or humidity adsorbed on the sample surface. Moreover, the detection capability of SIMS is higher for deuterium than for hydrogen. The results provide further insight on the hydrogenation of HTPC in general and are therefore of interest beyond the FPC.

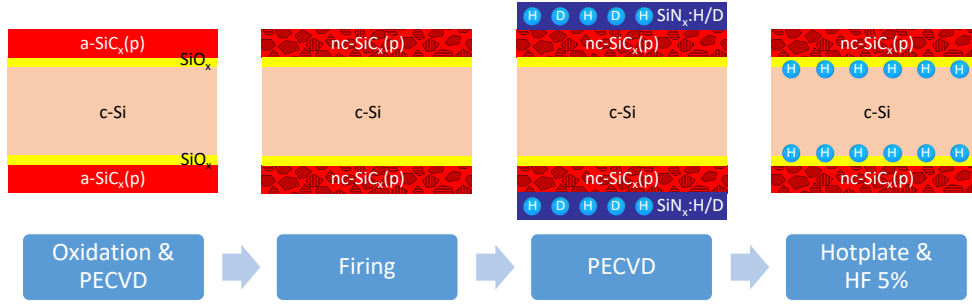


Figure 3.1 – Schematic illustration of the fabrication process using a sacrificial $\text{SiN}_x\text{:H/D}$ layer for hydrogenation. Note that a chemical cleaning was performed prior to the oxidation. Deuterium was incorporated into the layers by replacing the H_2 gas flows by D_2 in the two mentioned PECVD processes.

3.2 Experimental details

For these experiments, symmetrical test structures were fabricated, as depicted in Fig. 3.1. For samples to be analyzed by SIMS, DSP wafers were used, while SE wafers were used otherwise. All of them were *p*-type FZ with (100) surfaces. As described in chapter 2, the first processing step consisted of a wet chemical cleaning, ending with a hot HNO_3 treatment (69 %, 80 °C, 10 min) growing a ~1.3 nm thin chemical SiO_x layer on the wafer surfaces [Kobayashi et al., 2003], [Grant and McIntosh, 2009]. Next, ~25 nm¹ thick hydrogenated amorphous $\text{a-SiC}_x(p)\text{:H}$ (~2.5 at.% of carbon [Ingenito et al., 2018]) layers were deposited by PECVD. This was performed in the "Octopus" reactor, at 200 °C, with a pressure of 0.5 mbar, using SiH_4 , H_2 , CH_4 and $\text{B}(\text{CH}_3)_3$ as precursor gases. For the samples to be analyzed by SIMS, the H_2 was replaced by D_2 , incorporating deuterium alongside hydrogen into the $\text{a-SiC}_x(p)\text{:H/D}$ layers. Subsequently, the samples were fired for 3 s at ~800 °C. During this step, the initially amorphous film ($\text{a-SiC}_x(p)\text{:H}$) crystallizes into nanocrystalline $\text{nc-SiC}_x(p)$ and hydrogen and deuterium effuse from the layer. Hydrogenation was then performed either via FGA (4 % D_2 in N_2) for 30 min at 500 °C, or via H/D diffusion from a ~70 nm thick sacrificial layer of $\text{SiN}_x\text{:H/D}$ during 30 min on a hotplate at 450 °C [Nogay et al., 2017]. After this hydrogenation step, the $\text{SiN}_x\text{:H/D}$ layer was removed in a 5 % HF solution at room temperature. Note that the standard hydrogenation route used in this work is the one by sacrificial $\text{SiN}_x\text{:H/D}$ layer. FGA was applied only once for comparison.

Different experiments were performed, investigating the effect of various parameters on the hydrogenation of the FPC. In the first one, the distribution and migration of hydrogen during the processing sequence and its effect on passivation was studied. To do so, deuterium was incorporated into the samples and their passivation and chemical composition were measured at different steps of the processing sequence: 1) after $\text{a-SiC}_x(p)\text{:H/D}$ deposition, 2) after firing, and 3) after hydrogenation (FGA or $\text{SiN}_x\text{:H/D}$). All samples for this study were fabricated on

¹Note that after PECVD, the deposited $\text{a-SiC}_x(p)$ layer is ~30 nm thick, and shrinks to a ~25 nm thick $\text{nc-SiC}_x(p)$ layer upon firing. See also appendix A.

DSP wafers, as a flat surface is needed for SIMS measurements.

In a second experiment, the chemical SiO_x (HNO_3) was replaced by a ~ 25 nm thick thermally grown oxide (90 min in an oxygen ambient at 900°C , applying N_2 ambient while ramping the temperature up and down [Fossum and Burgess, 1978], [Blakers and Green, 1985], [Snel, 1981], [Yablonovitch et al., 1985]) in order to determine more accurately the location of the deuterium in the oxide layer (1.3 nm being smaller than the SIMS's depth resolution). A reference sample without oxide layer (HF stripping of the SiO_x before the $\text{SiC}_x(p)$ deposition) was also processed. For both samples SIMS and lifetime measurements were performed in the as-deposited and hydrogenated state, and compared to the previous samples featuring a chemical SiO_x .

In a third experiment, the effect of the interfacial oxide's nature on the passivation quality was investigated. The samples were fabricated on SE wafers, as no SIMS analysis was performed, and their lifetimes measured after hydrogenation (deposition of $\text{SiN}_x\text{:H}$, hotplate treatment, stripping of the $\text{SiN}_x\text{:H}$ in HF). Three different types of interfacial oxides used in this thesis were compared with each other, namely chemical oxide, grown in hot HNO_3 [Kobayashi et al., 2003], [Grant and McIntosh, 2009], UV-Ozone (UV-O_3) oxide, grown by exposing the wafer to UV radiation in ambient air (2 min each side) [Moldovan et al., 2015], [Fukano and Oyanagi, 2003], [Moldovan et al., 2014], and thermal oxide, grown in a tube furnace (as detailed above). The thicknesses of the interfacial oxides were ~ 1.3 nm for the chemical and the UV-O_3 oxides and ~ 25 nm for the thermal oxide, as measured by spectroscopic ellipsometry. Note that the latter sample has to be considered as a reference, as such a stack with a homogeneous 25 nm thick SiO_2 layer could not be applied as contact. Unfortunately, growing a homogeneous, 1.3 nm thin thermal oxide at 900°C is very challenging (and reducing the oxidation temperature affects the oxide quality [Lee et al., 2012]). Thus, a thickness of 25 nm was chosen, in order to enable comparison with the other experiments, where such thick thermal oxides were wanted.

Finally, the effect of the SiC_x layer on the hydrogenation process was studied. To do so, intrinsic, p -type and n -type $a\text{-SiC}_x$ layers were deposited on both sides of SE wafers covered with a ~ 25 nm thick thermal oxide. After firing and hydrogenation, the SiC_x layer was stripped by a selective etch-back in a 20 % KOH solution at 60°C . Lifetime measurements were performed after each processing step. Note that the samples with an intrinsic SiC_x layer were not fired. Indeed, the $\text{SiC}_x(i)$ was found to be more prone to blistering than the doped SiC_x layers. Thus, the firing step was replaced by a long HP anneal (7 h at 500°C) to effuse hydrogen out of the $\text{SiC}_x(i)$.

The passivation quality of the samples was assessed by measuring QSSPC, recording the injection dependent effective minority carrier lifetime (τ_{eff}) and computing the implied open circuit voltage (iV_{oc}) at 1 sun. The dark saturation current density (J_0) was extracted from this data according to the method published by Kimmerle *et al.* [Kimmerle et al., 2015]. The J_0 values are given per wafer side. From the lifetime, the S_{eff} was computed according to Sproul's equation [Sproul, 1994]. The value of the diffusivity needed for this computation was determined with the help of PV Lighthouse's mobility calculator [McIntosh et al., 2011].

The chemical composition of the layers was measured by SIMS, using a 1 keV Cs^+ primary ion beam. Deuterium was analyzed as D^- and DCs_2^+ . Ions were collected from an area of $60\text{ }\mu\text{m}$ in diameter, with a depth resolution of $\sim 4\text{ nm}$ (not element dependent) [Chanbasha and Wee, 2008]. A selection of samples was further characterized by RBS with a 2 MeV He ion beam [Nastasi et al., 2015]. Measurements were performed at the ETH Laboratory of Ion Beam Physics using a silicon PIN diode detector and an incident angle of 168° . The hydrogen and deuterium content of the samples' layers was determined by ERDA under 30° using a 2 MeV He beam and the absorber foil technique [Nastasi et al., 2015]. The collected RBS data was analyzed by the RUMP code [Doolittle, 1986]. Note that the depth resolution of H in Si of this measurement technique is about 50 nm [Nastasi et al., 2015]. Our layers being thinner than that, the hydrogen and deuterium contents are given as areal concentrations (at/cm^2), corresponding to the total amount of H and D throughout the layer stack. Layer thicknesses were measured by spectroscopic ellipsometry.

3.3 Hydrogen distribution and migration as a function of the processing step

Looking at the lifetime curves throughout the individual steps of the processing sequence (Fig. 3.2a), it can be observed that the samples do not reveal any appreciable surface passivation after SiC_x deposition. The firing process then slightly increases their iV_{oc} ($< 605\text{ mV}$, corresponding to $\tau_{\text{eff}@10^{15}\text{ cm}^{-3}} < 50\text{ }\mu\text{s}$). Finally, the hydrogenation process provides a significant improvement. It is interesting to observe that higher iV_{oc} values were reached when the hydrogenation was done with a sacrificial $\text{SiN}_x\text{:H}$, rather than via FGA. $\text{SiN}_x\text{:H}$ hydrogenation resulted in iV_{oc} values up to 693 mV ($\tau_{\text{eff}@10^{15}\text{ cm}^{-3}} = 950\text{ }\mu\text{s}$, $J_0 = 22 \pm 5\text{ fA}/\text{cm}^2$), whereas FGA treated samples reached only 649 mV ($\tau_{\text{eff}@10^{15}\text{ cm}^{-3}} = 190\text{ }\mu\text{s}$). To gain a deeper understanding of these iV_{oc} trends, deuterium profiles were measured by SIMS (Fig. 3.2b), analyzing negative secondary ions (high sensitivity to deuterium). First of all, it can be noticed that the deuterium content in the a- $\text{SiC}_x(p)\text{:H}$ layer in the as deposited state is high and homogeneous. Nevertheless, its iV_{oc} is low due to the defective nature of the $\text{SiO}_x/\text{c-Si}$ interface. During firing, deuterium effuses out of the $\text{SiC}_x(p)$ and its concentration drops below the detection limit of the SIMS. Finally, the hydrogenation results in an increase of the deuterium content in the $\text{SiC}_x(p)$ and a pronounced peak at the position of the SiO_x layer. The hydrogenation by a sacrificial $\text{SiN}_x\text{:H/D}$ layer introduces more deuterium than the FGA, explaining the lifetime trends observed in Fig. 3.2a. This is consistent with the work by Lelièvre *et al.* and Dekkers *et al.*, showing that part of the hydrogen released from $\text{SiN}_x\text{:H}$ is in its atomic form, which diffuses more rapidly than molecular hydrogen from FGA [Lelièvre et al., 2009], [Dekkers et al., 2006]. Other parameters potentially affecting the deuterium (and/or hydrogen) diffusion are the process temperature (450°C for the hotplate treatment, vs. 500°C for the FGA) and the concentration in the source ($\sim 12\text{ at.}\%$ of H (i.e. $\sim 1.2 \cdot 10^{22}\text{ cm}^{-3}$) and $6\text{ at.}\%$ of D for $\text{SiN}_x\text{:H/D}$, vs. $\sim 4\text{ at.}\%$ of D_2 (i.e. $\sim 2.0 \cdot 10^{15}\text{ cm}^{-3}$ at standard conditions) for FGA).

The total deuterium concentration in the layer, measured by He ERDA, is given in Fig. 3.2b

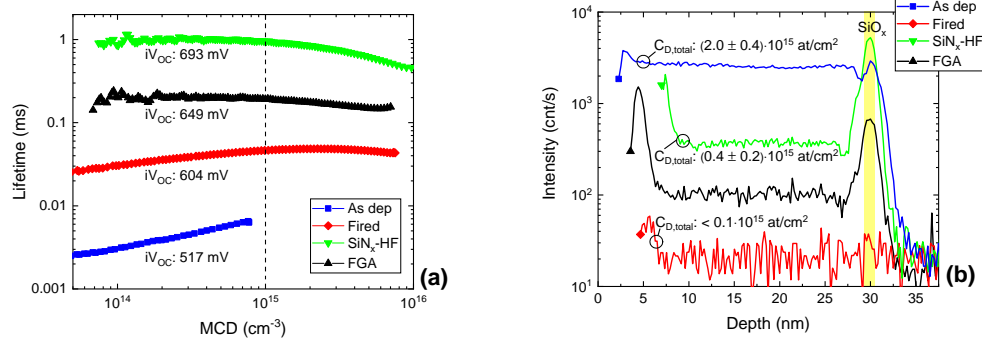


Figure 3.2 – (a): Minority carrier lifetime curves of selected samples at various processing stages, namely as deposited, fired, FGA, SiN_x:H hydrogenation (after deposition, hotplate anneal and removal of the SiN_x layer in HF), as a function of Minority Carrier Density (MCD). The dashed line marks the MCD of $1 \cdot 10^{15} \text{ cm}^{-3}$ at which $\tau_{\text{eff}@10^{15} \text{ cm}^{-3}}$ in the text are determined. (b): Deuterium depth profiles (D⁻ SIMS intensities) for samples at different processing stages. The total concentration of deuterium within the samples ($C_{\text{D,total}}$), measured by He ERDA, is given for the as deposited, fired and SiN_x:H/D hydrogenated samples.

for the as-deposited, fired and hydrogenated (by a sacrificial SiN_x:H/D layer) samples: $(2.0 \pm 0.4) \cdot 10^{15} \text{ at/cm}^2$, $< 0.1 \cdot 10^{15} \text{ at/cm}^2$ and $(0.4 \pm 0.2) \cdot 10^{15} \text{ at/cm}^2$, respectively. Besides the deuterium introduced through a D₂ gas flow, there is also hydrogen incorporated into the layers through precursor gases like SiH₄ and B(CH₃)₃. The profiles measured by SIMS for hydrogen are shown in Fig. 3.3. As can be observed, the trends are similar as for deuterium, but with a much higher background signal. This most likely comes from residual gas in the analysis chamber and H₂O adsorbed on the sample surface. Moreover, one notices that a trace amount of hydrogen remains within the sample after firing. As for the increase in signal after hydrogenation, it is absent for the sample treated by FGA, which was to be expected, as a D₂N₂ gas was used, and less pronounced than for deuterium in the case of hydrogenation with a SiN_x:H/D layer. However, the hydrogen content measured by He ERDA for the as-deposited, fired and hydrogenated (by a sacrificial SiN_x:H/D layer) samples were $(44 \pm 5) \cdot 10^{15} \text{ at/cm}^2$, $(3 \pm 1) \cdot 10^{15} \text{ at/cm}^2$ and $(5.8 \pm 0.6) \cdot 10^{15} \text{ at/cm}^2$, respectively, confirming the loss of hydrogen during firing, and its reintroduction upon hydrogenation. Assuming a background signal of $1 \cdot 10^{15} \text{ at/cm}^2$ of hydrogen (corresponding to a monolayer of H₂O adsorbed on the surface), a H/D ratio of ~12 is measured after hydrogenation. He ERDA measurements on the SiN_x:H/D layer reveal a H/D ratio of ~1.6, indicating a faster diffusion for hydrogen than for deuterium, in agreement with literature [Carlson and Magee, 1978]. The as-deposited sample displays a homogeneous hydrogen and deuterium distribution corresponding to a total combined concentration of H + D of $(1.8 \pm 0.4) \cdot 10^{22} \text{ at/cm}^3$, *i.e.* > 25 at.% according to [Smets and van de Sanden, 2007]. This amount was found to be much lower after firing and hydrogenation, as the layer crystallized, containing thus fewer structural defects to be hydrogenated. Note that the dip in SIMS signal at the SiC_x(p)/SiO_x interface is a measurement artefact inherent to

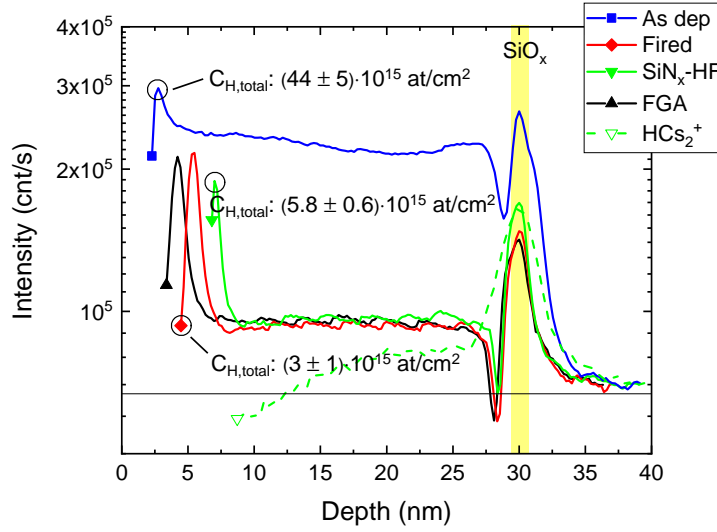


Figure 3.3 – Hydrogen depth profiles for samples at different processing stages. Solid lines are H^- SIMS intensities, while the dashed line is the profile for the " $\text{SiN}_x\text{-HF}$ " sample measured in HCS_2^+ mode. The horizontal black line is a guide to the eye marking the hydrogen level measured in the c-Si bulk (background). The total concentration of hydrogen within the samples ($C_{\text{H,total}}$), measured by He ERDA, is given for the as deposited, fired and $\text{SiN}_x\text{:H/D}$ hydrogenated samples.

the measurement in H^- mode, and disappears when measuring the profiles in HCS_2^+ mode. Several recent publications reported such an accumulation of hydrogen at the SiO_x layer too, corroborating the findings presented here [Lozac'h et al., 2020], [Lozac'h and Nunomura, 2020], [Park et al., 2019], [Morisset et al., 2021], [Truong et al., 2019b], [Holleman et al., 2021a].

3.4 Hydrogen distribution and migration for different thicknesses of the interfacial oxide

The SIMS depth profiles showed that the deuterium accumulates mainly at the position of the SiO_x layer, which is in agreement with the work performed by Schnabel *et al.* [Schnabel et al., 2018] and Dingemans *et al.* [Dingemans et al., 2010] using $\text{Al}_2\text{O}_3\text{:D}$ as deuterium reservoir layer. However, as the thickness of the chemical oxide is lower than the depth resolution of the SIMS (~ 4 nm), no conclusion about the exact location of the deuterium can be drawn from these measurements. For a deeper understanding of deuterium accumulation after the hydrogenation process, we analyzed the SIMS profile of a sample grown with a thick thermal oxide, and compared it to those of samples with a thin chemical tunneling oxide and no oxide (Fig. 3.4). For these measurements, DCS_2^+ secondary ions were analyzed, as this mode is less prone to matrix effects and thus a more suited approach to compare signals coming from different materials.

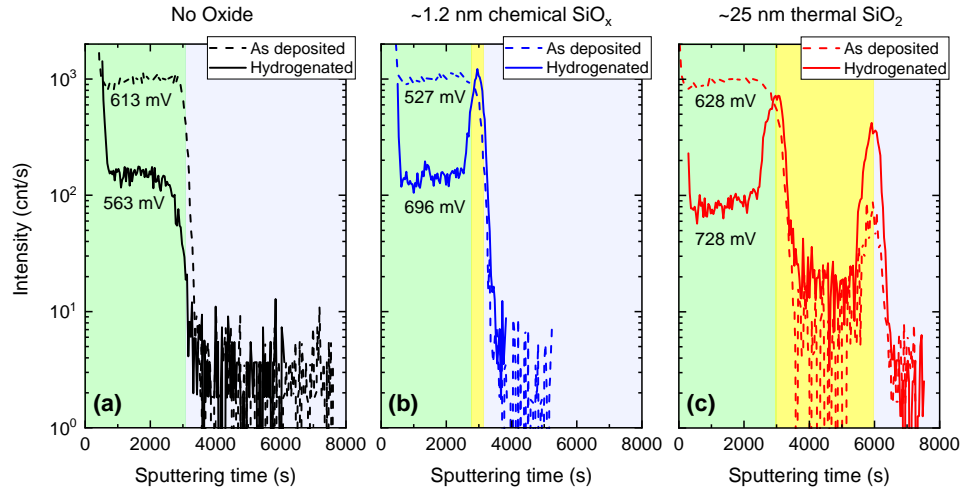


Figure 3.4 – Deuterium profiles (DCs_2^+ SIMS intensities) for samples with (a) no interfacial oxide, (b) a chemical tunneling oxide and (c) a thick thermal oxide, in the as deposited state (dashed line) or after hydrogenation (solid line). The yellow area indicates the region of the oxide. The purple region on the right side of the graph corresponds to the c-Si wafer, whereas the a-SiC_x(*p*) layer is located in the green region on the left. The iV_{oc} values of the samples (in mV) are given below the lines.

As shown in Fig. 3.4a, the sample without the interfacial SiO_x has a similar amount of D in the a-SiC_x(*p*) than the other samples, in both as-deposited and hydrogenated states. Despite that, surface passivation is poor ($iV_{\text{oc}} < 600$ mV after hydrogenation). The comparison with Fig. 3.4b illustrates that it is the previously observed accumulation of D at the SiO_x layer that enables high iV_{oc} values. Similar observations were made for heterojunction solar cells. Hydrogen profiles similar to those of Fig. 3.4a were measured by nuclear reaction analysis on c-Si/a-Si:H(*i*) stacks [Gotoh et al., 2019], while accumulation at a interfacial SiO_x was measured by SIMS in advanced c-Si/a-Si:H(*i*)/SiO_x/nc-Si:H(*p*) stacks [Antognini et al., 2021]. Finally, Fig. 3.4c shows that after hydrogenation, D accumulates at both SiO₂/nc-SiC_x(*p*) and SiO₂/c-Si wafer interfaces whereas its concentration is low within the SiO₂. Such results are in agreement with the work of Johnson *et al.* [Johnson et al., 1981] and corroborate the hypothesis that hydrogen accumulates at defective interfaces to passivate defects. In this specific case the H-accumulation at c-Si/SiO_x enables to reach high iV_{oc} values [A. Aberle et al., 1991], [Deal et al., 1969]. The especially high iV_{oc} value of 728 mV ($\tau_{\text{eff}@10^{15}\text{cm}^{-3}} = 3350 \mu\text{s}$, $J_0 = 1.4 \pm 0.5 \text{ fA/cm}^2$) obtained for the sample with the thermal oxide layer indicates potential for improvement for the thin interfacial oxides. It is also interesting to note that the thick thermal oxide layer provides much better passivation in the as deposited state than the chemical oxide.

In a further experiment, chemical profiles of a hydrogenated sample featuring a SiC_x(*p*) layer on top of a UV-O₃ SiO_x were measured by APT. As the depth resolution of this technique is 0.1–0.3 nm, it should resolve where the hydrogen is located withing the 1.3 nm thin tunneling

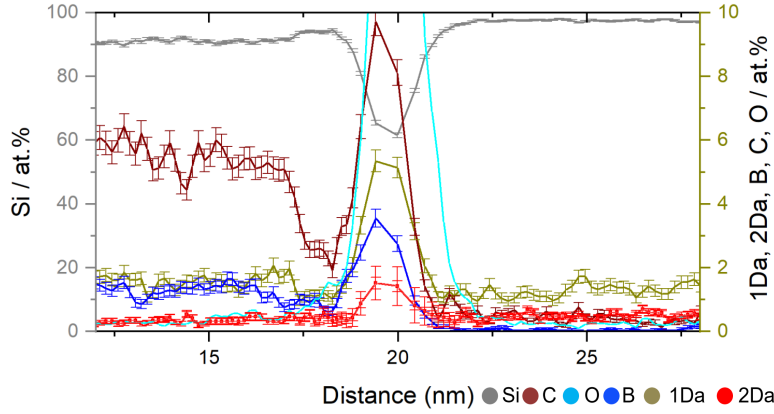


Figure 3.5 – Silicon, oxygen, carbon, boron, hydrogen and deuterium profiles of a $\text{SiC}_x(p)/\text{SiO}_x/\text{c-Si}$ sample measured by APT after hydrogenation. Since APT can not distinguish between D^+ and H_2^+ , the labels "1Da" and "2Da" are used for H^+ and D^+/H_2^+ , respectively. This data was also published in *Applied Surface Science* and is reproduced with permission from [Pal et al., 2021]. Copyright ©2021, Elsevier.

oxide or at its two interfaces with c-Si and $\text{SiC}_x(p)$. The results are shown in Fig. 3.5. As one can see, all measured elements accumulate within the SiO_x layer, indicating that it contains many defects capturing hydrogen. In contrast to a 25 nm thick thermal SiO_2 , that features two defective transition regions from c-Si to SiO_2 and from SiO_2 to $\text{SiC}_x(p)$, these defective regions seem to overlap in the case of a 1.3 nm thin tunneling oxide and extend over its whole thickness. The measured concentrations of Si, O, C and B are 59.1 at.%, 21.6 at.%, 9.9 at.% and 3.9 at.%, respectively. The SiO_x layer thus is sub-stoichiometric and most likely defect-rich, as the diffusion of C and B into silicon oxide was reported to create additional interfacial defects [Liu et al., 2019], [T. Yamamoto et al., 1999], [Snel, 1981]. In the case of boron, such accumulation within the oxide has been previously reported [Feldmann et al., 2019]. Moreover, these profiles show sharp interfaces, without in-diffusion of carbon or boron into the bulk c-Si. It has to be mentioned, that in contrast to SIMS, APT is not capable of distinguishing D^+ and H_2^+ (present also in the chamber). Hence, a quantification of deuterium is not directly possible with this method. However, it can be done combining APT, SIMS and TEM measurements, as shown in our 2021 study [Pal et al., 2021]. Doing so, reveals hydrogen concentrations of 4.3 at.% within the SiO_x layer and ~1 at.% in the $\text{SiC}_x(p)$, and deuterium concentrations of 1.2 at.% and ~0.2 at.% within the SiO_x and $\text{SiC}_x(p)$ layers, respectively. Surprisingly, the carbon content of this $\text{SiC}_x(p)$ layer measured by APT is approximately 5.5 at.%, which is higher than the previously reported 2.5 at.% measured by STEM-EDX [Ingenito et al., 2018]. The origin of this difference is unknown so far.

According to these measurements, the combined hydrogen and deuterium content of the SiO_x layer is of 5.5 at.%. Assuming a density of 2.25 g/cm^3 for the SiO_x layer [Moldovan et al., 2015] and the chemical composition mentioned above to be valid over its whole thickness, this results in an H+D concentration within the SiO_x of $3.4 \cdot 10^{21} \text{ cm}^{-3}$, equivalent to an areal

density of $4.5 \cdot 10^{14} \text{ cm}^{-2}$ for a 1.3 nm thick tunneling oxide. The interfacial defect densities D_{it} for these FPCs was reported to be around $3 \cdot 10^{11} \text{ cm}^{-2}$ [Haug et al., 2021b]. Note that this value was obtained from QSSPC measurements by numerical modelling. Several parameters, such as the electron and hole capture cross sections of the traps were taken from literature. Since no global agreement on their exact value exists [A. G. Aberle et al., 1992], this value for D_{it} has to be considered with some caution. Hollemann *et al.* reported D_{it} values after firing of $3.6 - 12 \cdot 10^{11} \text{ cm}^{-2}$ for 10 nm thick thermal oxides covered by 220 nm thick poly-Si(*n*) layers grown by LPCVD [Hollemann et al., 2021b], and $3.6 - 8.4 \cdot 10^{12} \text{ cm}^{-2}$ for 1.5 nm thick oxides grown by a wet chemical process in de-ionized water with diluted ozone, covered by 220 nm thick poly-Si(*n*) layers grown by LPCVD [Hollemann et al., 2021a]. From these values it becomes clear, that the concentration of hydrogen and deuterium accumulating at the SiO_x layer exceeds D_{it} by far. A more detailed discussion of this finding will be presented in section 4.6.

3.5 Effect of the interfacial oxide's nature on the passivation quality

In this section the impact of various interfacial oxides on the passivation is studied. To do so, $\text{SiC}_x(p)$ layers were deposited on SE wafers covered with a chemical oxide ($\sim 1.3 \text{ nm}$), a UV- O_3 oxide ($\sim 1.3 \text{ nm}$) or a thermal oxide (25 nm). The measured lifetime curves as a function of the injection level are shown in Fig. 3.6.

A first observation is a trend to higher iV_{oc} values when moving from chemical, to UV- O_3 , to thermal oxide: 706 mV, 720 mV and 737 mV, respectively, corresponding to $\tau_{eff@10^{15} \text{ cm}^{-3}}$ of 555 μs , 1100 μs and 3170 μs , and J_0 of $8.3 \pm 0.6 \text{ fA/cm}^2$, $7.5 \pm 0.3 \text{ fA/cm}^2$ and $2.3 \pm 0.5 \text{ fA/cm}^2$. This improvement is believed to be linked to changes in the oxide's chemistry, which, according to literature, becomes closer to the stoichiometric ratio of 1:2 when switching from a chemical, to a UV- O_3 , and then to a thermal oxide [Moldovan et al., 2015], [Stegemann et al., 2017], [Hollemann et al., 2020], Polzin et al., 2020.

Note that while the samples with chemical and UV- O_3 oxide can be compared directly, as the type of interfacial oxide was the only parameter varied, care has to be taken when comparing them with the sample with thermal oxide as the latter is thicker and has a different thermal history. Nevertheless, these results show that the nature of this oxide has a major influence on the final passivation quality.

A second observation is that all iV_{oc} values are $\sim 10 \text{ mV}$ higher than in the previous experiments, thus exceeding 700 mV even for the samples processed with a chemical oxide (as previously published in [Ingenito et al., 2018]). The J_0 value decreases from 22 to 8.3 fA/cm^2 for the samples featuring a chemical oxide on a DSP and SE wafer, respectively, and increases from 1.4 to 2.3 fA/cm^2 for the DSP and SE samples with a thermal oxide. The reason behind this difference is unclear. Potential factors are the nature of the surface and different bulk lifetimes (as these wafers are provided by different suppliers). Furthermore, it should be mentioned that the computation of J_0 becomes inaccurate and dominated by experimental uncertainties

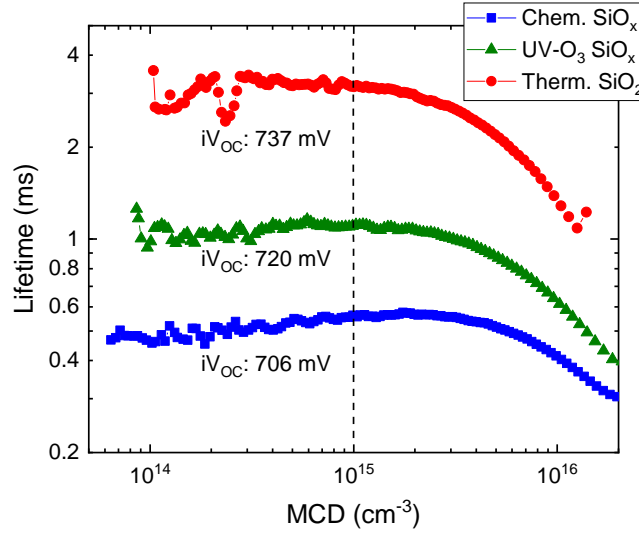


Figure 3.6 – Minority carrier lifetime curves, after hydrogenation, of samples with various interfacial oxides (chemical, UV-O₃, thermal) on *p*-type SE wafers. The dashed line marks the MCD of $1 \cdot 10^{15} \text{ cm}^{-3}$ at which $\tau_{\text{eff}@10^{15} \text{ cm}^{-3}}$ in the text are determined.

when approaching low values ($< 4 \text{ fA/cm}^2$) [Kimmerle et al., 2015].

Finally, the 720 mV of iV_{oc} reached for the sample with a UV-O₃ tunnelling oxide layer, corresponding to a J_0 of $7.5 \pm 0.3 \text{ fA/cm}^2$, confirm the high potential of the FPC.

3.6 Nature of the passivation

A set of samples with *p*-type, *n*-type, intrinsic and no SiC_x layers deposited by PECVD on thick thermal oxides was prepared to investigate whether the doping of the nc-SiC_x layer affects the hydrogenation process of the FPC, *i.e.* whether it influences the amount and charge state of the H diffused to the c-Si/SiO_x interface, thus affecting the passivation quality. Such an effect has been reported by Yang *et al.* [Yang et al., 2018]. The usual processing sequence was completed with a selective etch-back of the SiC_x layer in a KOH solution, in order to eliminate a potential field effect contribution by the doped layer to the surface passivation. Care was taken to selectively etch the partially crystallized SiC_x layer and not the underlying oxide layer, such that the passivation of the interface was not compromised. The results are reported in Fig. 3.7. For the sample without SiC_x layer, the SiN_x:H layer was removed in hot H₃PO₄ (85 %, 170 °C), as HF would have removed the underlying SiO₂ layer too.

As can be observed in Fig. 3.7a, all iV_{oc} values remain $< 690 \text{ mV}$ until the SiN_x:H deposition. Excellent passivation can then be obtained thanks to the diffusion of hydrogen from the nitride layer towards the c-Si/SiO₂ interface on a hotplate, reaching iV_{oc} values $> 740 \text{ mV}$ for

all SiC_x layers studied here. This value drops slightly (by 4–8 mV) after stripping of the SiN_x layer^{II}. Similarly, after etching off the SiC_x layer, only a slight degradation in iV_{oc} (by 1–8 mV) was observed, the exception being the SiC_x(*i*) which showed local blistering that probably induced inhomogeneous etching and thus locally severe damage of the oxide layer altering the surface passivation, as indicated by an increase in J_0 from 2.3 ± 0.5 fA/cm² to 13.2 ± 0.9 fA/cm². The sample without SiC_x layer reached a slightly lower iV_{oc} , and had a significant drop after removing the SiN_x, which is likely linked to some degradation of the unprotected SiO₂ layer during the H₃PO₄ etching.

Just after PECVD of the SiN_x:H layer, a difference of ~40 mV in iV_{oc} can be observed between samples featuring a SiC_x(*p*) layer and samples featuring a SiC_x(*i* or *n*) layer. The origin of this effect is still unclear and requires further investigation. This difference in iV_{oc} vanishes after hydrogenation. It is interesting to note that differences in lifetime can be observed (Fig. 3.7b), even though the iV_{oc} values are almost identical. However, the curves have similar shapes and the variation between the two SiC_x(*p*) samples is of similar magnitude as the one between the various doped layers. In the light of these results, it is concluded that the final amount of defects passivated by hydrogen (diffused for 30 min at 450 °C) is independent of the layer doping. Further experiments investigating the impact of the layer doping on the kinetics of this hydrogenation process are presented in chapter 4. Moreover, the fact that the SiC_x layer can be removed without major passivation loss indicates that, in the present case of a ~25 nm thick thermal SiO₂, the doped SiC_x layer does not contribute to the passivation. Assuming that the fixed charge density in the thermal oxide is low [Cuevas et al., 2015], [A. G. Aberle et al., 1992], the high iV_{oc} values can be predominantly attributed to the accumulation of hydrogen at the c-Si/SiO₂ interface. Whether it is chemical passivation alone or if, and to which extent, interfacial charges play a role, remains an open question.

In samples with ultra-thin tunnelling oxides additional mechanisms might come into play such as superficial changes in carrier concentrations within the wafer. Indeed, the band-bending induced by the doped SiC_x layer leads to an accumulation of free holes [Ingenito et al., 2018], whereas the positive fixed charges in the thick thermal SiO₂ repel them [Cuevas et al., 2015]. But the observations from section 3.3 suggest that hydrogen passivation of the c-Si/SiO_x interface is also the key element to reach high lifetime values with ultra-thin oxides. This statement is further corroborated by the fact that no significant lifetime improvement was observed in an experiment where the SiN_x:H/D layer was removed before the hotplate treatment, pointing again towards the central role played by hydrogen in the passivation process. Moreover, a recent publication by Morisset *et al.* reports an increase from 525 mV to 720 mV of iV_{oc} upon hydrogenation for samples featuring an intrinsic poly-Si layer on top of a 1.4 nm thin tunneling oxide, linked with accumulation of hydrogen at the SiO_x layer [Morisset et al., 2021]. And Park *et al.* observed no decrease in iV_{oc} upon gradual etching of a 300 nm thick poly-Si layer deposited on top of a 1.2 nm thin tunneling oxide [Park et al., 2019].

^{II}Truong *et al.* reported no impact on iV_{oc} and τ_{eff} upon stripping of SiN_x:H layers used as hydrogen source [Truong et al., 2019a]. In their case, the poly-Si layer was 80 nm thick, deposited by PECVD on top of a 1.3 nm chemical SiO_x and ex-situ doped by phosphorous diffusion from POCl₃.

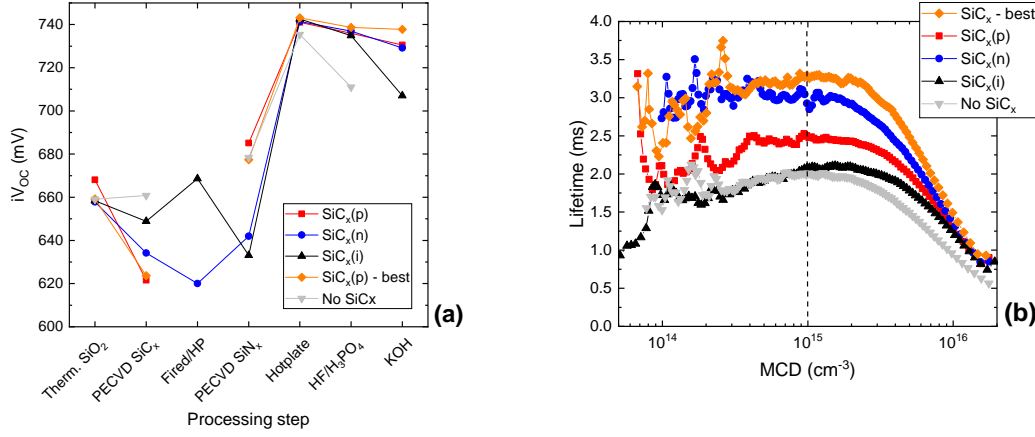


Figure 3.7 – (a): iV_{oc} values as a function of the processing step of samples fabricated with a p -type, n -type, intrinsic or no SiC_x layer on p -type SE wafers with a 25 nm thick thermal oxide. The values for the best sample processed are also shown. The passivation qualities after firing of the $SiC_x(p)$ samples, as well as the sample without SiC_x , were too low to measure an iV_{oc} . (b): Corresponding lifetime curves after hydrogen diffusion on the hotplate.

These results indicate once more that chemical passivation, achieved by hydrogenation, is the dominating mechanism for surface passivation.

In this experiment, iV_{oc} values up to 739 mV after hydrogenation and stripping of the $SiN_x:H$ layer were reached, corresponding to a $\tau_{eff@10^{15}cm^{-3}}$ of 3260 μs , a J_0 of 2.7 ± 0.7 fA/ cm^2 and a $S_{eff@10^{15}cm^{-3}}$ of 3 cm/s. According to literature, these values correspond to state-of-the-art passivation levels of p -type silicon wafers [Richter et al., 2012], [A. G. Aberle et al., 1992], [Glunz et al., 1994], [Kerr and Cuevas, 2002], [Mack et al., 2011], [Grant et al., 2017], [Niewelt et al., 2018], [Cuevas et al., 2018], [Descoeudres et al., 2013], [Bonilla et al., 2017]. Note also that the present samples have no in-diffused doped region, as stated previously, and that these oxides were grown at 900 °C, a comparably low temperature, and without addition of trichloroethane. Both, an increased oxidation temperature and an addition of trichloroethane may improve the passivation quality of the thermal oxide [Blakers and Green, 1985], [Bhan et al., 1987], but also increase the process' complexity.

3.7 Conclusions

The combination of lifetime measurements with SIMS analysis elucidated the key role of hydrogen in passivating defects at the c-Si/ SiO_x interface to reach high iV_{oc} values. Moreover, it could be observed that hydrogen almost completely effuses out of the $SiC_x(p)$ during firing and is later re-introduced during the hydrogenation step. Performing this hydrogenation step via a $SiN_x:H$ sacrificial layer was demonstrated to be more efficient than FGA, which could be correlated with a higher amount of deuterium diffused into the contact and especially to the

oxide-wafer interface. Further investigations revealed that in the case of ~25 nm thick thermal oxides, the accumulation of hydrogen at the c-Si/SiO₂ interface is the predominant factor enabling excellent passivation levels, and that the doping of the SiC_x layer does not affect the amount of interfacial defects passivated by our hydrogenation process. Furthermore, it was observed that the nature of the interfacial oxide has a major impact on the passivation quality. Thus, iV_{oc} values up to 720 mV could be reached using an ultra-thin UV-O₃ tunneling oxide, and up to 739 mV on a reference passivation sample using a ~25 nm thick thermal oxide.

In the next chapter, the focus will be set on the impact of firing and hydrogenation on the bulk lifetime, as it can become the limiting factor in the case of excellent surface passivation. Moreover, the kinetics of the hydrogenation process will be investigated, in order to gain further insight on the mechanisms at work.

4 Bulk defects and kinetics

Summary

This chapter presents the effect of the various processing steps during the fabrication of FPC on the silicon bulk lifetime, as well as the kinetics of defect deactivation by hydrogenation. It is found that the firing step at 800 °C induces shallow bulk defects in FZ silicon wafers, which can subsequently be passivated with hydrogen. Experimental results and numerical data treatment indicate a rapid passivation of the surface within less than 1 min, followed by a slower passivation of the shallow bulk defects. In situ lifetime measurements are consistent with a slow bulk lifetime improvement as they show similar lifetime evolutions for both *p*-type and *n*-type SiC_x layers. The kinetics of the hydrogenation process seems to be limited by the available hydrogen supply at the SiO_x/c-Si interface, rather than by its diffusion within the bulk of the wafer. Moreover, it is affected by the bulk doping, as well as the SiC_x layer thickness. Finally, it is shown that hydrogenation is also possible with a SiN_x reservoir layer deposited on one side of the wafer only, although resulting in a lower passivation level ($\tau_{\text{eff}} \sim 700 \mu\text{s}$ compared to $\tau_{\text{eff}} \sim 1300 \mu\text{s}$ for symmetrical samples), and slower kinetics ($\tau_{\text{reac}} \sim 5 \text{ min}$ compared to $\tau_{\text{reac}} \sim 0.8 \text{ min}$).

Part of this chapter's results were included in a manuscript, submitted to *IEEE Journal of Photovoltaics* and currently under review.

4.1 Introduction

Lately, in the field of poly-Si passivating contacts, a special focus has been put on the firing step, commonly used in industrial mass production to form the screen printed metallization. Compatibility with this process is crucial for a straightforward transfer of the technology from laboratories to industry [Allen et al., 2019]. The FPC introduced in the previous chapters uses this process as a low thermal budget approach to form the contact [Ingenito et al., 2018], [Merkle et al., 2018], [Desthieux et al., 2020a], [Ingenito et al., 2021]. The goal being to propose a cell architecture, for which the contact formation, hydrogenation and metallization would be

performed in a single firing step. However, this firing process has also been reported to damage the sample's passivation [Hollemann et al., 2021a], [Hollemann et al., 2020], [Çiftçinar et al., 2017], calling for further investigations of the effect of this step on the FPC performance. The kinetics of the hydrogenation process has also been studied in more detail recently, providing further insight on the mechanisms at work and the factors limiting the passivation. Dingemans *et al.* investigated it in the case of hydrogen diffusing from Al_2O_3 layers deposited on c-Si/ SiO_2 stacks [Dingemans et al., 2012], and Polzin *et al.* for various hydrogenation approaches for their TOPCon architecture [Polzin et al., 2021].

In this chapter, the evolution of the silicon bulk lifetime upon firing and hydrogenation is investigated, in order to discriminate between effective lifetime changes due to bulk or surface passivation variations, and to complement the findings of chapter 3, where the impact of various processing steps on the hydrogen distribution near the surface was studied. As the final goal was to assess the surface passivation quality provided by FPCs, FZ wafers were used. The latter are widely used in research laboratories as FZ silicon is of high purity, resulting in high minority carrier bulk lifetimes [Hiller et al., 2020], [Rougieux et al., 2015], [Goetzberger et al., 1997], [Von Ammon, 2014]. In the case of the hydrogenation process, its kinetics is investigated, trying again to discriminate between evolution of bulk and surface lifetimes upon diffusion of hydrogen from a $\text{SiN}_x\text{:H}$ reservoir layer, which was reported to be a key step for good passivation of FPCs. This investigation will also provide further insight to the question whether the SiC_x layer doping has an influence on the hydrogenation and passivation of the contact, since the experiment in chapter 3 surprisingly showed no significant difference after hydrogenation (30 min on the hotplate at 450 °C). Finally, the diffusion of hydrogen from a front $\text{SiN}_x\text{:H}$ layer through the whole wafer is investigated to provide additional insight into hydrogenation kinetics, and to test a passivation approach potentially interesting for a cell architecture featuring a *p*-type passivating contact at the rear side and the hydrogen reservoir in the $\text{SiN}_x\text{:H}$ layer doubling as anti-reflective coating on the front.

4.2 Experimental details

The samples presented in this chapter were processed similarly to those of chapter 3. The details are repeated here, as some of them are slightly different. The wafers used were FZ, (100) oriented, with a SE or DSP surface finish and a diameter of 10 cm. The SE wafers have a thickness of 200 μm and a resistivity of 2 Ωcm (or 10 Ωcm in some cases), while the DSP wafers are 280 μm thick and have a resistivity of 3 Ωcm . If not stated otherwise, they were boron-doped (*p*-type). The sample fabrication started with a chemical cleaning. Next, a SiO_x layer was grown at the surface. This was done either chemically (HNO_3 , 69%, 80 °C, 10 min) [Kobayashi et al., 2003], [Grant and McIntosh, 2009] or by exposing the wafer to UV radiation in ambient air (2–3 min each side) [Moldovan et al., 2015], [Fukano and Oyanagi, 2003], [Moldovan et al., 2014], both resulting in a ~1.3 nm thin tunneling oxide, or thermally (90 min at 900 °C in an oxygen ambient, applying N_2 ambient while ramping the temperature up and down) [Fossum and Burgess, 1978], [Snel, 1981], [Blakers and Green, 1985], [Yablonovitch

et al., 1985], resulting in a ~25 nm thick oxide. A hydrogenated amorphous a-SiC_x layer was then deposited by PECVD. Within the "Octopus" reactor, the layers were deposited at 200 °C, at a pressure of 0.5 mbar. For the SiC_x(*p*) layers, the precursor gases used were SiH₄, H₂, CH₄ and B(CH₃)₃, with a deposition time of 80 s, resulting in layers with a thickness of ~25 nm. For the SiC_x(*n*) layers, the gases used were SiH₄, H₂, CH₄ and PH₃, with a deposition time of 80 s, resulting in layers with a thickness of ~11 nm. Within the "Kai-M" reactor, the layers were deposited at 200 °C, at a pressure of 0.7 mbar. For the SiC_x(*p*) layers, SiH₄, H₂, CH₄ and B(CH₃)₃ were used as precursor gases, with a deposition time of 90 s, resulting in layers with a thickness of ~40 nm. The recipe for SiC_x(*n*) layers consists of several stages with varying gas flows of SiH₄, H₂, CH₄ and PH₃. The total deposition time is of 50 s and the resulting layer is ~20 nm thick^I. The samples were subsequently fired for 3 s at 800 °C, crystallizing the previously amorphous layers into nanocrystalline nc-SiC_x and effusing most of the hydrogen contained in the layer after deposition, as reported in chapter 3. Finally, the samples were hydrogenated. To do so, a ~70 nm thick SiN_x:H layer was deposited by PECVD at 250 °C on one or both sides of the wafers, releasing hydrogen during a subsequent hotplate anneal at 450 °C for 30 min [Nogay et al., 2017]. Deuterium was incorporated into the SiN_x:H/D layers by replacing the H₂ gas flow by D₂ in the PECVD process. In some cases, the SiN_x:H/D layer was removed after hydrogenation by dipping the samples in a 5% HF solution for 12 min.

To assess the passivation quality of the fabricated samples, QSSPC measurements and PL imaging were performed. QSSPC was measured using a Sinton WCT-120 instrument, providing τ_{eff} as function of the MCD, as well as the iV_{oc} at 1 Sun [Kane and Swanson, 1985], [R. Sinton et al., 1996], [Cuevas and Sinton, 1997]. As for PL imaging, it was measured with an in-house built setup. The samples are excited using an Ostech laser with a wavelength of 808 nm, operated with a power of 1.2 Suns, and the images are recorded with a PIXIS Princeton instrument silicon-based camera.

In situ MPL was used to track the evolution of the minority carrier lifetime in real time during the hydrogen diffusion step at 450 °C. In this setup, the minority carrier lifetime is determined through the measurement of the phase-shift between the modulated laser illumination and the photoluminescence signal, as described by Desthieux *et al.* [Desthieux et al., 2020b].

The chemical composition of some samples was measured by SIMS, using a CAMECA SC-Ultra instrument with a 1 keV Cs⁺ primary ions bombardment. Oxygen, hydrogen and deuterium were analyzed as MCs₂⁺ ions, collected from an area of 60 μm in diameter, with a depth resolution of ~4 nm (not element dependent) [Chanbasha and Wee, 2008].

4.3 Shallow bulk defects created upon firing

In order to assess the evolution of the bulk lifetime during the processing sequence, the deposited layers were removed from samples at various stages of the process, using HF to

^INote that all the layer thicknesses given here were measured after the firing step.

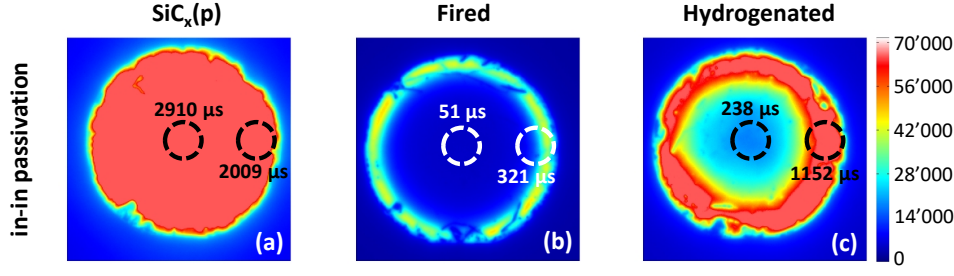


Figure 4.1 – PL images of samples at different processing stages which layers have been etched off by HF and CP4 and the surface repassivated using a-Si:H(*i*)/a-Si:H(*n*) stacks. Sample (a) has been etched and repassivated directly after PECVD of SiC_x(*p*) layers, sample (b) after subsequent firing for 3 s at 800 °C, sample (c) after subsequent hydrogenation by H-diffusion from a SiN_x:H reservoir layer. The circles indicate where QSSPC was measured and the resulting τ_{eff} values are given.

etch off SiN_x and CP4 to etch off SiC_x. Subsequently, their surfaces were repassivated with amorphous silicon layers, providing excellent surface passivation [Cuevas et al., 2015]. Doing so allows to observe bulk defects, as in their presence the measured effective lifetime becomes bulk limited. As can be seen in Fig. 4.1, a ring shape appears after firing, indicating that bulk defects have been created [Grant et al., 2016b]. These bulk defects can be passivated by hydrogen diffusion, as suggested by Fig. 4.1c and more clearly by Fig. 4.4 below. Hiller *et al.* and Guzman *et al.* reported similar findings, using FZ wafers too, and they proposed that the defect could be due to Si-vacancies that capture N-atoms, leading to dangling bonds that can be passivated with hydrogen [Hiller et al., 2020], [De Guzman et al., 2021]. The reason why the sample in Fig. 4.1c, that underwent a hydrogenation process, still displays some ring shape, is believed to be hydrogen effusion during the heating phase of the PECVD process prior to the deposition of the a-Si:H layers (200 °C under vacuum without any capping layer).

In order to gain further insight into the defect properties, lifetime measurements were performed at various temperatures, ranging from 25 °C to 190 °C, on hydrogenated samples still capped with SiN_x:H/D layers. Following the approach proposed by Murphy *et al.* [Murphy et al., 2012], we find that the dominating limitation is a shallow bulk defect, as indicated by the negative slope of the linear region at high excess carrier density in Fig. 4.2a. Defining $x = n/p$, where n and p are the electron and hole concentrations, respectively, and expressing this region through $\tau = a + b \cdot x$, extrapolation to $x \rightarrow 1$ yields the ambipolar lifetime $\tau_{\text{amb}} = a + b$, and the ratio ξ defined by $\xi = b/(a + b)$ yields a quantity that is characteristic for the defect, but independent of its concentration [Murphy et al., 2012], [Mundt et al., 2015]. The two fitting parameters a and b do not uniquely determine the properties of the defect, but they can be used to obtain a functional dependence between the ratio of the capture cross sections, k , and the defect energy E_t which is called Defect Parameter Solution Surface (DPSS) [Rein et al., 2002], [Rein, 2005]. Thus, $k = -(p_1/p_0 + \xi)/(\xi - 1 + n_1/p_0)$ where p_0 is the doping concentration of the wafer, and p_1 and n_1 are the parameters defined in SRH statistics [Shockley and Read,

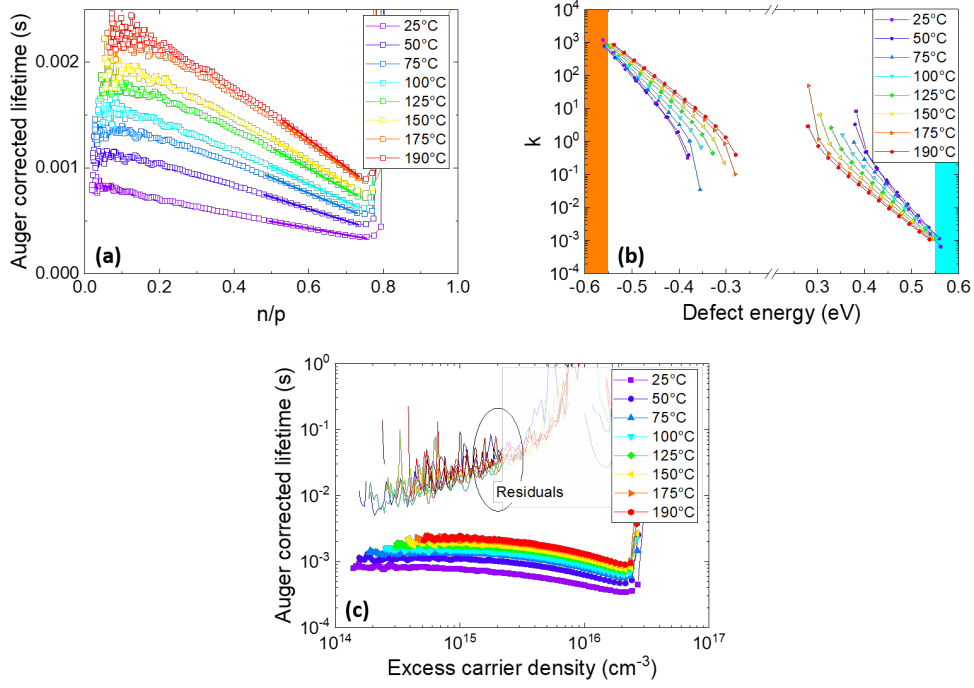


Figure 4.2 – (a) Linearized lifetime curves of QSSPC measurements at various stage temperatures and fits indicating shallow defects. (b) DPSS curves of the same samples, orange and light blue bars denote the valence band and the conduction band, respectively. (c) Original lifetime curves and residuals after subtraction of Auger and shallow bulk contributions.

1952], [Hall, 1952].

As the DPSS for the lifetime curves measured at various temperatures should intersect at the most likely values of E_t and k [Zhu et al., 2019], Fig. 4.2b indicates that the energy level of the defect should be very close to either the valence band or the conduction band. After subtraction of the contribution of the shallow bulk defect, a residual about an order of magnitude higher than the original lifetime curves is obtained (Fig. 4.2c), meaning that our passivation after hydrogenation is mainly limited by these shallow bulk defects, and not by recombinations at the c-Si/SiO_x interface as assumed so far (note that above $\Delta n = 2 \cdot 10^{15} \text{ cm}^{-3}$ the calculation of the residual is no longer trustworthy, hence the characteristics are shaded). This is a major finding, as it implies that the surface passivation of the present FPCs is much better than expected, and future work should focus on the passivation of bulk defects in order to further increase the minority carrier lifetime.

In the previous chapter, it was shown that the effective lifetime of the samples stays low until the hydrogenation step is performed. In the light of the results above, it can be concluded that in the as-deposited state, the bulk lifetime is still intact, but a low surface passivation is the limiting factor. After firing, both bulk and surface lifetime are low, and finally improve upon hydrogenation, with the bulk lifetime becoming the limiting one.

The work performed by Grant *et al.* [Grant et al., 2016b] and Hiller *et al.* [Hiller et al., 2020] suggests that these bulk defects can be fully cured by annealing for 30 min at temperatures above 800 °C and to a lesser extent by rapid thermal annealing for 30 s. In our case, we mainly create defects with the fast firing process of 3 s at 800 °C (resulting in $\tau_{\text{bulk}} \sim 50 \mu\text{s}$), and we observe only marginal improvement when increasing the firing temperature up to 930 °C and/or prolonging the dwell time up to 30 s. The ring shape disappears, but the best passivation reached after thermal treatment and surface repassivation was $\tau_{\text{eff, max}} = 279 \mu\text{s}$ (30 s firing at 860 °C), as shown in Fig. 4.3a. Moreover, previous experiments showed that the interfacial tunnel oxides seem to get damaged when moving to such harsh firing conditions [Libraro, 2019], [Haug et al., 2021b]. Hence, long furnace anneal was tried. Surprisingly, only 140 μs were reached after 30 min at 900 °C (Fig. 4.3b). So far, it is unknown, why even this process damages our bulk, whereas it cures it in the publication by Grant *et al.*. A possible explanation are the ambient gases present during these annealings. Indeed, the firing was done in an N₂ atmosphere, as well as the heating and cooling in the tube furnace, while only the 30 min plateau at 900 °C was done in O₂ ambient, as suggested by Grant *et al.*. Since the bulk defects are speculated to be linked to nitrogen incorporated within the bulk c-Si, it would be interesting to repeat these tests in Ar or O₂ atmospheres. According to literature, the ambient atmosphere has no significant impact for annealings at 500 °C [Mullins et al., 2018], whereas it does at 1100 °C [LaSalvia et al., 2018]. Moving to temperatures above 1000 °C might be interesting too, in order to perform a treatment similar to the “tabula rasa” for *n*-type Cz wafers ([LaSalvia et al., 2018], [Kelton et al., 1999], [Falster et al., 1997]), which could potentially avoid the formation of the shallow defects. This remains to be investigated and would allow assessing the full potential of the fired passivating contact. Potentially, this annealing of the defects could be integrated with the POCl₃ diffusion of an *n*-type front contact, thus maintaining the advantage of a low thermal budget for the formation of the passivating rear contact. Obviously, this long annealing compromises the long-term goal of a low thermal budget cell architecture with FPC at the front and the rear side. However, since hydrogenation allows largely recovering the bulk lifetime, this approach still has high potential. Moreover, further low thermal budget ideas to investigate are the use of nitrogen lean FZ material, which was reported to degrade less upon annealing [Mullins et al., 2018], [Grant et al., 2016b], or the implementation of FPCs on Cz wafers. Indeed, this ring shape issue seems to be inherent to FZ material as a preliminary test did not show them on Cz wafers after firing (Fig. 4.3c). However, the lifetime measured on these Cz samples after firing and a-Si:H(*i*)/a-Si:H(*n*) surface passivation stayed below 160 μs ($iV_{\text{oc}} < 675 \text{ mV}$). On the other hand, iV_{oc} values up to 730 mV have been reported for FPCs on Cz wafers after hydrogenation [Allebe et al., 2019]. Hence, further work is needed to understand the bulk lifetime evolution of Cz material upon firing and hydrogenation.

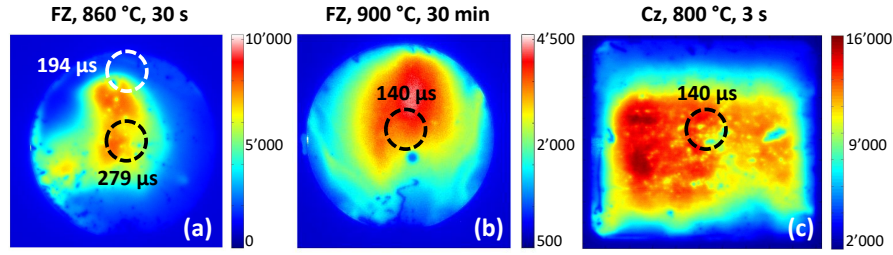


Figure 4.3 – PL images of wafers after cleaning, thermal treatment (short firing or long annealing) and subsequent HF dip to remove surface oxide and surface repassivation using a-Si:H(*i*)/a-Si:H(*n*) stacks. (a) FZ wafer, thermal treatment: Firing, 860 °C, 30 s, N₂ ambient. (b) FZ wafer, thermal treatment: 900 °C, 90 min, O₂ ambient. (c) Cz wafer, thermal treatment: Firing, 800 °C, 3 s, N₂ ambient. Note that no SiC_x layer was deposited in these experiments.

4.4 Hydrogenation kinetics

To investigate the evolution of the bulk and surface passivation during hydrogenation, a symmetrical test sample featuring a tunneling SiO_x/SiC_x(*p*)/SiN_x:H stack was annealed on the hotplate at 450 °C in consecutive steps, and PL images were recorded in between. Fig. 4.4 shows that the PL intensity improves already after 30 s in the outer regions of the wafer. As this is likely the region with fewer bulk defects [Grant et al., 2016a], [Voronkov, 1982], [Abe and Takahashi, 2011], we conclude that the interface defects are already passivated after this short time. The ensuing improvement of the PL signal over the full wafer is thus related to a gradual passivation of the bulk defects, in agreement with the above finding that the shallow bulk defects are the ones limiting the effective lifetime after hydrogenation. This conclusion is further supported by the fact, that for samples hydrogenated for 30 min at 350 °C, such a ring shape is visible too (not shown here), indicating that even at such a low temperature enough hydrogen was diffused to passivate the interface, but not yet enough to passivate the bulk. Indeed, the passivation level reached after 10 min of hydrogen diffusion on a hotplate depends strongly on the temperature of the latter, as shown in Fig. 4.5a. There is a sharp increase when moving from 400 °C to 425 °C, and a maximum around 450 °C. This maximum is interpreted as a trade-off between hydrogen diffusivity and release from the SiN_x:H layer increasing with temperature [Carlson and Magee, 1978], [Nogay et al., 2017], improving the passivation, and the breaking of hydrogen-defect-bonds, accelerated at higher temperatures, decreasing it. As shown in Fig. 4.5b, the surface passivation improves already at 350 °C (moving from 312 fA/cm² after PECVD of SiN_x:H, to < 20 fA/cm² after hotplate treatment), whereas temperatures above 400 °C are required to hydrogenate the bulk.

In order to allow for a quantitative comparison, the evolution of the passivation was also assessed by measuring the lifetime at regular intervals during the hydrogen diffusion on the hotplate. These curves were then fitted according to

$$\tau_{\text{eff}} = [1/\tau_{\text{end}} + A \cdot \exp(-t/\tau_{\text{reac}})]^{-1} \quad (4.1)$$

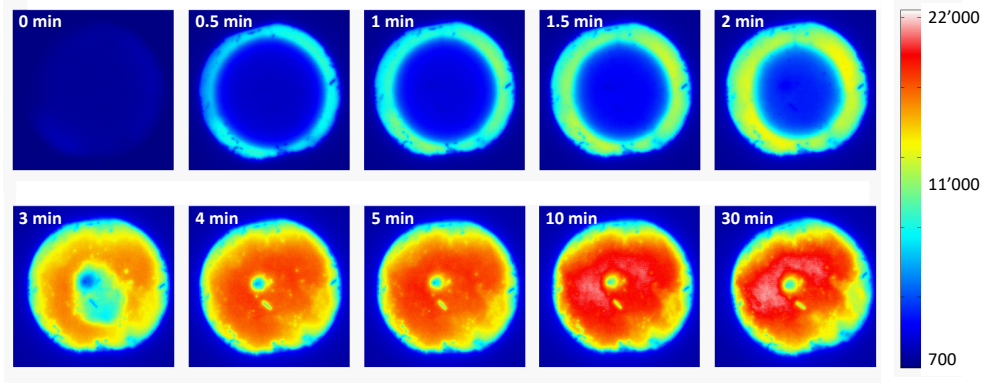


Figure 4.4 – PL images taken at various time intervals during the hydrogenation process, showing the evolution of the passivation with time spent on the hotplate.

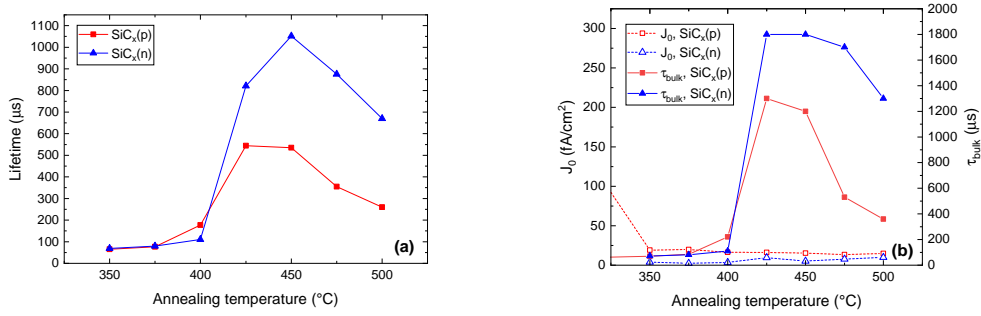


Figure 4.5 – (a) Evolution of $\tau_{\text{eff}@10^{15}\text{cm}^{-3}}$ in function of hotplate temperature. (b) Evolution of associated J_0 and τ_{bulk} , extracted following [Kimmerle et al., 2015].

as suggested by Mitchell *et al.* [Mitchell et al., 2009] and Polzin *et al.* [Polzin et al., 2021], where τ_{eff} is the measured effective minority carrier lifetime and τ_{end} and $1/\tau_{\text{reac}}$ are fitting parameters, corresponding to the minority carrier lifetime reached after hydrogenation and the reaction rate, respectively. Fig. 4.6 compares the kinetics of samples featuring 1.3 nm thin tunneling SiO_x and 25 nm thick thermal SiO_2 , as well as n -doped and p -doped SiC_x layers.

The most striking difference in kinetics is between samples with a thermal oxide (saturating within ~ 1 min, $\tau_{\text{reac}} < 0.2$ min) and those with a tunneling oxide (saturating within ~ 5 min, $\tau_{\text{reac}} \sim 0.8$ min). Most likely this is linked to the thermal history of the samples. The tunneling oxides are grown by UV- O_3 treatment at room temperature or in HNO_3 at 80°C , whereas the thermal oxide is grown during a 90 min annealing at 900°C , which most likely cured a significant amount of bulk defects [Grant et al., 2016b]. Thus, we hypothesize that for samples with thick thermal oxide mainly interfacial defects remain to be passivated, leading to a fast hydrogenation process, whereas for samples with tunneling oxide both interfacial and bulk

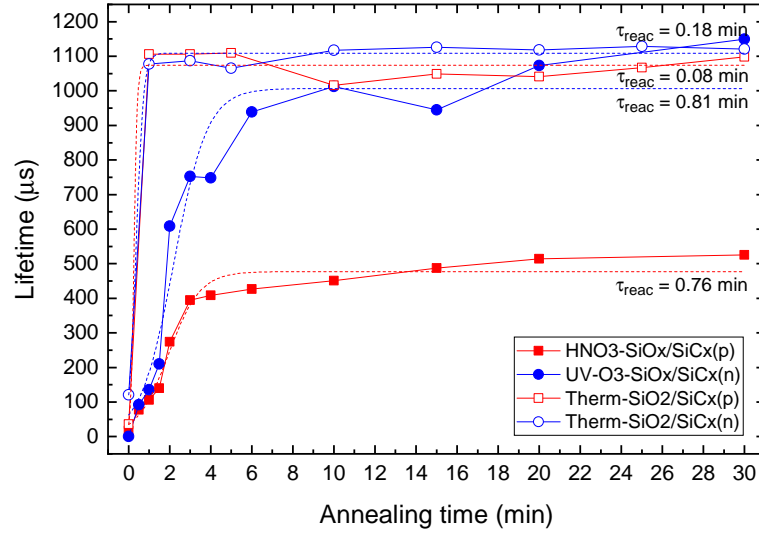


Figure 4.6 – Evolution of effective minority carrier lifetime (at MCD of $1 \cdot 10^{15} \text{ cm}^{-3}$) during hydrogenation on hotplate at 450°C for samples with $\text{SiC}_x(p)$ or $\text{SiC}_x(n)$ and $\sim 1.3 \text{ nm}$ tunneling SiO_x or $\sim 25 \text{ nm}$ thermal SiO_2 . The dashed lines give the fits according to $\tau_{\text{eff}} = [1/\tau_{\text{end}} + A \cdot \exp(-t/\tau_{\text{reac}})]^{-1}$.

defects remain to be passivated, the latter limiting the kinetics of the hydrogenation process as observed in Fig. 4.4 above.

Interestingly, no significant difference was observed between samples featuring n -doped and p -doped SiC_x layers. Such a difference was expected, since the position of the Fermi level was reported to have an influence on the charge-state of hydrogen [Herring et al., 2001], and hence on its diffusivity [Hamer et al., 2018], [B. Hallam et al., 2020], [Beyer and Zastrow, 2000]. Moreover, the Fermi level position influences the charge state and relative population of energy levels in the case of multivalent defects [Rougieux et al., 2018]. Therefore, the doping and Fermi level position are expected to have an impact on the ability of hydrogen to passivate the present defects, and on the kinetic of this process [B. Hallam et al., 2020]. Such an effect can however not be ruled out, as the $\text{SiC}_x(p)$ and $\text{SiC}_x(n)$ layers differ in thickness and in crystallinity, which both impact the diffusion of hydrogen through the layers. Indeed, the $\text{SiC}_x(n)$ layers are deposited with a much higher CH_4 flow than their $\text{SiC}_x(p)$ counterparts, suppressing the crystallization upon firing, as shown in appendix A. The diffusion coefficient of hydrogen being lower in a-Si:H than in c-Si [Carlson and Magee, 1978], the lower crystallinity counterbalances the lower thickness and a potential influence of the doping on the diffusivity.

Fig. 4.6 shows almost instantaneous passivation in the case of thick thermal oxides. In order to slow down the kinetics and to gain further insight in what is speculated to be the hydrogenation of interfacial defects, some samples were annealed on the hotplate at 350°C rather than 450°C . The passivation saturates within 5 min, as can be seen in Fig. 4.7a. In the plot over $x = n/p$, the characteristics show a linear behavior only in the as-deposited state and for short treatment

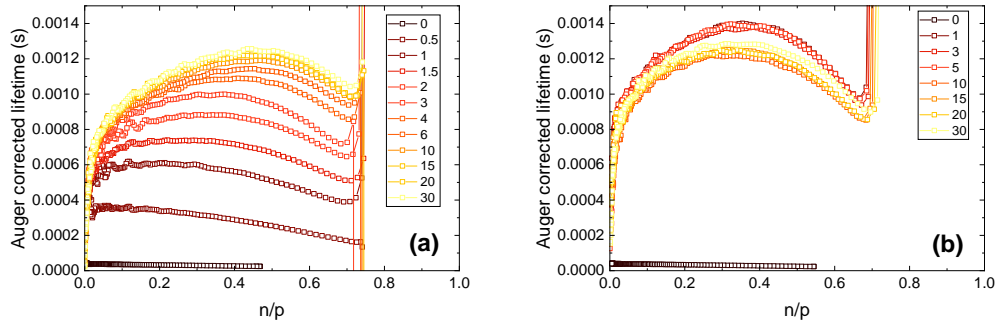


Figure 4.7 – Auger-corrected lifetimes over n/p of samples featuring a thick thermal SiO_2 measured at various time steps during the hydrogenation process at 350 °C (a) and 450 °C (b). The legend gives the total time (in minutes) the sample has spent on the hotplate.

times. For longer hydrogenation times, the curvature increases and reaches similar shapes as those hydrogenated at 450 °C, shown in Fig. 4.7b. Since linear behavior with negative slope is the signature of shallow bulk defects, this trend corroborates the interpretation made earlier, that in the case of samples with a thermal SiO_2 , the kinetics of the hydrogenation process are limited by the passivation of interfacial defects. Note the the curves in Fig. 4.7b correspond to open squares in Fig. 4.6, and display the same behaviour: almost instantaneous passivation, and a small decrease after 10 min. Annealing samples featuring a tunneling SiO_x at 350 °C resulted in final lifetimes below 100 μs (probably bulk limited), compromising the trustworthiness of the fitting.

4.5 In situ lifetime measurements in real time

So far, all kinetics measurements were performed by annealing the samples shortly on the hotplate in several steps, and measuring the effective lifetime at room temperature in between. In order to go one step further and measure the evolution of the lifetime in real time during the hydrogenation process, in situ MPL measurements were carried out [Desthieux et al., 2020b].

First, the evolution of the lifetime in a sample passivated with a chemical $\text{SiO}_x/\text{nc-SiC}_x(p)/\text{SiN}_x:\text{H/D}$ stack, that has been annealed for 30 min at 450 °C beforehand, was measured. This sample was subject to a new annealing experiment (30 min at 450 °C) during which the lifetime was monitored in real time by in situ MPL (see Fig. 4.8a). Note that in this setup, the lifetime is measured at chamber temperature (i.e. up to 450 °C). Large variations of the lifetime are measured during the heating and cooling phases: τ_{eff} increases with temperature up to 350 °C and severely drops when the temperature exceeds 350 °C. During the cooling phase τ_{eff} displays a "symmetrical" behavior, rising rapidly as the temperature drops below 350 °C again, and subsequently decreasing slowly with temperature. During the high temperature plateau (450 °C), the lifetime stays constant. The final lifetime measured by QSSPC is identical to the initial one meaning that the additional annealing did not change the passivation of

the sample. Consequently, these variations are reversible and are expected to result from two competing phenomena: reversible changes in the overall bulk and surface lifetimes (such as evolution of electron and hole trap capture cross sections) that increase with temperature [Desthieux et al., 2020b], [Bernardini et al., 2017] against Auger or SRH recombinations that are boosted at high temperature (the intrinsic carrier density under thermal equilibrium at 450 °C being around $4 \cdot 10^{16} \text{ cm}^{-3}$ [Sze and Ng, 2007], [Thurmond, 1975]). Another possible explanation could be a temperature dependent steady-state between hydrogen supply, Si-H bond forming and breaking. A similar interpretation was made by Dingemans et al. for their results, stating that passivation and dissociation processes take place in parallel, leading to a temperature-dependent equilibrium defect density [Dingemans et al., 2012], [Stesmans, 2000], [Stathis, 1995]. Therefore, these variations are not related to the studied hydrogenation process.

Fig. 4.8b shows the evolution of the lifetime during an annealing at 450 °C for 30 min on samples with nc-SiC_x(*p*) and nc-SiC_x(*n*) layers capped with a SiN_x:H/D layer (as-deposited samples)^{II}. Both samples display a similar behavior. At the beginning of the annealing step, the lifetime is very low and gradually increases during the temperature plateau at 450 °C until it saturates after 20 min. The second part of the graph (cooling phase) is similar to the one shown in Figure 4.8a. This can be interpreted as follows: at the beginning, the lifetime is limited by the bulk defects formed during the firing step, thus preventing the observation of the first lifetime “peak” observed in Fig 4.8a. At 450 °C, the lifetime increases exponentially, which is consistent with the progressive hydrogenation of the bulk defects, until it saturates when the bulk is completely passivated. At that point, the lifetime saturates but is still low (around 250 μs) since it is limited by Auger and SRH recombinations due to the high temperature.

In this setup, the hydrogenation seems to take longer than in the previous hotplate annealing experiments. This is most likely due to differences in the heating process. In the case of MPL, the samples are heated in a reactor under low pressure, which heats up relatively slowly (~30 °C/min), whereas in the case of hotplate treatment, the samples are put directly on the hotplate pre-heated to 450 °C and thermalize within ~6 s. However, the curves measured by MPL can be fitted with the same formula (Eq. 4.1) as the ones from the hotplate experiment, indicating that a similar mechanism is at work. Doing so yields $\tau_{\text{reac}} = 2.37 \text{ min}$ and $\tau_{\text{reac}} = 2.92 \text{ min}$ for the samples with nc-SiC_x(*p*) and nc-SiC_x(*n*), respectively. The passivation thus seems slightly faster for samples with a *p*-type layer, but otherwise the behavior is similar.

A more detailed analysis of the reversible temperature-dependent effects in these MPL measurements was done by A. Desthieux, who performed them, in chapter 4 of his thesis [Desthieux, 2021]. Among other data treatments, he separates the evolution of τ_{bulk} from other, tempera-

^{II}Note that in this experiment, the nc-SiC_x(*p*) layers were deposited on top of chemical SiO_x, whereas the nc-SiC_x(*n*) layers were grown on top of UV-O₃ SiO_x. This difference comes from the fact that at the time of fabrication of these samples, due to some unknown processing issues, the nc-SiC_x(*p*) layers performed poorly on UV-O₃ SiO_x, while achieving their usual passivation on chemical SiO_x, making the latter exceptionally the better option to reach high lifetime values.

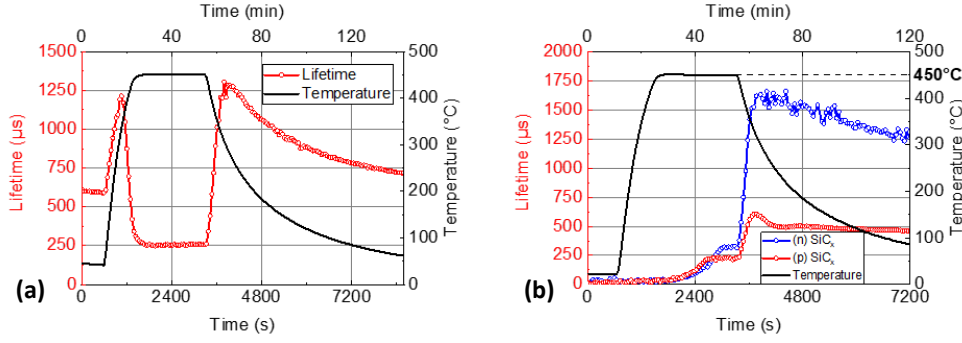


Figure 4.8 – (a): MPL measurement of lifetime (at MCD of $1 \cdot 10^{15} \text{ cm}^{-3}$) of a sample featuring $\text{SiC}_x(p)$ and having already been hydrogenated previously. (b): MPL measurement as function of time during hydrogenation process. Two samples are represented, featuring $\text{SiC}_x(p)$ and $\text{SiC}_x(n)$ layers, in order to compare their kinetics.

ture dependent evolutions of τ_{eff} by postulating

$$\frac{1}{\tau_{\text{eff}}} = \frac{1}{\tau_{\text{bulk}}} + \frac{1}{\tau_{\text{other}}} \quad (4.2)$$

Assuming τ_{bulk} in Fig. 4.8a to be constant (at a value of 2 ms chosen arbitrarily), he uses this measurement to compute the evolution of τ_{other} . Knowing this, the evolution of τ_{bulk} during hydrogenation can be extracted from the measurements of τ_{eff} such as the ones shown in Fig. 4.8b. The resulting curve displays an S-shape with an exponential increase and saturation, similar to the ones observed in Fig. 4.6, and compatible with equation 4.1.

4.6 Single sided hydrogen source

The saturating kinetics curves indicate that more than enough hydrogen is supplied by the $\text{SiN}_x\text{:H/D}$ reservoir layers. Moreover, hydrogen was reported to diffuse quickly through c-Si [Carlson and Magee, 1978]. Therefore, hydrogenation with the $\text{SiN}_x\text{:H/D}$ layer on only one side of the wafer was investigated (see Fig. 4.9a). Note the the samples of this experiment featured interfacial oxides grown by UV- O_3 treatment. The possibility to diffuse hydrogen from a front reservoir layer, through the wafer, to the back surface has been reported in literature [Nemeth et al., 2017], [Sio et al., 2019], [Sheoran et al., 2008]. Such an approach might be of interest, as it would simplify the production process of high efficiency solar cell architectures featuring a front $\text{SiN}_x\text{:H}$ layer as anti-reflective coating, but no such layer on the rear side [Richter et al., 2021]. As shown in Fig. 4.9b, the lifetime saturates at $\sim 700 \mu\text{s}$ (corresponding to iV_{oc} values $\sim 705 \text{ mV}$) after about 1 hour and remains constant for at least 8 hours. Samples from the same experiment, that had an $\text{SiN}_x\text{:H/D}$ reservoir layer on both sides, reached lifetimes of $\sim 1300 \mu\text{s}$ (corresponding to iV_{oc} values $\sim 718 \text{ mV}$). Moreover, none of these samples displayed ring shapes in PL measurements performed after hydrogenation. These results indicate that the hydrogenation of both surfaces, as well as the bulk, occurs

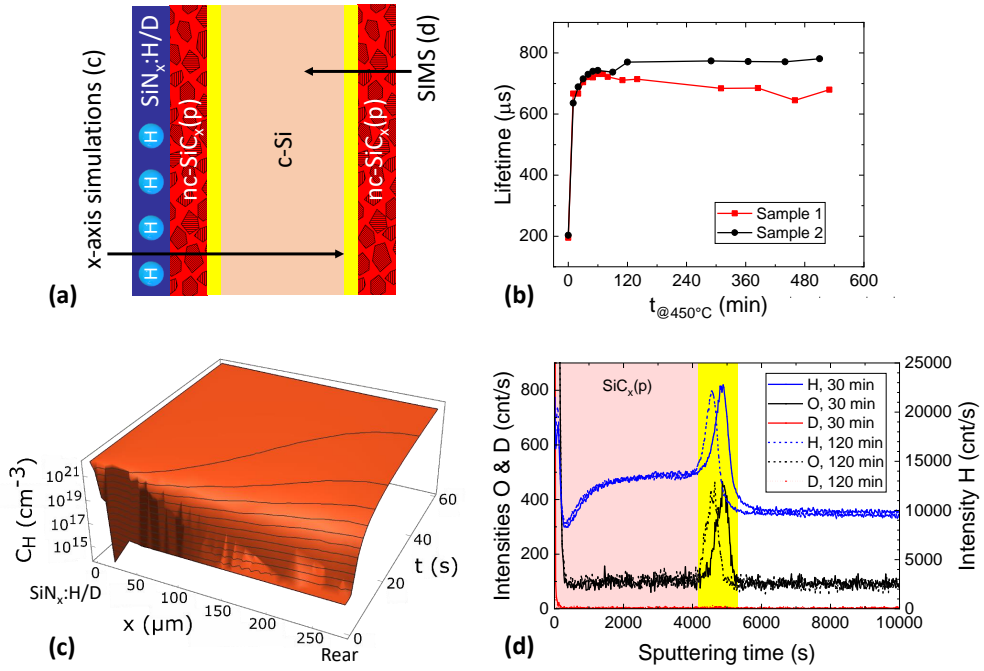


Figure 4.9 – (a) Schematic illustration of the processed samples. The arrows represent the cross sections along which the simulations and SIMS measurements were performed. (b) Lifetimes (at MCD of $1 \cdot 10^{15} \text{ cm}^{-3}$) measured at various time intervals during the hydrogenation process, showing the evolution of passivation with time spent on the hotplate, for samples featuring a SiN_x:H/D reservoir layer on the front side only. The two curves correspond to two identically processed samples. (c) Simulated hydrogen concentrations, across the whole wafer and in function of time, during diffusion at 450 °C from a single side SiN_x:H/D hydrogen source. (d) SIMS profiles of O, H and D at the back surface. The area highlighted in yellow indicates the SiO_x layer, while the area highlighted in red to the left indicates the SiC_x(p) layer.

also with the hydrogen source on only one side of the wafer, although to a lower level than with SiN_x:H/D on both sides. In addition, assuming the passivation level reached a steady-state between hydrogen supply, defect passivation and defect creation, it staying constant for 8 hours indicates that the SiN_x:H/D reservoir layer acts as a quasi-infinite source of hydrogen and deuterium in these experiments.

This observation of a continuously increasing passivation until saturation is in agreement with the results shown in Fig. 4.6 and Fig. 4.7. This indicates that in the present case of FPCs, accumulation of hydrogen until concentrations exceeding D_{it} , as reported in section 3.4, is beneficial for passivation. A possible explanation might be that excess hydrogen is required to enable sufficient chemical reactions between hydrogen and the present defects. Further investigations are required to clarify this point.

This is interesting, as a detrimental effect of excess hydrogen on passivation was reported by Kang *et al.* and Hollemann *et al.* on annealed HTPCs [D. Kang *et al.*, 2021a], [Hollemann

et al., 2021a]. Note that the estimated concentration of hydrogen of $4.5 \cdot 10^{14} \text{ cm}^{-2}$ in the SiO_x layer of FPCs is within the optimal range determined by Kang *et al.*, who reported passivation losses for hydrogen concentrations exceeding $6 \cdot 10^{14} \text{ cm}^{-2}$. Hence, excess hydrogen might be beneficial until that concentration and only become detrimental beyond it. On the other hand, Hollemann *et al.* reported passivation losses with hydrogen concentrations as low as $6 \cdot 10^{12} \text{ cm}^{-2}$ when firing at 863°C [Hollemann et al., 2021a]. In their case, no degradation was observed upon firing at 724°C . Note that for this kind of interpretation, the materials making up the contacting stack need to be taken into consideration. Indeed, the optimal hydrogenation conditions seem to depend strongly on the properties of the SiN_x layer [D. Kang et al., 2021a], [Nogay et al., 2017]. Moreover, the interfacial defect density D_{it} depends on the type of SiO_x layer implemented, as shown by Hollemann *et al.* [Hollemann et al., 2021b], [Hollemann et al., 2021a]. Further, Kang *et al.* and Hollemann *et al.* worked on annealed LPCVD layers, whereas the work presented here features SiC_x layers grown by PECVD in amorphous state and optimized for subsequent firing [Ingenito et al., 2018]. Hence, their behavior upon thermal treatments is likely to differ, leading to potential differences in the value of the optimal hydrogen concentration at the c-Si/ SiO_x interface. An additional difference might come from the thermal treatment used for hydrogen diffusion. In this work it was a hotplate anneal at 450°C , which most likely leads to a gentler hydrogenation process than the diffusion upon firing mostly used in the experiments of Kang *et al.* and Hollemann *et al.*. The lowest J_0 value reported by Kang *et al.* (8 fA/cm^2) was actually achieved by hydrogen diffusion from a $\text{SiN}_x\text{:H}$ reservoir layer during a FGA at 400°C , a process close to the one applied in this work. These results indicate that excess hydrogen alone is no immediate issue, but its combination with thermal stress induced by firings at temperatures above 725°C becomes detrimental, likely due to the formation of platelets [Hollemann et al., 2021a], [Johnson et al., 1987].

In order to quantify the passivation of the rear side, the back surface recombination velocity was computed, applying the method presented by Sproul *et al.* [Sproul, 1994], and assuming that the surface recombination velocity at the front side is equal to the one obtained on symmetrical samples with $\text{SiN}_x\text{:H}$ layer on both sides. As the calculation requires the bulk lifetime, which in our case changes over the course of the process (as shown above), only a lower limit is given, based on the assumption of $\tau_{\text{bulk}} = 3 \text{ ms}$ after hydrogenation (as measured in Fig. 4.1b for the sample after $\text{SiC}_x(p)$ deposition); thus, one obtains $S_{\text{front}} = 6.4 \text{ cm/s}$ and $S_{\text{back}} = 23.6 \text{ cm/s}$. However, it is unlikely that the bulk passivation is as good for a single side hydrogen source than for the case with $\text{SiN}_x\text{:H}$ on both sides, while the back surface passivation is not. Assuming $S_{\text{front}} = S_{\text{back}} = 6.4 \text{ cm/s}$, one obtains $\tau_{\text{bulk}} = 1.036 \text{ ms}$. Hence, it is likely that the value of τ_{bulk} is somewhere in between 1 and 3 ms, while S_{back} lies between 6 and 24 cm/s .

Finite elements simulations, shown in Fig. 4.9c, indicate that at 450°C hydrogen can diffuse through the whole wafer in less than a minute, indicating that the hydrogenation process is not diffusion limited. A possible candidate for the factor limiting the hydrogenation is the available hydrogen supply. This hypothesis is in agreement with the findings of Hong *et al.*, who reported that the bulk passivation of multicrystalline silicon cells depends on

the in-diffusion process of hydrogen from a $\text{SiN}_x\text{:H}$ reservoir layer into the bulk [Hong et al., 2003]. Another hypothesis is that the hydrogenation process is limited by the reaction rates (passivation and dissociation) of hydrogen with the defects, as highlighted by Stesmans [Stesmans, 2000]. For these simulations, a Wolfram Mathematica script was written, using the diffusion coefficients given by Carlson *et al.* [Carlson and Magee, 1978] for the 30 nm thick $\text{SiC}_x(p)$ layer and the 280 μm thick c-Si wafer, and those given by Tuttle [Tuttle, 2000] for the 1.2 nm thick SiO_x layer. For the initial conditions, a hydrogen concentration of $1.14 \cdot 10^{22} \text{ cm}^{-3}$ in the $\text{SiN}_x\text{:H}$ layer was used, as has been measured by ERDA. For the other layers and the bulk, a concentration of $1 \cdot 10^{16} \text{ cm}^{-3}$ was used, as different levels within the layers or lower concentrations in the bulk could no longer be solved by the script. Note also that the diffusion coefficient used for the $\text{SiC}_x(p)$ layer was the one for amorphous silicon ($5.77 \cdot 10^{-13} \text{ cm}^2/\text{s}$), which is lower than what is expected for a nanocrystalline layer, and still results in very rapid diffusion of hydrogen from the front source layer to the back side.

SIMS measurements on the rear side, shown in Fig. 4.9d, revealed the presence of hydrogen in the rear layers, but surprisingly no trace of deuterium could be found, neither after 30 min of diffusion, nor after 2 hours, even though it was incorporated into the $\text{SiN}_x\text{:H/D}$ reservoir layer too. Deuterium has a 1.41 times lower diffusion coefficient than hydrogen [Carlson and Magee, 1978], but is otherwise expected to behave similarly to hydrogen. Moreover, Mathematica simulations of deuterium diffusion through the wafer showed results very similar to those of hydrogen. Therefore, if the hydrogen observed at the rear side comes from the $\text{SiN}_x\text{:H/D}$ reservoir layer, both deuterium and hydrogen accumulation would be expected, as observed in chapter 3 and our previous studies [Lehmann et al., 2019], [Pal et al., 2021].

Since residual hydrogen was observed within the $\text{SiC}_x(p)$ layer after firing (Fig. 3.3), a possible explanation could be that the hydrogen observed at the rear side does not come from the front $\text{SiN}_x\text{:H/D}$ reservoir layer, but from the rear $\text{SiC}_x(p)$ layer. To test this hypothesis, PL imaging and lifetime measurements were performed at various processing steps on a sample without $\text{SiN}_x\text{:H/D}$ reservoir layer. The results are shown in Fig. 4.10. As one can observe, a ring shape appears upon firing, indicating an improvement of the surface passivation. However, the measured PL signal and lifetimes stay low. Assuming $\tau_{\text{bulk}} = 50 \mu\text{s}$ (as measured in Fig. 4.1b), S_{eff} can be computed from the lifetime measurements in the center of the samples, and compared to the values obtained earlier for samples with single or double sided $\text{SiN}_x\text{:H/D}$ layers (assuming $\tau_{\text{bulk}} = 3000 \mu\text{s}$). The results are given in table 4.1. Note that samples without $\text{SiN}_x\text{:H/D}$ layer were processed on SE wafers, whereas the ones with $\text{SiN}_x\text{:H/D}$ layers were processed on DSP wafers. This affects the computation, since their thickness and resistivity differ, but the resulting S_{eff} values can still be compared among each other. The results indicate a slight improvement upon hotplate treatment, however, as expected, the passivation reached is much worse than in the presence of a $\text{SiN}_x\text{:H/D}$ reservoir layer. According to Olibet *et al.* [Olibet et al., 2007], S_{eff} is directly proportional to the density of dangling bonds. From the computed values for S_{back} we therefore conclude that roughly 40%, 88% and 97% of dangling bonds are passivated upon hotplate treatment for samples with $\text{SiN}_x\text{:H/D}$ layers on no, one and both sides, respectively. Therefore, in the case of samples with $\text{SiN}_x\text{:H/D}$ on the front

Table 4.1 – S_{back} values computed for samples at various processing stages and with $\text{SiN}_x\text{:H/D}$ layers on none, one or both sides.

Process	$\text{SiN}_x\text{:H/D}$	S_{back} (cm/s)
Fired	None	189.3
HP 5 min	None	114.2
HP 30 min	Single side	23.6
HP 30 min	Both sides	6.4

side only, at least part of the hydrogen observed by SIMS on the rear side must come from the $\text{SiN}_x\text{:H/D}$ reservoir layer. Why no deuterium is observed thus remains an open question and further investigations are needed in order to fully understand the mechanisms at work.

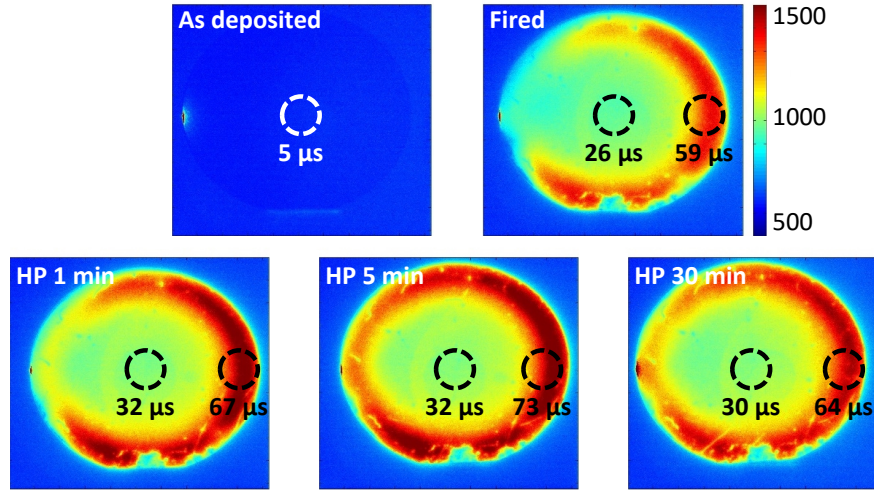


Figure 4.10 – PL images of samples without $\text{SiN}_x\text{:H}$ layer at different processing stages: After PECVD of $\text{SiC}_x(p)$, after firing, and after 1, 5 and 30 min on the hotplate at 450 °C. The circles indicate where QSSPC was measured and the resulting τ_{eff} values are given.

Kinetics experiments were also performed on these samples, using wafers of different doping types and resistivities, as well as SiC_x layers deposited in different tools. The results in Fig. 4.11 suggest that the kinetics are significantly slower than in the previous case with $\text{SiN}_x\text{:H}$ layers on both sides of the wafer, providing a further indication that the process is likely limited by the supply of hydrogen. This conclusion is further supported by the results in Fig. 4.12, collected on over 40 samples, indicating generally slower kinetics and lower end lifetimes for samples with $\text{SiN}_x\text{:H}$ layers on a single side. Moreover, in Fig. 4.11 the doping type of the wafer seems to play a major role for the hydrogenation kinetics, with $\tau_{\text{reac}} \sim 5$ min for p -type wafers, against $\tau_{\text{reac}} \sim 2.5$ min for n -type wafers capped with identical layers. As stated earlier, the wafer doping influences the charge state of diffusing hydrogen atoms [Herring et al., 2001], which in turn affects the diffusivity of these atoms as well as the efficiency of the chemical passivation process [Hamer et al., 2018], [B. Hallam et al., 2020]. However, the reported values

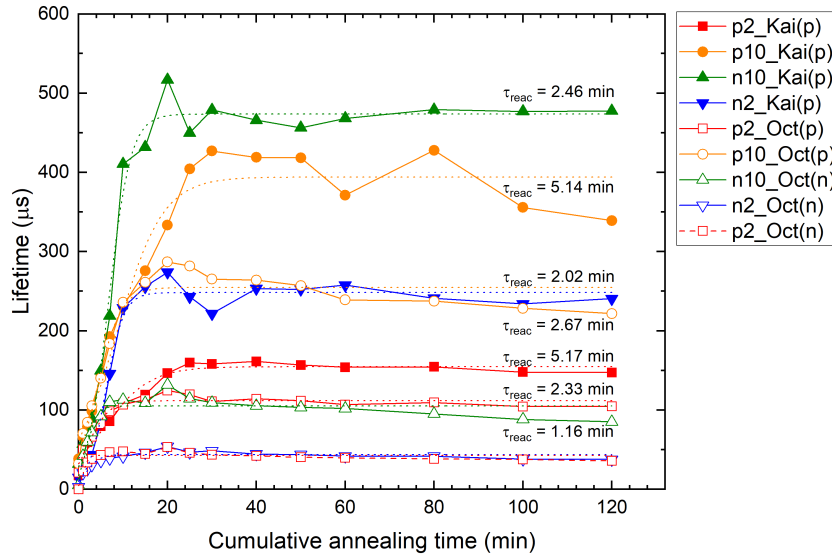


Figure 4.11 – Lifetimes (at MCD of $1 \cdot 10^{15} \text{ cm}^{-3}$) measured at various time intervals during the hydrogenation process, showing the evolution of passivation with time spent on the hotplate, for samples featuring a $\text{SiN}_x\text{:H/D}$ reservoir layer on the front side only. The dashed lines give the fits according to $\tau_{\text{eff}} = [1/\tau_{\text{end}} + A \cdot \exp(-t/\tau_{\text{reac}})]^{-1}$. In the legend, the first part gives details about the wafer (p - or n -type, 2 or 10 Ωcm), and the second part about the SiC_x layer (deposited in Kai-M or Octopus, p - or n -doped).

indicate faster diffusion in p -type silicon than in n -type, whereas we observe faster passivation using n -type wafers. A possible explanation would be that the type and concentration of these defects varies with the wafer doping.

Regarding the various SiC_x layers, the interpretation is complicated, as they differ not only in doping, but also in thickness, and most likely in crystallinity, all of which might impact the flow of hydrogen through these layers. Moreover, in the case of charged hydrogen atoms, electric fields built up at the interfaces might also influence the kinetics and distribution of hydrogen [Kail et al., 2005]. Further investigations are required to elucidate the mechanisms at work. Nevertheless, one results stands out: The thicknesses measured by ellipsometry for the $\text{SiC}_x(p)$ layers deposited in the Kai-M, the $\text{SiC}_x(p)$ layers deposited in the Octopus and the $\text{SiC}_x(n)$ layers in the Octopus, are $\sim 41 \text{ nm}$, $\sim 25 \text{ nm}$ and $\sim 11 \text{ nm}$, respectively. The corresponding τ_{reac} on 2 Ωcm p -type wafers are 5.17 min, 2.33 min and 0.54 min. The last value is to be taken with care, as the lifetime values were low and hence the fit less trustworthy. Nevertheless, the trend indicates slower hydrogenation for thicker layers, which was to be expected, as hydrogen has a much lower diffusivity in these still partially amorphous layers than in crystalline silicon [Carlson and Magee, 1978], turning them into a significant diffusion barrier, despite thicknesses below 50 nm. This conclusion is further supported by the fact that

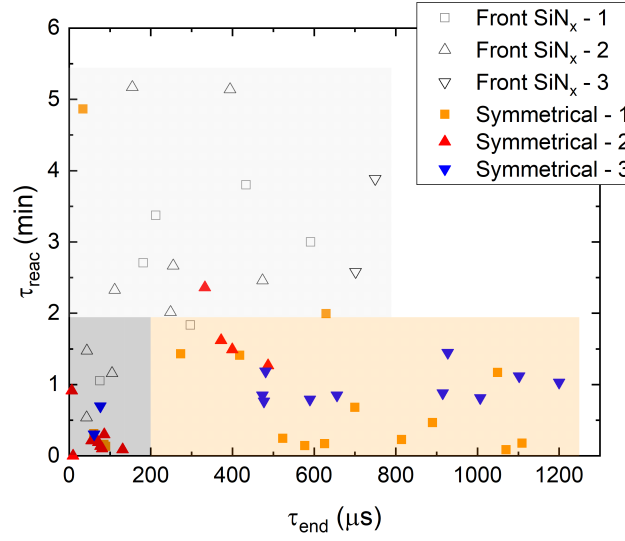


Figure 4.12 – Compilation of all τ_{end} and τ_{reac} , obtained from 6 different experiments when fitting the kinetics measurements according to $\tau_{\text{eff}} = [1/\tau_{\text{end}} + A \cdot \exp(-t/\tau_{\text{reac}})]^{-1}$. These experiments contain samples with $\text{SiN}_x\text{:H/D}$ donor layers on both or a single side, as well as various SiC_x layers (*p*- or *n*-doped, intrinsic, none). The various SiC_x layers were not differentiated in this graph. However, the zones in which most single or double-sided $\text{SiN}_x\text{:H/D}$ samples fall were highlighted. The results in the bottom left of the graph are considered irrelevant, since their low end lifetimes compromise the trustworthiness of the fitting procedure for such fast processes.

samples without SiC_x layer consistently displayed slightly faster hydrogenation (not shown here).

When plotting the linearized lifetime curves of QSSPC measurements for this kinetics experiment, one observes again the presence of shallow bulk defects (see Fig. 4.13a). In the plot of the residuals (Fig. 4.13b), there are apparently three different regimes. The curve before hydrogenation differs significantly from all the other ones, which could indicate that, in this case, the surface passivation is still the main limitation. The curves after 1 to 5 min of hydrogen diffusion overlap, with lifetime values about an order of magnitude higher than the original lifetime, indicating that the observed improvement of the lifetime is linked to the passivation of these shallow bulk defects. The subsequent curves overlap at a slightly higher value, but the reason for this additional improvement after 5 min is unclear.

4.7 Conclusions

The main finding of this chapter is the fact that firing induces shallow bulk defects within the FZ wafers which can subsequently be passivated with hydrogen, and that these shallow defects limit the kinetics of the hydrogenation process and the ultimately obtainable lifetime. Hence,

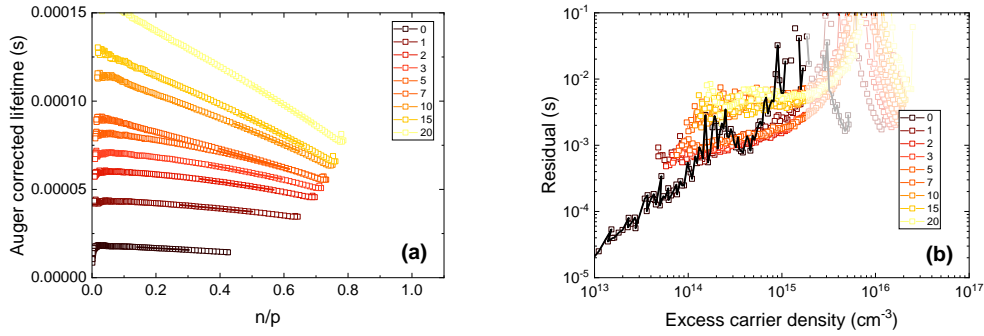


Figure 4.13 – (a) Linearized lifetime curves of QSSPC measurements for various hydrogenation times and fits indicating shallow defects. (b) Residuals after subtraction of Auger and shallow bulk contributions. The legend gives the total time (in minutes) the sample has spent on the hotplate.

the passivation potential of these contact structure might be higher than previously reported, since so far they seem to be bulk limited, rather than surface limited. The experimental results indicate a rapid passivation of the surface, taking place in less than 1 min, followed by a slower passivation of the shallow bulk defects. A long thermal pre-treatment of the wafers seems to be a possible way to improve the bulk, accelerating the hydrogenation process.

In situ lifetime measurements by MPL were carried out during hydrogenation processes. They revealed that the lifetime improvement follows an exponential saturation when the temperature of the sample reaches 450°C . This plateau is expected to correspond to the best possible bulk defect passivation. No major impact of the SiC_x doping on the evolutions of the lifetime was found, which is consistent with a bulk limited hydrogenation process. Its kinetics seems to be limited by the available hydrogen supply at the $\text{SiO}_x/\text{c-Si}$ interface, rather than by its diffusion within the bulk of the wafer. Moreover, it is affected by the bulk doping, as well as the SiC_x layer thickness.

Hydrogenation is also possible with a SiN_x reservoir layer deposited on one side of the wafer only, although resulting in a lower passivation level ($\tau_{\text{eff}} \sim 700 \mu\text{s}$ compared to $\tau_{\text{eff}} \sim 1300 \mu\text{s}$ for symmetrical samples), and slower kinetics ($\tau_{\text{reac}} \sim 5 \text{ min}$ compared to $\tau_{\text{reac}} \sim 0.8 \text{ min}$). The rear surface recombination velocity achieved for $\text{UV-O}_3 \text{ SiO}_x/\text{SiC}_x(p)$ stacks with a SiN_x layer on the front only most likely lies between 6 and 24 cm/s .

So far, the key role of hydrogen for passivation and its diffusion into the FPC was studied. The next chapter presents investigations on the long-term evolution of the lifetime of such samples. Indeed, the incorporation of hydrogen into c-Si was reported to induce degradation [Winter et al., 2020], [D. Chen et al., 2020]. Moreover, conditions under which hydrogen might again diffuse out of the hydrogenated passivating contact were explored.

5 Stability of the passivation

Summary

This chapter presents the evolution of the passivation after hydrogenation, both on short and long terms. So far, no degradation was observed upon 80 days of light soaking (80 °C, 1 sun illumination) for samples featuring tunneling oxides. Moreover, the lifetime remains stable upon thermal treatments up to 30 min at 170 °C. These are encouraging results, since they indicate that the investigated FPCs are not prone to the so-called Light- and elevated Temperature Induced Degradation (LeTID) or Light-Induced Degradation (LID) under operating conditions, and offer some flexibility for post-hydrogenation processing steps. Surprisingly, changes in lifetime upon storage were observed: some samples degraded, others stayed constant, and some even improved. Further investigations are needed to elucidate the mechanisms at work.

5.1 Introduction

As shown in the previous chapters, hydrogen diffusion from a $\text{SiN}_x\text{:H}$ reservoir layer into the sample is a key step to fabricate FPCs, passivating defects at the c-Si/ SiO_x interface and within the bulk. However, the presence of hydrogen has also been reported to cause lifetime degradation. In multicrystalline silicon, the LeTID has been intensively studied and linked to the presence of hydrogen in the bulk [Bredemeier et al., 2019], [Jensen et al., 2018] and within the dopant-diffused layers at the surface [D. Chen et al., 2020]. While some articles report that the firing step allows eliminating LeTID [Jensen et al., 2018], others claim it should be avoided [Sen et al., 2020]. Winter *et al.* investigated the stability of fired-only contacts, hence similar to the ones in this thesis, but in their case on Cz wafers. They reported a degradation and regeneration of the lifetime upon annealing, with or without illumination [Winter et al., 2020]. Most likely, this effect is linked to instabilities in the hydrogen passivation of the c-Si/ SiO_x interface, triggered by the firing process. Moreover, Niewelt *et al.* reported LID and regeneration in FZ samples upon light soaking at 75 °C under 1 sun illumination, as shown in Fig. 5.1 [Niewelt et al., 2017]. They conclude that the degradation is caused by bulk defects

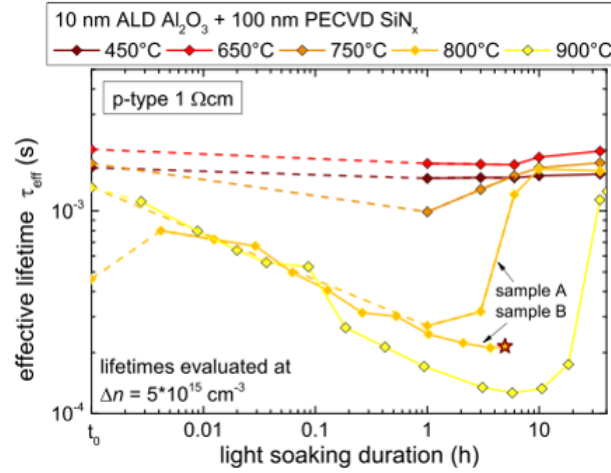


Figure 5.1 – Degradation (LID) and recovery of effective minority carrier lifetime upon light soaking, observed by Niewelt *et al.*. The samples were prepared on 1 Ωcm *p*-type FZ wafers and passivated with a stack of 10 nm of Al_2O_3 deposited by plasma-assisted ALD and 100 nm of a-SiN_x deposited by PECVD. The thermal treatment after deposition was varied, as stated in the legend. Reproduced without modifications from [Niewelt et al., 2017] licensed under a (CC BY) license (<https://creativecommons.org/licenses/by/4.0/>). Copyright ©2017, Niewelt *et al.*.

that might be related to hydrogen complexes.

In this chapter, it was tested if such degradation and regeneration phenomena are observed for our FPC samples upon long-term exposure to 1 sun illumination at 80 °C. These conditions were chosen as they are widely used to test for LID and LeTID [Fritz et al., 2017], [Jensen et al., 2018], [Winter et al., 2020] and are close to the operation conditions of a solar cell [D’Orazio et al., 2014]. Additionally, given the importance of hydrogen passivation for FPCs, it was tested from which temperature on hydrogen effuses from the samples again. This information is important regarding sample processing after the hydrogenation step was performed. Finally, we report on observed passivation changes upon storage of the samples.

5.2 Experimental details

For the following experiments, symmetrical samples were tested. Some came from previous experiments and were re-used; others were processed specifically for these tests, in the same ways as described in chapters 3 and 4. Some samples were processed on 280 μm thick DSP wafers (3 Ωcm), others on 200 μm thick SE wafers (2 Ωcm), all of them *p*-type. As a reminder: DSP wafers feature atomically flat surfaces, whereas SE ones have some surface roughness, as shown in Fig. 2.2, but are considered flat too. Regarding the interfacial oxide, all three types used so far have been implemented: 1.3 nm thick chem SiO_x (HNO₃), 1.3 nm thick UV-O₃ SiO_x and 25 nm thick therm SiO₂. With one exception, all samples feature SiC_x(*p*) layers and have been hydrogenated via hydrogen diffusion from a SiN_x:H reservoir layer. This SiN_x:H layer

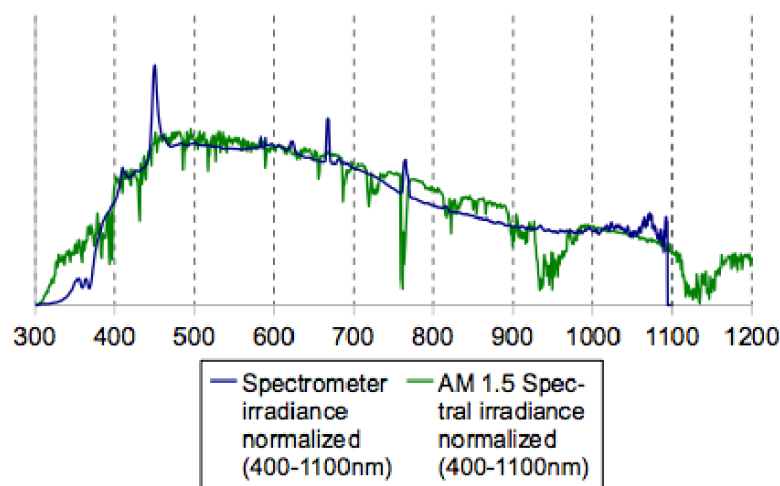


Figure 5.2 – Measured spectrum of the light soaker, provided by the manual^I, compared to the solar irradiance AM 1.5G.

was subsequently etched off (12 min in 5% HF at room temperature) for part of the samples, whereas it remained on top of the $\text{SiC}_x(p)$ for others. For the one exceptional sample, featuring a thermal oxide, the $\text{SiC}_x(p)$ layer was also etched off. To do so, it was immersed for ~20 min in a 20% (weight) KOH solution kept at 60 °C. This is a selective etch, which is almost harmless to the thermal SiO_2 below the $\text{SiC}_x(p)$.

For the long-term stability experiments, the samples were placed into a Solaronix Sunirad A-65 light soaker. Within it, the samples were placed on a plate kept at 80 °C and constantly illuminated with an intensity of ~1 sun. The spectrum of the light is close to the solar irradiance (AM 1.5G), as can be seen in Fig. 5.2. Note that the UV part of the spectrum (below 380 nm) is low compared to AM 1.5G, but some UV irradiation is present nevertheless. As for the hydrogen effusion experiments, the samples were simply placed on a hotplate, kept at various temperatures between 80 °C and 500 °C.

5.3 Long-term evolution of the passivation upon light soaking

The curves in Fig. 5.3 show the lifetime evolution over 80 days of various samples under light soaking (80 °C, 1 sun). As described earlier, the samples differed in wafer and oxide type. Moreover, some samples were still capped with the $\text{SiN}_x\text{:H}$ reservoir layer, whereas it was removed for others. For one sample, the $\text{SiC}_x(p)$ layer had also been removed. As can be observed, these samples do not show the typical degradation and recovery behavior reported for LeTID and LID, and shown in Fig. 5.1. In fact, the lifetimes of samples featuring a 1.3 nm thin tunneling oxide (HNO_3 or UV-O_3) stayed almost constant, with no significant difference between samples with chem SiO_x and UV-O_3 SiO_x , nor between samples processed on DSP

^IThis spectrum is also available on the website of Solaronix, in the brochure of the Solixion A-70, which features the same light engine as the Sunirad A-65 [Solaronix, n.d.].

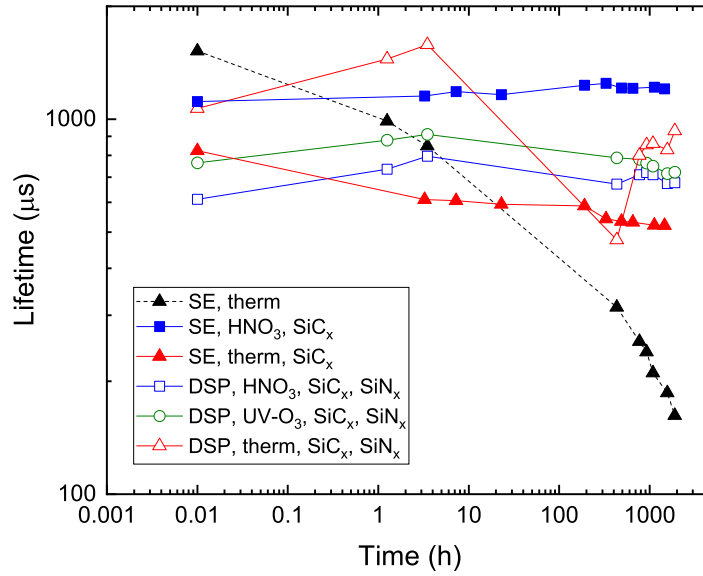


Figure 5.3 – Long-term evolution of $\tau_{\text{eff}@10^{15}\text{cm}^{-3}}$ of various samples kept at 80 °C and under 1 sun of illumination for 80 days. QSSPC measurements were performed intermittently at room temperature. The samples were processed using SE or DSP wafers, growing chem SiO_x , UV- O_3 SiO_x or therm SiO_2 , and with or without SiN_x :H capping layer. Moreover, one sample had its $\text{SiC}_x(p)$ layer removed in KOH prior to this experiment.

wafers and still capped with the SiN_x :H reservoir layers and samples processed on SE wafers which had their SiN_x :H layer removed. For samples with therm SiO_2 , the lifetime is less stable. For the case where the $\text{SiC}_x(p)$ layer was removed, a strong and continuous degradation is observed. A continuous degradation is also observed for the sample with therm SiO_2 on a SE wafer capped with $\text{SiC}_x(p)$, but it is much slower, and the lifetime seems to stabilize with time. As for the sample with therm SiO_2 on a DSP wafer and still capped with SiN_x :H, the results are quite variable. Here one actually observes some degradation followed by regeneration. However, since it is the only such occurrence and since the degradation happened in a single time step, this result has to be treated with care. Luckily, these thick oxides are only used for tests. In contrast, samples with tunneling oxides that allow current extraction in solar cells, were observed to be stable. Of course, the conditions used in this experiment were rather gentle (80 °C). However, as they are close to the operating conditions of solar cells, the observed stability for samples featuring a tunneling oxide is encouraging. Moreover, Chen *et al.* used similar conditions to demonstrate LeTID-free industrial solar cells featuring a hydrogenated TOPCon rear contact [R. Chen et al., 2021].

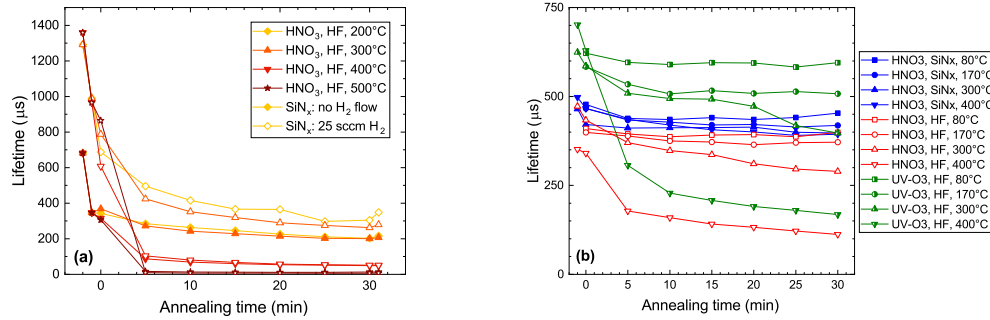


Figure 5.4 – (a) Evolution of $\tau_{\text{eff}@10^{15}\text{cm}^{-3}}$ measured in 5 min intervals upon hotplate treatment at various temperatures after hydrogenation and SiN_x :H removal. The SiN_x :H reservoir layers were deposited with two different recipes: one featuring only SiH_4 and NH_3 gas flows, the other one featuring an additional H_2 gas flow. The lifetime value given at -2 min was measured right after SiN_x :H removal, while the one given at -1 min was measured 40 days later, just before cleaving the wafer in four pieces for this experiment. (b) Similar experiment, but varying the interfacial oxide layer and for samples with and without SiN_x :H layer on top of SiC_x (p). In this case, all SiN_x :H/D layers were deposited with a 25 sccm D_2 gas flow. The lifetime value given at -1 min was measured right after SiN_x :H/D removal, 7 days prior to the present experiment.

5.4 Hydrogen outdiffusion

The previous experiment showed no lifetime degradation at 80 °C for samples featuring a tunneling SiO_x . Since chapters 3 and 4 revealed the key role of hydrogen diffusing into the sample to passivate defects at the c-Si/ SiO_x interface and within the c-Si bulk, the question arose at which temperature this hydrogen effuses out of the sample again. To test this, various hydrogenated samples were again put on the hotplate at different temperatures, and their lifetime measured every 5 min by QSSPC (at room temperature). A first experiment, shown in Fig. 5.4a, shows that the lifetime drops mainly during the first 5 min, and then stabilizes. According to these results, hydrogen effusion seems to take place already at 200 °C, and its effect gets dramatic at temperatures ≥ 400 °C. These findings corroborate the hypothesis made in section 4.3 for the sample shown in Fig. 4.1c, regarding loss of hydrogen from the bulk during the heating phase prior to a-Si:H(*i*)/a-Si:H(*n*) deposition. A second experiment, shown in Fig. 5.4b, allows some further conclusions. First of all, samples still capped with SiN_x :H/D show almost no degradation. This is in line with the results of Fig. 4.9b, which indicated that SiN_x :H/D reservoir layers contain enough hydrogen to maintain a steady-state during several hours at temperatures up to 450 °C. Second, the lifetime stays fairly stable at 80 °C and 170 °C. A small drop occurs in the beginning, but then the lifetime stabilizes and stays constant for the rest of the process. This means, that processes up to 170 °C can still be performed after hydrogenation, such as for example sputter damage curings, as are performed after PVD of TCOs. At temperatures ≥ 300 °C lifetime degradation is observed, which is interpreted as hydrogen effusing from the samples.

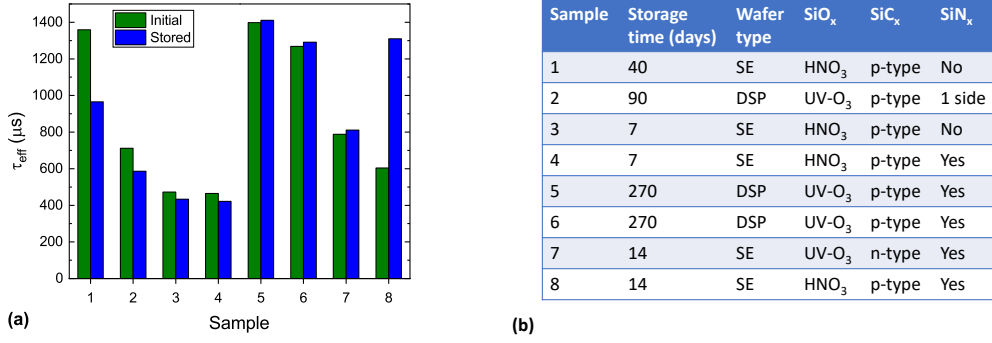


Figure 5.5 – (a) $\tau_{\text{eff}@10^{15}\text{cm}^{-3}}$ of various samples measured directly after hydrogenation and some time later. In the meantime, the samples were stored at room temperature, in an N₂-flushed cupboard within the clean room. (b) Table providing further details about each sample.

When looking at the lifetime measurements of Fig. 5.4 before hotplate treatments, one observes that the lifetime degraded upon storage. This was an unexpected effect and will be investigated a bit closer in the next section.

5.5 Passivation changes upon storage

As observed during the previous experiments, the lifetime after hydrogenation of some samples degrades upon storage. To get a broader picture, several samples were re-measured, all of them having been stored for several days at room temperature in an N₂-flushed cupboard within the clean room. The results are shown in Fig. 5.5. As one can see, some samples degrade, whereas others stay stable or even improve. Comparing these results with observations of other people from the laboratory, stable cells seem to be the baseline. Degradation with time has for example also been observed by the heterojunction group in the case of a-Si:H(*i*)/c-Si(*n*)/a-Si:H(*i*) structures, i.e. before deposition of doped layers and capping with TCO. As for the improvement, it was surprising, but has actually already been observed by Dr. Audrey Morisset. She observed lifetime improvements of up to 1 ms in FPCs stored for 1 month, featuring both SiC_x(*p*) and SiC_x(*n*) layers, as well as chem SiO_x and UV-O₃ SiO_x. Hence all these effects seem to be reproducible. However, the mechanisms behind them remain speculative so far.

For the degradation, Nie *et al.* observed a 5% drop in lifetime upon dark annealing at 100 °C that they linked to instabilities of the hydrogen passivation [Nie et al., 2021]. Assuming a similar effect to take place also at room temperature, this might be an explanation for the observed degradation, especially in the cases where the samples are no longer capped with SiN_x:H layers. As for the lifetime improvement, a possible explanation would be the release of strain at the c-Si/SiO_x interface. Indeed, Hollemann *et al.* reported an increase in interfacial defect density upon firing due to thermal stress [Hollemann et al., 2020]. A subsequent

annealing allows for strain release through structural rearrangement of atomic bonds in the c-Si/SiO_x transition region [Polzin et al., 2020]. Cao *et al.* observed a drop of almost 50% in film stress upon 3 h of annealing at 500 °C of a 10 µm thick SiO_x layer deposited by PECVD [Cao and Zhang, 2006]. According to Fargeix *et al.* the viscosity of a SiO₂ film varies exponentially with temperature, leading to a 50 orders of magnitude higher viscosity at room temperature than at 500 °C [Fargeix and Ghibaudo, 1983]. Whether such stress release could occur in 1.3 nm thin tunneling SiO_x layers at room temperature over a time scale of weeks, remains an open question. Other publications reported improvement in passivation upon exposure to UV radiation [Dingemans and Kessels, 2012], [Dingemans et al., 2009]. In our case, this is unlikely, since the samples were stored in a cupboard within the clean room.

Surprisingly, the large improvement in lifetime observed for sample 8 in Fig. 5.5 seems to be linked to an improvement in bulk lifetime, as shown in Fig. 5.6. This trend has to be considered with caution, since the resistivity of the used wafers was rather low, leading to fits that are outside the recommended range. However, the results obtained with this method in chapters 3 and 4 made sense, increasing the confidence in this result, too. Grant *et al.* and Sperber *et al.* reported on a metastable bulk defect in p-type FZ silicon, possibly due to vacancy-hydrogen complexes [Grant et al., 2015], [Sperber et al., 2017a], [Sperber et al., 2017b]. This defect would suit our samples, since hydrogen diffusion into the bulk was highlighted in chapter 4, and firing was reported to amplify the instability [Sperber et al., 2016]. However, degradation and regeneration reported in these studies happened at temperatures ≥ 80 °C. Whether a similar phenomenon could take place at room temperature remains an open question. Hence, further investigations are necessary to elucidate the effects at the origin of the observed lifetime changes upon storage.

5.6 Conclusions

In this chapter, the evolution of the passivation after hydrogenation was investigated. So far, no degradation was observed upon 80 days of light soaking (80 °C, 1 sun illumination) for samples featuring tunneling oxides. Moreover, the lifetime remains stable upon thermal treatments up to 30 min at 170 °C. These are encouraging results, since they indicate that the investigated FPCs are not prone to LeTID or LID under operating conditions, and offer some flexibility for post-hydrogenation processing steps. Changes in lifetime upon storage were observed in some cases: some samples degraded, others stayed constant, and some even improved. Further investigations are needed to elucidate the mechanisms at work.

So far, the main focus was set on investigating the hydrogenation of FPCs. However, several experiments have been included, that provided insight about potential solar cell fabrication routes, such as hydrogenation of the rear contact from a front SiN_x:H layer, or the possibility for post-hydrogenation annealing steps up to 170 °C mentioned above. Going one step further, the next chapter presents results of investigations regarding the metallization of FPCs and the performances of co-fired cells featuring FPCs at the front and rear sides.

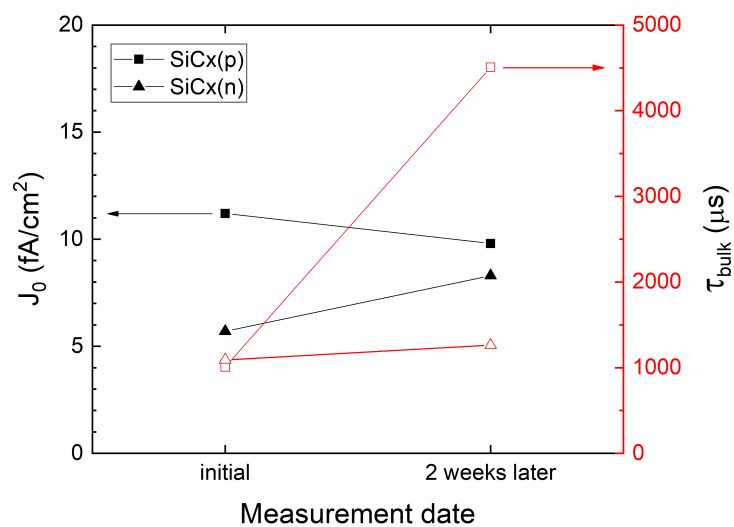


Figure 5.6 – Changes in J_0 and τ_{bulk} upon storage of samples 7 and 8 in Fig. 5.5, extracted following [Kimmerle et al., 2015].

6 Metallization of Fired Passivating Contacts

Summary

The first section of this chapter reports on the development of $\text{SiC}_x(p)/\mu\text{c-Si:H}(p)$ stacks with a total thickness of ~ 90 nm. The aim being to have a thick layer to stop screen printed aluminium paste during firing-through metallization. The motivation for this bi-layer stacks was to combine the passivation results obtained with $\text{SiC}_x(p)$ and the higher doping potential of microcrystalline layers, leading to lower contact resistivities. Unfortunately, despite an H_2/SiH_4 dilution ratio > 130 the presupposed microcrystalline layer turned out to be amorphous, even after firing. Further development of its PECVD recipe is therefore needed. When increasing layer thickness, blistering upon firing becomes an issue. In the present case, the introduction of a thermal pre-treatment of 10 min at 500°C , effusing most of the hydrogen from the layers, resulted in mostly blister free $\text{SiC}_x(p)/\text{a-Si:H}(p)$ stacks upon firing for 8 s at 800°C and iV_{oc} values > 709 mV after hydrogenation. However, the contact resistivity after screen printing of Al pastes and firing-through seems to take random values, ranging from $26 \text{ m}\Omega\text{cm}^2$, interpreted as direct contact between Al and the c-Si wafer, to values too high to be measured by TLM, indicating that the paste did not fire through the $\text{SiN}_x\text{:H}$ layer.

Closer investigations, presented in the second section, revealed that Al replaces Si in the $\text{SiN}_x\text{:H}$ layer, forming an Al-N compound. The diffusion of Al sometimes stopped within the $\text{SiN}_x\text{:H}$ layer, while it diffused into the a-Si:H(p) layer in other cases. The $\text{SiC}_x(p)$ layer seems to hinder the diffusion of Al, making it a promising layer to stop the paste during firing-through. However, Al accumulation at the tunneling SiO_x was observed, which most likely degrades the passivation. In addition, potential spiking-through of Al was observed in places with direct contact between aluminium particles from the paste and the deposited layers. So far, samples contacted by firing-through featured either high contact resistivity or significant passivation damages due to the metallization. Nevertheless, the ability to grow thick blister free layers and the observation that $\text{SiC}_x(p)$ layers hinder the diffusion of Al are promising results towards a low cost metallization route by firing-through of screen printed Al paste. Further investigation of this approach will be performed.

The third section therefore treats the evaporation of aluminium directly on the $\text{SiC}_x(p)/\text{a-Si:H}(p)$ layers, reducing the mechanical and thermal impact of the metallization compared to firing-through. Unfortunately, also in this case good contact could only be achieved at the expense of passivation. A potential explanation might be the amorphous nature of the $\text{a-Si:H}(p)$ layer, making it more difficult to contact. Adapting the PECVD recipe to grow a microcrystalline layer would likely enable good contact and passivation, making it a promising topic for future work.

For the fabrication of solar cells featuring co-fired FPCs on both sides, reported in the final section of this chapter, this $\text{a-Si:H}(p)$ layer was therefore dropped. Several batches of cells were produced, featuring co-fired layers of $\text{nc-SiC}_x(p)$ at the rear and $\text{nc-SiC}_x(n)$ at the front, implementing various metallization strategies. Unfortunately, the cells with evaporated aluminium at the rear seemed to be shunted. Moreover, a drop of more than 30 mV was observed between iV_{oc} after hydrogenation and V_{oc} of the finished cells. Nevertheless, efficiencies up to 20.5% were obtained for cells with ITO/Ag metallization on both sides, demonstrating the potential of such an approach. To our knowledge, this is the first report of a solar cell featuring co-fired passivating contacts.

6.1 Introduction

So far, the main focus was set on investigating the hydrogenation of FPCs. However, several experiments have been included in the previous chapters, that provided insight about potential solar cell fabrication routes, such as the possibility for post-hydrogenation annealing steps up to 170 °C. Going one step further, this chapter presents results of investigations regarding the metallization of FPCs. As stated previously, the ultimate motivation behind FPCs is to enable a solar cell architecture fabricated with a low thermal budget and a lean process flow, as illustrated in Fig. 1.10. Colleagues at CSEM and Meyer Burger Technology AG developed PECVD $\text{SiN}_x\text{:H}$ reservoir layers optimized for hydrogen diffusion during a firing step (as opposed to the hotplate treatment applied so far) [Ingenito et al., 2021], [Haug et al., 2021c]. Note that J_0 values of 7 fA/cm² were reported using this hydrogenation process on $\text{SiC}_x(p)$ based FPC stacks [Ingenito et al., 2021]. This value is as good as the ones obtained for tunneling oxides in section 3.5 with hotplate hydrogenation, indicating that the FPCs, optimized for fabrication during a firing step, are not prone to the formation of platelets, speculated to be at the origin of passivation losses upon firing in the presence of excess hydrogen, as discussed in section 4.6.

Using these $\text{SiN}_x\text{:H}$ reservoir layers optimized for hydrogen diffusion during a firing step, combined hydrogenation of FPC rear stacks and their metallization by firing-through of screen printed metal paste was investigated. To do so, highly doped presupposed $\mu\text{c-Si:H}(p)$ layers were deposited on top of the $\text{SiC}_x(p)$, as thicker layers are required to stop the paste during firing-through and avoid it punching through the tunneling oxide layer, damaging the passivation [Çiftipinar et al., 2017], [Duttagupta et al., 2018], [Bivour et al., 2017], [Stodolny

et al., 2016]. The idea behind this double layer stack being to enable good electrical contact thanks to the $\mu\text{c-Si:H}(p)$ layer, while still having the excellent passivation provided by the $\text{SiO}_x/\text{SiC}_x(p)$ stack. Indeed, the addition of carbon was reported to hinder crystallization (see appendix A). Hence, higher crystallinity is expected for the $\mu\text{c-Si:H}(p)$ layer, enabling higher active dopant concentrations and therefore lower contact resistivities [Haug et al., 2019], [Seif et al., 2016]. Moreover, the higher carbon content in the $\text{SiC}_x(p)$ layer might help stopping the paste during firing-through [Viala et al., 1990], hence preserving high passivation levels. Motivated by this publication and the excellent stability of the $\text{nc-SiC}_x(p)$ layer against thermal and chemical treatments observed so far, metallizing the FPC by firing-through of screen printed aluminium paste was tested. If successful, this would represent a significant cost reduction compared to commonly used Ag or AgAl pastes [Riegel et al., 2012].

Unfortunately, despite the absence of CH_4 in the precursor gas mix and an H_2/SiH_4 dilution ratio > 130 , the presupposed microcrystalline layer turned out to be amorphous, even after firing. Therefore, the presupposed $\text{SiC}_x(p)/\mu\text{c-Si:H}(p)$ stack will be referred to as $\text{SiC}_x(p)/\text{a-Si:H}(p)$ in the following. Note that the amorphous nature of this layer was a late finding, that retrospectively explained some of the results. Indeed, this layer had been used before in annealed HTPCs and had been found to be microcrystalline. Why it grew and stayed amorphous in the present case is unknown so far.

The first part of this chapter focuses on the development of firing stable $\text{SiC}_x(p)/\text{a-Si:H}(p)$ layer stacks, as the increasing layer thickness lead to blistering issues. In the second part, a detailed investigation of the firing-through process is presented; and the third part discusses the use of evaporated aluminium instead of screen-printed pastes for contact formation. Ideally, one would reach $\rho_c < 100\text{m}\Omega\text{cm}^2$, without damaging the passivation. Indeed, Schmidt *et al.* reported no loss in efficiency for full area passivating contacts featuring such low ρ_c values [Schmidt et al., 2018]. Finally, first results on solar cells featuring co-fired FPCs ($\text{SiC}_x(p)$ at the rear and $\text{SiC}_x(n)$ at the front) are shown.

6.2 Experimental details

The wafers used for these studies were boron-doped, FZ, (100) oriented, with a SE or DSP surface finish and a diameter of 10 cm. The SE wafers have a thickness of $200\mu\text{m}$ and a resistivity of $2\Omega\text{cm}$, whereas the DSP wafers are $280\mu\text{m}$ thick and have a resistivity of $3\Omega\text{cm}$. As in the previous experiments, the wafers were chemically cleaned, and a 1.3 nm thin tunneling oxide grown at the surfaces, either chemically (HNO_3 , 69%, 80°C , 10 min) or by exposing the wafer to UV radiation in ambient air (2–3 min each side). Next, the rear side was capped with an $\text{a-SiC}_x(p)$ layer, and the front with an $\text{a-SiC}_x(p)/\text{a-Si:H}(p)$ stack. All these layers were deposited by PECVD in the "Kai-M" reactor, at 200°C . For the $\text{SiC}_x(p)$ layers, the pressure was 0.7 mbar, and SiH_4 , H_2 , CH_4 and $\text{B}(\text{CH}_3)_3$ were used as precursor gases, with an H_2 flux slightly higher than the SiH_4 flux and a deposition time of 45–90 s. The recipe for the highly doped $\text{a-Si:H}(p)$ layers consists of a pressure of 6.5 mbar, using SiH_4 , H_2 , and $\text{B}(\text{CH}_3)_3$ as precursor gases, with

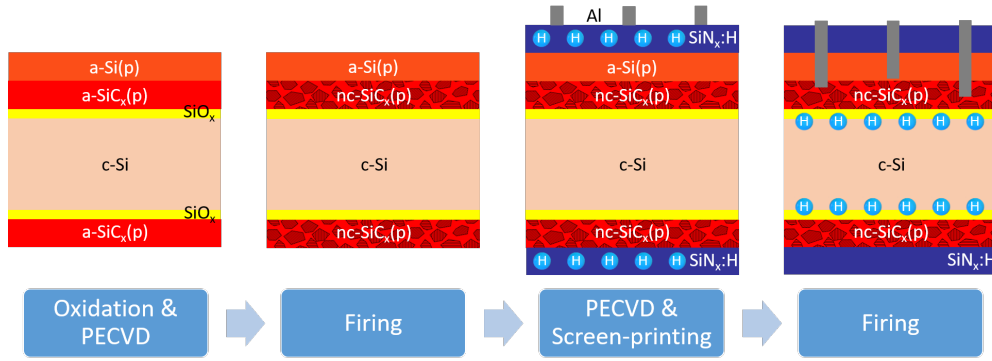


Figure 6.1 – Fabrication process for firing-through test samples featuring $\text{SiC}_x(p)/\text{a-Si:H}(p)$ layer stacks at the front side.

an H_2 flux more than 100 times higher than the SiH_4 flux and a deposition time of 315–550 s. The samples were subsequently fired for 8 s at 800 °C. This step will be called "pre-firing" in the present chapter. Following that, $\text{SiN}_x\text{:H}$ layers were deposited by PECVD on both sides. These layers were deposited according to recipes developed by colleagues at CSEM and Meyer Burger Technology AG, optimized either for hydrogen release during firing or to act as ARC. Metallic contacts were then deposited on the front side, by screen printing of commercial aluminium pastes or evaporation of aluminium. The used masks contained TLM pads to measure contact resistivity and in some cases up to five $15 \times 21 \text{ mm}^2$ pads of $\sim 70 \mu\text{m}$ wide fingers, to evaluate passivation damage by PL imaging (see Fig. 2.3a). Finally, the samples were fired a second time, in a Meyer Burger Camini ceramic roller furnace, with a peak temperature set to 830 °C and a transport speed of 5 m/s. During this last firing step, the hydrogen was diffused from the $\text{SiN}_x\text{:H}$ reservoir layers to the c-Si/ SiO_x interface, and the metallic contacts fired through the $\text{SiN}_x\text{:H}$ layers into the $\text{SiC}_x(p)/\text{a-Si:H}(p)$ stack below. The fabrication process is illustrated in Fig. 6.1. Note that for some experiments, some adjustments were made compared to the sequence described here. These will be mentioned explicitly in the corresponding result sections.

To assess the passivation quality of the fabricated samples, QSSPC measurements and PL imaging were performed. QSSPC was measured using a Sinton WCT-120 instrument, providing τ_{eff} as function of the MCD, as well as the iV_{oc} at 1 Sun [Kane and Swanson, 1985], [R. Sinton et al., 1996], [Cuevas and Sinton, 1997]. As for PL imaging, it was measured with an in-house built setup. The samples are excited using an Ostech laser with a wavelength of 808 nm, operated with a power of 1.2 Suns, and the images are recorded with a PIXIS Princeton instrument silicon-based camera.

Spectroscopic ellipsometry and Raman spectroscopy were used to assess the layer thicknesses and crystallinities, respectively. FTIR measurements were performed to assess the hydrogen content of the samples. Further characterizations were performed using optical microscopy, SIMS, SEM and TEM. SIMS measurements were performed using a 1 keV Cs^+ primary ion beam. Elements were analyzed as MCs_2^+ . Ions were collected from an area of $33 \mu\text{m}$ in diameter.

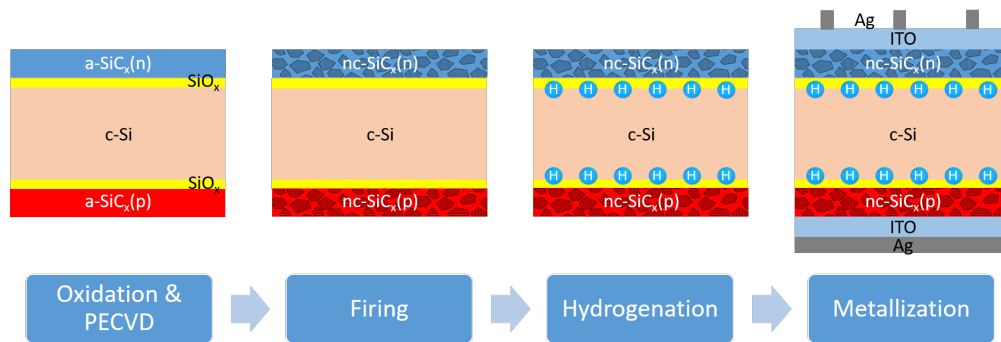


Figure 6.2 – Fabrication process for a low thermal budget solar cell, featuring FPCs on both front and rear side, and metallized via a low temperature approach.

For TEM, the samples were analyzed using a Tecnai Osiris microscope from Thermo Fisher Scientific, which was operated at 200 kV in STEM mode. EDX chemical maps were obtained using a super-X system featuring 4 silicon-drift detectors.

The contact resistivity was measured by TLM. Two different patterns were used. The first one, used for screen-printing, was made of 6 pads, being 12.5 mm wide and 1.45 mm long, and separated by 0.27, 0.41, 0.61, 0.81 and 1.01 mm. Note that actually the pattern is made of 9 pads (see Fig. 2.3a), but due to inhomogeneity in the print the first three pads are most often in contact with each other. The second one, used for evaporation, featured 10 pads, being 6 mm wide and 1.6 mm long, and separated by 0.25, 0.5, 1.0, 1.5, 2.0, 2.5, 3.0, 4.0 and 5.0 mm.

Solar cells were fabricated on boron-doped, (100), 190 μm thick FZ wafers, with a resistivity of 2 Ωcm . The rear side has a SE surface finish, while the front side is textured. The tunneling oxide was grown by a 4 min long UV exposure. FPC were deposited on both sides, $\text{SiC}_x(p)$ at the rear, and an $\text{SiC}_x(n)$ layer on the front. Both were deposited in the "Kai-M" reactor, at 200 $^\circ\text{C}$, a pressure of 0.7 mbar and with an excitation power of 160 W. The recipe for $\text{SiC}_x(p)$ layer is identical to the one given above. As for $\text{SiC}_x(n)$ layers, it consists of several stages with varying gas flows of SiH_4 , H_2 , CH_4 and PH_3 . The total deposition time is of 50 s and the resulting layer is ~ 20 nm thick. The samples were then fired for 8 s at 800 $^\circ\text{C}$. To hydrogenate the FPCs, $\text{SiN}_x\text{:H/D}$ layers were deposited by PECVD on both sides, followed by a 30 min long hotplate treatment at 450 $^\circ\text{C}$. These $\text{SiN}_x\text{:H/D}$ reservoir layer were then removed by dipping the samples for 12 min in an HF 5% solution. Directly after this step, the contacts were metallized by sputtering ITO on the front side, and ITO/Ag on the rear. Fingers were screen printed on the front side using a low-temperature Ag paste, cured for 30 min at 130 $^\circ\text{C}$. The fabrication process is illustrated in Fig. 6.2. The finished cells, shown in Fig. 2.3b, were characterized by J-V measurements.

In addition to these cells with double side ITO/Ag metallization, Al evaporation on the rear $\text{SiC}_x(p)$ layer was tested. The fabrication process stayed the same until the PECVD of $\text{SiN}_x\text{:H/D}$. For one type of cells, the samples then underwent hydrogen diffusion on a hotplate at 450 $^\circ\text{C}$, followed by removal of the $\text{SiN}_x\text{:H/D}$ reservoir layers in an HF 5% solution. Then, aluminium

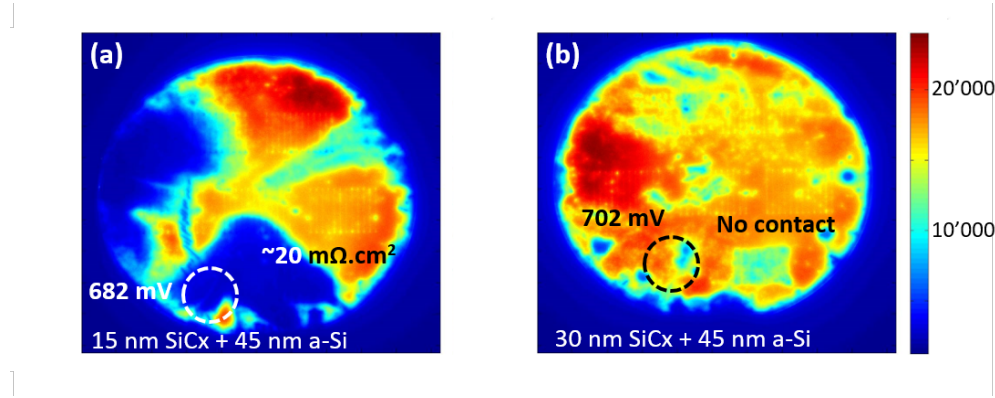


Figure 6.3 – PL images of samples featuring $\text{SiC}_x(p)/\text{a-Si:H}(p)/\text{SiN}_x\text{:H}$ stacks after firing-through metallization. Sample (a) and (b) differ in thickness of the $\text{SiC}_x(p)$ layer, with 15 nm and 30 nm, respectively. The circles indicate where QSSPC was measured and the resulting iV_{oc} values are given. The corresponding $\tau_{\text{eff}@10^{15}\text{cm}^{-3}}$ are 373 μs and 438 μs for (a) and (b), respectively. Moreover, the ρ_c measured by TLM is indicated on top of the metallic pads.

was evaporated on the rear side, followed by ITO sputtering on the front. Part of them were standard $2 \times 2 \text{ cm}^2$ cells, whose Ag fingers were then screen printed using a low-temperature Ag paste, cured for 30 min at 130°C . Others were $1 \times 1 \text{ cm}^2$ cells, as illustrated in Fig. 2.3c, for which the fingers and the bus bar were deposited by sputtering Ag through a mask. Obviously, this design is much less optimized, leading to 18–25% shading losses. In another type of cells, no $\text{SiN}_x\text{:H/D}$ layer was deposited on the rear side. Instead, aluminium was directly evaporated on the $\text{SiC}_x(p)$. Hydrogenation then happened by diffusing hydrogen (and deuterium) from the front $\text{SiN}_x\text{:H/D}$ reservoir layer to both interfaces and the bulk, as investigated in section 4.6. This front $\text{SiN}_x\text{:H/D}$ layer was subsequently removed by placing it over a beaker filled with an HF 50% solution, leading to a single sided etch by vapor HF. After this, the front $\text{SiC}_x(n)$ was contacted by ITO sputtering and screen printing of Ag fingers, followed by a curing for 30 min at 130°C .

6.3 Thick firing stable layers

In the first experimental runs, various thicknesses of the $\text{SiC}_x(p)$ and $\text{a-Si:H}(p)$ layers were tested. Blistering occurred during the pre-firing for $\text{a-Si:H}(p)$ thicknesses $\geq 45 \text{ nm}$. The PL images after hydrogenation and firing-through of two selected samples are shown in Fig. 6.3, along with the results of QSSPC and TLM measurements. As one can see, the resulting passivation is decent if the layers stayed intact, with lifetimes up to 815 μs (719 mV iV_{oc}). This record test sample was processed identically to the one in Fig. 6.3b, with a 30 nm $\text{SiC}_x(p)$ and 45 nm $\text{a-Si:H}(p)$ deposited on top of a UV- O_3 SiO_x . Despite the variations in achieved passivation, this layer combination seemed the most promising. Regarding passivation damages through metallization, the fingers are only slightly visible in the top part of the PL images, which is encouraging. However, the PL signal is much lower beneath the metallic pads for TLM

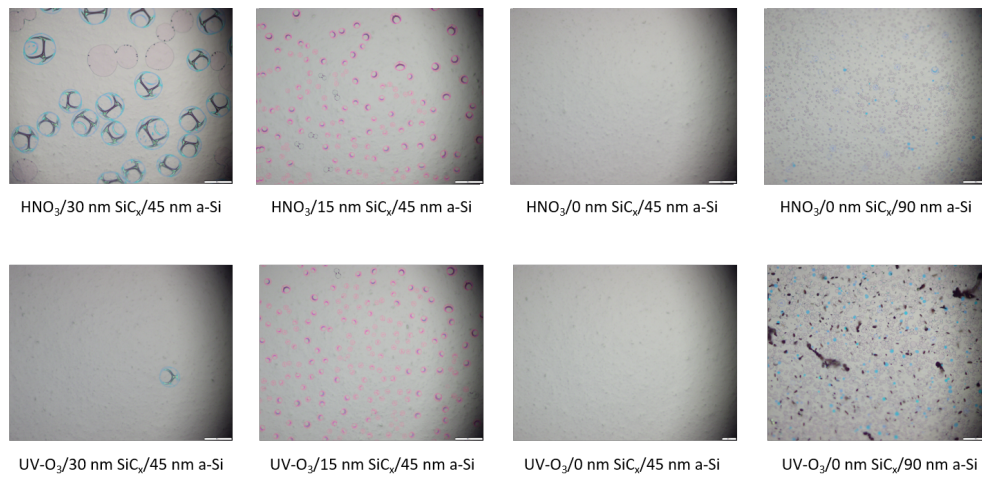


Figure 6.4 – Images of the blistering taken by optical microscopy after firing. The samples differed in type of the tunneling oxide, either grown chemically (HNO₃) or by exposing the wafer to UV radiation (UV-O₃), as well as thicknesses of the SiC_x(*p*) and a-Si:H(*p*) layers. The scale bar in the bottom right of each image is equivalent to 100 μm.

measurements, indicating that the firing-through process damaged the passivation. Despite this, no electrical current could be measured for the sample shown in Fig. 6.3b. In contrast, 20 mΩcm² were measured for the sample in Fig. 6.3a. Since blistering was observed after firing-through in the region around the TLM pad (dark blue area in the PL image shown in Fig. 6.3a), these 20 mΩcm² likely correspond to direct contact between the Al paste and the c-Si wafer. This conclusion is supported by the contact resistivity values reported by Allen *et al.* for screen printed Al and Ag/Al pastes on silicon with a surface dopant concentration around $7 \cdot 10^{15} \text{ cm}^{-3}$ (corresponding to wafer resistivities of 2 Ωcm) [Allen et al., 2019]. Further investigations on the issue of firing-through metallization will be presented later in this chapter. As for the blistering, one observes that in the case of the samples shown in Fig. 6.3, the one with a 30 nm thick SiC_x(*p*) layer stayed intact, while the one with 15 nm blistered. This is surprising and hence the blistering issue was studied in more detail.

To do so, samples with 30 nm and 15 nm thick SiC_x(*p*) layers, capped with 45 nm of a-Si:H(*p*), were processed, as well as 45 nm and 90 nm thick a-Si:H(*p*) without SiC_x(*p*) layer; all of them on chemical SiO_x (HNO₃) and UV-O₃ SiO_x. After PECVD, they were pre-fired and subsequently observed under an optical microscope. The results are shown in Fig. 6.4. As one can observe, the 45 nm thick a-Si:H(*p*) layer alone does not blister. From the previous chapters we know that the 30 nm thick SiC_x(*p*) layer alone does not blister either. However, they do when put together. In the case of the 30 nm SiC_x(*p*)/45 nm a-Si:H(*p*) stack, the layers stayed mainly intact upon pre-firing when deposited on UV-O₃ SiO_x, providing further incentive to continue the testing using this stack.

Since the SiC_x(*p*)/a-Si:H(*p*) stacks blister, while each layer alone does not (as long as it is not grown too thick), the question arose whether both layers pop off the wafer upon pre-firing, or

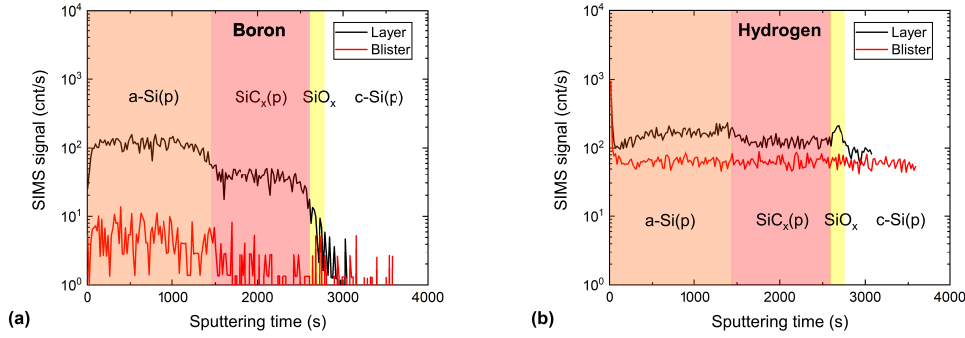


Figure 6.5 – Boron (a) and Hydrogen (b) profiles measured by SIMS on fired $\text{SiC}_x(p)/\text{a-Si:H}(p)$ stacks. The black curves were measured in a spot where the layers were intact, while the red curves were measured inside a blister. The orange, red and yellow regions highlight the $\text{a-Si:H}(p)$, $\text{SiC}_x(p)$ and SiO_x layers, respectively, for the measurement where they were intact.

if the hydrogen effusing from the $\text{SiC}_x(p)$ delaminates the $\text{a-Si:H}(p)$ layer above it. To answer this, SIMS measurements were performed on such blistered layers, comparing profiles taken inside a blister to such taken on regions where the layers were intact. As can be observed in Fig. 6.5a, two separate boron-rich regions can be distinguished, representing the $\text{SiC}_x(p)$ and $\text{a-Si:H}(p)$ layers. However, for the profile measured inside the blister, the SIMS signal stays low, indicating that both layers delaminated. Since the 90 nm thick $\text{a-Si:H}(p)$ layer in Fig. 6.4 blistered too, it may be concluded that the total layer thickness ($\text{SiC}_x(p) + \text{a-Si:H}(p)$) has to stay below a critical value to avoid blistering. Fig. 6.5a also shows a higher boron content for the highly doped $\text{a-Si:H}(p)$ layer than for the $\text{SiC}_x(p)$, as expected. However, Fig. 6.5b shows that it also has a higher hydrogen content, which was the first clue towards this presupposed $\mu\text{c-Si:H}(p)$ layer actually being amorphous, since the hydrogen content decreases when the layer crystallinity increases. Therefore, a closer look was taken at the properties of these layers.

A bright field STEM image of a $\text{c-Si}/\text{SiC}_x(p)/\text{a-Si:H}(p)/\text{SiN}_x\text{:H}$ stack after hydrogenation is shown in Fig. 6.6. A first observation is that the $\text{SiC}_x(p)$ layer is much thicker than expected: instead of the targeted 30 nm, it is actually 48 nm thick. The two boron-doped layers are therefore of similar thickness. Secondly, knowing that crystallites appear darker in such a bright field STEM image, the homogeneously bright aspect of the presupposed $\mu\text{c-Si:H}(p)$ layer indicates that it actually stayed amorphous, despite two firings, whereas the $\text{SiC}_x(p)$ crystallized. These findings were confirmed by Raman spectroscopy measurements (presented in the next paragraph). The used recipe to deposit the presupposed $\mu\text{c-Si:H}(p)$ therefore does not provide a microcrystalline layer, but rather a boron and hydrogen rich amorphous layer ($\text{a-Si:H}(p)$), that does not crystallize upon firing. Carbon profiles measured by SIMS indicate slightly higher carbon content for the $\text{a-Si:H}(p)$ than the $\text{SiC}_x(p)$, which is likely the reason why it stays amorphous. Therefore, further development of the PECVD recipe would be necessary to actually deposit a microcrystalline layer.

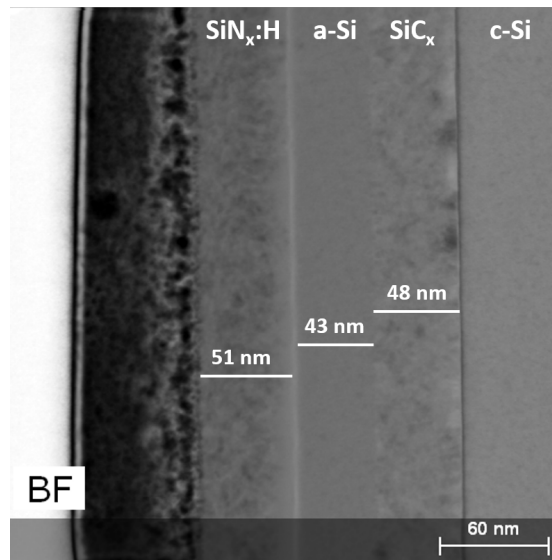


Figure 6.6 – Bright field image of a $\text{SiO}_x/\text{SiC}_x(p)/\text{a-Si:H}(p)/\text{SiN}_x\text{:H}$ stack taken in STEM mode. The measured layer thicknesses are indicated on the respective layers.

In addition to STEM images, FTIR and RS measurements were performed to characterize the $\text{SiC}_x(p)/\text{a-Si:H}(p)$ stacks. This was done in the as deposited state, after a subsequent thermal treatment of 10 min at 500 °C, and after an additional pre-firing (8 s at 800 °C). This "plateau" at 500 °C was introduced to provide further insight in the blistering mechanisms. Indeed, as shown in Fig. 6.7 hydrogen effuses from layers at this temperature (Si-H peaks in FTIR measurements disappear), whereas the crystallinity of the layers is not affected (RS spectra do not change). The introduction of this additional thermal plateau helped significantly reducing blistering, indicating that rapid hydrogen effusion during firing is most likely its cause, rather than strain due to changes in crystallinity. Regarding layer properties, the FTIR measurements in Fig. 6.7a additionally show an increasing Si-C peak intensity upon thermal treatments, as previously observed by [Ingenito et al., 2018], indicating chemical rearrangements. However, the strong Si-O peak in the as-deposited state was not observed by Ingenito *et al.* and remains to be investigated. The slight CO_2 peak is due to residual air in the sample compartment of the spectrometer. As for the RS measurements, they indicate crystallization of the layer stack upon pre-firing. The shown spectra were taken with a blue laser (442 nm), which penetrated the whole stack, as indicated by the sharp c-Si peak coming from the wafer below. Fitting these peaks yields crystallinity fractions of 11% before and 27% after firing. Doing the same on measurements taken with a UV laser (325 nm), probing only the top 15–20 nm of the material, *i.e.* only the $\text{a-Si:H}(p)$ layer, yields crystallinity fractions of 1% before and 5% after firing. These values have to be taken with care, since the measurements were quite noisy. However, they indicate that the $\text{a-Si:H}(p)$ layer stayed amorphous, while the $\text{SiC}_x(p)$ crystallized, confirming the observation made by TEM in Fig. 6.6.

As stated above, the introduction of an additional thermal treatment of 10 min at 500 °C

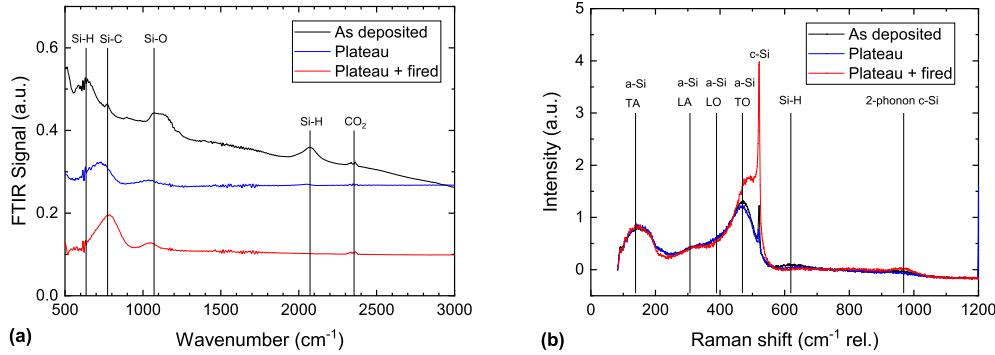


Figure 6.7 – (a) FTIR measurements of a $\text{SiC}_x(p)/\text{a-Si:H}(p)$ stack in the as deposited state, as well as after a 10 min treatment at 500 °C (Plateau) and after such a treatment followed by a firing (8 s at 800 °C). The vertical lines indicate the wavenumbers at which Si-H, Si-C, Si-O and CO₂ peaks are expected. (b) Corresponding RS measurements (taken using the blue laser). The vertical lines indicate the wavenumber shifts at which a-Si, c-Si, Si-H and 2-phonon-c-Si peaks are expected. The abbreviations TA, LA, LO and TO stand for Transverse Acoustic, Longitudinal Acoustic, Longitudinal Optical and Transverse Optical, respectively, which are various vibrational modes of the Si-Si bonds in amorphous silicon.

significantly reduces blistering. Therefore, six samples featuring 30 nm $\text{SiC}_x(p)/45$ nm $\text{a-Si:H}(p)$ stacks on top of UV-O₃ SiO_x were processed and pre-fired with such a 500 °C plateau included before the firing peak, followed by $\text{SiN}_x\text{:H}$ deposition and firing-through metallization. From these samples, 5 out of 6 remained blister-free. The passivation and contact resistivity values, measured by QSSPC and TLM, are given in table 6.1 (the blistered sample was n°3). As one can see, all displayed promising passivation results, with $\tau_{\text{eff}@10^{15}\text{cm}^{-3}} > 500 \mu\text{s}$ and $iV_{\text{oc}} > 709 \text{ mV}$. However, the contact resistivity values seem totally random, going from 26 mΩcm² to not measurable, indicating that in some cases the metallic paste most likely penetrated the whole stack and contacted directly the c-Si wafer below, while in other cases it did not even fire through the whole $\text{SiN}_x\text{:H}$ layer. Therefore, a closer investigation of this firing-through process was undertaken, and will be presented in the next section.

6.4 Firing through

To study the metallization, STEM images of cross-sections below the fired-through fingers were taken. Two lamellae were prepared out of a sample featuring a 30 nm $\text{SiC}_x(p)/45$ nm $\text{a-Si:H}(p)$ stack deposited on a UV-O₃ SiO_x, capped with $\text{SiN}_x\text{:H}$ and metallized by screen-printed and fired-through aluminium paste. The chemical mapping showed the presence of many elements within the paste alongside aluminium, such as lead, iron, gallium, copper, molybdenum and chlorine. Selected images are shown in Fig. 6.8 and Fig. 6.9. As can be observed, the aluminium did not spike through the $\text{SiN}_x\text{:H}$ layer, but replaced the Si within

Table 6.1 – Results of QSSPC (passivation) and TLM (contact resistivity) measurements for $\text{SiC}_x(p)/\text{a-Si:H}(p)$ stacks that were annealed for 10 min at 500 °C, subsequently fired (8 s at 800 °C), capped with an $\text{SiN}_x\text{:H}$ layer and finally hydrogenated and metallized by firing-through of a screen-printed Al-paste.

Sample	$\tau_{\text{eff}@10^{15}\text{cm}^{-3}}$ (μs)	iV_{oc} (mV)	ρ_c ($\text{m}\Omega\text{cm}^2$)
1	555	711.3	26
2	540	709.8	∞
3	793	712.4	104
4	546	710.1	1120
5	576	710.9	∞
6	833	717.1	∞

it, forming an Al-N compound. The lateral distribution of aluminium within the former $\text{SiN}_x\text{:H}$ layer is homogeneous. However, the diffusion depth varies. In Fig. 6.8 the diffusion of aluminium stopped within the $\text{SiN}_x\text{:H}$ layer, while it went through it in Fig. 6.9 and diffused into the a-Si:H(*p*) below. These two sets of images were taken on the two different lamellae, but similar variations could be also observed within a single lamella. Despite the conductivity of the Al-N compound being unknown so far, these results point towards a bad contact between the aluminium fingers and the a-Si:H(*p*) layer, providing an explanation for the samples where no contact could be measured.

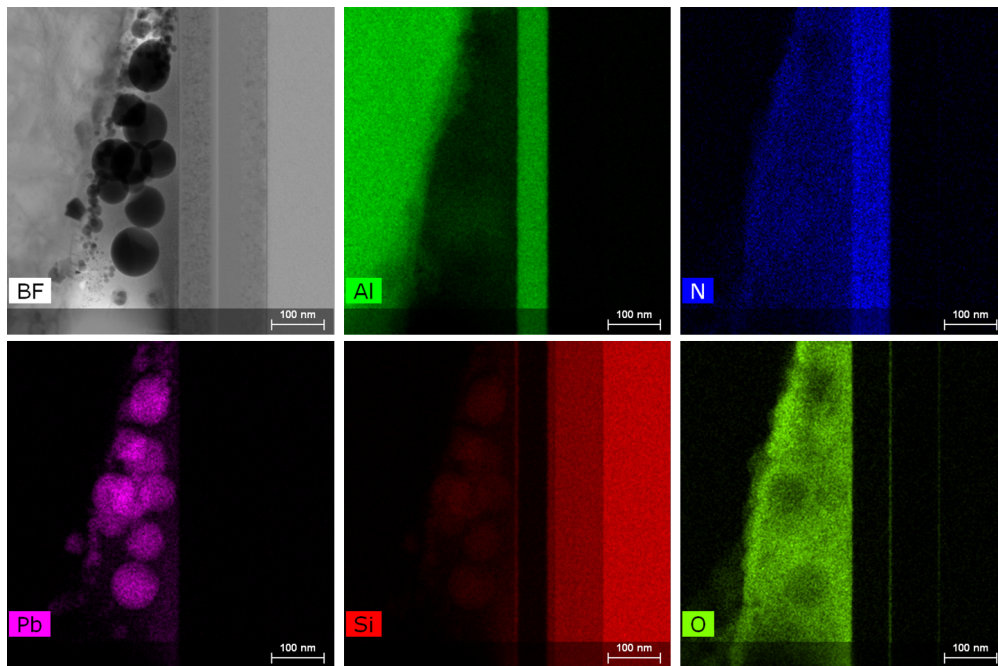


Figure 6.8 – STEM bright field (BF) image and EDX maps for aluminium (Al), nitrogen (N), lead (Pb), silicon (Si) and oxygen (O) of a metallized $\text{SiO}_x/\text{SiC}_x(p)/\text{a-Si:H}(p)/\text{SiN}_x\text{:H}$ stack.

Joonwichien *et al.* also observed such a diffusion of aluminium into SiN_x layers [Joonwichien et

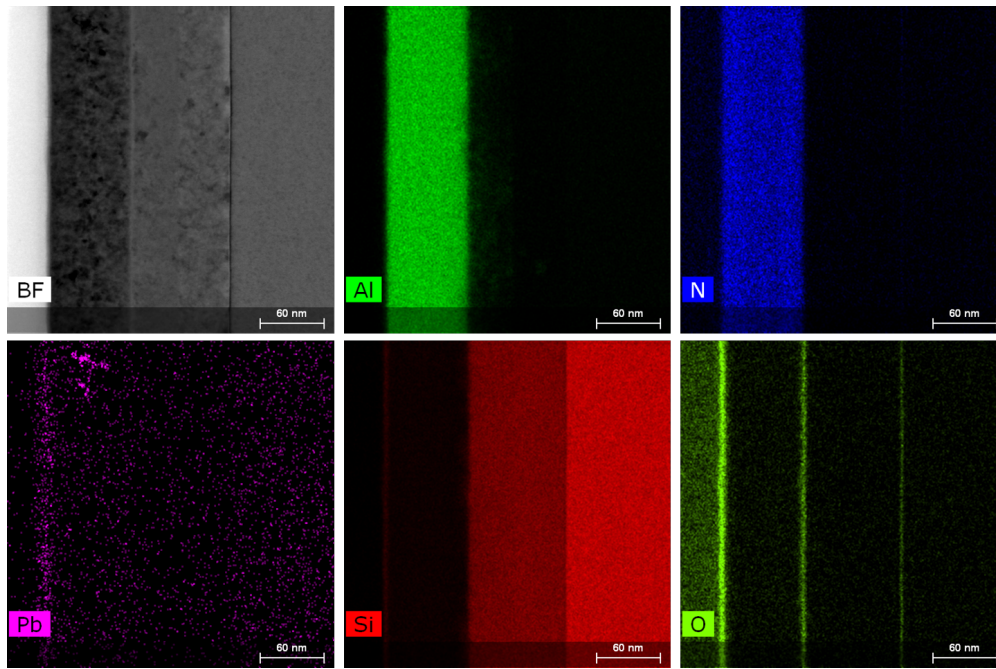


Figure 6.9 – STEM bright field (BF) image and EDX maps for aluminium (Al), nitrogen (N), lead (Pb), silicon (Si) and oxygen (O) of a metallized $\text{SiO}_x/\text{SiC}_x(p)/\text{a-Si:H}(p)/\text{SiN}_x\text{:H}$ stack. The images were taken in a different region of the same sample as those in Fig. 6.8.

al., 2019]. As in our case, Al replaced Si within the layer and homogeneous lateral diffusion was observed. In their experiment, the samples featured a stack of two SiN_x layers with different refractive indices. Interestingly, Al diffused into the layer with $n = 2.7$, but not into the one with $n = 2.1$. Song *et al.* also reported strong dependence on the refractive index of the SiN_x layer for the firing-through of aluminium pastes [Song et al., 2012]. These results highlight the importance of controlling the properties of the $\text{SiN}_x\text{:H}$ layer, as well as of the poly-Si layers below, to fine-tune the firing-through process.

For samples with $\rho_c \sim 20 \text{ m}\Omega\text{cm}^2$, interpreted as direct contact between the Al and c-Si wafer, a possible explanation comes from the SEM image shown in Fig. 6.10. It shows a tilted view of a finger cross-section, obtained by cleaving the sample. As can be seen, the finger consists of aluminium particles packed together. The $\text{SiN}_x\text{:H}$ layer on the surface of the wafer shows contrasts in color. Brighter circles can be observed. They seem to form around points where an aluminium particle is in contact with the layer, as can be seen in the right part of the image. In the bottom part, where the aluminium particles are missing (probably they were mechanically removed in the cleaving process), some sort of droplet lies in the middle of the bright circles. These droplets are most likely originating from aluminium molten during firing.

In a further experiment, performed by my colleague Sofia Libraro, the aluminium fingers and the $\text{SiN}_x\text{:H}$ layer were etched away by dipping the sample in HCl and HF solutions, and SEM images and EDX chemical mappings were taken in top view. These results, shown in Fig. 6.11,

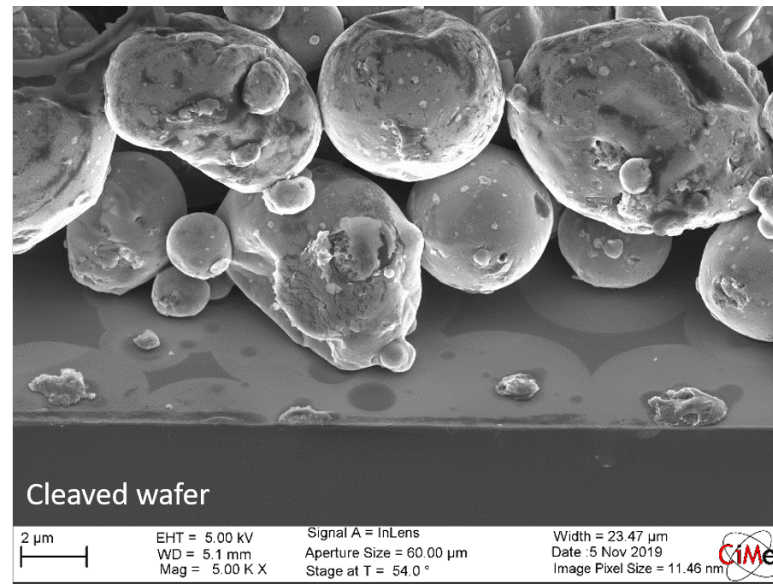


Figure 6.10 – Tilted view SEM image of a screen-printed fired-through aluminium paste finger. The sample has been cleaved perpendicularly to the printed fingers.

feature aluminium and nitrogen rich circles, with a silicon rich crater in the middle. Combining these results with the observations made in Fig. 6.10, one can conclude that the bright circles are regions where Al replaced Si within the $\text{SiN}_x\text{:H}$, forming an Al-N compound, and that the droplets visible in their center punched through the $\text{SiN}_x\text{:H}$ layer into the silicon rich layers or even the c-Si wafer below. This might explain the low contact resistivities measured for some samples.

Regarding the measured ρ_c values, it has to be mentioned that the interaction of the metallic paste with the layers beneath it is not the same in the case of fingers and the larger TLM pads. Fig. 6.12 shows top view SEM images of such regions after etching off the aluminium and the $\text{SiN}_x\text{:H}$. As can be observed, the regions below the pads feature more bright circles and craters than those below the fingers. Hence, the contact resistivity of the fingers is most likely higher than the one measured by TLM.

In a further experiment, performed in collaboration with my colleague Sofia Libraro, firing-through of evaporated (instead of screen printed) aluminium contacts was tested. The results were presented with a poster at the 2021 online "Microscopy Conference" [Libraro et al., 2021]. Here too, Al replacing Si within the $\text{SiN}_x\text{:H}$ layer was observed. As for the contacts, they featured a trade-off between passivation and contact resistivity: all samples with $\rho_c < 100 \text{ m}\Omega\text{cm}^2$ (approximate limit above which the FF deteriorates significantly) showed dramatic loss in PL signal under the metallic pads. STEM images and chemical mapping were taken on these samples too (see Fig. 6.13). For the sample shown in Fig. 6.13, the Al diffused entirely through the $\text{SiN}_x\text{:H}$ and into the a-Si:H(p) layer below. It seems that Al replaced Si also in the latter. However, the $\text{SiC}_x(p)$ layer apparently blocked the Al diffusion, except for a spike visible on

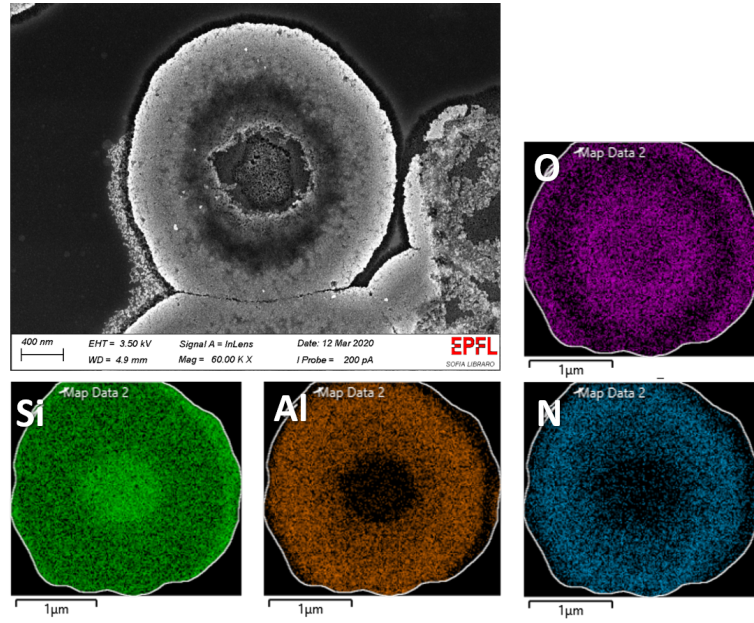


Figure 6.11 – Top view SEM images and EDX maps of metallized regions (fingers) after etching away aluminium and $\text{SiN}_x\text{:H}$ in HCl and HF solutions, respectively. Courtesy of Sofia Libraro.

the right of the images. This is an encouraging finding, as it corroborates the hypothesis that higher carbon content in the $\text{SiC}_x(p)$ layer might help stopping the paste during firing-through. Unfortunately, the chemical mapping shows also aluminium accumulation at the SiO_x layer, which likely damages the passivation. Indeed, Sharma *et al.* reported that Al reacts with the SiO_x , forming AlO_x , which degrades the surface passivation [Sharma et al., 2022].

As can be concluded from all these results, the firing-through process is not yet fully understood and mastered, leading to the random variations in measured ρ_c reported in table 6.1. Further development of this process seemed to require a workload beyond the scope of this thesis and was therefore taken over by my colleague Sofia Libraro.

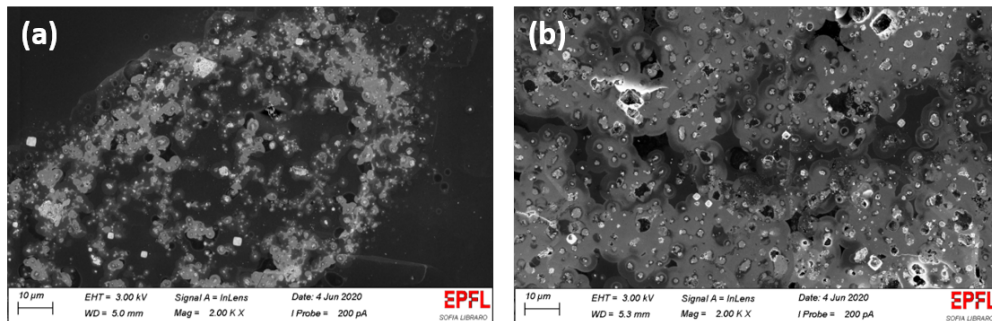


Figure 6.12 – Top view SEM images of finger and TLM pad regions after etching away aluminium and $\text{SiN}_x\text{:H}$ in HCl and HF solutions, respectively. Courtesy of Sofia Libraro.

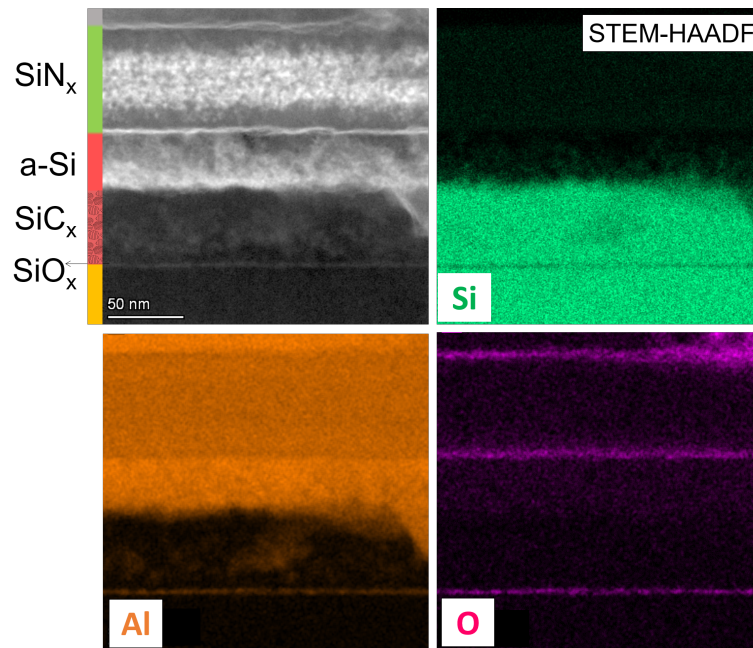


Figure 6.13 – STEM images and chemical mappings of a $\text{SiO}_x/\text{SiC}_x(p)/\text{a-Si:H}(p)/\text{SiN}_x\text{:H}$ stack contacted with fired-through evaporated aluminium fingers. Adapted from [Libraro et al., 2021].

6.5 Aluminium evaporation

Since the firing-through of aluminium pastes resulted either in bad contact or in passivation damages, contacting the $\text{SiC}_x(p)/\text{a-Si:H}(p)$ stacks directly with evaporated aluminium was tested. Indeed, removing the necessity to fire through a $\text{SiN}_x\text{:H}$ layer allows avoiding a high temperature treatment after Al deposition, reducing the risk of passivation damages due to Al diffusion or spiking. Moreover, PVD substantially reduces mechanical and thermal impact on the wafer compared to screen printing and firing-through [Balaji et al., 2019]. In addition, good contact resistances were reported for sputtered aluminium on $\text{a-Si:H}(p)$ followed by a 20 min long sintering at 180°C ($48\text{ m}\Omega\text{cm}^2$) [Bryan et al., 2021] and evaporated aluminium on p -type c-Si ($< 1\text{ m}\Omega\text{cm}^2$) [Y. Chen et al., 2015] with only little degradation of the passivation. My former colleague Josua Stuckelberger also obtained $\rho_c < 100\text{ m}\Omega\text{cm}^2$ by evaporating aluminium on highly doped $\text{nc-Si}(n)$ layers (without subsequent sintering) [Stuckelberger et al., 2016b].

For these tests, samples featuring $\text{SiC}_x(p)/\text{a-Si:H}(p)$ stacks were hydrogenated by depositing $\text{SiN}_x\text{:H/D}$ reservoir layers and diffusing hydrogen during a 30 min hotplate treatment at 450°C . The $\text{SiN}_x\text{:H/D}$ was subsequently removed in a 5% HF solution before evaporating $1 \pm 0.2\text{ }\mu\text{m}$ thick aluminium contacts by electron beam. Six TLM pads were evaporated through masks on each wafer. The wafers were then cleaved, in order to isolate the TLM patterns from each other. Various sintering conditions were tested, trying to find the post-metallization treatment

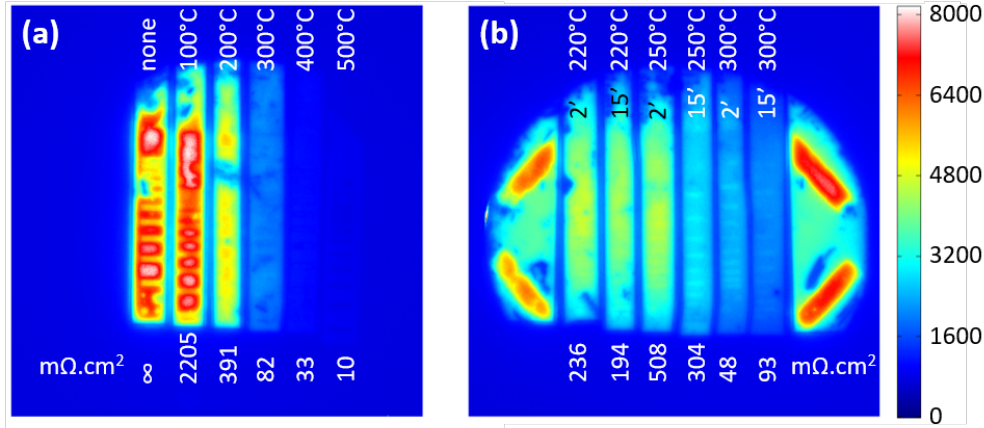


Figure 6.14 – PL images of TLM pads, deposited by aluminium evaporation, after subsequent sintering. The samples in (a) were sintered for 15 min at the temperatures indicated in the top part of the image, while those in (b) were sintered for 2 or 15 min, as indicated in the top part of the image too. The measured values for ρ_c are given below the samples.

leading to the best trade-off between contact resistivity and passivation. Fig. 6.14a shows decreasing ρ_c with increasing sintering temperature, with $\rho_c < 100 \text{ m}\Omega\text{cm}^2$ from 300 °C on. However, the passivation significantly degrades from 300 °C on too, in agreement with the findings reported in chapter 5. Hence, More conditions between 200 °C and 300 °C were tested, as shown in Fig. 6.14b. The most promising option seems to be a 2 min long sintering at 300 °C, which however still yields significant passivation losses. Even shorter sintering times at 300 °C were also tested, but resulted $\rho_c > 100 \text{ m}\Omega\text{cm}^2$, while still showing similar degradation in PL.

Evaporated Al was reported to contact both *n*-type and *p*-type layers [Bryan et al., 2021], [Y. Chen et al., 2015]. Therefore, the results of Stuckelberger *et al.* [Stuckelberger et al., 2016b] strongly suggest that Al evaporation on our *p*-type layers should yield decent contact resistivity without sintering too. The high ρ_c values measured in these experiments for temperatures below 300 °C might be linked to the amorphous nature of the a-Si:H(*p*) layer, leading to low levels of active dopants. As already mention in section 6.3, further development of the PECVD recipe of the a-Si:H(*p*) layer would be necessary to increase its crystallinity, which would most likely improve the contact resistivity.

6.6 Co-fired solar cells

Finally, co-fired solar cells were produced, demonstrating the feasibility of such a low thermal budget approach. In the light of the previous results, several batches were fabricated. All of them feature a nc-SiC_x(*p*) layer at the rear and a nc-SiC_x(*n*) layer at the front, crystallized during a single co-firing step. The a-Si:H(*p*) layer was dropped, as it revealed to remain amorphous so far, impeding good contact with the metal deposited on top. The first batch of

cells, made according to the process flow shown in Fig. 6.2, featured ITO/Ag metallization on both the front and the rear. It serves as a reference process, as it implements a widely used metallization approach giving excellent results on heterojunction cells. For the second batch, the rear nc-SiC_x(*p*) layer was contacted with direct evaporation of aluminium. The third batch featured rear Al and front ITO/Ag too, but the fingers of the metallization grid were deposited by PVD and 1x1 cm² cells were made, instead of the 2x2 cm² cells with screen printed fingers as in the reference process. Finally, in the fourth batch, the rear contact, metallized with evaporated Al, was hydrogenated by diffusing hydrogen (and deuterium) from a SiN_x:H/D layer located at the front, simplifying the fabrication process, as no SiN_x:H/D layer needs to be deposited and subsequently removed on the rear side before Al evaporation.

The finished cells were characterized by J-V measurements. The measured parameters for each batch of cells are given in Fig. 6.15. To our knowledge, this is the first report of a cell with co-fired contacts. As can be observed, the reference cells with ITO/Ag metallization on both front and rear display good properties, with an efficiency of 20.5% achieved for the best cell, demonstrating the potential of such an approach. The J-V curve of this cell is shown in Fig. 6.16a. As expected, they yield excellent electrical properties, with *FF* values up to 80%. As for the current, all *J*_{sc} values were lower than 37 mAcm², most likely limited by parasitic absorption in the front nc-SiC_x(*n*) layer. The *V*_{oc} values, reaching a maximum of 700 mV were lower than expected and will be discussed in more details later on.

Unfortunately, the other two batches with screen printed fingers, featuring evaporated Al at the rear, perform poorly. As can be deduced from the *R*_{SC} values close to zero, these cells seem to be shunted, explaining their low fill factor and efficiency. Their J-V curves are almost linear, as shown in Fig. 6.16b. Most likely, some error was made during processing.

As for the batch with 1x1 cm² cells featuring sputtered fingers, their best cell had an efficiency of 12.7%. Note that the shading losses are much higher for this cell design compared to the one with screen printed fingers, explaining the low *J*_{sc} values. Assuming a *J*_{sc} matching those of the first batch of cells, the efficiency would rise to 14.7%. Looking at their J-V curves (not shown here), the low *FF* seems to be mainly linked to the high *R*_{OC} values, indicating high series resistance. This is likely due to a rather high contact resistivity between the nc-SiC_x(*p*) layer and the evaporated Al at the rear. The measured *V*_{oc} values are also much lower than for the cells with ITO/Ag metallization at both rear and front. The process of evaporation of aluminium at the rear therefore needs further optimization, in order to reduce passivation losses and contact resistivity.

Curing of the finished cells at temperatures between 80 °C and 400 °C was tested. This was done for parts of the cells from the first batch, featuring ITO/Ag metallization on both sides, as well as some of the 1x1 cm² cells. Note that in the case of cells with screen printed fingers, a sintering at 130 °C was already performed to dry the paste. The energy conversion efficiency of all tested cells decreased. In the case of the cells from the first batch, the degradation was only minimal (up to 210 °C), while it was more pronounced for the 1x1 cm² cells with

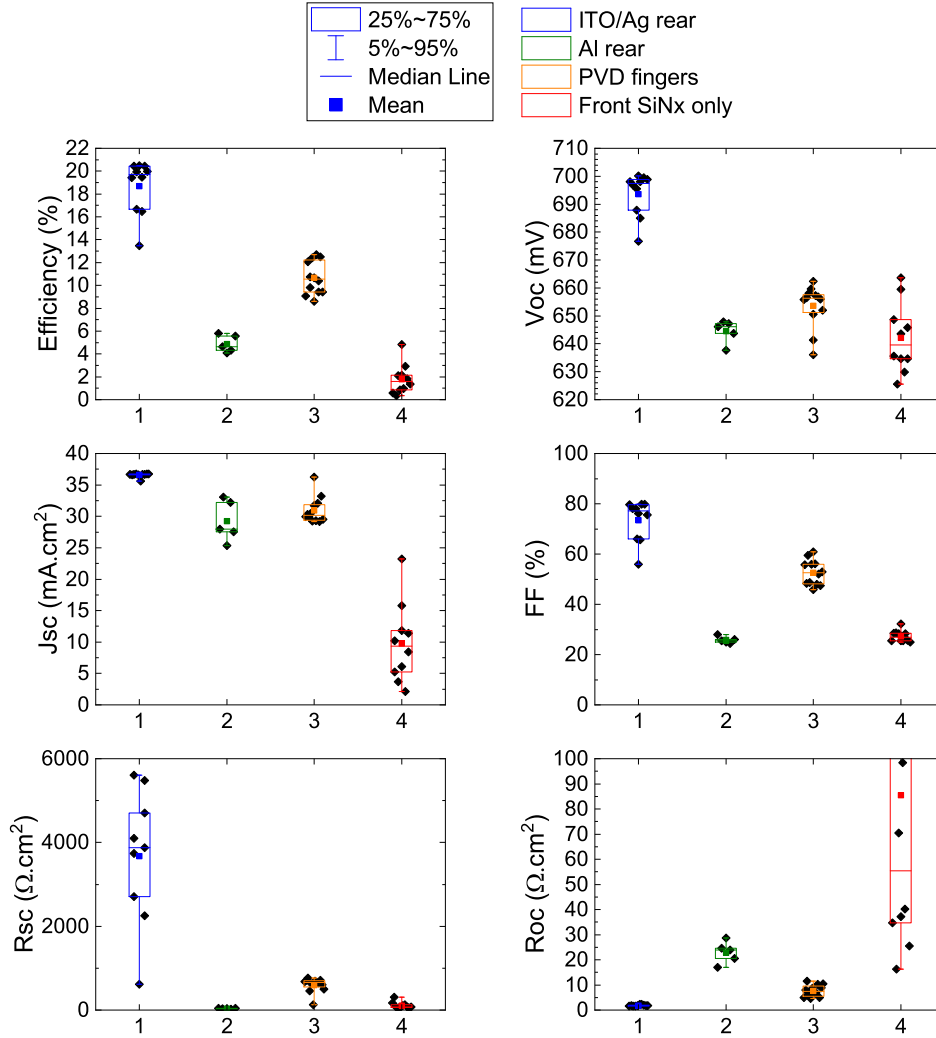


Figure 6.15 – Efficiency, V_{oc} , J_{sc} , FF, short circuit resistance (R_{sc}) and open circuit resistance (R_{oc}) of co-fired cells. Each box plot summarizes the results, measured by J-V, of a batch of similarly processed cells. The first batch consists of 2x2 cm² cells featuring ITO/Ag metallization of both front and rear contact, with screen printed fingers; for the second batch, the rear was contacted with evaporated Al; the third consists of 1x1 cm² cells with evaporated Al at the rear and ITO/Ag at the front, with fingers deposited by PVD; and the fourth batch consists of 2x2 cm² cells again, with evaporated Al at the rear and screen printed fingers on ITO at the front, but featuring an SiN_x:H/D layer at the front only during hydrogenation.

sputtered fingers as shown in Fig. 6.17. For the latter, V_{oc} improved upon sintering, while the FF decreased. Hence, a sintering alone unfortunately does not resolve the issues regarding passivation and contact resistivity for cells with evaporated aluminium on nc-SiC_x(*p*) layers.

Regarding the passivation, all wafers featured iV_{oc} values > 720 mV after hydrogen diffusion with SiN_x:H/D reservoir layers on both sides, and > 700 mV after hydrogenation with SiN_x:H/D

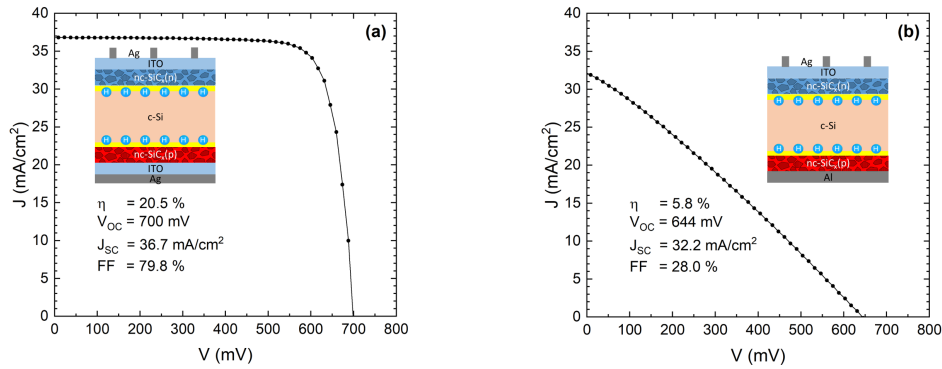


Figure 6.16 – J-V curves of two of the processed co-fired solar cells. (a) Cell with highest efficiency, from the first batch featuring ITO/Ag metallization at both rear and front. (b) Shunted cell from the second batch, featuring evaporated Al at the rear and screen printed Ag fingers on ITO at the front.

on the front side only. The difference between these iV_{oc} values and the V_{oc} of the final cells is shown in Fig. 6.18. The results from previous experiments showed only minor losses in passivation upon removal of the SiN_x-H/D layer in HF (see for example Fig. 3.7a). Hence, it is speculated that most of the losses observed in Fig. 6.18 are due to the metallization process, such as sputtering damage during PVD of ITO [Haschke et al., 2019], [Demaurex et al., 2012], [Zhang et al., 2011]. In the publication by Ingenito *et al.*, the difference between iV_{oc} and V_{oc} for cells featuring FPCs contacted with ITO/Ag was rather in the range of 10 mV [Ingenito et al., 2018]. In our case, the losses are > 30 mV, and are not recovered upon annealing in the case of cells with front and rear ITO/Ag metallization. Feldmann *et al.* also reported significantly lowered iV_{oc} upon ITO sputtering that could only be partially recovered upon annealing for a cell featuring TOPCon contacts on both sides [Feldmann et al., 2014b]. For the presented cells, the ~20 nm thin nc-SiC_x(n) layer might be particularly sensitive to sputter damage. Why the drop is even higher for samples featuring evaporated aluminium at the rear remains an open question. Further investigations are required to understand and mitigate these passivation losses.

6.7 Conclusions

Working towards firing-through metallization, SiC_x(p)/a-Si:H(p) stacks with a total thickness of ~90 nm were developed. When introducing a thermal pre-treatment of 10 min at 500 °C, effusing most of the hydrogen from the layers, these stacks were mostly blister free upon firing for 8 s at 800 °C and reached iV_{oc} values > 709 mV after hydrogenation. However, the contact resistivity after screen printing of Al pastes and firing-through seems to take random values, ranging from 26 mΩcm², interpreted as direct contact between Al and the c-Si wafer,

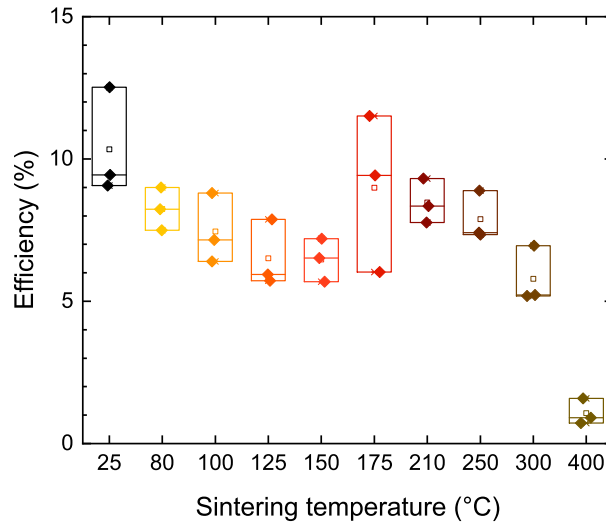


Figure 6.17 – Evolution of the energy conversion efficiency, measured by J-V, upon sintering the finished cells at increasing temperatures. The cells used for this experiment were $1 \times 1 \text{ cm}^2$ cells with evaporated Al at the rear and sputtered Ag fingers on ITO at the front.

to values too high to be measured by TLM, indicating that the paste did not fire through the $\text{SiN}_x\text{:H}$ layer. Closer investigations revealed that Al replaces Si in the $\text{SiN}_x\text{:H}$ layer, forming an Al-N compound. The diffusion of Al sometimes stopped within the $\text{SiN}_x\text{:H}$ layer, while it diffused into the a-Si:H(*p*) layer in other cases. The $\text{SiC}_x(\text{p})$ layer seems to hinder the diffusion of Al, making it a promising layer to stop the paste during firing-through. However, Al accumulation at the tunneling SiO_x was observed, which most likely degrades the passivation. In addition, potential spiking-through of Al was observed in places with direct contact between aluminium particles from the paste and the deposited layers. So far, samples contacted by firing-through featured either high contact resistivity or significant passivation damages due to the metallization. Therefore, evaporation of aluminium directly on the $\text{SiC}_x(\text{p})/\text{a-Si:H}(\text{p})$ layers was tested. Also in this case, good contact was only achieved at the expense of passivation. A potential explanation might be the fact that the a-Si:H(*p*) layer, presupposed to have been grown microcrystalline, was found to be amorphous, even after firing. Further development of its PECVD recipe is therefore needed. For the fabrication of solar cells featuring co-fired FPCs on both sides, this a-Si:H(*p*) layer was therefore dropped. Several batches of cells were produced, featuring nc- $\text{SiC}_x(\text{p})$ layers at the rear and nc- $\text{SiC}_x(\text{n})$ at the front, implementing various metallization strategies. Unfortunately, the cells with evaporated aluminium at the rear seemed to be shunted. Moreover, a drop of more than 30 mV was observed between iV_{oc} after hydrogenation and V_{oc} of the finished cells. Nevertheless, efficiencies up to 20.5% were obtained for cells with ITO/Ag metallization on both sides, demonstrating the potential of such an approach. To our knowledge, this is the first report of a solar cell featuring co-fired passivating contacts.

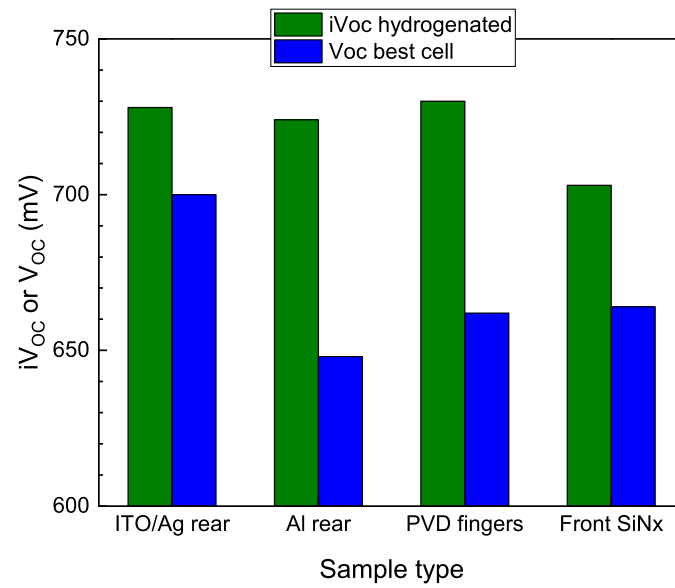


Figure 6.18 – iV_{oc} values measured after hydrogenation and V_{oc} value of best cell for each batch of solar cells shown in Fig. 6.15.

7 Summary and perspectives

7.1 Summary

The first chapter of this thesis provided the context of the performed work. The motivation for FPCs was presented, as well as the state of the art in the field and the theoretical background necessary to assess recombination, passivation and solar cell performance. In short, improved surface passivation is one of the main driving forces towards higher conversion efficiencies and a lot of research, including this work, focuses on developing passivating contacts with simple and low-cost fabrication processes that are easily transferable to industry. FPCs are particularly interesting in this regard, as they reduce the required thermal budget while maintaining compatibility with the mainstream firing-through metallization approach.

The various fabrication processes and characterization techniques used throughout this work were described in the second chapter. The wide range of tools allowed broad and detailed investigations. Some fast and inexpensive measurements, such as QSSPC, were performed routinely, whereas more complicated ones, such as SIMS, were used selectively.

Chapter 3 focused on the hydrogenation of the FPC. Combining QSSPC, SIMS, APT and ERDA, diffusion of hydrogen/deuterium from a $\text{SiN}_x\text{:H/D}$ reservoir layer and its accumulation at the c-Si/ SiO_x interface was evidenced as the key mechanism for surface passivation. Using ~25 nm thick thermal SiO_2 it was shown that the SiC_x layer could be etched off, without major loss in iV_{oc} , corroborating the predominance of chemical passivation by hydrogen in FPC structures. Moreover, the type of interfacial oxide was found to influence the passivation quality: iV_{oc} values around 710 mV, 720 mV and 740 mV were reached with chemical SiO_x (1.3 nm), UV- O_3 SiO_x (1.3 nm) and thermal SiO_2 (25 nm), respectively. Higher passivation seems to be linked with an SiO_x composition closer to stoichiometric SiO_2 .

Results on the evolution of the bulk lifetime were presented in chapter 4. It was found that the firing process induces shallow bulk defects within the FZ wafers, which could result from Si-vacancies capturing N-atoms, leading to dangling bonds in the bulk that can be passivated by hydrogen. The kinetics of the hydrogenation appear to be limited by these bulk defects:

the experimental results indicate a rapid passivation of the c-Si/SiO_x interface, taking place in less than 1 min, followed by a slower passivation of the shallow bulk defects. Long thermal pre-treatment of the wafer resulted in faster passivation, indicating that these defects can also be cured thermally, as reported in literature. Moreover, numerical simulations predicted rapid diffusion of hydrogen. Hence, the hydrogenation kinetics seem to be limited by the available hydrogen supply at the c-Si/SiO_x interface, rather than its diffusion within the wafer. In addition, the possibility to hydrogenate both surfaces with a SiN_x:H reservoir layer deposited on one side of the wafer only was demonstrated, although resulting in lower passivation levels ($\tau_{\text{eff}} \sim 700 \mu\text{s}$ rather than $\sim 1300 \mu\text{s}$). This finding provides further flexibility to the fabrication process of FPC based solar cells.

In chapter 5 the stability of the passivation provided by hydrogen was investigated, both short- and long-term. Indeed, elevated temperatures lead to effusion of hydrogen, and its presence in the bulk was reported (in literature) to cause LeTID. So far, no degradation was observed for FPCs upon 80 days of light soaking (1 sun illumination) at 80 °C, which are widely used conditions to test for LID and LeTID. Moreover, the minority carrier lifetimes remained stable upon thermal treatments of 30 min up to 170 °C. Changes in lifetime upon storage were observed in some cases, but could not yet be explained.

The last chapter was dedicated to the metallization of FPCs, one of the main remaining challenges for their integration in solar cells, especially on the front side. Indeed, the deposited layers need to stop the metallic paste during firing-through, to avoid direct metal-c-Si contact and damaging of the SiO_x layer. A layer stack with a total thickness of ~ 90 nm was developed and remained mostly blister free upon firing thanks to a thermal pre-treatment of 10 min at 500 °C. Unfortunately, so far good contact resistivities could only be achieved at the expense of passivation. Closer investigations revealed diffusion of Al from the metallic paste into the SiN_x layer, forming an Al-N compound, and in some cases accumulating at the SiO_x layer. Nevertheless, using a low temperature metallization approach (sputtering of ITO and Ag), solar cells featuring co-fired SiC_x(*n*) and SiC_x(*p*) FPCs at the front and rear were processed, reaching up to 20.5% in efficiency. This corroborates the potential of FPCs for high efficiency solar cells with a simple and low-cost fabrication process.

7.2 Perspectives

As mentioned throughout this document, several topics require further investigations to complement the findings and interpretations made so far. A first one is the issue of FZ wafers being affected by shallow bulk defects appearing upon firing. In the perspective of transfer to industry, it would be interesting to analyze the evolution of bulk lifetime of Cz wafers during the processing steps of FPCs. Indeed, the suggested defect nature of Si-vacancies capturing N-atoms is inherent to FZ wafers. In the short term, applying an annealing at temperatures above 1000 °C might allow to annihilate these defects in FZ material, enabling the investigation of the kinetics of the surface passivation, as well as assessing the FPCs full potential. Most likely,

iV_{oc} values beyond 720 mV and 730 mV are possible for $\text{SiC}_x(p)$ and $\text{SiC}_x(n)$ layers on UV- O_3 SiO_x , respectively. Repeating the experiments presented in appendix C on such pre-treated wafers would also be highly interesting, as surface passivation with fluorine diffused during the firing step seems feasible.

Regarding contact resistivity, a possible optimization route would be to adapt the PECVD recipe of the a-Si:H(p) layer deposited on top of $\text{SiC}_x(p)$, such as to grow a layer that is actually microcrystalline. This should increase its stability against blistering and its concentration of active dopants, allowing the growth of thicker layers making good electrical contact with the metallic paste. Doing so would most likely result in layers with carrier densities $> 5 \cdot 10^{19} \text{ cm}^{-3}$, allowing contact resistivities $< 10 \text{ m}\Omega\text{cm}^2$, limited by the tunneling transport through the SiO_x layer [Haug et al., 2019]. Potential starting points are to further increase the H_2 flux, or replacing the TMB precursor with BF_3 . Indeed, higher dilution in H_2 and the formation of HF within the plasma were reported to enhance the crystallinity of the deposited silicon layers [Dornstetter, 2014].

As for the work on metallization, it has been taken over by my colleague Sofia Libraro and will be part of her PhD thesis. The ability to metallize these FPCs using an approach compatible with industry and maintaining the passivation would allow their integration in high efficiency solar cells with a low thermal budget and a lean process flow. The most straightforward approach would be to implement an FPC as rear contact of a PERC, as some companies are already doing using TOPCons. The advantage of FPC in this case being to reduce the thermal budget, replacing the annealing of the passivating contact in a tube furnace by a firing.

As the ability to co-fire $\text{SiC}_x(n)$ and $\text{SiC}_x(p)$ layers deposited on the front and the rear side of a wafer has been demonstrated, as well as the ability to hydrogenate FPCs with an $\text{SiN}_x\text{:H}$ layer optimized for hydrogen release upon firing, a promising longer term goal is the co-fired cell schematized in Fig. 1.10. Metallizing the contacts by firing-through would need to deposit locally thicker $\text{SiC}_x(n)$ layers under the fingers to minimize parasitic absorption at the front. This could be achieved using a hard mask during PECVD. Another idea, potentially avoiding the need for localization, would be to metallize the $\text{SiC}_x(n)$ layer directly, using screen-printing of pastes without glass frit or evaporation through a mask. The $\text{SiN}_x\text{:H}$ reservoir layer would then be deposited on top of the fingers and hydrogen diffused during a firing or a hotplate treatment.

A further possibility would be to integrate FPCs in an IBC architecture, lifting the requirement for thin layers. In this case, using a recombination junction is a promising approach to keep a simple process flow, eliminating the patterning of one of the SiC_x layers [Tomasi et al., 2017], [Haug et al., 2021c].

A Analysis of SiC_x layers

The SiC_x layers used in this work have been developed by former colleagues and hence already studied quite intensively [Nogay et al., 2016], [Nogay et al., 2017], [Ingenito et al., 2018], [Ingenito et al., 2019], [Haug et al., 2019], [Ingenito et al., 2021]. In the course of this thesis, some further insight into these layers has been gained and is presented in this appendix.

Parts of these results were published in *Applied Surface Science* and are reproduced with permission from [Pal et al., 2021]. Copyright ©2021, Elsevier.

The experiments presented below were performed on c-Si/SiO_x/SiC_x(*p*) samples after hydrogenation via a sacrificial SiN_x:H/D layer. APT allowed a 3-dimensional atom by atom reconstruction of the sample, as shown in Fig. A.1a. As one can see, boron and carbon are distributed inhomogeneously. Fig. A.1b displays the 1.5 at.% iso-concentration surface of carbon, showing that carbon forms clusters. The current hypothesis is that during crystallization of the a-SiC_x layer, carbon is driven out of the crystallizing region due to low solubility of C in c-Si [Beaudhuin et al., 2011], [Olesinski and Abbaschian, 1984], resulting in a nc-SiC_x layer made of small c-Si grains within an a-SiC_x matrix.

To support this hypothesis, the same sample was analyzed by STEM, STEM-EDX and EELS. The results showed that the ~32 nm thick a-SiC_x layer crystallizes upon firing and shrinks in thickness to ~26.5 nm. Fig. A.2a shows 5–10 nm large crystalline grains in an amorphous matrix for the c-Si/SiO_x/nc-SiC_x(*p*) stack after firing and hydrogenation via a sacrificial SiN_x:H/D layer. As can be seen in the STEM-EDX mapping of carbon (Fig. A.2b and Fig. A.2c), it seems to form clusters upon crystallization, in agreement with the APT results. The EELS measurements show clustering upon crystallization too (Fig. A.2d and Fig. A.2e). However, it is not clear, whether the clusters of carbon and EELS are linked with each other, and whether they are linked to the crystalline grains.

The crystallization of the SiC_x layer can also be observed by Raman spectroscopy. The samples shown in Fig. A.3 were deposited in the Octopus SHJ reactor, with two different CH₄ gas flows (differing by a factor of ~5), and measured before and after firing. As one can observe, the

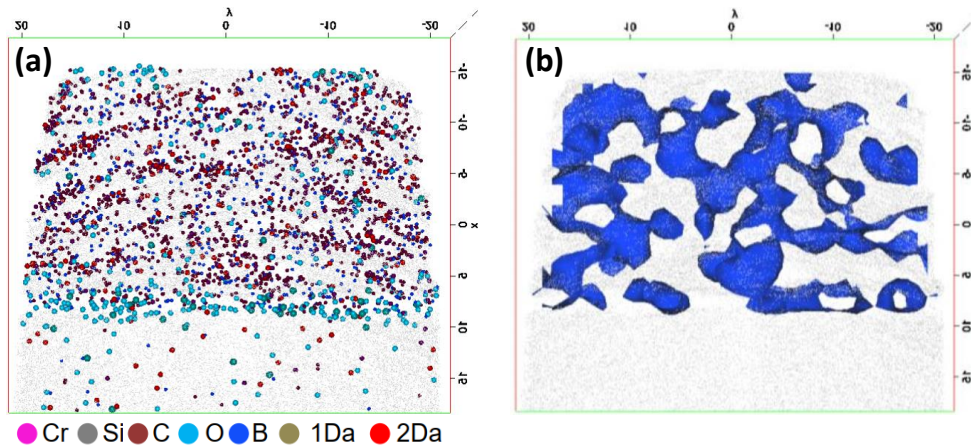


Figure A.1 – (a) APT reconstruction of a c-Si/SiO_x/SiC_x(*p*) sample after hydrogenation via a sacrificial SiN_x:H/D layer. (b) 1.5 at.% C iso-concentration surface within the SiC_x(*p*) layer.

layers with the usual carbon content (low C) crystallize upon firing, whereas the ones with high carbon content (high C) stay amorphous. According to Smit *et al.*, one can extract the crystallinity fraction by fitting the measured spectra with a series of Gaussian peaks and taking the ratio of the peak areas of the crystalline and amorphous parts [Smit et al., 2003]. Doing so with a MATLAB[®] script (courtesy of Luca Antognini), one obtains the following crystallinity fractions: 4% (low C, as deposited), 32% (low C, fired), 3% (high C, as deposited), 6% (high C, fired), confirming that only the layer with low carbon content crystallized upon firing. This result is in agreement with the findings of Xu *et al.*, who reported decreasing crystalline fractions upon annealing of SiC_x(*n*) layers with increasing carbon content [Xu et al., 2020].

When looking again at the same sample with SIMS (Fig. A.4) we observe a carbon and boron signal within the SiC_x(*p*) layer that decays rapidly within the c-Si bulk, indicating no/little in-diffusion, as was observed by APT in chapter 3. For both hydrogen and oxygen, quite a high background signal is observed, most likely linked to residual H₂O present in the chamber. Surprisingly, low levels of nitrogen are detected within the SiC_x(*p*) layer, most likely diffused alongside hydrogen and deuterium from the SiN_x:H/D layer upon hotplate treatment.

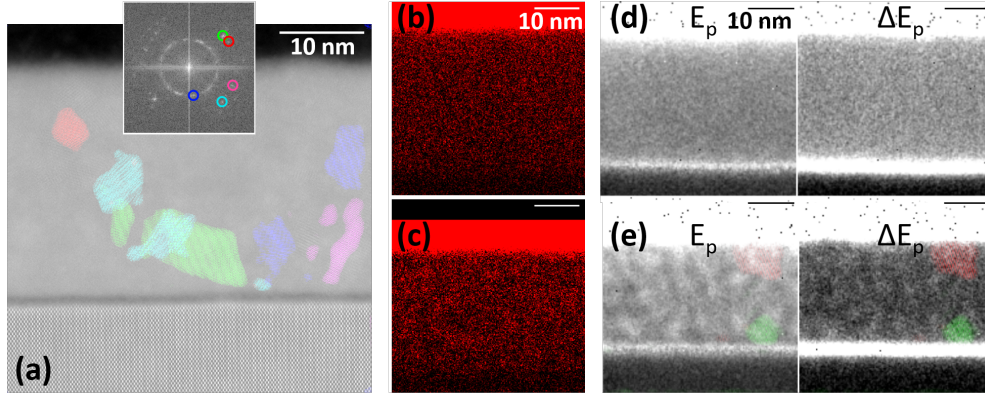


Figure A.2 – (a) STEM-High-Angle Annular Dark Field (HAADF) image of a c-Si/SiO_x/SiC_x(*p*) sample after hydrogenation via a sacrificial SiN_x:H/D layer. Some crystallites are highlighted in color. (b) Carbon content measured by STEM-EDX for the amorphous layer before firing, and (c) after firing and hydrogenation. (d) Energy E_p and full width at half maximum ΔE_p of plasmon peaks for the amorphous layer, and (e) after crystallization.

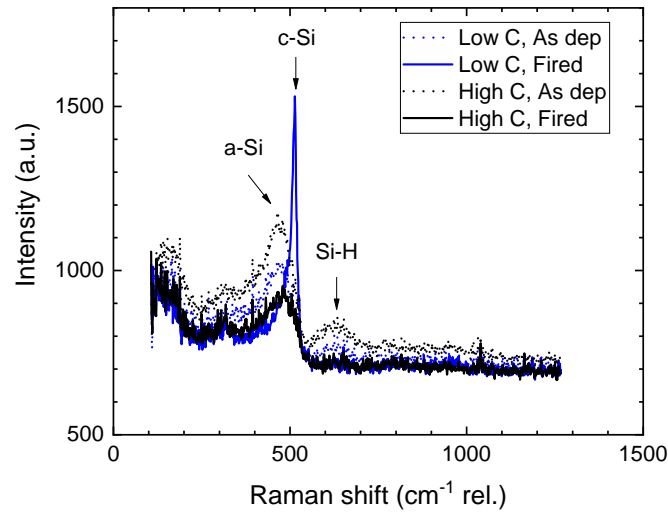


Figure A.3 – Raman spectroscopy of SiC_x layers with low and high carbon content, measured before (as deposited) and after (fired) firing (measurements taken using UV laser excitation at 325 nm). Peaks positions are marked according to [Bermejo and Cardona, 1979].

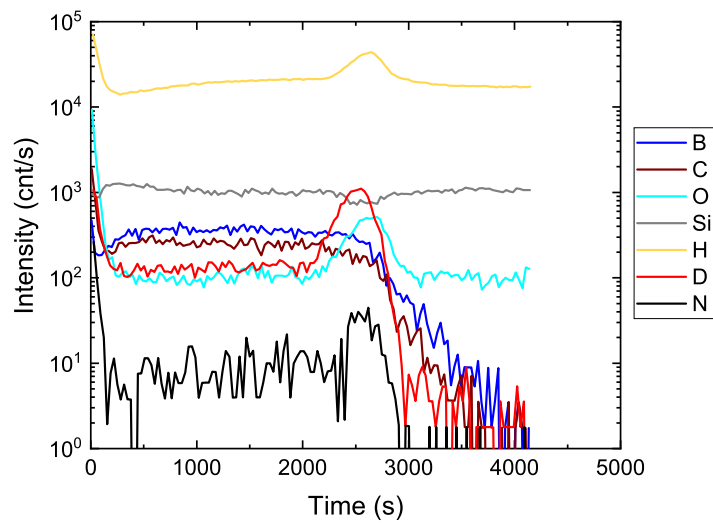


Figure A.4 – SIMS profiles of silicon, oxygen, carbon, boron, hydrogen, deuterium and nitrogen measured in a c-Si/SiO_x/SiC_x(*p*) sample after hydrogenation via a sacrificial SiN_x:H/D layer in MCs₂⁺ mode.

B Quantification of H and D in SiN_x:H/D layers

For the experiments in chapter 3, deuterium was incorporated in the SiN_x layer by adding a 25 sccm D₂ flow during PECVD. To investigate the effect of this additional gas flow on the composition of the layer, FTIR measurements were taken on samples with 0, 25 and 100 sccm of D₂ flow during PECVD of SiN_x:H/D, while the flows for SiH₄ and NH₃ were kept constant at 5.5 and 10.4 sccm, respectively. As one can observe in Fig. B.1, the intensities of the Si-H and N-H peaks decrease with increasing D₂ flow, while those of Si-D and N-D increase. This indicates, that hydrogen gets replaced by deuterium in the SiN_x:H/D layer. Note that FTIR measurements were also taken after 30 min of hydrogen diffusion on the hotplate at 450 °C (not shown here). No difference could be observed with the spectra before this treatment, pointing once more towards these layers acting as quasi-infinite source of hydrogen and deuterium in this range of temperature and diffusion time.

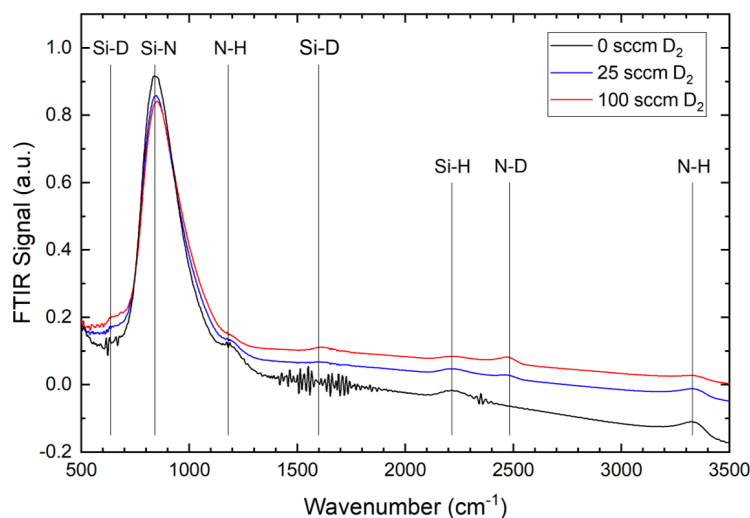


Figure B.1 – FTIR measurements after PECVD of SiN_x:H/D layers with varying deuterium content. The gas flows were kept constant for SiH₄ and NH₃. As for D₂, it was set to 0, 25 and 100 sccm. The vertical lines indicate the wavenumbers at which Si-D, Si-N, Si-H, N-D and N-H peaks are expected.

For quantitative data, the samples with 25 and 100 sccm of D₂ flow were analyzed by RBS and ERDA. These measurements, shown in Fig. B.2, confirm the observation made by FTIR, that hydrogen gets replaced by Deuterium. The concentrations move from 11.7 at.% of H and 6.2 at.% of D for the layer with a 25 sccm flow, to 7.3 at.% of H and 13.0 at.% of D for the layer with 100 sccm. The total concentration of hydrogen and deuterium thus stays more or less constant (moving from 18 to 20 at.%), but the H/D ratio switches from $\sim 2/1$ to $\sim 1/2$. RBS measurements reveal a total concentration of Si and N atoms of $7.67 \cdot 10^{22} \text{ cm}^{-3}$ and a ratio of 3/4 for the SiN_x:H/D layer with a D₂ flow of 25 sccm. The corresponding values for the layer with a 100 sccm flow are $7.93 \cdot 10^{22} \text{ cm}^{-3}$ and a ratio of 3/3.9. In addition, the refractive index measured by ellipsometry displayed values of 1.98–2.00 at a wavelength of 632 nm with similar variations among different spots on the same sample as between the two different layers. The properties of these SiN_x:H/D layers hence seem almost independent of the D₂ flow.

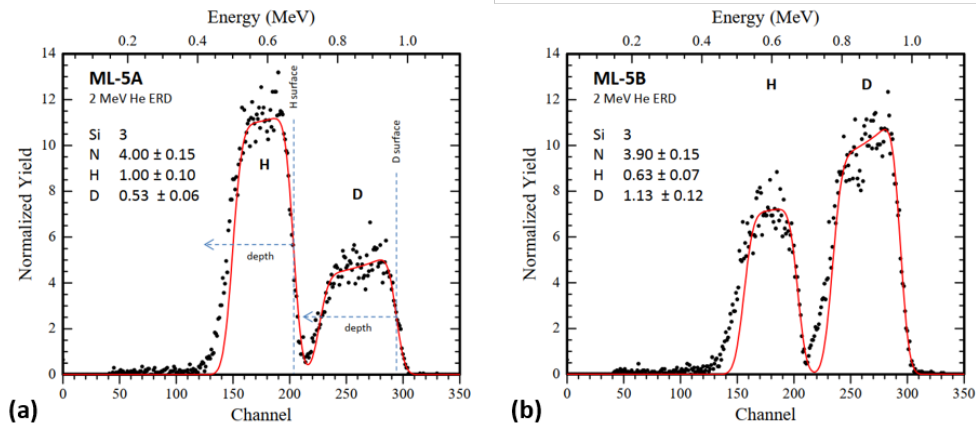


Figure B.2 – Results of RBS and ERDA measurements on SiN_x:H/D layers with varying deuterium content. For the sample shown in (a), 25 sccm of D₂ were added during PECVD of SiN_x:H/D, while for (b) it was 100 sccm.

Since the trends observed by FTIR and ERDA correspond well, the question arose whether the hydrogen and deuterium content can be determined from the FTIR spectra. This would allow for a much more convenient measurement of their concentration. According to literature, the concentration N of a given atomic bond can be extracted by computing the area under the corresponding peak and multiplying it with an experimentally determined proportionality constant A^s [Dexter, 1956], [Shih et al., 2001], [Shih et al., 2000], [Brodsky et al., 1977]:

$$N_{N-H} = A_{N-H}^s \cdot \int \frac{\alpha(\omega)}{\omega} d\omega = \frac{cn\omega_t}{2\pi^2} \cdot \frac{\mu}{e_s^{*2}} \cdot \int \frac{\alpha(\omega)}{\omega} d\omega \quad (\text{B.1})$$

where $\alpha(\omega)$ is the absorption coefficient, ω is the wavenumber, c the speed of light, n the refractive index of the layer (SiN_x:H/D in this case), ω_t the position of the peak, μ the reduced mass of N and H, and e_s^* the effective charge of the N–H bond. Equivalent expressions hold for N–D, Si–H and Si–D bonds. The concentrations of H and D are then given by $N_H = N_{N-H} + N_{Si-H}$ and $N_D = N_{N-D} + N_{Si-D}$, respectively. Since the value plotted in the FTIR

Table B.1 – Hydrogen and deuterium content of SiN_x:H/D layers computed from FTIR spectra and measured by RBS and ERDA.

SiN _x :H/D	FTIR and A^s		RBS and ERDA	
	N_H (at.%)	N_D (at.%)	N_H (at.%)	N_D (at.%)
25 sccm D ₂ flow	11.5	8.4	11.7 ± 2	6.2 ± 1
100 sccm D ₂ flow	7.2	14.0	7.3 ± 1	13.0 ± 2

spectra is $-\ln(I_{layer}/I_{ref}) = \alpha \cdot d$ (as explained in chapter 2), dividing it by the total thickness d of SiN_x:H/D (front and rear of sample), measured by spectroscopic ellipsometry, yields the absorption coefficient α . The proportionality constants determined by Shih *et al.* are: $A_{N-H}^s = 2.6 \cdot 10^{20} \text{ cm}^{-2}$, $A_{N-D}^s = 3.7 \cdot 10^{20} \text{ cm}^{-2}$, $A_{Si-H}^s = 6.9 \cdot 10^{19} \text{ cm}^{-2}$, $A_{Si-D}^s = 1.0 \cdot 10^{20} \text{ cm}^{-2}$. As can be observed, the proportionality constants for the bonds with deuterium are ~1.4 times higher than those for the bonds with hydrogen, which is linked to their higher mass. The only difference between H and D being the mass, their product $\mu\omega_t$ is the only value changing in the expression of A^s . Assuming the bond vibrations to behave like harmonic oscillators, we obtain $\mu\omega_t = \sqrt{\mu} \cdot \frac{1}{2\pi c} \sqrt{k}$. Hence, $\frac{A_{Si-D}^s}{A_{Si-H}^s} = \sqrt{\frac{\mu_{Si-D}}{\mu_{Si-H}}} = 1.39$ and $\frac{A_{N-D}^s}{A_{N-H}^s} = \sqrt{\frac{\mu_{N-D}}{\mu_{N-H}}} = 1.37$.

The area under the FTIR peaks was computed using the software OriginPro® 2018, allowing to subtract a baseline, fit the peak with a Gaussian curve and integrate its area. Applying the proportionality constants from Shih *et al.* resulted in overestimated H and D concentrations. Multiplying all these constants by 0.9 yields results close to those measured by ERDA and RBS for the hydrogen content, as can be seen in table B.1. The deuterium content is still overestimated. Moreover, it is surprising that the A^s values are lower for our SiN_x:H/D layers than those of Shih *et al.*, since they depend mainly on the refractive index, which was lower for the layers investigated by Shih *et al.* ($n = 1.8$) compared to ours ($n = 2.0$).

In conclusion, the presented method can be applied to extract the hydrogen and deuterium content of our layers from FTIR measurements. The absolute values have to be taken with some care, however it provides a good estimate and determines the trends correctly.

C Chemical passivation using fluorine

In this thesis, a focus was set on the hydrogen passivation of FPCs. Having a single electron, hydrogen attaches to dangling bonds, which act as defects, thus passivating them. These dangling bonds can also be passivated by other elements, such as fluorine, which has 7 valence electrons, thus bonding readily with another single electron. Passivation of the c-Si/SiO₂ interface by fluorine was already investigated in the 1980/90s by the metal-oxide-semiconductor transistor community [Wright and Saraswat, 1989], [Ono et al., 1993], [Moiseiwitsch and Ashburn, 1994]. The idea is to diffuse fluorine from a source layer to the c-Si/SiO₂ interface during a thermal treatment, as shown in Fig. C.1. Applying this to solar cells, incorporating fluorine into SiO_x/poly-Si contacts was reported to improve their iV_{oc} , thanks to fluorine passivating defects at the c-Si/SiO_x interface [Castaner et al., 1998], [Reichel et al., 2015]. Bulk defect passivation by fluorine diffusion from a deposited reservoir layer was also reported [Sio et al., 2021]. Further advantages of fluorine passivation are that it might avoid long term degradation linked to the presence of hydrogen (as reported in chapter 5), and that it effuses at higher temperatures than hydrogen [Fang et al., 1980]. In their theses, Gizem Nogay and Josua Stückelberger achieved iV_{oc} values above 720 mV before hydrogenation, depositing fluorinated Si layer on tunneling SiO_x by PECVD, followed by a high temperature annealing [Nogay, 2018], [Stuckelberger, 2018].

In this chapter, passivation of the c-Si/SiO_x interface by diffusing fluorine from a SiC_x(*p*):F layer during the firing step is investigated. Such an approach would remove the need for a hydrogenation step and thus simplify the fabrication process.

For these experiments, samples were made similarly to those of chapter 3 and following the process shown in Fig. 3.1. In general, SE wafers were used, except for the samples made for TEM analysis, which were processed on DSP wafers. The tunneling oxide was grown wet chemically, or by UV-O₃. The PECVD recipes to deposit the a-SiC_x(*p*) layers were adapted, such as to incorporate fluorine. In the first experiments, SiH₄ was replaced with SiF₄. The recipe for these layers consisted of a ~4 nm thin protective intrinsic a-Si:H layer, followed by a *p*-type fluorinated layer, deposited during 3 min at 200 °C, under pressures of 2–4 mbar, using SiF₄, Ar, B(CH₃)₃ and H₂ as precursor gases. In a second set of experiments, fluorine was

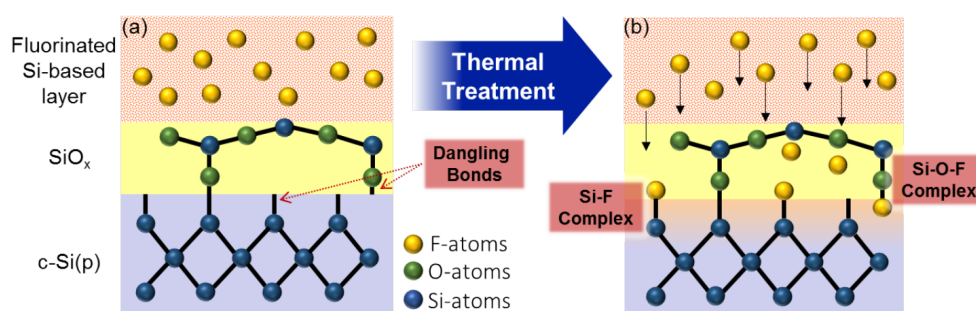


Figure C.1 – Schematic illustration of the c-Si/SiO_x interface passivation by fluorine. The c-Si/SiO_x/SiC_x:F samples are represented before (a) and after (b) thermal treatment. Reproduced with the author's permission and without modifications from [Nogay, 2018]. Copyright ©2018, G. Nogay.

incorporated by replacing B(CH₃)₃ by BF₃. This recipe did not feature a protective layer, and consisted of a 170 s long deposition at 200 °C, under a pressure of 0.7 mbar, using SiH₄, CH₄ and BF₃ as precursor gases. The samples were then fired for 3–15 s at 800–850 °C. QSSPC and PL measurements were performed at this stage, to see if passivation by fluorine diffusion was achieved. Subsequently, the samples were hydrogenated via H diffusion from a ~70 nm thick sacrificial layer of SiN_x:H during 30 min on a hotplate at 450 °C. Finally, the SiN_x:H layer was removed in a 5 % HF solution at room temperature.

For the samples featuring layers deposited using SiF₄, no significant passivation was achieved after firing, despite varying the B(CH₃)₃ flow, the chamber pressure and excitation power during PECVD, and the firing conditions. Even after hydrogenation, $\tau_{\text{eff}@10^{15}\text{cm}^{-3}}$ was below 130 μs and iV_{oc} below 660 mV. High Resolution TEM (HR-TEM) investigations, shown in Fig. C.2a, revealed epitaxial regrowth of the deposited layer, indicating that the SiO_x layer broke up. In addition, STEM-HAADF (Fig. C.2b) and STEM-EDX (not shown here) displayed severe damages of the protective intrinsic layer, as well as many voids within the fluorinated layer, indicated by the dark regions in the STEM-HAADF image and high oxygen signal in the STEM-EDX maps. Due to these many issues, SiF₄ was replaced by BF₃ as fluorine source, since the PECVD recipe using BF₃ features more gentle conditions (power and pressure) than the one using SiF₄.

Samples featuring SiC_x(p):F layers deposited using BF₃ performed much better. Various BF₃ flows were tested and an optimum determined, maximizing the passivation achieved after firing. In addition, layers deposited on UV-O₃ SiO_x tunneling oxide layers performed better than those deposited on chemical SiO_x, in line with the findings from section 3.5. The best obtained iV_{oc} values for various processing conditions are given in table C.1. As can be observed, before hydrogenation, the samples fired for 15 s at 850 °C featured significantly higher iV_{oc} values than their counterparts fired for 3 s at 800 °C, reaching up to 682 mV. This indicates that diffusing enough fluorine to passivate the present defects is a challenge during such a rapid thermal processing step. Increasing the firing temperature and time further

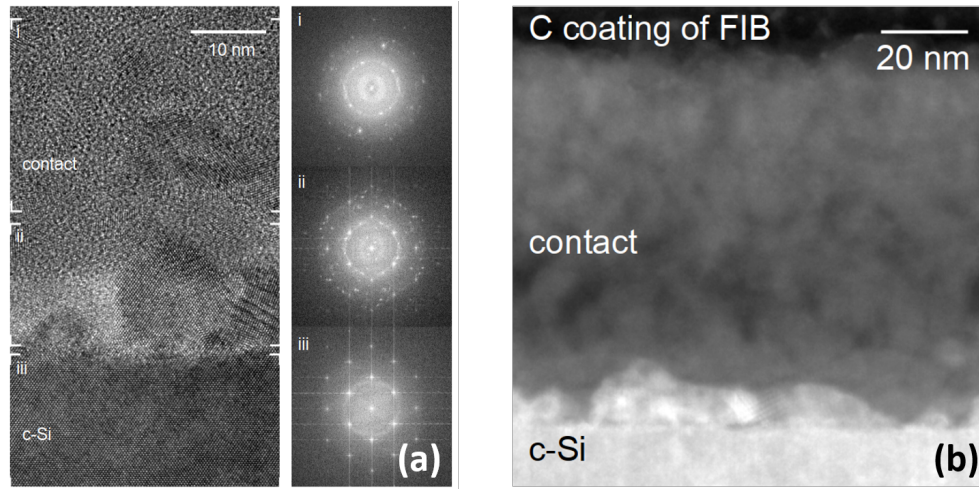


Figure C.2 – (a) HR-TEM micrograph of a fluorinated FPC deposited using SiF_4 and $\text{B}(\text{CH}_3)_3$ gas flows. Fourier transforms of three regions are given. iii (bottom one) corresponds to the c-Si wafer region, while i and ii correspond to the top and bottom part of the $\text{SiC}_x(p):\text{F}$ layer. (b) STEM-HAADF image taken on the same sample.

revealed to damage the tunneling oxide [Libraro, 2019], [Haug et al., 2021b]. Hence, adding a 2 min long thermal treatment on the hotplate at 500°C after firing was tested, but did not result in improved passivation.

The 736 mV of iV_{oc} reached after hydrogenation are a noteworthy result too. Indeed, this result is on par with passivation levels achieved in chapter 3 with thick thermal SiO_2 layers, while being processed on a thin UV- O_3 SiO_x layer allowing current extraction by tunneling. Unfortunately, the passivation drops significantly upon removal of the $\text{SiN}_x:\text{H/D}$ layer. The reason for this is unknown so far, but might be linked to solvable processing issues.

As stated above, fluorine incorporation into $\text{SiC}_x(p):\text{F}$ layers resulted in up to 682 mV of iV_{oc} before hydrogenation. This result becomes even more promising, when considering the PL images shown in Fig. C.3. Indeed, ring shapes similar to those reported in chapter 4 can be observed after firing for 3 s at 800°C (Fig. C.3a). It is therefore possible, that the diffusion of fluorine from the $\text{SiC}_x(p):\text{F}$ layer during firing actually provides good surface passivation; the effective lifetime and iV_{oc} measured by QSSPC hence being limited by shallow bulk defects. The improved passivation but inhomogeneous PL signal for the sample fired for 15 s at 850°C (Fig. C.3b) could be explained by fluorine diffusion into the bulk, but local damages to the tunneling SiO_x layer. As for the inhomogeneities observed after hydrogenation (Fig. C.3c), they remain an open question so far.

In conclusion, it was shown that incorporating fluorine into the $\text{SiC}_x(p)$ layers of FPCs results in improved passivation upon firing, allowing to reach iV_{oc} values up to 682 mV before, and up to 736 mV after hydrogenation. As in chapter 4, the passivation seems to be limited by shallow bulk defects. Solving this issue would therefore be necessary to assess the full potential of

Table C.1 – Best iV_{oc} values obtained with fluorinated FPCs. The three columns correspond to the tested material combinations: chemical SiO_x or UV- O_3 SiO_x , and $\text{SiC}_x(p)$:F layers deposited using SiF_4 and $\text{B}(\text{CH}_3)_3$ gas flows or using SiH_4 and BF_3 . The lines give the processing state of the characterized sample: After firing at 800 °C or 850 °C, after subsequent hydrogenation (still capped with $\text{SiN}_x\text{:H}$) and after removal of the $\text{SiN}_x\text{:H}$ reservoir layer in an HF 5% solution.

Sample condition	Chem SiO_x / SiF_4	Chem SiO_x / BF_3	UV- O_3 SiO_x / BF_3
Fired (800 °C)	628 mV	641 mV	647 mV
Fired (850 °C)	633 mV	670 mV	682 mV
Hydrogenated (800 °C)	637 mV	712 mV	730 mV
Hydrogenated (850 °C)	652 mV	712 mV	736 mV
$\text{SiN}_x\text{:H/D}$ removed (800 °C)	610 mV	698 mV	720 mV
$\text{SiN}_x\text{:H/D}$ removed (850 °C)	613 mV	700 mV	720 mV

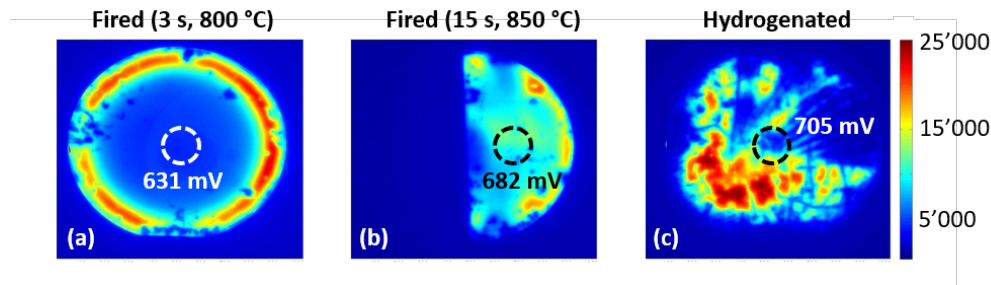


Figure C.3 – PL images of fluorinated FPCs featuring UV- O_3 SiO_x and $\text{SiC}_x(p)$:F layers deposited using SiH_4 and BF_3 . (a) Sample after firing for 3 s at 800 °C, (b) sample after firing for 15 s at 850 °C, (c) same sample as in (a) but after subsequent hydrogenation and removal of the $\text{SiN}_x\text{:H}$ reservoir layer in an HF 5% solution. The circles indicate where QSSPC was measured and resulting iV_{oc} values are given.

c-Si/ SiO_x interface passivation by fluorine diffusion during firing of a $\text{SiC}_x(p)$:F layer.

Bibliography

- Abe, T., & Takahashi, T. (2011). Intrinsic point defect behavior in silicon crystals during growth from the melt: A model derived from experimental results. *Journal of Crystal Growth*, 334(1), 16–36. <https://doi.org/10.1016/j.jcrysgro.2011.07.027>
- Aberle, A., Glunz, S., Warta, W., Kopp, J., & Knobloch, J. (1991). SiO₂ -passivated High Efficiency Silicon Solar Cells : Process Dependence of Si-SiO₂ Interface Recombination. In A. Luque, G. Sala, W. Palz, G. Dos Santos, & P. Helm (Eds.), *Tenth e.c. photovoltaic solar energy conference* (pp. 10–14). Springer, Dordrecht. https://doi.org/10.1007/978-94-011-3622-8_161
- Aberle, A. G. (2000). Surface passivation of crystalline silicon solar cells: a review. *Progress in Photovoltaics: Research and Applications*, 8(5), 473–487. [https://doi.org/10.1002/1099-159X\(200009/10\)8:5<473::AID-PIP337>3.0.CO;2-D](https://doi.org/10.1002/1099-159X(200009/10)8:5<473::AID-PIP337>3.0.CO;2-D)
- Aberle, A. G., Glunz, S., & Warta, W. (1992). Impact of illumination level and oxide parameters on Shockley-Read-Hall recombination at the Si-SiO₂ interface. *Journal of Applied Physics*, 71(9), 4422–4431. <https://doi.org/10.1063/1.350782>
- Allebe, C., Ballif, C., Leon, J. J. D., Ingenito, A., Descocudres, A., Nogay, G., Wyss, P., Haug, F.-J., Despeisse, M., & Nicolay, S. (2019). PECVD based layers for improved high temperature industrial Solar cell processes. *2019 IEEE 46th Photovoltaic Specialists Conference (PVSC)*, 2196–2199. <https://doi.org/10.1109/PVSC40753.2019.8980583>
- Allen, T. G., Bullock, J., Yang, X., Javey, A., & De Wolf, S. (2019). Passivating contacts for crystalline silicon solar cells. *Nature Energy*, 2–3. <https://doi.org/10.1038/s41560-019-0463-6>
- Antognini, L., Paratte, V., Haschke, J., Cattin, J., Dreon, J., Lehmann, M., Senaud, L.-l., Jeangros, Q., Ballif, C., & Boccad, M. (2021). Influence of the Dopant Gas Precursor in P-Type Nanocrystalline Silicon Layers on the Performance of Front Junction Heterojunction Solar Cells. *IEEE Journal of Photovoltaics*, 1–13. <https://doi.org/10.1109/JPHOTOV.2021.3074072>
- Balaji, N., C. Raval, M., & Saravanan, S. (2019). Review on Metallization in Crystalline Silicon Solar Cells. *Solar cells*. IntechOpen. <https://doi.org/10.5772/intechopen.84820>
- Bao, J., Chen, C., Ma, L., Huang, C., Zhang, X., Wang, Z., Chen, C., Zhan, S., Liu, R., Qiao, Z., Du, Z., Liu, Z., & Chen, J. (2020). Towards 24% Efficiency for Industrial n-type Bifacial Passivating-Contact Solar Cells with Homogeneous Emitter. *37th European*

- Photovoltaic Solar Energy Conference and Exhibition*, 160–163. <https://doi.org/10.4229/EUPVSEC20202020-2AO.6.1>
- Beaudhuin, M., Duffar, T., Lemiti, M., & Zaidat, K. (2011). One-dimensional model of the equiaxed grain formation in multi-crystalline silicon. *Journal of Crystal Growth*, 319(1), 106–113. <https://doi.org/10.1016/j.jcrysgro.2011.02.001>
- Berger, H. H. (1972). Contact Resistance and Contact Resistivity. *Journal of The Electrochemical Society*, 119(4), 507. <https://doi.org/10.1149/1.2404240>
- Bermejo, D., & Cardona, M. (1979). Raman scattering in pure and hydrogenated amorphous germanium and silicon. *Journal of Non-Crystalline Solids*, 32(1-3), 405–419. [https://doi.org/10.1016/0022-3093\(79\)90085-1](https://doi.org/10.1016/0022-3093(79)90085-1)
- Bernardini, S., Naerland, T. U., Blum, A. L., Coletti, G., & Bertoni, M. I. (2017). Unraveling bulk defects in high-quality c-Si material via TIDLS. *Progress in Photovoltaics: Research and Applications*, 25(3), 209–217. <https://doi.org/10.1002/pip.2847>
- Beyer, W., & Zastrow, U. (2000). Dependence of H Diffusion in Hydrogenated Silicon on Doping and the Fermi Level. *MRS Proceedings*, 609, A20.4. <https://doi.org/10.1557/PROC-609-A20.4>
- Bhan, R., Lomash, S., Basu, P., & Cahabra, K. (1987). Interface Properties of Thermal SiO₂ using 1,1,1, Trichloroethane(TCA). *Journal of the Electrochemical Society*, 134(11), 2826–2828. <https://doi.org/10.1149/1.2100296>
- Bivour, M., Bartsch, J., Clement, F., Cimiotti, G., Erath, D., Feldmann, E., Fellmeth, T., Glatthaar, M., Hermle, M., Jahn, M., Kluska, S., Keding, R., Lorenz, A., Lacmago-Lontchi, I., Mack, S., Moldovan, A., Nekarda, J., Pospischil, M., Rodofili, A., ... Glunz, S. W. (2017). Metallization of passivating and carrier selective contacts: status and perspectives at Fraunhofer ISE. *7th Workshop on Metallization and Interconnection for Crystalline Silicon Solar Cells*, (October).
- Blakers, A. W., & Green, M. A. (1985). Oxidation condition dependence of surface passivation in high efficiency silicon solar cells. *Applied Physics Letters*, 47(8), 818–820. <https://doi.org/10.1063/1.95994>
- Blakers, A. W., & Green, M. A. (1986). 20% Efficiency Silicon Solar Cells. *Applied Physics Letters*, 48(3), 215–217. <https://doi.org/10.1063/1.96799>
- Bonilla, R. S., Hoex, B., Hamer, P., & Wilshaw, P. R. (2017). Dielectric surface passivation for silicon solar cells: A review. *physica status solidi (a)*, 214(7), 1700293. <https://doi.org/10.1002/pssa.201700293>
- Bredemeier, D., Walter, D. C., Heller, R., & Schmidt, J. (2019). Impact of Hydrogen-Rich Silicon Nitride Material Properties on Light-Induced Lifetime Degradation in Multicrystalline Silicon. *Physica Status Solidi - Rapid Research Letters*, 13(8), 1–5. <https://doi.org/10.1002/pssr.201900201>
- Breitenstein, L., Richter, A., Hermle, M., & Warta, W. (2011). Impact of wet-chemical cleaning on the passivation quality of Al₂O₃ layers. *Conference Record of the IEEE Photovoltaic Specialists Conference*, (1), 001400–001404. <https://doi.org/10.1109/PVSC.2011.6186218>

- Brendel, R., & Peibst, R. (2016). Contact Selectivity and Efficiency in Crystalline Silicon Photovoltaics. *IEEE Journal of Photovoltaics*, 6(6), 1413–1420. <https://doi.org/10.1109/JPHOTOV.2016.2598267>
- Brodsky, M. H., Cardona, M., & Cuomo, J. J. (1977). Infrared and Raman spectra of the silicon-hydrogen bonds in amorphous silicon prepared by glow discharge and sputtering. *Physical Review B*, 16(8), 3556–3571. <https://doi.org/10.1103/PhysRevB.16.3556>
- Brüggemann, R., & Reynolds, S. (2006). Modulated photoluminescence studies for lifetime determination in amorphous-silicon passivated crystalline-silicon wafers. *Journal of Non-Crystalline Solids*, 352(9-20 SPEC. ISS.), 1888–1891. <https://doi.org/10.1016/j.jnoncrysol.2005.11.092>
- Bruhat, E., Desrues, T., Blanc-Pelissier, D., Martel, B., Cabal, R., & Dubois, S. (2020). Contacting n + Poly-Si Junctions with Fired AZO Layers: A Promising Approach for High Temperature Passivated Contact Solar Cells, 2319–2324. <https://doi.org/10.1109/pvsc40753.2019.8980652>
- Bryan, J. L., Carpenter III, J. V., Yu, Z. J., Leilaieoun, A. (, Shi, J., Weigand, W., Fisher, K. C., & Holman, Z. C. (2021). Aluminum–silicon interdiffusion in silicon heterojunction solar cells with a-Si:H(i)/a-Si:H(n/p)/Al rear contacts. *Journal of Physics D: Applied Physics*, 54(13), 134002. <https://doi.org/10.1088/1361-6463/abd5e5>
- Campa, A., Smole, F., Folchert, N., Wietler, T., Min, B., Brendel, R., & Topic, M. (2019). Detailed Analysis and Understanding of the Transport Mechanism of Poly-Si-Based Carrier Selective Junctions. *IEEE Journal of Photovoltaics*, 9(6), 1575–1582. <https://doi.org/10.1109/JPHOTOV.2019.2943610>
- Campbell, P., & Green, M. A. (1987). Light trapping properties of pyramidally textured surfaces. *Journal of Applied Physics*, 62(1), 243–249. <https://doi.org/10.1063/1.339189>
- Cao, Z., & Zhang, X. (2006). Experiments and theory of thermally-induced stress relaxation in amorphous dielectric films for MEMS and IC applications. *Sensors and Actuators A: Physical*, 127(2), 221–227. <https://doi.org/10.1016/j.sna.2005.08.025>
- Carlson, D. E., & Magee, C. W. (1978). A SIMS analysis of deuterium diffusion in hydrogenated amorphous silicon. *Applied Physics Letters*, 33(1), 81–83. <https://doi.org/10.1063/1.90153>
- Carpenter, J. V., Bailly, M., Boley, A., Shi, J., Minjares, M., Smith, D. J., Bowden, S., & Holman, Z. C. (2017). Substrate-independent analysis of microcrystalline silicon thin films using UV Raman spectroscopy. *Physica Status Solidi (B)*, 254(9), 1700204. <https://doi.org/10.1002/pssb.201700204>
- Castaner, L., Silvestre, S., Carter, J., Partron, D., & Ashburn, P. (1998). Effects of fluorine in silicon solar cells with polysilicon contacts. *Solar Energy Materials and Solar Cells*, 53(1-2), 115–129. [https://doi.org/10.1016/S0927-0248\(98\)00017-8](https://doi.org/10.1016/S0927-0248(98)00017-8)
- Chanbasha, A. R., & Wee, A. T. (2008). Ultralow-energy SIMS for shallow semiconductor depth profiling. *Applied Surface Science*, 255(4), 1307–1310. <https://doi.org/10.1016/j.apsusc.2008.05.030>
- Chen, D., Hamer, P., Kim, M., Chan, C., Ciesla née Wenham, A., Rougieux, F., Zhang, Y., Abbott, M., & Hallam, B. (2020). Hydrogen-induced degradation: Explaining the mechanism

- behind light- and elevated temperature-induced degradation in n- and p-type silicon. *Solar Energy Materials and Solar Cells*, 207(July 2019), 110353. <https://doi.org/10.1016/j.solmat.2019.110353>
- Chen, K., Nemeth, W., Theingi, S., Page, M., & Stradins, P. (2021). Effective Dielectric Passivation Scheme in Area-Selective Front / Back Poly-Si / SiO_x Passivating Contact Solar Cells. *2021 IEEE 48th Photovoltaic Specialist Conference, PVSC 2021*, 5–8.
- Chen, R., Wright, M., Chen, D., Yang, J., Zheng, P., Zhang, X., Wenham, S., & Ciesla, A. (2021). 24.58% efficient commercial n-type silicon solar cells with hydrogenation. *Progress in Photovoltaics: Research and Applications*, (August), 1–6. <https://doi.org/10.1002/pip.3464>
- Chen, Y., Chen, D., Liu, C., Wang, Z., Zou, Y., He, Y., Wang, Y., Yuan, L., Gong, J., Lin, W., Zhang, X., Yang, Y., Shen, H., Feng, Z., Altermatt, P. P., & Verlinden, P. J. (2019). Mass production of industrial tunnel oxide passivated contacts (i-TOPCon) silicon solar cells with average efficiency over 23% and modules over 345 W. *Progress in Photovoltaics: Research and Applications*, pip.3180. <https://doi.org/10.1002/pip.3180>
- Chen, Y., Yang, Y., Zhang, X., Xu, G., Marmon, J. K., Li, Z., Feng, Z., Verlinden, P. J., & Shen, H. (2015). Forming aluminum electrodes by screen printing and electron-beam evaporation for high performance interdigitated back contact solar cells. *Solar Energy Materials and Solar Cells*, 143, 205–211. <https://doi.org/10.1016/j.solmat.2015.06.057>
- Ciesla, A., Wenham, S., Chen, R., Chan, C., Chen, D., Hallam, B., Payne, D., Fung, T., Kim, M., Liu, S., Wang, S., Kim, K., Samadi, A., Sen, C., Vargas, C., Varshney, U., Stefani, B. V., Hamer, P., Nampalli, N., ... Abbott, M. (2018). Hydrogen-Induced Degradation. *7th World Conference on Photovoltaic Energy Conversion*, (July).
- Çiftçipinar, H. E., Stodolny, M. K., Wu, Y., Janssen, G. J., Löffler, J., Schmitz, J., Lenes, M., Luchies, J. M., & Geerligs, L. J. (2017). Study of screen printed metallization for polysilicon based passivating contacts. *Energy Procedia*, 124, 851–861. <https://doi.org/10.1016/j.egypro.2017.09.242>
- Cousins, P. J., Smith, D. D., Luan, H. C., Manning, J., Dennis, T. D., Waldhauer, A., Wilson, K. E., Harley, G., & Mulligan, W. P. (2010). Generation 3: Improved performance at lower cost. *Conference Record of the IEEE Photovoltaic Specialists Conference*, 275–278. <https://doi.org/10.1109/PVSC.2010.5615850>
- Cuevas, A. (2013). Physical model of back line-contact front-junction solar cells. *Journal of Applied Physics*, 113(16), 164502. <https://doi.org/10.1063/1.4800840>
- Cuevas, A., Allen, T., Bullock, J., Yimao Wan, Di Yan, & Xinyu Zhang. (2015). Skin care for healthy silicon solar cells. *2015 IEEE 42nd Photovoltaic Specialist Conference (PVSC)*, (1), 1–6. <https://doi.org/10.1109/PVSC.2015.7356379>
- Cuevas, A., Wan, Y., Yan, D., Samundsett, C., Allen, T., Zhang, X., Cui, J., & Bullock, J. (2018). Carrier population control and surface passivation in solar cells. *Solar Energy Materials and Solar Cells*, 184(February), 38–47. <https://doi.org/10.1016/j.solmat.2018.04.026>
- Cuevas, A., & Macdonald, D. (2004). Measuring and interpreting the lifetime of silicon wafers. *Solar Energy*, 76(1-3), 255–262. <https://doi.org/10.1016/j.solener.2003.07.033>

Bibliography

- Cuevas, A., & Sinton, R. A. (1997). Prediction of the open-circuit voltage of solar cells from the steady-state photoconductance. *Progress in Photovoltaics: Research and Applications*, 5(2), 79–90. [https://doi.org/10.1002/\(SICI\)1099-159X\(199703/04\)5:2<79::AID-PIP155>3.0.CO;2-J](https://doi.org/10.1002/(SICI)1099-159X(199703/04)5:2<79::AID-PIP155>3.0.CO;2-J)
- De Guzman, J. A., Markevich, V. P., Hiller, D., Hawkins, I. D., Halsall, M. P., & Peaker, A. R. (2021). Passivation of thermally-induced defects with hydrogen in float-zone silicon. *Journal of Physics D: Applied Physics*, 54(27). <https://doi.org/10.1088/1361-6463/abf807>
- Deal, B. E., MacKenna, E. L., & Castro, P. L. (1969). Characteristics of Fast Surface States Associated with SiO₂-Si and Si₃N₄-SiO₂-Si Structures. *Journal of The Electrochemical Society*, 116(7), 997. <https://doi.org/10.1149/1.2412205>
- Dekkers, H. F., Beaucarne, G., Hiller, M., Charifi, H., & Slaoui, A. (2006). Molecular hydrogen formation in hydrogenated silicon nitride. *Applied Physics Letters*, 89(21). <https://doi.org/10.1063/1.2396900>
- Demaurex, B., De Wolf, S., Descoedres, A., Charles Holman, Z., & Ballif, C. (2012). Damage at hydrogenated amorphous/crystalline silicon interfaces by indium tin oxide overlayer sputtering. *Applied Physics Letters*, 101(17). <https://doi.org/10.1063/1.4764529>
- Descoedres, A., Holman, Z. C., Barraud, L., Morel, S., De Wolf, S., & Ballif, C. (2013). >21% Efficient Silicon Heterojunction Solar Cells on N-and P-Type Wafers Compared. *IEEE Journal of Photovoltaics*, 3(1), 83–89. <https://doi.org/10.1109/JPHOTOV.2012.2209407>
- Desrues, T., Lanterne, A., Seron, C., Rousseau, S., Pihan, E., Dubois, S., Borvon, G., Torregrosa, F., & Roux, L. (2021). Poly-Si/SiO_x Passivating Contacts on Both Sides: A Versatile Technology for High Efficiency Solar Cells. *Conference Record of the IEEE Photovoltaic Specialists Conference*, (857793), 1069–1072. <https://doi.org/10.1109/PVSC43889.2021.9518773>
- Desthieux, A. (2021). *Development and characterization of fired passivating contacts for p-type silicon solar cells fabrication* (Doctoral dissertation) [NNT: 2021IPPAX091]. Ecole Polytechnique, Institut Polytechnique de Paris. <http://www.theses.fr/2021IPPAX091>
- Desthieux, A., Posada, J., Grand, P.-P., Broussillou, C., Bazer-Bachi, B., Goaer, G., Messou, D., Bouttemy, M., Drahi, E., & Roca i Cabarrocas, P. (2020a). Impact of PECVD $\mu\text{c-Si:H}$ deposition on tunnel oxide for passivating contacts. *EPJ Photovoltaics*, 11, 3. <https://doi.org/10.1051/epjpv/2020001>
- Desthieux, A., Sreng, M., Bulkin, P., Florea, I., Drahi, E., Bazer-Bachi, B., Vanel, J. C., Silva, F., Posada, J., & I Cabarrocas, P. R. (2020b). In Situ Modulated PhotoLuminescence for Process Optimization of Crystalline Silicon Passivation. *Conference Record of the IEEE Photovoltaic Specialists Conference, 2020-June*, 0964–0968. <https://doi.org/10.1109/PVSC45281.2020.9300631>
- DeWolf, S., Descoedres, A., Holman, Z. C., & Ballif, C. (2012). High-efficiency silicon heterojunction solar cells: A review. *Green*, 2(1), 7–24. <https://doi.org/10.1515/green-2011-0018>
- Dexter, D. L. (1956). Absorption of Light by Atoms in Solids. *Physical Review*, 101(1), 48–55. <https://doi.org/10.1103/PhysRev.101.48>

- Dingemans, G., Beyer, W., Van De Sanden, M. C. M., & Kessels, W. M. M. (2010). Hydrogen induced passivation of Si interfaces by Al₂O₃ films and SiO₂/Al₂O₃ stacks. *Applied Physics Letters*, 97(15), 2008–2011. <https://doi.org/10.1063/1.3497014>
- Dingemans, G., Einsele, F., Beyer, W., Van De Sanden, M. C., & Kessels, W. M. (2012). Influence of annealing and Al₂O₃ properties on the hydrogen-induced passivation of the Si/SiO₂ interface. *Journal of Applied Physics*, 111(9). <https://doi.org/10.1063/1.4709729>
- Dingemans, G., Engelhart, P., Seguin, R., Einsele, F., Hoex, B., van de Sanden, M. C. M., & Kessels, W. M. M. (2009). Stability of Al₂O₃ and Al₂O₃/a-SiN_x:H stacks for surface passivation of crystalline silicon. *Journal of Applied Physics*, 106(11), 114907. <https://doi.org/10.1063/1.3264572>
- Dingemans, G., & Kessels, W. M. M. (2012). Status and prospects of Al₂O₃-based surface passivation schemes for silicon solar cells. *Journal of Vacuum Science & Technology A: Vacuum, Surfaces, and Films*, 30(4), 040802. <https://doi.org/10.1116/1.4728205>
- Doolittle, L. R. (1986). A semiautomatic algorithm for rutherford backscattering analysis. *Nuclear Instruments and Methods in Physics Research Section B: Beam Interactions with Materials and Atoms*, 15(1-6), 227–231. [https://doi.org/10.1016/0168-583X\(86\)90291-0](https://doi.org/10.1016/0168-583X(86)90291-0)
- D’Orazio, M., Di Perna, C., & Di Giuseppe, E. (2014). Experimental operating cell temperature assessment of BIPV with different installation configurations on roofs under Mediterranean climate. *Renewable Energy*, 68, 378–396. <https://doi.org/10.1016/j.renene.2014.02.009>
- Dornstetter, J.-C. (2014). *Microcrystalline silicon deposited from sif₄/h₂/ar plasmas and its application to photovoltaics* (Doctoral dissertation) [HAL Id: tel-01111141]. Ecole Polytechnique. <https://pastel.archives-ouvertes.fr/tel-01111141>
- Duchamp, M., Boothroyd, C. B., Moreno, M. S., van Aken, B. B., Soppe, W. J., & Dunin-Borkowski, R. E. (2013). Electron energy-loss spectroscopy of boron-doped layers in amorphous thin film silicon solar cells. *Journal of Applied Physics*, 113(9), 093513. <https://doi.org/10.1063/1.4793587>
- Dutta, A. (2017). Fourier Transform Infrared Spectroscopy. *Spectroscopic methods for nanomaterials characterization* (pp. 73–93). Elsevier. <https://doi.org/10.1016/B978-0-323-46140-5.00004-2>
- Duttagupta, S., Nandakumar, N., Padhamnath, P., Buatis, J. K., Stangl, R., & Aberle, A. G. (2018). monoPoly™ cells: Large-area crystalline silicon solar cells with fire-through screen printed contact to doped polysilicon surfaces. *Solar Energy Materials and Solar Cells*, 187(8), 76–81. <https://doi.org/10.1016/j.solmat.2018.05.059>
- Eidelloth, S., & Brendel, R. (2014). Analytical theory for extracting specific contact resistances of thick samples from the transmission line method. *IEEE Electron Device Letters*, 35(1), 9–11. <https://doi.org/10.1109/LED.2013.2290602>
- Faes, A., Despeisse, M., Levrat, J., Champlaud, J., Badel, N., Kiaee, M., Söderström, T., Yao, Y., Grischke, R., Gragert, M., Ufheil, J., Papet, P., Strahm, B., Cattaneo, B., Cattin, J., Baumgartner, Y., Hessler-Wyser, A., & Ballif, C. (2014). SmartWire Solar Cell Interconnection

- Technology. *29th European Photovoltaic Solar Energy Conference and Exhibition*, 2555–2561. <https://doi.org/10.4229/EUPVSEC20142014-5DO.16.3>
- Falster, R. J., Cornara, M., Gambaro, D., Olmo, M., & Pagani, M. (1997). Effect of High Temperature Pre-Anneal on Oxygen Precipitates Nucleation Kinetics in Si. *Solid State Phenomena*, 57-58, 123–128. <https://doi.org/10.4028/www.scientific.net/SSP.57-58.123>
- Fang, C. J., Ley, L., Shanks, H. R., Gruntz, K. J., & Cardona, M. (1980). Bonding of fluorine in amorphous hydrogenated silicon. *Physical Review B*, 22(12), 6140–6148. <https://doi.org/10.1103/PhysRevB.22.6140>
- Fargeix, A., & Ghibaudo, G. (1983). Dry oxidation of silicon: A new model of growth including relaxation of stress by viscous flow. *Journal of Applied Physics*, 54(12), 7153–7158. <https://doi.org/10.1063/1.331986>
- Feldmann, F., Steinhauser, B., Arya, V., Büchler, A., Brand, A. A., Kluska, S., Hermle, M., & Glunz, S. W. (2017a). EVALUATION OF TOPCON TECHNOLOGY ON LARGE AREA SOLAR CELLS. *33rd European PV Solar Energy Conference and Exhibition*. https://www.ise.fraunhofer.de/content/dam/ise/de/documents/publications/conference-paper/33-eupvsec-2017/Feldmann_2DO33.pdf
- Feldmann, F., Bivour, M., Reichel, C., Hermle, M., & Glunz, S. W. (2014a). Passivated rear contacts for high-efficiency n-type Si solar cells providing high interface passivation quality and excellent transport characteristics. *Solar Energy Materials and Solar Cells*, 120(PART A), 270–274. <https://doi.org/10.1016/j.solmat.2013.09.017>
- Feldmann, F., Nogay, G., Löper, P., Young, D. L., Lee, B. G., Stradins, P., Hermle, M., & Glunz, S. W. (2018). Charge carrier transport mechanisms of passivating contacts studied by temperature-dependent J-V measurements. *Solar Energy Materials and Solar Cells*, 178, 15–19. <https://doi.org/10.1016/j.solmat.2018.01.008>
- Feldmann, F., Reichel, C., Müller, R., & Hermle, M. (2017b). The application of poly-Si/SiO_x contacts as passivated top/rear contacts in Si solar cells. *Solar Energy Materials and Solar Cells*, 159, 265–271. <https://doi.org/10.1016/j.solmat.2016.09.015>
- Feldmann, F., Schön, J., Niess, J., Lerch, W., & Hermle, M. (2019). Studying dopant diffusion from Poly-Si passivating contacts. *Solar Energy Materials and Solar Cells*, 200(April), 109978. <https://doi.org/10.1016/j.solmat.2019.109978>
- Feldmann, F., Simon, M., Bivour, M., Reichel, C., Hermle, M., & Glunz, S. W. (2014b). Efficient carrier-selective p- and n-contacts for Si solar cells. *Solar Energy Materials and Solar Cells*, 131, 100–104. <https://doi.org/10.1016/j.solmat.2014.05.039>
- Feldmann, F., Steinhauser, B., Pernau, T., Nagel, H., Fellmeth, T., Mack, S., Ourinson, D., Lohmüller, E., Polzin, J., Moldovan, A., Bivour, M., Clement, F., Rentsch, J., Hermle, M., & Glunz, S. W. (2020). Industrial TOPCon Solar Cells Realized by a PECVD Tube Process. *37th European PV Solar Energy Conference and Exhibition*, (September).
- Folchert, N., Rienäcker, M., Yeo, A. A., Min, B., Peibst, R., & Brendel, R. (2018). Temperature-dependent contact resistance of carrier selective Poly-Si on oxide junctions. *Solar Energy Materials and Solar Cells*, 185(March), 425–430. <https://doi.org/10.1016/j.solmat.2018.05.046>

- Fossum, J. G., & Burgess, E. L. (1978). High-efficiency p+-n-n+ back-surface-field silicon solar cells. *Applied Physics Letters*, 33(3), 238–240. <https://doi.org/10.1063/1.90311>
- Fritz, J. M., Zuschlag, A., Skorka, D., Schmid, A., & Hahn, G. (2017). Temperature dependent degradation and regeneration of differently doped mc-Si materials. *Energy Procedia*, 124, 718–725. <https://doi.org/10.1016/j.egypro.2017.09.085>
- Fujiwara, H., & Kondo, M. (2007). Impact of epitaxial growth at the heterointerface of a-Si:H/c-Si solar cells. *Applied Physics Letters*, 90(1). <https://doi.org/10.1063/1.2426900>
- Fukano, A., & Oyanagi, H. (2003). Highly insulating ultrathin SiO₂ film grown by photooxidation. *Journal of Applied Physics*, 94(5), 3345–3349. <https://doi.org/10.1063/1.1597940>
- Gao, T., Yang, Q., Guo, X., Huang, Y., Zhang, Z., Wang, Z., Liao, M., Shou, C., Zeng, Y., Yan, B., Hou, G., Zhang, X., Zhao, Y., & Ye, J. (2019). An industrially viable TOPCon structure with both ultra-thin SiO_x and n+-poly-Si processed by PECVD for p-type c-Si solar cells. *Solar Energy Materials and Solar Cells*, 200(May), 109926. <https://doi.org/10.1016/j.solmat.2019.109926>
- Giesecke, J. A., Glunz, S. W., & Warta, W. (2013). Understanding and resolving the discrepancy between differential and actual minority carrier lifetime. *Journal of Applied Physics*, 113(7). <https://doi.org/10.1063/1.4790716>
- Glunz, S. W., Feldmann, F., Richter, A., Bivour, M., Reichel, C., Steinkemper, H., Benick, J., & Hermle, M. (2015). The Irresistible Charm of a Simple Current Flow Pattern – 25% With a Solar Cell Featuring a Full-Area Back Contact. *Proceedings of the 31st European Photovoltaic Solar Energy Conference and Exhibition*, (September), 259–263. <https://doi.org/10.4229/EUPVSEC20152015-2BP.1.1>
- Glunz, S. W., Preu, R., & Biro, D. (2012). *Crystalline silicon solar cells. State-of-the-art and future developments* (Vol. 1). <https://doi.org/10.1016/B978-0-08-087872-0.00117-7>
- Glunz, S. W., & Feldmann, F. (2018). SiO₂ surface passivation layers – a key technology for silicon solar cells. *Solar Energy Materials and Solar Cells*, 185(February), 260–269. <https://doi.org/10.1016/j.solmat.2018.04.029>
- Glunz, S. W., Sproul, A. B., Warta, W., & Wettling, W. (1994). Injection-level-dependent recombination velocities at the Si-SiO₂ interface for various dopant concentrations. *Journal of Applied Physics*, 75(3), 1611–1615. <https://doi.org/10.1063/1.356399>
- Goetzberger, A., Voss, B., & Knobloch, J. (1997). *Sonnenenergie: Photovoltaik* (2nd ed.). B. G. Teubner.
- Gotoh, K., Wilde, M., Kato, S., Ogura, S., Kurokawa, Y., Fukutani, K., & Usami, N. (2019). Hydrogen concentration at a-Si:H/c-Si heterointerfaces—The impact of deposition temperature on passivation performance. *AIP Advances*, 9(7), 075115. <https://doi.org/10.1063/1.5100086>
- Grant, N. E., & McIntosh, K. R. (2009). Surface Passivation Attained by Silicon Dioxide Grown at Low Temperature in Nitric Acid. *24th European Photovoltaic Solar Energy Conference*, 30(9), 1676–1679. <https://doi.org/10.1109/LED.2009.2025898>
- Grant, N. E., Rougieux, F. E., Macdonald, D., Bullock, J., & Wan, Y. (2015). Grown-in defects limiting the bulk lifetime of p-type float-zone silicon wafers. *Journal of Applied Physics*, 117(5), 055711. <https://doi.org/10.1063/1.4907804>

Bibliography

- Grant, N. E., Markevich, V. P., Mullins, J., Peaker, A. R., Rougieux, F., & Macdonald, D. (2016a). Thermal activation and deactivation of grown-in defects limiting the lifetime of float-zone silicon. *Physica Status Solidi - Rapid Research Letters*, 10(6), 443–447. <https://doi.org/10.1002/pssr.201600080>
- Grant, N. E., Markevich, V. P., Mullins, J., Peaker, A. R., Rougieux, F., Macdonald, D., & Murphy, J. D. (2016b). Permanent annihilation of thermally activated defects which limit the lifetime of float-zone silicon. *Physica Status Solidi (A) Applications and Materials Science*, 213(11), 2844–2849. <https://doi.org/10.1002/pssa.201600360>
- Grant, N. E., & Murphy, J. D. (2017). Temporary Surface Passivation for Characterisation of Bulk Defects in Silicon: A Review. *Physica Status Solidi - Rapid Research Letters*, 11(11), 1–18. <https://doi.org/10.1002/pssr.201700243>
- Grant, N. E., Niewelt, T., Wilson, N. R., Wheeler-Jones, E. C., Bullock, J., Al-Amin, M., Schubert, M. C., Van Veen, A. C., Javey, A., & Murphy, J. D. (2017). Superacid-Treated Silicon Surfaces: Extending the Limit of Carrier Lifetime for Photovoltaic Applications. *IEEE Journal of Photovoltaics*, 7(6), 1574–1583. <https://doi.org/10.1109/JPHOTOV.2017.2751511>
- Green, M. A. (1982). Accuracy of analytical expressions for solar cell fill factors. *Solar Cells*, 7(3), 337–340. [https://doi.org/10.1016/0379-6787\(82\)90057-6](https://doi.org/10.1016/0379-6787(82)90057-6)
- Green, M. A. (2008). Self-consistent optical parameters of intrinsic silicon at 300 K including temperature coefficients. *Solar Energy Materials and Solar Cells*, 92(11), 1305–1310. <https://doi.org/10.1016/j.solmat.2008.06.009>
- Grübel, B., Cimiotti, G., Arya, V., Fellmeth, T., Feldmann, F., Steinhäuser, B., Kluge, T., Landgraf, D., & Glatthaar, M. (2019). Plated Ni/Cu/Ag for TOPCon Solar Cell Metallization. *Presented at the 36th European PV Solar Energy Conference and Exhibition*, (September), 9–13.
- Haase, F., Hollemann, C., Schäfer, S., Merkle, A., Rienäcker, M., Krügener, J., Brendel, R., & Peibst, R. (2018). Laser contact openings for local poly-Si-metal contacts enabling 26.1%-efficient POLO-IBC solar cells. *Solar Energy Materials and Solar Cells*, 186(May), 184–193. <https://doi.org/10.1016/j.solmat.2018.06.020>
- Hall, R. N. (1952). Electron-Hole Recombination in Germanium. *Physical Review*, 87(2), 387–387. <https://doi.org/10.1103/PhysRev.87.387>
- Hallam, B., Chen, D., Kim, M., Stefani, B., Hoex, B., Abbott, M., & Wenham, S. (2017). The role of hydrogenation and gettering in enhancing the efficiency of next-generation Si solar cells: An industrial perspective. *Physica Status Solidi (A) Applications and Materials Science*, 214(7). <https://doi.org/10.1002/pssa.201700305>
- Hallam, B., Hamer, P. G., Ciesla née Wenham, A. M., Chan, C. E., Vicari Stefani, B., & Wenham, S. (2020). Development of advanced hydrogenation processes for silicon solar cells via an improved understanding of the behaviour of hydrogen in silicon. *Progress in Photovoltaics: Research and Applications*, (October 2019). <https://doi.org/10.1002/pip.3240>
- Hallam, B. J., Hamer, P. G., Wang, S., Song, L., Nampalli, N., Abbott, M. D., Chan, C. E., Lu, D., Wenham, A. M., Mai, L., Borojevic, N., Li, A., Chen, D., Kim, M. Y., Azmi, A., & Wenham,

- S. (2015). Advanced Hydrogenation of Dislocation Clusters and Boron-oxygen Defects in Silicon Solar Cells. *Energy Procedia*, 77, 799–809. <https://doi.org/10.1016/j.egypro.2015.07.113>
- Hamer, P., Hallam, B., Bonilla, R. S., Altermatt, P. P., Wilshaw, P., & Wenham, S. (2018). Modelling of hydrogen transport in silicon solar cell structures under equilibrium conditions. *Journal of Applied Physics*, 123(4). <https://doi.org/10.1063/1.5016854>
- Hamer, P., Hallam, B., Wenham, S., & Abbott, M. (2014). Manipulation of hydrogen charge states for passivation of P-type wafers in photovoltaics. *IEEE Journal of Photovoltaics*, 4(5), 1252–1260. <https://doi.org/10.1109/JPHOTOV.2014.2339494>
- Hangleiter, A., & Häcker, R. (1990). Enhancement of band-to-band Auger recombination by electron-hole correlations. *Physical Review Letters*, 65(2), 215–218. <https://doi.org/10.1103/PhysRevLett.65.215>
- Haschke, J., Lemerle, R., Aissa, B., Abdallah, A. A., Kivambe, M. M., Boccard, M., & Ballif, C. (2019). Annealing of Silicon Heterojunction Solar Cells: Interplay of Solar Cell and Indium Tin Oxide Properties. *IEEE Journal of Photovoltaics*, 9(5), 1202–1207. <https://doi.org/10.1109/JPHOTOV.2019.2924389>
- Haug, F.-J., Ballif, C., Seif, J., & Cattin, J. *Fundamentals and processes for photovoltaic devices*. Script for the identically titled lectures given at EPFL by Prof. Ballif and Dr. Haug. 2021.
- Haug, F.-J., Ingenito, A., Meyer, F., Libraro, S., Bolis, N., Leon, J. J. D., Allebe, C., & Ballif, C. (2019). Contributions to the Contact Resistivity in Fired Tunnel-Oxide Passivating Contacts for Crystalline Silicon Solar Cells. *IEEE Journal of Photovoltaics*, 1–6. <https://doi.org/10.1109/JPHOTOV.2019.2939880>
- Haug, F.-J., Libraro, S., Lehmann, M., Morisset, A., Ingenito, A., & Ballif, C. (2021b). *Separating bulk and surface recombination mechanisms in fz silicon with fired passivating contacts* [Manuscript in preparation].
- Haug, F.-J., Morisset, A., Wyss, P., Lehmann, M., Hessler-Wyser, A., Jeangros, Q., Ingenito, A., Ballif, C., Kumar, C. N. S., Eswara, S., & Valle, N. (2021c). Passivating Polysilicon Recombination Junctions for Crystalline Silicon Solar Cells. *physica status solidi (RRL) – Rapid Research Letters*. <https://doi.org/10.1002/pssr.202100272>
- Hayes, M., Martel, B., Dubois, S., Morisset, A., & Palais, O. (2019). Study of non fire-through metallization processes of boron-doped polysilicon passivated contacts for high efficiency silicon solar cells. *AIP Conference Proceedings*, 2147. <https://doi.org/10.1063/1.5123833>
- Hermle, M., Feldmann, F., Bivour, M., Goldschmidt, J. C., & Glunz, S. W. (2020). Passivating contacts and tandem concepts: Approaches for the highest silicon-based solar cell efficiencies. *Applied Physics Reviews*, 7(2), 021305. <https://doi.org/10.1063/1.5139202>
- Herring, C., Johnson, N. M., & Van de Walle, C. G. (2001). Energy levels of isolated interstitial hydrogen in silicon. *Physical Review B*, 64(12), 125209. <https://doi.org/10.1103/PhysRevB.64.125209>
- Hezel, R., Blumenstock, K., & Schoerner, R. (1983). Fixed Insulator Charges and Interface States in Mnos Structures With Apcvd and Pecvd Silicon Nitride. *Proceedings - The Electrochemical Society*, 83-8, 280–292.

Bibliography

- Hiller, D., Markevich, V. P., de Guzman, J. A. T., König, D., Prucnal, S., Bock, W., Julin, J., Peaker, A. R., Macdonald, D., Grant, N. E., & Murphy, J. D. (2020). Kinetics of Bulk Lifetime Degradation in Float-Zone Silicon: Fast Activation and Annihilation of Grown-In Defects and the Role of Hydrogen versus Light. *physica status solidi (a)*, 217(17), 2000436. <https://doi.org/10.1002/pssa.202000436>
- Hollemann, C., Folchert, N., Harvey, S. P., Stradins, P., Young, D. L., Salles de Souza, C. L., Rienäcker, M., Haase, F., Brendel, R., & Peibst, R. (2021a). Changes in hydrogen concentration and defect state density at the poly-Si/SiO_x/c-Si interface due to firing. *Solar Energy Materials and Solar Cells*, 231(5), 111297. <https://doi.org/10.1016/j.solmat.2021.111297>
- Hollemann, C., Haase, F., Krügener, J., Brendel, R., & Peibst, R. (2020). Firing stability of n-type poly-Si on oxide junctions formed by quartz tube annealing. *IEEE 47th Photovoltaic Specialist Conference (PVSC)*.
- Hollemann, C., Haase, F., Schäfer, S., Krügener, J., Brendel, R., & Peibst, R. (2019). 26.1%-efficient POLO-IBC cells: Quantification of electrical and optical loss mechanisms. *Progress in Photovoltaics: Research and Applications*, (October 2018), 1–9. <https://doi.org/10.1002/pip.3098>
- Hollemann, C., Rienäcker, M., Soeriyadi, A., Madumelu, C., Haase, F., Krügener, J., Hallam, B., Brendel, R., & Peibst, R. (2021b). Firing stability of tube furnace-annealed n-type poly-Si on oxide junctions. *Progress in Photovoltaics: Research and Applications*, (July), 1–16. <https://doi.org/10.1002/pip.3459>
- Hong, J., Kessels, W. M. M., Soppe, W. J., Weeber, A. W., Arnoldbik, W. M., & van de Sanden, M. C. M. (2003). Influence of the high-temperature “firing” step on high-rate plasma deposited silicon nitride films used as bulk passivating antireflection coatings on silicon solar cells. *Journal of Vacuum Science & Technology B: Microelectronics and Nanometer Structures*, 21(5), 2123. <https://doi.org/10.1116/1.1609481>
- Hu, S. M. (1991). Stress-related problems in silicon technology. *Journal of Applied Physics*, 70(6). <https://doi.org/10.1063/1.349282>
- IEA. (2021). *Key World Energy Statistics 2021* (tech. rep.). International Energy Agency. <https://www.iea.org/>
- Ingenito, A., Libraro, S., Wyss, P., Allebé, C., Despeisse, M., Nicolay, S., Haug, F. J., & Ballif, C. (2021). Implementation and understanding of p+ fired rear hole selective tunnel oxide passivating contacts enabling >22% conversion efficiency in p-type c-Si solar cells. *Solar Energy Materials and Solar Cells*, 219(September 2020). <https://doi.org/10.1016/j.solmat.2020.110809>
- Ingenito, A., Limodio, G., Procel, P., Yang, G., Dijkslag, H., Isabella, O., & Zeman, M. (2017). Silicon Solar Cell Architecture with Front Selective and Rear Full Area Ion-Implanted Passivating Contacts. *Solar RRL*, 1(7), 1700040. <https://doi.org/10.1002/solr.201700040>
- Ingenito, A., Nogay, G., Jeangros, Q., Rucavado, E., Allebé, C., Eswara, S., Valle, N., Wirtz, T., Horzel, J., Koida, T., Morales-Masis, M., Despeisse, M., Haug, F. J., Löper, P., & Ballif, C. (2018). A passivating contact for silicon solar cells formed during a single firing thermal annealing. *Nature Energy*, 3(9), 800–808. <https://doi.org/10.1038/s41560-018-0239-4>

- Ingenito, A., Nogay, G., Stuckelberger, J., Wyss, P., Gnocchi, L., Allebe, C., Horzel, J., Despeisse, M., Haug, F. J., Loper, P., & Ballif, C. (2019). Phosphorous-Doped Silicon Carbide as Front-Side Full-Area Passivating Contact for Double-Side Contacted c-Si Solar Cells. *IEEE Journal of Photovoltaics*, 9(2), 346–354. <https://doi.org/10.1109/JPHOTOV.2018.2886234>
- IPCC, Masson-Delmotte, V., Zhai, P., Pirani, A., Connors, S., Péan, C., Berger, S., Caud, N., Chen, Y., Goldfarb, L., Gomis, M., Huang, M., Leitzell, K., Lonnoy, E., Matthews, J., Maycock, T., Waterfield, T., Yelekçi, O., Yu, R., & Zhou (eds.), B. (2021). IPCC, 2021: Summary for Policymakers. *Climate change 2021: the physical science basis. contribution of working group I to the sixth assessment report of the intergovernmental panel on climate change* (In Press). Cambridge University Press.
- IRENA. (2021a). *Renewable Power Generation Costs in 2020* (tech. rep.). International Renewable Energy Agency.
- IRENA. (2021b). *World Energy Transitions Outlook: 1.5C Pathway* (tech. rep.). International Renewable Energy Agency. <https://irena.org/publications/2021/March/World-Energy-Transitions-Outlook>
- ITRPV. (2018). *International Technology Roadmap for Photovoltaic (ITRPV) - Results 2017* (tech. rep.). VDMA e.V. <http://scholar.google.com/scholar?hl=en&btnG=Search&q=intitle:International+Technology+Roadmap+for+Photovoltaic#1>
- ITRPV. (2021). *International Technology Roadmap for Photovoltaic (ITRPV) - 2020 Results* (tech. rep.). VDMA e.V. <https://itrpv.vdma.org/documents/27094228/29066965/20210ITRPV/08ccda3a-585e-6a58-6afa-6c20e436cf41>
- Jensen, M. A., Zuschlag, A., Wieghold, S., Skorka, D., Morishige, A. E., Hahn, G., & Buonassisi, T. (2018). Evaluating root cause: The distinct roles of hydrogen and firing in activating light- and elevated temperature-induced degradation. *Journal of Applied Physics*, 124(8), 085701. <https://doi.org/10.1063/1.5041756>
- JinkoSolar. (2021). *Jinkosolar large-area n-type monocrystalline silicon solar cell reaches record-breaking new high efficiency of 25.25%*. Retrieved November 10, 2021, from <http://jinkosolar.com.au/2021/05/jinkosolar-large-area-n-type-monocrystalline-silicon-solar-cell-reaches-record-breaking-new-high-efficiency-of-25-25/>
- Johnson, N. M., Biegelsen, D. K., & Moyer, M. D. (1981). Low-Temperature Annealing and Hydrogenation of Defects at the Si-SiO₂ Interface. *Journal of vacuum science & technology*, 19(3), 390–394. <https://doi.org/10.1116/1.571070>
- Johnson, N. M., Ponce, F. A., Street, R. A., & Nemanich, R. J. (1987). Defects in c-Si induced by hydrogenation. *Phys. Rev. B*, 35(8), 4166–4169.
- Joonwichien, S., Moriya, M., Utsunomiya, S., Kida, Y., Shirasawa, K., & Takato, H. (2019). Metal-induced Recombination Losses associated with Si present within Passivation Layers and Aluminum Paste for PERCs. *2019 IEEE 46th Photovoltaic Specialists Conference (PVSC)*, 3252–3257. <https://doi.org/10.1109/PVSC40753.2019.8981135>
- Kail, F., Hadjadj, A., & Roca i Cabarrocas, P. (2005). Hydrogen diffusion and induced-crystallization in intrinsic and doped hydrogenated amorphous silicon films. *Thin Solid Films*, 487(1–2), 126–131. <https://doi.org/10.1016/j.tsf.2005.01.049>

Bibliography

- Kale, A. S., Nemeth, W., Nanayakkara, S. U., Guthrey, H., Page, M., Al-jassim, M., Agarwal, S., & Stradins, P. (2018). Tunneling or Pinholes : Understanding the Transport Mechanisms in SiO_x Based Passivated Contacts for High-Efficiency Silicon Solar Cells. *45th IEEE PVSC*, 1–4.
- Kane, D. E., & Swanson, R. M. (1985). Measurement of the emitter saturation current by a contactless photoconductivity decay method. *Proceedings of the 18th IEEE PVSC*, 578–583.
- Kang, D., Sio, H. C., Stuckelberger, J., Liu, R., Yan, D., Zhang, X., & Macdonald, D. (2021a). Optimum Hydrogen Injection in Phosphorus-Doped Polysilicon Passivating Contacts. *ACS Applied Materials & Interfaces*, acsami.1c17342. <https://doi.org/10.1021/acsami.1c17342>
- Kang, D., Sio, H. C., Stuckelberger, J., Yan, D., Nguyen, H. T., Truong, T. N., Liu, R., & MacDonald, D. (2021b). Firing Stability of Polysilicon Passivating Contacts: The Role of Hydrogen. *Conference Record of the IEEE Photovoltaic Specialists Conference*, 701–705. <https://doi.org/10.1109/PVSC43889.2021.9519080>
- Kang, D., Sio, H. C., Yan, D., Stuckelberger, J., Zhang, X., & Macdonald, D. (2022). Firing stability of phosphorus-doped polysilicon passivating contacts: Factors affecting the degradation behavior. *Solar Energy Materials and Solar Cells*, 234(May 2021), 111407. <https://doi.org/10.1016/j.solmat.2021.111407>
- Kang, J. S., & Schroder, D. K. (1989). Gettering in silicon. *Journal of Applied Physics*, 65(8), 2974–2985. <https://doi.org/10.1063/1.342714>
- Kelton, K. F., Falster, R., Gambaro, D., Olmo, M., Cornara, M., & Wei, P. F. (1999). Oxygen precipitation in silicon: Experimental studies and theoretical investigations within the classical theory of nucleation. *Journal of Applied Physics*, 85(12), 8097–8111. <https://doi.org/10.1063/1.370648>
- Kern, W. (1990). The Evolution of Silicon Wafer Cleaning Technology. *Journal of The Electrochemical Society*, 137(6), 1887–1892. <https://doi.org/10.1149/1.2086825>
- Kerr, M. J., & Cuevas, A. (2002). Very low bulk and surface recombination in oxidized silicon wafers. *Semiconductor Science and Technology*, 17(1), 35–38. <https://doi.org/10.1088/0268-1242/17/1/306>
- Kimmerle, A., Greulich, J., & Wolf, A. (2015). Carrier-diffusion corrected J₀-analysis of charge carrier lifetime measurements for increased consistency. *Solar Energy Materials and Solar Cells*, 142, 116–122. <https://doi.org/10.1016/j.solmat.2015.06.043>
- Kobayashi, H., Asuha, M., Maida, O., Takahashi, M., & Iwasa, H. (2003). Nitric acid oxidation of Si to form ultrathin silicon dioxide layers with a low leakage current density. *Journal of Applied Physics*, 94(11), 7328–7335. <https://doi.org/10.1063/1.1621720>
- Kwark, Y., Sinton, R., & Swanson, R. (1984). SIPOS Heterojunction contacts to silicon. *IEDM*, 94305(415), 742–745. <https://doi.org/10.1109/IEDM.1984.190832>
- Lanterne, A., Yang, J., Loretz, J. C., Martel, B., Caruel, M., Enjalbert, N., Lignier, H., & Dubois, S. (2020). LPCV-Deposited Poly-Si Passivated Contacts: Surface Passivation, Gettering and Integration in High Efficiency Devices. *Conference Record of the IEEE Photovoltaic*

- Specialists Conference, 2020-June*, 2675–2678. <https://doi.org/10.1109/PVSC45281.2020.9300425>
- LaSalvia, V., Youssef, A., Jensen, M. A., Looney, E. E., Nemeth, W., Page, M., Nam, W., Buonassisi, T., & Stradins, P. (2018). Tabula Rasa for n-Cz silicon-based photovoltaics. *Progress in Photovoltaics: Research and Applications*, (February), 1–8. <https://doi.org/10.1002/pip.3068>
- Lee, Y., Oh, W., Dao, V. A., Hussain, S. Q., & Yi, J. (2012). Ultrathin Oxide Passivation Layer by Rapid Thermal Oxidation for the Silicon Heterojunction Solar Cell Applications. *International Journal of Photoenergy*, 2012, 1–5. <https://doi.org/10.1155/2012/753456>
- Lehmann, M., Valle, N., Horzel, J., Pshenova, A., Wyss, P., Döbeli, M., Despeisse, M., Eswara, S., Wirtz, T., Jeangros, Q., Hessler-Wyser, A., Haug, F.-J., Ingenito, A., & Ballif, C. (2019). Analysis of hydrogen distribution and migration in fired passivating contacts (FPC). *Solar Energy Materials and Solar Cells*, 200(June), 110018. <https://doi.org/10.1016/j.solmat.2019.110018>
- Leilaieioun, M., & Holman, Z. C. (2016). Accuracy of expressions for the fill factor of a solar cell in terms of open-circuit voltage and ideality factor. *Journal of Applied Physics*, 120(12). <https://doi.org/10.1063/1.4962511>
- Lelièvre, J. F., Fourmond, E., Kaminski, A., Palais, O., Ballutaud, D., & Lemiti, M. (2009). Study of the composition of hydrogenated silicon nitride SiN_x:H for efficient surface and bulk passivation of silicon. *Solar Energy Materials and Solar Cells*, 93(8), 1281–1289. <https://doi.org/10.1016/j.solmat.2009.01.023>
- Libraro, S. (2019). *Advanced characterization of fired passivating contacts for silicon solar cells* (Master's thesis). Università di Bologna. <https://amslaurea.unibo.it/>
- Libraro, S., Lehmann, M., Leon, J. J. D., Allebé, C., Descoeudres, A., Nicolay, S., Ballif, C., Ingenito, A., Haug, F.-j., & Hessler-Wyser, A. (2021). Investigation of Al-SiN_x interactions for firing-through metallization of passivating contacts solar cells [Poster]. *Microscopy Conference*.
- Liu, W., Yang, X., Kang, J., Li, S., Xu, L., Zhang, S., Xu, H., Peng, J., Xie, F., Fu, J. H., Wang, K., Liu, J., Alzahrani, A., & De Wolf, S. (2019). Polysilicon Passivating Contacts for Silicon Solar Cells: Interface Passivation and Carrier Transport Mechanism. *ACS Applied Energy Materials*, 2(7), 4609–4617. <https://doi.org/10.1021/acs.aem.8b02149>
- LONGi Solar. (2021). *Longi breaks three world records for solar cell efficiency of n-type topcon, p-type topcon and hjt*. Retrieved November 9, 2021, from <https://www.prnewswire.com/news/longi-solar/>
- Louwen, A., Van Sark, W., Schropp, R., & Faaij, A. (2016). A cost roadmap for silicon heterojunction solar cells. *Solar Energy Materials and Solar Cells*, 147, 295–314. <https://doi.org/10.1016/j.solmat.2015.12.026>
- Lozac'h, M., & Nunomura, S. (2020). Role of silicon surface, polished <100> and <111> or textured, on the efficiency of double-sided TOPCon solar cells. *Progress in Photovoltaics: Research and Applications*, 28(10), 1001–1011. <https://doi.org/10.1002/pip.3304>

- Lozac'h, M., Nunomura, S., & Matsubara, K. (2020). Double-sided TOPCon solar cells on textured wafer with ALD SiO_x layer. *Solar Energy Materials & Solar Cells*, 207(November 2019), 110357. <https://doi.org/10.1016/j.solmat.2019.110357>
- Lozac'h, M., Nunomura, S., Umishio, H., Matsui, T., & Matsubara, K. (2019). Roles of Hydrogen Atoms in p-type Poly-Si/SiO_x Passivation Layer for Crystalline Silicon Solar Cell Applications. *Japanese Journal of Applied Physics*, (2), 1–3. <https://doi.org/10.7567/1347-4065/ab14fe>
- Mack, S., Schube, J., Fellmeth, T., Feldmann, F., Lenes, M., & Luchies, J.-M. (2017). Metallisation of Boron-Doped Polysilicon Layers by Screen Printed Silver Pastes. *physica status solidi (RRL) - Rapid Research Letters*, 1700334, 1700334. <https://doi.org/10.1002/pssr.201700334>
- Mack, S., Wolf, A., Brosinsky, C., Schmeisser, S., Kimmerle, A., Saint-Cast, P., Hofmann, M., & Biro, D. (2011). Silicon Surface Passivation by Thin Thermal Oxide/PECVD Layer Stack Systems. *IEEE Journal of Photovoltaics*, 1(2), 135–145. <https://doi.org/10.1109/JPHOTOV.2011.2173299>
- McIntosh, K., Abbott, M., & Sudbury, B. (2011). *Mobility calculator*. Retrieved March 20, 2019, from <https://www2.pvlighthouse.com.au/calculators/Mobility%20calculator/Mobility%20calculator.aspx>
- McPhail, D., & Dowsett, M. (2009). Dynamic SIMS. In J. C. Vickerman & I. S. Gilmore (Eds.), *Surface analysis, the principal techniques* (2nd Editio, pp. 207–268). John Wiley & Sons, Ltd.
- Melskens, J., Palmans, J., Karwal, S., Yang, G., Stodolny, M., Romijn, I., Janssen, G., Creatore, M., & Kessels, W. (2017). Ultrathin silicon oxide: what makes it suitable as interlayer in passivating contacts for silicon solar cells? *33rd EUPVSEC*, (September).
- Merkle, A., Seren, S., Knauss, H., Min, B., Steffens, J., Terheiden, B., Brendel, R., & Peibst, R. (2018). Atmospheric Pressure Chemical Vapor Deposition of In-Situ Doped Amorphous Silicon Layers for Passivating Contacts. *35th European Photovoltaic Solar Energy Conference and Exhibition*, 785–791. <https://www.eupvsec-proceedings.com/proceedings?top100&paper=46005>
- Meyer, F., Ingenito, A., Diaz Leon, J. J., Niquille, X., Allebé, C., Nicolay, S., Haug, F. J., & Ballif, C. (2022). Localisation of front side passivating contacts for direct metallisation of high-efficiency c-Si solar cells. *Solar Energy Materials and Solar Cells*, 235(May 2021). <https://doi.org/10.1016/j.solmat.2021.111455>
- Meyer, F., Savoy, A., Diaz Leon, J. J., Persoz, M., Niquille, X., Allebé, C., Nicolay, S., Haug, F. J., Ingenito, A., & Ballif, C. (2021). Optimization of front SiN_x/ITO stacks for high-efficiency two-side contacted c-Si solar cells with co-annealed front and rear passivating contacts. *Solar Energy Materials and Solar Cells*, 219. <https://doi.org/10.1016/j.solmat.2020.110815>
- Meyer Burger. (2020). *Meyer burger and csem extend collaboration for the joint development of novel solar cells and modules*. Retrieved November 30, 2021, from <https://www.meyerburger.com/en/newsroom/artikel/meyer-burger-and-csem-extend-collaboration-for-the-joint-development-of-novel-solar-cells-and-modules>

- Meyer Burger. (2021). *Meyer burger eröffnet neues werk zur herstellung von hochleistungs-solarzellen in thalheim (stadt bitterfeld-wolfen)*. Retrieved November 30, 2021, from <https://www.meyerburger.com/de/newsroom/artikel/meyer-burger-eroeffnet-neues-werk-zur-herstellung-von-hochleistungs-solarzellen-in-thalheim-stadt-bitterfeld-wolfen>
- Mitchell, J., Macdonald, D., & Cuevas, A. (2009). Thermal activation energy for the passivation of the n-type crystalline silicon surface by hydrogenated amorphous silicon. *Applied Physics Letters*, 94(16), 162102. <https://doi.org/10.1063/1.3120765>
- Moiseiwitsch, N. E., & Ashburn, P. (1994). The Benefits of Fluorine in pnp Polysilicon Emitter Bipolar Transistors. *IEEE Transactions on Electron Devices*, 41(7), 1249–1256. <https://doi.org/10.1109/16.293355>
- Moldovan, A., Feldmann, F., Krugel, G., Zimmer, M., Rentsch, J., Hermle, M., Roth-Fölsch, A., Kaufmann, K., & Hagendorf, C. (2014). Simple Cleaning and Conditioning of Silicon Surfaces with UV/Ozone Sources. *Energy Procedia*, 55, 834–844. <https://doi.org/10.1016/j.egypro.2014.08.067>
- Moldovan, A., Feldmann, F., Zimmer, M., Rentsch, J., Benick, J., & Hermle, M. (2015). Tunnel oxide passivated carrier-selective contacts based on ultra-thin SiO₂ layers. *Solar Energy Materials and Solar Cells*, 142, 123–127. <https://doi.org/10.1016/j.solmat.2015.06.048>
- Morisset, A. (2019). *Integration of poly-si/siox contacts in silicon solar cells : optimization and understanding of conduction and passivation properties* (Doctoral dissertation) [NNT: 2019SACLS443]. Université Paris-Saclay. <http://www.theses.fr/2019SACLS443>
- Morisset, A., Cabal, R., Giglia, V., Boulineau, A., De Vito, E., Chabli, A., Dubois, S., Alvarez, J., & Kleider, J. P. (2021). Evolution of the surface passivation mechanism during the fabrication of ex-situ doped poly-Si(B)/SiO_x passivating contacts for high-efficiency c-Si solar cells. *Solar Energy Materials and Solar Cells*, 221(December 2020). <https://doi.org/10.1016/j.solmat.2020.110899>
- Morisset, A., Cabal, R., Grange, B., Marchat, C., Alvarez, J., Gueunier-Farret, M. E., Dubois, S., & Kleider, J. P. (2019). Highly passivating and blister-free hole selective poly-silicon based contact for large area crystalline silicon solar cells. *Solar Energy Materials and Solar Cells*, 200(April), 109912. <https://doi.org/10.1016/j.solmat.2019.109912>
- Mullins, J., Markevich, V. P., Vaqueiro-Contreras, M., Grant, N. E., Jensen, L., Jabłoński, J., Murphy, J. D., Halsall, M. P., & Peaker, A. R. (2018). Thermally activated defects in float zone silicon: Effect of nitrogen on the introduction of deep level states. *Journal of Applied Physics*, 124(3), 035701. <https://doi.org/10.1063/1.5036718>
- Mundt, L. E., Schubert, M. C., Schon, J., Michl, B., Niewelt, T., Schindler, F., & Warta, W. (2015). Spatially Resolved Impurity Identification via Temperature- and Injection-Dependent Photoluminescence Imaging. *IEEE Journal of Photovoltaics*, 5(5), 1503–1509. <https://doi.org/10.1109/JPHOTOV.2015.2447837>
- Murphy, J. D., Bothe, K., Krain, R., Voronkov, V. V., & Falster, R. J. (2012). Parameterisation of injection-dependent lifetime measurements in semiconductors in terms of Shockley-Read-Hall statistics: An application to oxide precipitates in silicon. *Journal of Applied Physics*, 111(11). <https://doi.org/10.1063/1.4725475>

- Nagel, H., Berge, C., & Aberle, A. G. (1999). Generalized analysis of quasi-steady-state and quasi-transient measurements of carrier lifetimes in semiconductors. *Journal of Applied Physics*, 86(11), 6218–6221. <https://doi.org/10.1063/1.371633>
- Nastasi, M., Mayer, J. W., & Wang, Y. (2015). *Ion Beam Analysis: Fundamentals and Applications*. CRC Press.
- Nemeth, B., Harvey, S. P., Li, J. V., Young, D. L., Upadhyaya, A., LaSalvia, V., Lee, B. G., Page, M. R., & Stradins, P. (2017). Effect of the SiO₂ interlayer properties with solid-source hydrogenation on passivated contact performance and surface passivation. *Energy Procedia*, 124, 295–301. <https://doi.org/10.1016/j.egypro.2017.09.302>
- Nicolai, M., Zanuccoli, M., Feldmann, F., Hermle, M., & Fiegna, C. (2018). Analysis of Silicon Solar Cells With Poly-Si/SiO_x Carrier-Selective Base and Emitter Contacts. *IEEE Journal of Photovoltaics*, 8(1), 103–109. <https://doi.org/10.1109/JPHOTOV.2017.2775142>
- Nie, S., Bonilla, R. S., & Hameiri, Z. (2021). Unravelling the silicon-silicon dioxide interface under different operating conditions. *Solar Energy Materials and Solar Cells*, 224(September 2020), 111021. <https://doi.org/10.1016/j.solmat.2021.111021>
- Niewelt, T., Richter, A., Kho, T. C., Grant, N. E., Bonilla, R. S., Steinhauser, B., Polzin, J. I., Feldmann, F., Hermle, M., Murphy, J. D., Phang, S. P., Kwapil, W., & Schubert, M. C. (2018). Taking monocrystalline silicon to the ultimate lifetime limit. *Solar Energy Materials and Solar Cells*, 185(May), 252–259. <https://doi.org/10.1016/j.solmat.2018.05.040>
- Niewelt, T., Selinger, M., Grant, N. E., Kwapil, W., Murphy, J. D., & Schubert, M. C. (2017). Light-induced activation and deactivation of bulk defects in boron-doped float-zone silicon. *Journal of Applied Physics*, 121(18), 185702. <https://doi.org/10.1063/1.4983024>
- Niewelt, T., Steinhauser, B., Richter, A., Veith-Wolf, B., Fell, A., Hammann, B., Grant, N. E., Black, L., Tan, J., Youssef, A., Murphy, J. D., Schmidt, J., Schubert, M. C., & Glunz, S. W. (2022). Reassessment of the intrinsic bulk recombination in crystalline silicon. *Solar Energy Materials and Solar Cells*, 235, 111467. <https://doi.org/10.1016/j.solmat.2021.111467>
- Nogay, G. (2018). *Full-area passivating contacts with high and low thermal budgets: solutions for high efficiency c-si solar cells* (Doctoral dissertation) [Thèse n°8707]. Ecole Polytechnique Fédérale de Lausanne. <https://doi.org/10.5075/epfl-thesis-8707>
- Nogay, G., Ingenito, A., Rucavado, E., Jeangros, Q., Stuckelberger, J., Wyss, P., Morales-Masis, M., Haug, F.-J., Loper, P., & Ballif, C. (2018). Crystalline Silicon Solar Cells With Coannealed Electron- and Hole-Selective SiC_x Passivating Contacts. *IEEE Journal of Photovoltaics*, 8(6), 1478–1485. <https://doi.org/10.1109/JPHOTOV.2018.2866189>
- Nogay, G., Stuckelberger, J., Wyss, P., Jeangros, Q., Allebé, C., Niquille, X., Debrot, F., Despeisse, M., Haug, F. J., Löper, P., & Ballif, C. (2016). Silicon-Rich Silicon Carbide Hole-Selective Rear Contacts for Crystalline-Silicon-Based Solar Cells. *ACS Applied Materials and Interfaces*, 8(51), 35660–35667. <https://doi.org/10.1021/acsami.6b12714>
- Nogay, G., Stuckelberger, J., Wyss, P., Rucavado, E., Allebé, C., Koida, T., Morales-Masis, M., Despeisse, M., Haug, F. J., Löper, P., & Ballif, C. (2017). Interplay of annealing temperature and doping in hole selective rear contacts based on silicon-rich silicon-carbide thin

- films. *Solar Energy Materials and Solar Cells*, 173, 18–24. <https://doi.org/10.1016/j.solmat.2017.06.039>
- NREL. (2021). *Best research-cell efficiency chart*. Retrieved November 9, 2021, from <https://www.nrel.gov/pv/cell-efficiency.html>
- Olesinski, R. W., & Abbaschian, G. J. (1984). The C-Si Carbon-Silicon system. *Bulletin of Alloy Phase Diagrams*, 5(5), 486–489. <https://doi.org/10.1007/BF02872902>
- Olibet, S., Vallat-Sauvain, E., & Ballif, C. (2007). Model for a-Si:H/c-Si interface recombination based on the amphoteric nature of silicon dangling bonds. *Physical Review B - Condensed Matter and Materials Physics*, 76(3), 1–14. <https://doi.org/10.1103/PhysRevB.76.035326>
- Oliveau, C., Desrues, T., Lanterne, A., Seron, C., Rousseau, S., & Dubois, S. (2020). Double-Side Integration of High Temperature Passivated Contacts: Application to Cast-Mono Si. *Conference Record of the IEEE Photovoltaic Specialists Conference, 2020-June*, 1163–1166. <https://doi.org/10.1109/PVSC45281.2020.9300752>
- Ono, Y., Tabe, M., & Sakakibara, Y. (1993). Segregation and defect termination of fluorine at SiO₂/Si interfaces. *Applied Physics Letters*, 62(4), 375–377. <https://doi.org/10.1063/1.108961>
- Padhamnath, P., Khanna, A., Nandakumar, N., Nampalli, N., Shanmugam, V., Aberle, A. G., & Duttagupta, S. (2020). Development of thin polysilicon layers for application in monoPoly™ cells with screen-printed and fired metallization. *Solar Energy Materials and Solar Cells*, 207(November 2019), 110358. <https://doi.org/10.1016/j.solmat.2019.110358>
- Pal, S., Barrirero, J., Lehmann, M., Jeangros, Q., Valle, N., Haug, F. J., Hessler-Wyser, A., Shyam Kumar, C. N., Mücklich, F., Wirtz, T., & Eswara, S. (2021). Quantification of hydrogen in nanostructured hydrogenated passivating contacts for silicon photovoltaics combining SIMS-APT-TEM: A multiscale correlative approach. *Applied Surface Science*, 555(March), 149650. <https://doi.org/10.1016/j.apsusc.2021.149650>
- Pankove, J. I., & Tarng, M. L. (1979). Amorphous silicon as a passivant for crystalline silicon. *Applied Physics Letters*, 34(2), 156–157. <https://doi.org/10.1063/1.90711>
- Park, H., Bae, S., Park, S. J., Hyun, J. Y., Lee, C. H., Choi, D., Kang, D., Han, H., Kang, Y., Lee, H. S., & Kim, D. (2019). Role of polysilicon in poly-Si/SiO_x passivating contacts for high-efficiency silicon solar cells. *RSC Advances*, 9(40), 23261–23266. <https://doi.org/10.1039/c9ra03560e>
- Peibst, R., Römer, U., Larionova, Y., Rienäcker, M., Merkle, A., Folchert, N., Reiter, S., Turcu, M., Min, B., Krügener, J., Tetzlaff, D., Bugiel, E., Wietler, T., & Brendel, R. (2016). Working principle of carrier selective poly-Si/c-Si junctions: Is tunnelling the whole story? *Solar Energy Materials and Solar Cells*, 158, 60–67. <https://doi.org/10.1016/j.solmat.2016.05.045>
- Peibst, R., Larionova, Y., Reiter, S., Wietler, T. F., Orlowski, N., Schafer, S., Min, B., Stratmann, M., Tetzlaff, D., Krügener, J., Hohne, U., Kahler, J.-D., Mehlich, H., Frigge, S., & Brendel, R. (2018). Building Blocks for Industrial, Screen-Printed Double-Side Contacted POLO

- Cells With Highly Transparent ZnO:Al Layers. *IEEE Journal of Photovoltaics*, 1–7. <https://doi.org/10.1109/JPHOTOV.2018.2813427>
- Polzin, J.-I., Hammann, B., Niewelt, T., Kwapil, W., Hermle, M., & Feldmann, F. (2021). Thermal activation of hydrogen for defect passivation in poly-Si based passivating contacts. *Solar Energy Materials and Solar Cells*, 230(June), 111267. <https://doi.org/10.1016/j.solmat.2021.111267>
- Polzin, J.-I., Lange, S., Richter, S., Moldovan, A., Bivour, M., Hagendorf, C., Hermle, M., Glunz, S. W., & Feldmann, F. (2020). Temperature-induced stoichiometric changes in thermally grown interfacial oxide in tunnel-oxide passivating contacts. *Solar Energy Materials and Solar Cells*, 218(8), 110713. <https://doi.org/10.1016/j.solmat.2020.110713>
- Qiu, K., Pomaska, M., Li, S., Lambert, A., Duan, W., Gad, A., Geitner, M., Brugger, J., Liang, Z., Shen, H., Finger, F., Rau, U., & Ding, K. (2020). Development of Conductive SiC_xH as a New Hydrogenation Technique for Tunnel Oxide Passivating Contacts. *ACS Applied Materials and Interfaces*, 12(26), 29986–29992. <https://doi.org/10.1021/acsami.0c06637>
- Reeves, G., & Harrison, H. (1982). Obtaining the specific contact resistance from transmission line model measurements. *IEEE Electron Device Letters*, 3(5), 111–113. <https://doi.org/10.1109/EDL.1982.25502>
- Reichel, C., Feldmann, F., Müller, R., Reedy, R. C., Lee, B. G., Young, D. L., Stradins, P., Hermle, M., & Glunz, S. W. (2015). Tunnel oxide passivated contacts formed by ion implantation for applications in silicon solar cells. *Journal of Applied Physics*, 118(20), 205701. <https://doi.org/10.1063/1.4936223>
- Rein, S., Rehrl, T., Warta, W., & Glunz, S. W. (2002). Lifetime spectroscopy for defect characterization: Systematic analysis of the possibilities and restrictions. *Journal of Applied Physics*, 91(3), 2059–2070. <https://doi.org/10.1063/1.1428095>
- Rein, S. (2005). *Lifetime Spectroscopy* (Vol. 85). Springer Berlin Heidelberg. <https://doi.org/10.1007/3-540-27922-9>
- Richter, A., Benick, J., Feldmann, F., Fell, A., Steinhäuser, B., Polzin, J.-I., Tücher, N., Murthy, J. N., Hermle, M., & Glunz, S. W. (2019). Both Sides Contacted Silicon Solar Cells: Options for Approaching 26% Efficiency. *36th European PV Solar Energy Conference and Exhibition*, (September).
- Richter, A., Benick, J., Feldmann, F., Fell, A., Hermle, M., & Glunz, S. W. (2017). N-Type Si solar cells with passivating electron contact: Identifying sources for efficiency limitations by wafer thickness and resistivity variation. *Solar Energy Materials and Solar Cells*, 173(March), 96–105. <https://doi.org/10.1016/j.solmat.2017.05.042>
- Richter, A., Glunz, S. W., Werner, F., Schmidt, J., & Cuevas, A. (2012). Improved quantitative description of Auger recombination in crystalline silicon. *Physical Review B - Condensed Matter and Materials Physics*, 86(16), 1–14. <https://doi.org/10.1103/PhysRevB.86.165202>
- Richter, A., Müller, R., Benick, J., Feldmann, F., Steinhäuser, B., Reichel, C., Fell, A., Bivour, M., Hermle, M., & Glunz, S. W. (2021). Design rules for high-efficiency both-sides-

- contacted silicon solar cells with balanced charge carrier transport and recombination losses. *Nature Energy*, 6(4), 429–438. <https://doi.org/10.1038/s41560-021-00805-w>
- Riegel, S., Mutter, F., Lauermann, T., Terheiden, B., & Hahn, G. (2012). Review on screen printed metallization on p-type silicon. *Energy Procedia*, 21(October 2011), 14–23. <https://doi.org/10.1016/j.egypro.2012.05.003>
- Römer, U., Peibst, R., Ohrdes, T., Lim, B., Krügener, J., Bugiel, E., Wietler, T., & Brendel, R. (2014). Recombination behavior and contact resistance of n+ and p+ poly-crystalline Si/mono-crystalline Si junctions. *Solar Energy Materials and Solar Cells*, 131, 85–91. <https://doi.org/10.1016/j.solmat.2014.06.003>
- Rougieux, F. E., Grant, N. E., Barugkin, C., MacDonald, D., & Murphy, J. D. (2015). Influence of annealing and bulk hydrogenation on lifetime-limiting defects in nitrogen-doped floating zone silicon. *IEEE Journal of Photovoltaics*, 5(2), 495–498. <https://doi.org/10.1109/JPHOTOV.2014.2367912>
- Rougieux, F. E., Sun, C., & Macdonald, D. (2018). Determining the charge states and capture mechanisms of defects in silicon through accurate recombination analyses: A review. *Solar Energy Materials and Solar Cells*, 187(February), 263–272. <https://doi.org/10.1016/j.solmat.2018.07.029>
- Schmidt, J., Peibst, R., & Brendel, R. (2018). Surface passivation of crystalline silicon solar cells: Present and future. *Solar Energy Materials and Solar Cells*, 187(July), 39–54. <https://doi.org/10.1016/j.solmat.2018.06.047>
- Schnabel, M., van de Loo, B. W. H., Nemeth, W., Macco, B., Stradins, P., Kessels, W. M. M., & Young, D. L. (2018). Hydrogen passivation of poly-Si/SiO_x contacts for Si solar cells using Al₂O₃ studied with deuterium. *Applied Physics Letters*, 112(20), 203901. <https://doi.org/10.1063/1.5031118>
- Seibt, M., Sattler, A., Rudolf, C., Voß, O., Kveder, V., & Schröter, W. (2006). Gettering in silicon photovoltaics: Current state and future perspectives. *Physica Status Solidi (A) Applications and Materials Science*, 203(4), 696–713. <https://doi.org/10.1002/pssa.200664516>
- Seif, J. P., Descoeur, A., Nogay, G., Hanni, S., de Nicolas, S. M., Holm, N., Geissbühler, J., Hessler-Wyser, A., Duchamp, M., Dunin-Borkowski, R. E., Ledinsky, M., De Wolf, S., & Ballif, C. (2016). Strategies for Doped Nanocrystalline Silicon Integration in Silicon Heterojunction Solar Cells. *IEEE Journal of Photovoltaics*, 6(5), 1132–1140. <https://doi.org/10.1109/JPHOTOV.2016.2571619>
- Sen, C., Chan, C., Hamer, P., Wright, M., Chong, C. M., Hallam, B., & Abbott, M. (2020). Eliminating light- and elevated temperature-induced degradation in P-type PERC solar cells by a two-step thermal process. *Solar Energy Materials and Solar Cells*, 209(December 2019), 110470. <https://doi.org/10.1016/j.solmat.2020.110470>
- Sharma, R., Szlufcik, J., Radhakrishnan, H. S., & Poortmans, J. (2022). P-type poly-Si/SiO contact by aluminium-induced crystallization of amorphous silicon. *Solar Energy Materials and Solar Cells*, 234(October 2021), 111416. <https://doi.org/10.1016/j.solmat.2021.111416>
- Sheoran, M., Kim, D. S., Rohatgi, A., Dekkers, H. F., Beaucarne, G., Young, M., & Asher, S. (2008). Hydrogen diffusion in silicon from plasma-enhanced chemical vapor deposited

Bibliography

- silicon nitride film at high temperature. *Applied Physics Letters*, 92(17), 1–4. <https://doi.org/10.1063/1.2917467>
- Shih, A., Yeh, J. L., Lee, S. C., & Yang, T. R. (2000). Structural and electronic differences between deuterated and hydrogenated amorphous silicon. *Journal of Applied Physics*, 88(3), 1684–1687. <https://doi.org/10.1063/1.373872>
- Shih, A., Yeh, S. H., Lee, S. C., & Yang, T. R. (2001). Structural differences between deuterated and hydrogenated silicon nitride/oxynitride. *Journal of Applied Physics*, 89(10), 5355–5361. <https://doi.org/10.1063/1.1364645>
- Shockley, W., & Read, W. T. (1952). Statistics of the Recombinations of Holes and Electrons. *Physical Review*, 87(5), 835–842. <https://doi.org/10.1103/PhysRev.87.835>
- Sinton, R., Cuevas, A., & Stuckings, M. (1996). Quasi-steady-state photoconductance, a new method for solar cell material and device characterization. *Conference Record of the Twenty Fifth IEEE Photovoltaic Specialists Conference - 1996*, 457–460. <https://doi.org/10.1109/PVSC.1996.564042>
- Sinton, R., & Cuevas, A. (1996). Contactless determination of current-voltage characteristics and minority-carrier lifetimes in semiconductors from quasi-steady-state photoconductance data. *Applied Physics Letters*, 69(17), 2510–2512. <https://doi.org/10.1063/1.117723>
- Sinton Instruments. (n.d.). *Wct-120ts*. Retrieved November 2, 2021, from <https://www.sintoninstruments.com/products/wct-120ts/%20calculator/Mobility%20calculator.aspx>
- Sio, H. C., Kang, D., Liu, R., Stuckelberger, J., Samundsett, C., & Macdonald, D. (2021). Fluorine Passivation of Defects and Interfaces in Crystalline Silicon. *ACS Applied Materials and Interfaces*, 13(27), 32503–32509. <https://doi.org/10.1021/acsami.1c07221>
- Sio, H. C., Phang, S. P., Nguyen, H. T., Hameiri, Z., & Macdonald, D. (2019). Hydrogenation in multicrystalline silicon: The impact of dielectric film properties and firing conditions. *Progress in Photovoltaics: Research and Applications*, 12(August), 10–12. <https://doi.org/10.1002/pip.3199>
- Smets, A. H. M., & van de Sanden, M. C. M. (2007). Relation of the Si-H stretching frequency to the nanostructural Si-H bulk environment. *Physical Review B*, 76(7), 073202. <https://doi.org/10.1103/PhysRevB.76.073202>
- Smit, C., Van Swaaij, R. A., Donker, H., Petit, A. M., Kessels, W. M., & Van de Sanden, M. C. (2003). Determining the material structure of microcrystalline silicon from Raman spectra. *Journal of Applied Physics*, 94(5), 3582–3588. <https://doi.org/10.1063/1.1596364>
- Smith, D. D., Reich, G., Baldrias, M., Reich, M., Boitnott, N., & Bunea, G. (2016). Silicon solar cells with total area efficiency above 25%. *2016 IEEE 43rd Photovoltaic Specialists Conference (PVSC), 2016-Novem*, 3351–3355. <https://doi.org/10.1109/PVSC.2016.7750287>
- Snel, J. (1981). The doped Si/SiO₂ interface. *Solid-State Electronics*, 24(2), 135–139. [https://doi.org/10.1016/0038-1101\(81\)90008-3](https://doi.org/10.1016/0038-1101(81)90008-3)
- Solaronix. (n.d.). *Solixon a-70 brochure*. Retrieved October 29, 2021, from <https://www.solaronix.com/equipment/mediumunits/>

- Song, J., Park, S., Kwon, S., Kim, S., Kim, H., Tark, S. J., Yoon, S., & Kim, D. (2012). A study on the aluminum fire-through to a-SiN_x:H thin film for crystalline solar cells. *Current Applied Physics*, 12(1), 313–318. <https://doi.org/10.1016/j.cap.2011.06.028>
- Sopori, B. L., Deng, X., Benner, J. P., Rohatgi, A., Sana, P., Estreicher, S. K., Park, Y. K., & Roberson, M. A. (1996). Hydrogen in silicon: A discussion of diffusion and passivation mechanisms. *Solar Energy Materials and Solar Cells*, 41-42, 159–169. [https://doi.org/10.1016/0927-0248\(95\)00098-4](https://doi.org/10.1016/0927-0248(95)00098-4)
- Sperber, D., Furtwängler, F., Herguth, A., & Hahn, G. (2016). On the Stability of Dielectric Passivation Layers Under Illumination and Temperature Treatment. *32nd European Photovoltaic Solar Energy Conference and Exhibition*, 523–526. <https://doi.org/10.4229/EUPVSEC20162016-2DO.3.4>
- Sperber, D., Heilemann, A., Herguth, A., & Hahn, G. (2017a). Temperature and Light-Induced Changes in Bulk and Passivation Quality of Boron-Doped Float-Zone Silicon Coated With SiN_x:H. *IEEE Journal of Photovoltaics*, 7(2), 463–470. <https://doi.org/10.1109/JPHOTOV.2017.2649601>
- Sperber, D., Herguth, A., & Hahn, G. (2017b). A 3-state defect model for light-induced degradation in boron-doped float-zone silicon. *Physica Status Solidi - Rapid Research Letters*, 11(3), 1–4. <https://doi.org/10.1002/pssr.201600408>
- Sproul, A. B. (1994). Dimensionless solution of the equation describing the effect of surface recombination on carrier decay in semiconductors. *Journal of Applied Physics*, 76(5), 2851–2854. <https://doi.org/10.1063/1.357521>
- Sreng, M. (2019). *Development of in-situ photoluminescence characterization tools for the study of semiconductors for photovoltaics application* (Doctoral dissertation) [NNT: 2019IPPAX003]. Institut Polytechnique de Paris. <http://www.theses.fr/2019IPPAX003>
- Stathis, J. H. (1995). Dissociation kinetics of hydrogen-passivated (100) Si/SiO₂ interface defects. *Journal of Applied Physics*, 77(12), 6205–6207. <https://doi.org/10.1063/1.359148>
- Stegemann, B., Gad, K. M., Balamou, P., Sixtensson, D., Vössing, D., Kasemann, M., & Angermann, H. (2017). Ultra-thin silicon oxide layers on crystalline silicon wafers: Comparison of advanced oxidation techniques with respect to chemically abrupt SiO₂/Si interfaces with low defect densities. *Applied Surface Science*, 395, 78–85. <https://doi.org/10.1016/j.apsusc.2016.06.090>
- Steinhauser, B., Feldmann, F., Ourinson, D., Nagel, H., Fellmeth, T., & Hermle, M. (2020). On the Influence of the SiN_x Composition on the Firing Stability of Poly-Si/SiN_x Stacks. *Physica Status Solidi (A) Applications and Materials Science*, 2000333, 1–5. <https://doi.org/10.1002/pssa.202000333>
- Steinhauser, B., Feldmann, F., Polzin, J.-i., Tutsch, L., Arya, V., Fischer, A., Moldovan, A., Benick, J., Richter, A., Brand, A. A., & Hermle, M. (2018). Large Area TOPCon Technology Achieving 23.4% Efficiency. *45th IEEE PVSC*.
- Stesmans, A. (2000). Interaction of Pb defects at the (111)Si/SiO₂ interface with molecular hydrogen: Simultaneous action of passivation and dissociation. *Journal of Applied Physics*, 88(1), 489–497. <https://doi.org/10.1063/1.373684>

- Stodolny, M., Lenes, M., Wu, Y., Janssen, G., Romijn, I., Luchies, J., & Geerligs, L. (2016). n-Type polysilicon passivating contact for industrial bifacial n-type solar cells. *Solar Energy Materials and Solar Cells*, 158, 24–28. <https://doi.org/10.1016/j.solmat.2016.06.034>
- Stöhr, M., Aprojanz, J., Brendel, R., & Dullweber, T. (2021). Firing-Stable PECVD SiO_xN_y/n-Poly-Si Surface Passivation for Silicon Solar Cells. *ACS Applied Energy Materials*, 4(5), 4646–4653. <https://doi.org/10.1021/acsaem.1c00265>
- Stuckelberger, J., Nogay, G., Wyss, P., Lehmann, M., Allebe, C., Debrot, F., Ledinsky, M., Fejfar, A., Despeisse, M., Haug, F. J., Loper, P., & Ballif, C. (2016a). Passivating contacts for silicon solar cells with 800 °C stability based on tunnel-oxide and highly crystalline thin silicon layer. *Conference Record of the IEEE Photovoltaic Specialists Conference, 2016-Novem*, 2518–2521. <https://doi.org/10.1109/PVSC.2016.7750100>
- Stuckelberger, J. (2018). *Transparent passivating contacts for front side application in crystalline silicon solar cells* (Doctoral dissertation) [Thèse n°8701]. Ecole Polytechnique Fédérale de Lausanne. <https://doi.org/10.5075/epfl-thesis-8701>
- Stuckelberger, J., Nogay, G., Wyss, P., Ingenito, A., Allebe, C., Horzel, J., Kamino, B. A., Despeisse, M., Haug, F.-j., Loper, P., & Ballif, C. (2018). Recombination Analysis of Phosphorus-Doped Nanostructured Silicon Oxide Passivating Electron Contacts for Silicon Solar Cells. *IEEE Journal of Photovoltaics*, 1–8. <https://doi.org/10.1109/JPHOTOV.2017.2779871>
- Stuckelberger, J., Nogay, G., Wyss, P., Jeangros, Q., Allebé, C., Debrot, F., Niquille, X., Ledinsky, M., Fejfar, A., Despeisse, M., Haug, F. J., Löper, P., & Ballif, C. (2016b). Passivating electron contact based on highly crystalline nanostructured silicon oxide layers for silicon solar cells. *Solar Energy Materials and Solar Cells*, 158, 2–10. <https://doi.org/10.1016/j.solmat.2016.06.040>
- Stuckelberger, J., Yan, D., Phang, S. P., Samundsett, C., & Macdonald, D. (2019). Industrial solar cells featuring carrier selective front contacts. *Asia-Pacific Solar Research Conference*.
- Swanson, R. M. (2005). Approaching the 29% limit efficiency of silicon solar cells. *Conference Record of the Thirty-first IEEE Photovoltaic Specialists Conference, 2005*.
- Sze, S. M., & Ng, K. K. (2007). *Physics of Semiconductor Devices* (3rd Editio). John Wiley & Sons, Ltd.
- Tao, Y., Upadhyaya, V., Chen, C.-W., Payne, A., Chang, E. L., Upadhyaya, A., & Rohatgi, A. (2016). Large area tunnel oxide passivated rear contact n -type Si solar cells with 21.2% efficiency. *Progress in Photovoltaics: Research and Applications*, 24(6), 830–835. <https://doi.org/10.1002/pip.2739>
- Tarr, N. (1985). A polysilicon emitter solar cell. *IEEE Electron Device Letters*, 6(12), 655–658. <https://doi.org/10.1109/EDL.1985.26264>
- Thurmond, C. D. (1975). The Standard Thermodynamic Functions for the Formation of Electrons and Holes in Ge, Si, GaAs , and GaP. *Journal of The Electrochemical Society*, 122(8), 1133–1141. <https://doi.org/10.1149/1.2134410>
- Tomasi, A., Paviet-Salomon, B., Jeangros, Q., Haschke, J., Christmann, G., Barraud, L., Descoeurdres, A., Seif, J. P., Nicolay, S., Despeisse, M., De Wolf, S., & Ballif, C. (2017). Simple pro-

- cessing of back-contacted silicon heterojunction solar cells using selective-area crystalline growth. *Nature Energy*, 2(5), 17062. <https://doi.org/10.1038/nenergy.2017.62>
- Truong, T. N., Yan, D., Chen, W., Tebyetekerwa, M., Young, M., Al-Jassim, M., Cuevas, A., Macdonald, D., & Nguyen, H. T. (2019a). Hydrogenation mechanisms of poly-Si/SiO_x passivating contacts by different capping layers. *Solar RRL*, 1900476, solr.201900476. <https://doi.org/10.1002/solr.201900476>
- Truong, T. N., Yan, D., Samundsett, C., Liu, A., Harvey, S. P., Young, M. R., Ding, Z., Tebyetekerwa, M., Kremer, F., Al-Jassim, M. M., Cuevas, A., MacDonald, D., & Nguyen, H. (2019b). Hydrogen-assisted defect engineering of doped poly-Si films for passivating contact solar cells. *ACS Applied Energy Materials*, acsaem.9b01771. <https://doi.org/10.1021/acsaem.9b01771>
- Trupke, T., Bardos, R. A., Schubert, M. C., & Warta, W. (2006). Photoluminescence imaging of silicon wafers. *Applied Physics Letters*, 89(4), 1–4. <https://doi.org/10.1063/1.2234747>
- Trupke, T., Green, M. A., Würfel, P., Altermatt, P. P., Wang, A., Zhao, J., & Corkish, R. (2003). Temperature dependence of the radiative recombination coefficient of intrinsic crystalline silicon. *Journal of Applied Physics*, 94(8), 4930. <https://doi.org/10.1063/1.1610231>
- Tutsch, L., Feldmann, F., MacCo, B., Bivour, M., Kessels, E., & Hermle, M. (2020). Improved Passivation of n-Type Poly-Si Based Passivating Contacts by the Application of Hydrogen-Rich Transparent Conductive Oxides. *IEEE Journal of Photovoltaics*, 10(4), 986–991. <https://doi.org/10.1109/JPHOTOV.2020.2992348>
- Tuttle, B. (2000). Energetics and diffusion of hydrogen. *Physical Review B - Condensed Matter and Materials Physics*, 61(7), 4417–4420. <https://doi.org/10.1103/PhysRevB.61.4417>
- UNDP. (2020). *The Next Frontier: Human Development and the Anthropocene* (tech. rep.). <http://hdr.undp.org/en/2020-report>
- van de Loo, B. W., Macco, B., Schnabel, M., Stodolny, M. K., Mewe, A. A., Young, D. L., Nemeth, W., Stradins, P., & Kessels, W. M. (2020). On the hydrogenation of Poly-Si passivating contacts by Al₂O₃ and SiN_x thin films. *Solar Energy Materials and Solar Cells*, 215(April), 3–8. <https://doi.org/10.1016/j.solmat.2020.110592>
- Vaqueiro-Contreras, M., Markevich, V. P., Halsall, M. P., Peaker, A. R., Santos, P., Coutinho, J., Öberg, S., Murin, L. I., Falster, R., Binns, J., Monakhov, E. V., & Svensson, B. G. (2017). Powerful recombination centers resulting from reactions of hydrogen with carbon–oxygen defects in n-type Czochralski-grown silicon. *Physica Status Solidi - Rapid Research Letters*, 11(8), 6–11. <https://doi.org/10.1002/pssr.201700133>
- Viala, J. C., Fortier, P., & Bouix, J. (1990). Stable and metastable phase equilibria in the chemical interaction between aluminium and silicon carbide. *Journal of Materials Science*, 25(3), 1842–1850. <https://doi.org/10.1007/BF01045395>
- Von Ammon, W. (2014). FZ and CZ crystal growth: Cost driving factors and new perspectives. *Physica Status Solidi (A) Applications and Materials Science*, 211(11), 2461–2470. <https://doi.org/10.1002/pssa.201400043>
- Voronkov, V. (1982). The mechanism of swirl defects formation in silicon. *Journal of Crystal Growth*, 59(3), 625–643. [https://doi.org/10.1016/0022-0248\(82\)90386-4](https://doi.org/10.1016/0022-0248(82)90386-4)

- Walter, D., Steckenreiter, V., Helmich, L., & Schmidt, J. (2017). PRODUCTION-COMPATIBLE REGENERATION OF BORON-DOPED CZOCHRALSKI-SILICON IN A COMBINED FAST-FIRING AND REGENERATION BELT-LINE FURNACE. *33rd European Photovoltaic Solar Energy Conference and Exhibition*, (November). <https://doi.org/10.4229/EUPVSEC20172017-2CO.9.4>
- Wang, P., Sridharan, R., Ng, X. R., Khanna, A., Venkataraj, S., & Stangl, R. (2019). Investigating Industrial Metallization Solutions for Double-side Contact Passivated biPoly Solar Cells. *2019 IEEE 46th Photovoltaic Specialists Conference (PVSC)*, 1143–1147. <https://doi.org/10.1109/PVSC40753.2019.8980500>
- Weeber, A. W., Rieffe, H. C., Romijn, I. G., Sinke, W. C., & Soppe, W. J. (2005). The fundamental properties of SiNx:H that determine its passivating qualities. *Conference Record of the IEEE Photovoltaic Specialists Conference*, 1043–1046. <https://doi.org/10.1109/pvsc.2005.1488312>
- Winter, M., Bordihn, S., Peibst, R., Brendel, R., & Schmidt, J. (2020). Degradation and Regeneration of n+-Doped Poly-Si Surface Passivation on p-Type and n-Type Cz-Si Under Illumination and Dark Annealing. *IEEE Journal of Photovoltaics*, 10(2), 1–8. <https://doi.org/10.1109/jphotov.2020.2964987>
- Wright, P., & Saraswat, K. (1989). The effect of fluorine in silicon dioxide gate dielectrics. *IEEE Transactions on Electron Devices*, 36(5), 879–889. <https://doi.org/10.1109/16.299669>
- Wu, W., Bao, J., Ma, L., Chen, C., Liu, R., Qiao, Z., Chen, J., & Liu, Z. (2019). Development of Industrial n-Type Bifacial TOPCon Solar Cells and Modules. *36th European Photovoltaic Solar Energy Conference and Exhibition*. <https://doi.org/10.4229/EUPVSEC20192019-2BP.1.5>
- Wurfel, P., & Würfel, U. (2016). *Physics of Solar Cells: From Basic Principles to Advanced Concepts* (3rd ed.). Wiley-VCH.
- Würfel, U., Cuevas, A., & Würfel, P. (2015). Charge carrier separation in solar cells. *IEEE Journal of Photovoltaics*, 5(1), 461–469. <https://doi.org/10.1109/JPHOTOV.2014.2363550>
- Wyss, P., Jeangros, Q., Diaz Leon, J. J., Allebé, C., Nicolay, S., Haug, F.-J., Ingenito, A., & Ballif, C. (2020a). Firing-through metallisation of PERT-like cells using $\mu\text{c-Si (n)}$ as thin rear side full area passivating contact. *Proceedings of the EU PVSEC 2020*. <https://doi.org/10.4229/eupvsec20202020-2bo.2.5>
- Wyss, P., Stuckelberger, J., Nogay, G., Horzel, J., Jeangros, Q., Mack, I., Lehmann, M., Niquille, X., Allebe, C., Despeisse, M., Haug, F.-J., Ingenito, A., Loper, P., & Ballif, C. (2020b). A Mixed-Phase SiO_x Hole Selective Junction Compatible With High Temperatures Used in Industrial Solar Cell Manufacturing. *IEEE Journal of Photovoltaics*, 10(5), 1262–1269. <https://doi.org/10.1109/JPHOTOV.2020.3006979>
- Xu, Z., Tao, K., Jiang, S., Jia, R., Li, W., Zhou, Y., Jin, Z., & Liu, X. (2020). Application of polycrystalline silicon carbide thin films as the passivating contacts for silicon solar cells. *Solar Energy Materials and Solar Cells*, 206(August 2019), 110329. <https://doi.org/10.1016/j.solmat.2019.110329>

- Yablonovitch, E., Gmitter, T., Swanson, R. M., & Kwark, Y. H. (1985). A 720 mV open circuit voltage SiO_x:c-Si/SiO_x double heterostructure solar cell. *Applied Physics Letters*, 47(11), 1211–1213. <https://doi.org/10.1063/1.96331>
- Yamamoto, K., Adachi, D., Yoshikawa, K., Yoshida, W., Irie, T., Konishi, K., Fujimoto, T., Kawasaki, H., Kanematsu, M., Ishibashi, H., Uto, T., Takahashi, Y., Terashita, T., Koizumi, G., Nakanishi, N., & Yoshimi, M. (2017). Record-Breaking Efficiency Back-Contact Heterojunction Crystalline Si Solar Cell and Module. *33rd European Photovoltaic Solar Energy Conference and Exhibition RECORD-BREAKING*, 201–204. <https://doi.org/10.4229/EUPVSEC20172017-2BP1.1>
- Yamamoto, T., Uwasawa, K., & Mogami, T. (1999). Bias temperature instability in scaled p⁺-polysilicon gate p-MOSFET's. *Electron Devices, IEEE Transactions on*, 46(5), 921–926. http://ieeexplore.ieee.org/xpls/abs_all.jsp?arnumber=760398
- Yan, D., Cuevas, A., Michel, J. I., Zhang, C., Wan, Y., Zhang, X., & Bullock, J. (2021). Polysilicon passivated junctions: The next technology for silicon solar cells? *Joule*, 5(4), 811–828. <https://doi.org/10.1016/j.joule.2021.02.013>
- Yang, Y., Altermatt, P. P., Cui, Y., Hu, Y., Chen, D., Chen, L., Xu, G., Zhang, X., Chen, Y., Hamer, P., Bonilla, R. S., Feng, Z., & Verlinden, P. J. (2018). Effect of carrier-induced hydrogenation on the passivation of the poly-Si/SiO_x/c-Si interface. *AIP Conference Proceedings*, 1999, 040026. <https://doi.org/10.1063/1.5049289>
- Ye, F., Deng, W., Guo, W., Liu, R., Chen, D., Chen, Y., Yang, Y., Yuan, N., Ding, J., Feng, Z., Altermatt, P. P., & Verlinden, P. J. (2016). 22.13% Efficient industrial p-type mono PERC solar cell. *2016 IEEE 43rd Photovoltaic Specialists Conference (PVSC)*, 3360–3365. <https://doi.org/10.1109/PVSC.2016.7750289>
- Young, D. L., Theingi, S., Lasalvia, V., Chen, K., Nemeth, W., Findley, D., Page, M., Stradins, P., Young, D. L., Theingi, S., Lasalvia, V., Chen, K., Nemeth, W., Findley, D., Page, M., & Stradins, P. (2019). Self-Aligned , Selective Area Poly-Si / SiO₂ Passivated Contacts for Enhanced Photocurrent in Front / Back Solar Cells. *46th IEEE PVSC*, (November). <https://www.nrel.gov/docs/fy20osti/74072.pdf>
- Zhang, D., Tavakoliyaraki, A., Wu, Y., Van Swaaij, R. A., & Zeman, M. (2011). Influence of ITO deposition and post annealing on HIT solar cell structures. *Energy Procedia*, 8(April), 207–213. <https://doi.org/10.1016/j.egypro.2011.06.125>
- Zhu, Y., Rougieux, F., Grant, N., Mullins, J., De Guzman, J. A., Murphy, J. D., Markevich, V. P., Coletti, G., Peaker, A. R., & Hameiri, Z. (2019). New insights into the thermally activated defects in n-type float-zone silicon. *AIP Conference Proceedings*, 2147(August). <https://doi.org/10.1063/1.5123901>

List of publications

Publications in peer-reviewed journals

- M. Lehmann, S. Libraro, A. Morisset, P. Wyss, N. Badel, C. Allebé, J. Diaz Leon, A. Ingenito, F.-J. Haug, C. Ballif, (2022). Both-sides-contacted solar cells featuring *p*- and *n*-type passivating contacts formed during a single co-firing. Letter planned.
- M. Lehmann, A. Desthieux, N. Valle, A. Morisset, P. Wyss, S. Eswara, T. Wirtz, A. Ingenito, P. Roca i Cabarrocas, C. Ballif, F.-J. Haug, (2022). Bulk Defects and Hydrogenation Kinetics in Fired Passivating Contacts. *IEEE Journal of Photovoltaics*. Manuscript submitted.
- C.N.S. Kumar, S. Tabeau, A. Morisset, P. Wyss, M. Lehmann, F.-J. Haug, Q. Jeangros, A. Hessler-Wyser, N. Valle, T. Wirtz, S. Eswara, (2021). Evaluation of secondary electron intensities for dopant profiling in ion implanted semiconductors: a correlative study combining SE, SIMS and ECV methods. *Semiconductor Science and Technology*, 36, 085003. <https://doi.org/10.1088/1361-6641/ac0854>.
- F.-J. Haug, A. Morisset, P. Wyss, M. Lehmann, A. Hessler-Wyser, Q. Jeangros, A. Ingenito, C. Ballif, C.N.S. Kumar, S. Eswara, N. Valle, (2021). Passivating Polysilicon Recombination Junctions for Crystalline Silicon Solar Cells. *Physica Status Solidi – Rapid Research Letters*, 2100272. <https://doi.org/10.1002/pssr.202100272>.
- L. Antognini, V. Paratte, J. Haschke, J. Cattin, J. Dreon, M. Lehmann, L. Senaud, Q. Jeangros, C. Ballif, M. Boccard, (2021). Influence of the Dopant Gas Precursor in P-Type Nanocrystalline Silicon Layers on the Performance of Front Junction Heterojunction Solar Cells. *IEEE Journal of Photovoltaics*, 11, 4, 944–956. <https://doi.org/10.1109/JPHOTOV.2021.3074072>.
- S. Pal, J. Barrirero, M. Lehmann, Q. Jeangros, N. Valle, F.J. Haug, A. Hessler-Wyser, C.N. Shyam Kumar, F. Mücklich, T. Wirtz, S. Eswara, (2021). Quantification of hydrogen in nanostructured hydrogenated passivating contacts for silicon photovoltaics combining SIMS-APT-TEM: A multiscale correlative approach. *Applied Surface Science*, 555, 149650. <https://doi.org/10.1016/j.apsusc.2021.149650>.
- P. Wyss, J. Stuckelberger, G. Nogay, J. Horzel, Q. Jeangros, I. Mack, M. Lehmann, X. Niquille, C. Allebe, M. Despeisse, F.-J. Haug, A. Ingenito, P. Loper, C. Ballif, (2020). A

Mixed-Phase SiO_x Hole Selective Junction Compatible With High Temperatures Used in Industrial Solar Cell Manufacturing. *IEEE Journal of Photovoltaics*, 10, 5, 1262–1269. <https://doi.org/10.1109/JPHOTOV.2020.3006979>.

- M. Lehmann, N. Valle, J. Horzel, A. Pshenova, P. Wyss, M. Döbeli, M. Despeisse, S. Eswara, T. Wirtz, Q. Jeangros, A. Hessler-Wyser, F.-J. Haug, A. Ingenito, C. Ballif, (2019). Analysis of hydrogen distribution and migration in fired passivating contacts (FPC). *Solar Energy Materials and Solar Cells*, 200, 110018. <https://doi.org/10.1016/j.solmat.2019.110018>.
- S. Eswara, A. Pshenova, E. Lentzen, G. Nogay, M. Lehmann, A. Ingenito, Q. Jeangros, F.-J. Haug, N. Valle, P. Philipp, A. Hessler-Wyser, T. Wirtz, (2019). A method for quantitative nanoscale imaging of dopant distributions using secondary ion mass spectrometry: an application example in silicon photovoltaics. *MRS Communications*, 9, 3, 916–923. <https://doi.org/10.1557/mrc.2019.89>.
- S. Thomas, P. Peralta, R. Mottet, M. Lehmann, Y. Civet, Y. Perriard, (2018). Analysis and Reduction of Time Response in Thermally Activated Shape Memory Alloys. *Proceedings of the 21st International Conference on Electrical Machines and Systems (ICEMS)*, 1783–1788, IEEE, Jeju, Korea. <https://doi.org/10.23919/ICEMS.2018.8549332>.

Contributions in conferences

- M. Lehmann, A. Desthieux, N. Valle, A. Morisset, P. Wyss, S. Eswara, T. Wirtz, A. Ingenito, P. Roca i Cabarrocas, C. Ballif, F.-J. Haug, (2021). Bulk Defects and Hydrogenation Kinetics in Fired Passivating Contacts. *31st International PV Science and Engineering Conference (PVSEC-31)*, online/Sydney, Australia. Oral presentation.
- M. Lehmann, P. Wyss, S. Librario, N. Valle, B. El Adib, X. Niquille, F. Meyer, E. Genç, J. Diaz Leon, C. Allebé, M. Despeisse, S. Eswara, T. Wirtz, Q. Jeangros, A. Hessler-Wyser, A. Ingenito, F.-J. Haug, C. Ballif, (2020). Further Insight into Hydrogenation of Fired Passivating Contacts. *SiliconFOREST Workshop 2020*, Falkau, Germany. Oral presentation.
- M. Lehmann, N. Valle, J. Horzel, A. Pshenova, P. Wyss, X. Niquille, M. Döbeli, G. Nogay, J. Stuckelberger, F. Meyer, A. Savoy, C. Allebé, M. Despeisse, S. Eswara, T. Wirtz, Q. Jeangros, A. Hessler-Wyser, F.-J. Haug, A. Ingenito, C. Ballif, (2019). Analysis of Hydrogen Distribution and Migration in Fired Passivating Contacts. *9th International Conference on Crystalline Silicon Photovoltaics (SiliconPV)*, Leuven, Belgium. Oral presentation. Received the **SiliconPV Award** for one of the 10 best ranked contributions.
- M. Lehmann, N. Valle, J. Horzel, A. Pshenova, X. Niquille, P. Wyss, G. Nogay, J. Stuckelberger, F. Meyer, A. Savoy, C. Allebé, M. Despeisse, S. Eswara, T. Wirtz, Q. Jeangros, A. Hessler-Wyser, A. Ingenito, F.-J. Haug, C. Ballif, (2019). Untersuchung und Entwicklung von Gefeuerten Passivierenden Kontakten. *SiliconFOREST Workshop 2019*, Falkau, Germany. Oral presentation.

Mario LEHMANN

Erlacherweg 37
2503 Biel/Bienne
079 475 20 25
mariolehmman@gmx.ch

30 years old (29.07.1991)
Swiss
Single



EDUCATION

EPFL, Ecole Polytechnique Fédérale de Lausanne, Lausanne

- PhD in Physics, research on potential next generation of industrial solar cells 09.2017 - 01.2022
- Master in Applied Physics, specialisation in solid-state physics 09.2013 - 07.2015
- Bachelor in Physics 09.2010 - 07.2013

Kantonsschule am Burggraben, St.Gallen

- Swiss Matura diploma, major subject : latin, minor subject : physics 08.2006 - 07.2009

PROFESSIONAL EXPERIENCE

SPF, HSR (Hochschule Rapperswil), Rapperswil, civilian service (3 months)

03.2016 – 06.2016

- Characterisation of solar panels with a mobile laboratory
- Literature reviews (life-cycle assessments of PV-systems, coatings for solar collectors)

PV-Lab, EPFL, Neuchâtel, internship (6 months)

09.2015 – 03.2016

- Optimisation of minority carrier lifetime using annealing with a hydrogen donor layer
- Co-planning of a customised experimental setup to be acquired and built
- Supervision of a semester project student (1.5 days per week)

Rolex SA, Genève, Materials and Technologies Research Department, internship (6 months)

08.2014 - 02.2015

- Creation and optimisation of a model for optical measurements
- Mechanical measurements and analysis to optimise the coating of a certain component

ACADEMIC PROJECTS

PV-Lab, EPFL, Neuchâtel, Master Project

02.2015 – 07.2015

- Optimisation of the back contact in silicon heterojunction solar cells : Reduction of the contact resistivity by moving from amorphous to microcrystalline silicon layers

Laboratory of Complex Matter Physics, EPFL, Lausanne

- Study of the formation mechanism of nanofilaments : Design and realisation of a synthesis method allowing a study by scanning electron microscopy 09.2013 - 02.2014
- Opto-electronic characterisation of hybrid organic-inorganic perovskite-graphene phototransistors: Article published (DOI: 10.1002/sml.201501257) 02.2014 - 07.2014

TECHNICAL AND COMPUTER SKILLS

Technical	Thin film deposition (PECVD, sputtering), wet chemistry, cleanroom experience Characterisation: SEM, SIMS (data analysis), ellipsometry, FTIR, Raman, PL & EL imaging Lectures in physics of materials (semiconductors, dislocations, diffusion, phase transformations)
Computer	MATLAB®, C++, Mathematica, Origin® (basic skills), LabVIEW (basic skills), LaTeX, MS Office

LANGUAGES

Bilingual	Swiss German (mother tongue) and French
English	Level C1 (Certificate in Advanced English, Cambridge ESOL, 06.2010)

EXTRA-CURRICULAR ACTIVITIES

Work with youth

- Scout leader, Flambeaux de l'Evangile d'Orvin: biweekly meetings counting about 25 kids and teens (7-17 years old), camps, bushcraft, sports, orienteering, zipline, first aid, morse 11.2018 - present
- J+S certifications (leader, camp director, safety modules) in camp sports/trekking 06.2014 - present
- Camp counsellor and director, various organisations: adventure, sports, skiing, outdoors 08.2014 - 07.2018
- Leader in a scouting movement (BESJ) counting about thirty 6-13 years old children 08.2007 - 10.2009

AVC Hellas, Athens, Greece, humanitarian volunteering (refugee aid)

03.2017 - 06.2017

- Creation of teaching material for English classes & teaching English and German

Hobbies

- Ski touring, climbing, hiking, playing the drums, floorball, board games, singing

Acknowledgements

This manuscript is the result of more than 4 years of research at the EPFL's photovoltaics and thin-film electronics laboratory (PV-Lab) and was financed by the Swiss National Science Foundation (SNF), under grant no. 200021L_172924/1, whose support is gratefully acknowledged.

Firstly, I want to thank my thesis director Franz-Josef Haug. Thank you for your guidance, your availability, insight and moral support whenever needed. I appreciated your detailed understanding of the theory behind our work, your passion for thorough understanding, and all the efforts you invested into analyzing my measurements with your numerical models. Thank you also for the discussion about science, research and life, as well as your guidance and insight during ski touring, climbing and hiking. I want to thank also my thesis co-director, Christophe Ballif. Thank you for your supervision and feedbacks, your broad and detailed understanding of the field and the strategic meetings reorienting my work. I also want to thank Andrea Ingenito, who followed my work closely too. Thanks for all the advice and practical support. My thanks go also to Quentin Jeangros and Aïcha Hessler-Wyser who set up this project and supported it.

My gratitude goes also towards the members of my jury, Prof. Frédéric Mila, Prof. Stefan Glunz, Dr. Sébastien Dubois and Prof. Paul Mural, for taking the time to read this thesis, attend its defense and for their valuable expertise and feedback.

I warmly thank the members of the HTPC group. Thank you Josua and Gizem, for sharing your know-how on passivating contacts. Thank you Philippe, our dear (and a bit crazy) chemist, for all your help and the countless hours shared in the clean room. Thank you Audrey, for your technical and moral support during the final part of this adventure. Thank you Sofia, Ezgi, Frank, Arnaud, Xavier, HyunJung, Joël and Julien. It was a pleasure to work and spend time with all of you. I also want to thank all the people from other institutions I had the chance to collaborate with: Jörg, Priscille, Anatole, Pere, Max, Christoph, Brahime, Santhana, Alisa, Shyam, Soupitak, Juan, Christophe, Fabien, Patrick, Nicolas and Ludovic. A special thank you to Nathalie for all the discussions about SIMS and advanced characterization of my samples.

A big thank you to our technical staff: Cédric, Lionel, Aymeric, Nicolas, Nathanaël, Xavier and Sylvain. Your dedication to keeping the equipment up and running and your quick help whenever needed were highly appreciated. Thank you Mary-Claude and Karine for the administrative support. And thanks also to Hassan for taking care of the IT infrastructure.

My warm thanks go also to Peter, Luca, Olatz and Terry, with whom I shared the office, and all my colleagues from Neuchâtel. All of you make this lab an amazing place to be and filled the past years with fond memories. Thanks for your motivation to work hard for a shared cause, the funny, deep and philosophical conversations around a coffee and all the good times spent besides work. Thank you Lionel, for dragging me along running up to Chaumont, ski touring up to the Tschingellochtighore or climbing La Nostalgique. Thanks to Olivier, Jean, Delphine, Janina, Marion, Peter, Stefanie, Franz and Quentin for the bouldering, climbing, slacklining and ski touring outings. Thank you also Laurie-Lou, Luca, Julie, Jordan, Jonathan, Samira, Quentin and Alejandro for your fellowship on this journey as PhD students.

I am also deeply grateful towards all my friends distributed all over Switzerland and beyond, for their encouragements, interest, prayers and love, for challenging me and believing in me. It makes life beautiful, allows overcoming hardship and catalyzes joy. Thank you Benoît and Clément for your precious friendship, for all the good memories, and for being there for me. Thank you Micha, Simona and Simon. Thank you Valentine, Maude, Antoine and Vanessa for your companionship and for sharing the vision of La grande tablée. Many thanks also to my friends from the Flambeaux d'Orvin and the Jahu for welcoming me in Biel/Bienne. And thank you Christof, Jan, Gabriel, David, Taco, Jonathan and Ben for sharing life as flatmates over the past years.

Thank you, from the bottom of my heart, Mama, Papa, Jaël, Simone and Pietro. Your unconditional love and support throughout my life give me roots and wings.

Finally, I want to thank my God, Father and King, from whom, through whom and for whom I believe all things were, are, and will be.

Neuchâtel, November 2021

Mario Lehmann